Numerical analysis of partial differential equations for viscoelastic and free surface flows.

Al-Muslimawi, Alaa Hasan A

Numerical Analysis of Partial Differential Equations for Viscoelastic and Free Surface Flows

Alaa Hasan A. Al-Muslimawi

Thesis submitted to Swansea University

in fulfilment of the requirements for the degree of Doctor of Philosophy

Department of Mathematics

University of Swansea

2013

DEDICATION

Praise and give thanks to God

To my Mother's spirit,

To my Dear Father,

To my Brother, Firas and his family,

To my wife and my sons,

To my sisters,

To my friends,

I dedicate this work

DECLARATION

This work has not previously been accepted in substance for any degree and is not being concurrently submitted in candidature for any degree.

Signed ..... (candidate)

Date ....26/07/2013.....

STATEMENT 1

This thesis is the result of my own investigations, except where otherwise stated. Where correction services have been used, the extent and nature of the correction is clearly marked in a footnote(s).

Other sources are acknowledged by footnotes giving explicit references. A bibliography is appended.

Signed ..... (candidate)

Date ....26/07/2013.....

STATEMENT 2

I hereby give consent for my thesis, if accepted, to be available for photocopying and for inter-library loan, and for the title and summary to be made available to outside organisations.

Signed ..... (candidate)

Date ....26/07/2013.....

Acknowledgement

This work was carried out during the years from 2010 to 2013 at the Department of Mathematics/ College of Science/ Swansea University.

It is with massive gratitude that I acknowledge the constant optimism concerning this work, enthusiasm, encouragement and support of my supervisor Prof. M. F. Webster, without which this study would hardly have been completed. I also express my warmest gratitude to my other supervisor Dr. Ian M. Davies. Their guidance and advice have been essential during this work. I would like to also show my gratitude to Dr H.R. Tamaddon-Jahromi for his interest, help and valuable hints during my study. I have an honour to express my deep appreciation to the Ministry of Higher Education/ Iraq for sponsoring this project and I give my warm appreciation to the Iraqi Cultural Office/ London for their efforts during this study period. Many thanks to all those who assisted me and believed in the importance of this research.

Abstract

This thesis is concerned with the numerical solution of the partial differential equation system that governs incompressible viscous, viscoelastic and viscoelastoplastic flows in the presence of dynamic free-surfaces. The Navier-Stokes momentum differential equation and continuity differential equation govern the Newtonian and inelastic fluids, whilst for the viscoelastic case different constitutive equations are utilised. Numerically, a hybrid finite element/finite volume discretisation (*fe/fv)* scheme is proposed to solve the corresponding system of partial differential equations. In this context, a Taylor-Galerkin/pressure correction finite element method has been adopted for the parabolic-elliptic momentum-continuity equations, whilst a finite volume implementation is utilised for the hyperbolic sub-system comprising of the constitutive equation.

Certainly, the free surface treatment represents the main part of this study. Initially, the die-swell benchmark problem with a single moving free-surface has been studied, using a time-dependent free-surface predictions technique, termed the Phan-Thien (*dh/dt*) approach. Subsequently, and as begun under the die-swell problem, the work has been extended to address a cable-coating flow problem with two separate free-surfaces, presenting inner and outer (lower/bottom and upper/top) surfaces to a moving melt-conduit. Here, a new robust free-surface location technique has been proposed, utilising a decoupled (independent) approach in calculation between top and bottom conduit surfaces. Moreover, different alternative stabilisation strategies have been analysed to enhance the numerical stability of this overall procedure.

Concerning viscoelastic fluids, two different constitutive models have been adopted to describe and simulate rheological response. Under the die-swell flow problem an exponential Phan-Thien Tanner (EPTT) type model has been implemented, with properties of shear-thinning, strain-hardening/softening, moderate-high Trouton ratios. In addition, a combination of viscoplastic models with the viscoelastic models has been considered: using a Papanastasiou-Bingham for the viscoplastic approximation, and an exponential Phan-Thien Tanner (EPTT) for the viscoelastic contribution.

Moreover, the cable coating problem has been investigated under the umbrella of the exponential Phan-Thien Tanner (EPTT) and Single Extended pom–pom model (SXPP).

Contents

Chapter 1

Introduction

Partial differential equations (PDE) are equations involving unknown functions of two or more variables and their partial derivatives [107]. A PDE is said to be of order p if it contains at least one derivative of order p and does not contain derivatives of higher order. The general form of a PDE of order p for an unknown function u is:

$$\phi(x_1,\cdots,x_n,u,\frac{\partial u}{\partial x_1},\cdots,\frac{\partial u}{\partial x_n},\frac{\partial^2 u}{\partial x_1^2},\cdots,\frac{\partial^2 u}{\partial x_1 \partial x_2},\cdots,\frac{\partial^p u}{\partial x_n^p})=0, \tag{1.1}$$

where, ϕ is a function of the indicated quantities. Equation (1.1) is in general a nonlinear relationship. These equations are classified into three types: elliptic, parabolic and hyperbolic. This body of research is mainly concerned with the partial differential equations for fluid dynamics. In particular, the Navier-Stokes equations will be studied, including time dependent terms to govern the Newtonian case, while a number of models have been developed for the non-Newtonian case.

In the field of Computational Fluid Dynamics (CFD), the solution of a non-linear system of partial differential equations, which govern the complex flows of compressible and incompressible, Newtonian and non-Newtonian fluids, has attracted considerable attention in the literature (see for example Crochet et al. [43], Kikuchi [67], Bird et al. [23], Abbott and Basco [1], and Zienkiewicz et al. [147]). As is well known, fluid response may be classified as Newtonian or/and non-Newtonian [14]. For a simple shear flow, under

constant pressure and temperature, Newtonian fluids exhibit a linear relationship between shear stress and shear rate through a constant viscosity. The behaviour of such fluids can be predicted on the basis of the Navier-Stokes differential equations. In contrast, non-Newtonian fluids depart from such a linear relationship, and show a variable relationship between shear stress and shear rate. Shear-thinning/shear-thickening are typical examples of such behaviour. Such fluids may be termed non-Newtonian viscous fluids or generalised Newtonian fluids in the absence of elasticity. Shear-thinning demands that viscosity decreases with increasing shear rate, whilst shear-thickening designates the opposite trend. In such a context, the Navier-Stokes equations may prove less adequate to predict the flow behaviour of such fluids. Consequently, additional constitutive differential equations must be advanced to characterise the flow behaviour for such fluids.

In classical CFD, a broad spectrum of numerical algorithms is offered based on finite difference, finite element, finite volume, boundary integral, spectral methods, and combinations thereof. Yet, the range of applications of a particular numerical technique may be problem and context dependent. For typical flow problems, it is not possible to solve such problems analytically. Throughout the history of computation, numerical investigation has advanced in addressing many and various scientific problems. In this context several numerical techniques have been developed to solve systems of partial differential equations. Indeed, for such problems three main methods have appeared: finite difference method (FDM) [113], finite element method (FEM) [148], [149], [150], [151] and finite volume method (FVM) [131].

Recently, the finite element method (FEM) has become the most widespread numerical scheme used to solve scientific problems (see for example [152], [153], [154], [38]). In fact, this method is widely used in numerical procedures to solve systems of differential or integral equations (change of type of the equations and mesh refinements can improve solution accuracy). Moreover, the finite element method has been applied to a large number of physical problems. The method essentially consists of assuming a piecewise continuous form for the solution and obtaining the weights of the functions in a manner that reduces

the weighted residual error in the solution. In this method of analysis, a complex region defining a continuum is discretised into simple geometric shapes called finite elements. The material properties and governing relationships are considered over these elements and expressed in terms of unknown values at element junctions. A discretisation (interpolation and weighting) and assembly process, duly considering the loading and constraints, results in a corresponding set of algebraic equations. Solution of these equations gives the approximate behaviour of the continuum. One advantage of the finite element method, over the finite difference method, is the relative comfort with which associated boundary conditions are handled. Many physical problems have boundary conditions involving derivatives and, in general, finite difference techniques require a derivative to be approximated by a difference quotient at the grid points; often a difficult task to perform to high precision. The finite element method includes the boundary conditions naturally, as integrals in a functional to be minimized, so the construction procedure is independent of the particular nature of the boundary conditions applied. In contrast, the disadvantage of this method lies in the size of the mesh and the computational time needed for the solution process with complex flow problems.

The considerable computational demands in modelling complex flows require advanced numerical strategies including upwinding, accurate representation of velocity gradients, and couplings within the system. Hence, alternative techniques have arisen, such as the finite volume approach, which requires less memory and CPU time than the well-known FEM. This method is control-volume oriented, being derived from the ideology behind the finite difference scheme, and can often be interpreted directly as a finite difference approximation to the differential equation [58]. As is well known, the finite difference approximation is employed to solve the system of finite-difference algebraic equations equivalent to the differential equations, while the finite volume method solves the integral form of the differential equations. However, FVM is based on the integral form of the conservation law, a starting point that turns out to have many advantages. One of the main advantages of the FVM method over the FDM is that it is more appropriate for complex geometries. In

addition, the FVM is suitable for the numerical investigation of different types (elliptic, parabolic or hyperbolic, for example) of conservation laws; it has been widely utilised in diverse fields, such as fluid mechanics, heat and mass transfer (see for example [3], [19], [46], [61], [88], [106], [109], [142]). Some of the important features of the finite volume method are similar to those of the finite element method, see Oden [98]: it might be used on arbitrary geometries, utilising structured or unstructured meshes, and it leads to robust schemes. An additional feature is the local conservation property for the numerical fluxes, conserved across the boundary between one discretization cell and another. This last feature makes the finite volume method quite attractive when modelling problems for which the flux is of importance, such as in fluid mechanics, semi-conductor device simulation, heat and mass transfer. The finite volume method is locally conservative because it is based on a "balanced" approach (a local balance is written for each control-volume discretization cell) and via the divergence formula, gives an integral formulation of the fluxes over the boundaries. The fluxes across the boundaries can then be discretized with respect to the discrete unknowns.

A hybrid finite element/finite volume *(fe/fv)* algorithm is introduced to address the more complex flows. Here, a combination of finite element method (FEM) and finite volume method (FVM) is performed to achieve a much more stable method. The features of this approach are the use of the finite element method for elliptic mass and momentum balance, and the finite volume method for hyperbolic constitutive equations ([137], [138]).

On another hand, the free-surface concept remains a numerical challenge due to accuracy requirements and computational costs. Many schemes can be used to treat free-surface computations, such as the volume of fluid (VOF) scheme ([59], [116]) marker and cell method (MAC), the arbitrary Lagrangian Eulerian technique (ALE) ([116], [62]), and Phan-Thien *(dh/dt)* method [103]. Under the VOF-method, the flow domain is divided into two distinct parts: one wet and another dry. Here, the interface between wet and dry zones is defined by the position of the free-surface. When utilising the VOF-method to model the free-surface deformation, the initial rectangular mesh is stretched in the axial direction

alone, with axial redistribution performed through an elliptic-mapping mesh redistribution strategy. In contrast, with ALE methods, the mesh itself is transported with a mesh velocity, a suitable choice of which constitutes one of the major aspects involved. The *dh/dt* scheme has been employed within the current study, proving ideal to accommodate the particular free-surface nodal movement encountered, by restricting this to radial motion alone (so with no loss or gain of particle nodes) ([35], [139]). This is equivalent to a constrained ALE-algorithm.

The present work is concerned with the numerical solution of extrusion problems (so-called extrudate swell flow), which are of particular importance in industrial polymer melt processing, involving Newtonian, general Newtonian, and viscoelastic fluid properties. Here, a finite element method (FEM) is used alone to address the Newtonian and general Newtonian cases, whilst a hybrid finite element/finite volume (*fe/fv*) approach is employed to solve for viscoelastic fluids. In addition, this research is associated with problems that involve free-surface boundaries. Consequently, emphasis is given to address two different problems; die-swell and cable-coating. Schematic diagrams to illustrate the settings for these two problems, of die-swell and cable-coating, are presented below in Figure 1.1.

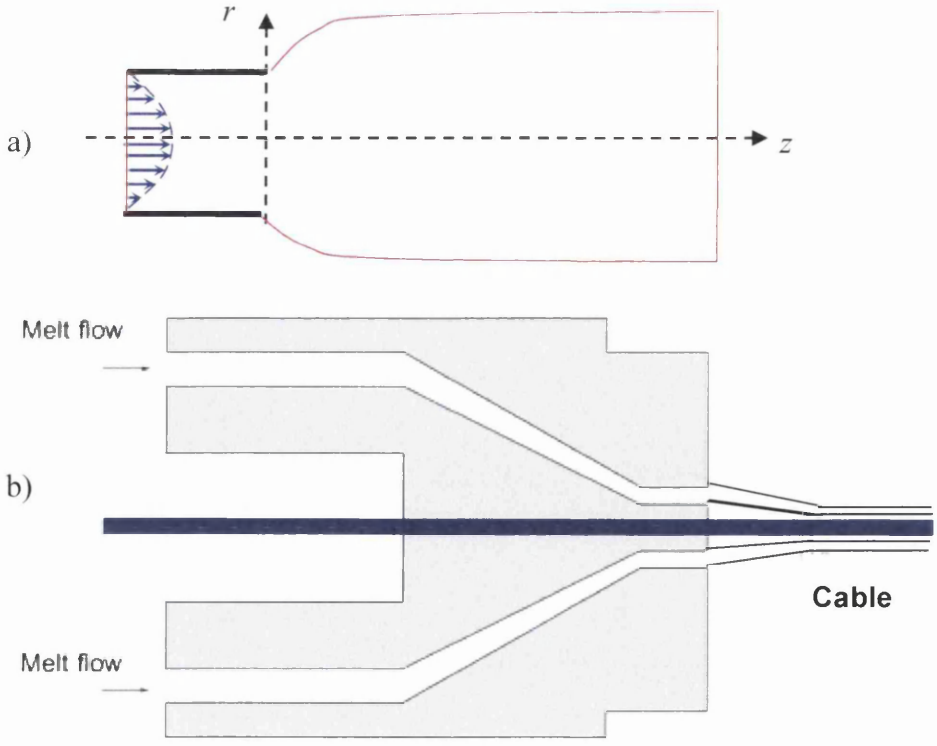

Figure 1.1: Schematic diagram: a) die-swell, b) cable-coating

The mathematical equations of fluid motion are introduced in chapter two, including constitutive equations relation for Newtonian and non- Newtonian fluids. A detailed study is introduced through the network class of models, of exponential Phan-Thien Tanner (EPTT) type; shear-thinning, strain-hardening/softening, moderate-high Trouton ratios and eXtended pom-pom (XPP) model. The analysis is then extended into viscoelastoplasticity through the viscous-limiting Papanastasiou approximation, coupling this with the Phan-Thien Tanner model. Here, the rheological properties are described for the Papanastasiou-Exponential Phan-Thien Tanner (Pap-EPTT) model with respect to the model parameters in question. In particular, steady-state shear (η) and extensional (η_E) viscosities, the shear stress (τ_{rz}) and first normal stress difference (N_1) are presented. Additional focus is given to the pom-pom model and the relationship between this model and the others in this chapter.

In chapter three, the theory and implementation of the numerical techniques are presented. In this study, a semi-implicit time-stepping Taylor-Galerkin/pressure-correction finite element method is used to solve the momentum and continuity flow equations whilst the constitutive partial differential equation is dealt with by a cell-vertex finite volume (*cv/fv*) algorithm. In addition, spatial discretisation has been introduced, the strain-rate stabilization (SRS) (D-D_c), and free-surface techniques are all features that are analysed. Moreover, the main steps of free-surface calculation are introduced.

Two dimensional/axisymmetric free-surface flows are introduced in chapter four through the study of die-swell flow, taking into account shear-thinning, strain-hardening/softening, and moderate-high Trouton ratios. This is achieved by combining the viscoplastic Papanastasiou-Bingham model with the viscoelastic Phan-Thien Tanner–(EPTT) model, suitable for polymer melt response. This permits a systematic study to be conducted on swelling ratio and flow response, as a consequence of viscous, plastic and viscoelastic material behaviour.

The numerical study of cable coating flows with tube-tooling type is dealt with in chapter five. The investigations are performed for Newtonian and inelastic fluids, with an axisymmetric system, involving the prediction of free-surfaces. Here, the finite element

method is utilised. Such a complex polymer melt extrusion-draw-coating flow displays a dynamic contact line, slip, die-swell and two separate free-surfaces, presenting an inner and outer conduit surface to the melt-coating. The application of free-surface location methodology, to determine the free-surface position has been considered in this chapter by employing coupled and decoupled schemes. The practical interest lies in determining efficient windows for process control over variation in material properties, stressing levels generated and vacuum pressure levels imposed. In addition, the influence of singularity capturing on the die-exit solution is explored using a *strain-rate stabilization* (*SRS*) technique. Moreover, some alternative numerical stability schemes are also examined in order to enhance temporal stability.

In chapter six, numerical investigation of tube-tooling cable-coating flow for viscoelastic fluids is demonstrated through the use of an exponential Phan-Thien Tanner (EPTT) model. Here, the hybrid finite element/finite volume discretisation *fe/fv* (*sc*) scheme is considered under both coupled and decoupled solution approaches (across the sub-stages within a time-step)). The effect of elasticity, solvent-fraction and second normal stress difference are presented in this chapter.

The numerical solution of viscoelastic tube tooling cable coating flow is presented in chapter seven using the single extended Pom-Pom model. Again a hybrid finite element/finite volume *fe/fv* (*sc*) approached is adopted in this study. Through this study, comparison between pom-pom model and EPTT model is conducted.

Finally, overall conclusions and future directions to this study are presented in chapter eight.

Chapter 2

Mathematical modelling

In this chapter, the structure of the basic mathematical equations are presented which relates surrounding forces to the internal response from the fluid along with the basic equations of fluid mechanics that allow the description of motion and conservation of mass. Various sets of differential equations (models) governing the flow of viscoelastic fluids are briefly explained, such as the Maxwell model, Oldroyd-B model, Phan-Thien/Tanner model and the Single Extended form of the pom-pom model (SXPP). A combination of the viscoplastic Papanastasiou-Bingham model with the viscoelastic Phan-Thien Tanner-(EPTT) model is also considered throughout this study.

2.1 Introduction

The definition of rheology is provided by Professor Bingham (Lafayette College, Indiana) as the study of the deformation and flow of matter. This definition extends to, on the one hand, Newtonian viscous liquids and on the other, Hookean elastic solids. In recent years the study of rheology has become much broader, including almost every aspect of the internal responses in deformed matter under the influence of imposed stress. The main subject of rheology is to map out the kinematics of the continuum within the system from the relationships among the material stresses. The equations governing such a relationship are known as the constitutive equations or stress equations of state.

The system of differential equations governing the flow of Newtonian and non-Newtonian fluids with both viscous and elastic properties has attracted some considerable attention in the literature in recent years [43]. This system is presented by the momentum (Navier-Stokes) equations. Consequently, mass conservation and momentum partial differential equations are exhibited for the Newtonian case. In contrast for non-Newtonian fluids, the Navier-Stokes equation must be generalised to spawn non-linear constitutive differential equations to describe the stress components. The highly non-linear nature of the mathematical constitutive equations ensures that, the solutions may only be obtained using numerical methods.

Furthermore, many free-surface flow problems are of interest in rheological computation, as in so-called die-swell, exhibited by an elastic liquid as it emerges from a capillary. For these types of flow and Newtonian fluids, the diameter of the issuing liquids is either slightly greater than or slightly less than the diameter of the capillary, depending on the value of the Reynolds number. In contrast, for elastic liquids, the diameter of the jet can be significantly greater than that of the capillary, and their ratio has been observed to reach four in some cases. Another effect is the so-called Weissenberg phenomenon or red-climbing effect. When a rotating rod is dipped into a vessel containing an elastic liquid, viscoelasticity, manifested through normal stress effects, generates a substantial rise in the free-surface near the rotating rod. Meanwhile, for the Newtonian fluid there is substantial drop or dip in the free surface to compensate for centrifugal forces.

2.2 Rheology and material functions

Rheology, defined as the science of deformation and flow, is now distinguished as an important field of scientific research in its own right (see for example [133,134,135]). Simple shear flow and extensional deformation flow represent examples of ideal rheometrical flows.

2.2.1 Simple shear flow

Under simple shear deformation and within a Cartesian coordinate system (x, y, z), the velocity components $u = (u_x, u_y, u_z)$ are defined as:

$$u_x = \dot{\gamma} y, \quad u_y = u_z = 0 \tag{2.1}$$

here $\dot{\gamma}$ represents the shear-rate define as $\dot{\gamma} = \frac{du_x}{dy}$.

The deformation rate tensor d is given by

$$d = \frac{1}{2}(\nabla u + \nabla u^T) = \frac{1}{2}\begin{bmatrix} 0 & \dot{\gamma} & 0 \\ \dot{\gamma} & 0 & 0 \\ 0 & 0 & 0 \end{bmatrix}. \tag{2.2}$$

Also, the first (N_1) and second (N_2) normal stress differences are expressed in the normal stress components, τ_{xx}, τ_{yy} and τ_{zz} as

$$N_1 = \tau_{xx} - \tau_{yy} = \dot{\gamma}^2 \psi_1(\dot{\gamma}) \tag{2.3}$$

$$N_2 = \tau_{yy} - \tau_{zz} = \dot{\gamma}^2 \psi_2(\dot{\gamma}) \tag{2.4}$$

where, ψ_1 and ψ_2 are the first and second normal stress coefficients (see for example Bird et al. [23] for details).

2.2.2 Elongational (Uniaxial extensional) flow

For steady uniaxial extensional flow, the velocity field is given by

$$u_x = \dot{\varepsilon} x, \quad u_y = -\frac{\dot{\varepsilon}}{2} y \quad \text{and} \quad u_z = -\frac{\dot{\varepsilon}}{2} z, \tag{2.5}$$

here $\dot{\varepsilon}$ represents the elongational rate. Correspondingly, the deformation rate tensor d is defined as

$$d = \frac{1}{2}(\nabla u + \nabla u^T) = \begin{bmatrix} \dot{\varepsilon} & 0 & 0 \\ 0 & -\frac{1}{2}\dot{\varepsilon} & 0 \\ 0 & 0 & -\frac{1}{2}\dot{\varepsilon} \end{bmatrix}. \tag{2.6}$$

In contrast, the stress differences then take the form

$$\tau_{xx} - \tau_{yy} = \tau_{yy} - \tau_{zz} = \dot{\varepsilon}\mu_e(\dot{\varepsilon}), \tag{2.7}$$

$$\tau_{xy} = \tau_{xz} = \tau_{yz} = 0, \tag{2.8}$$

where μ_e is an extensional viscosity which describes the flow behaviour in this state of deformation. Usually, the zero extension-rate viscosity μ_e for Newtonian fluids is constant, and satisfies the following relationship

$$\mu_e = 3\mu_0, \tag{2.9}$$

where μ_0 is the zero shear-rate viscosity in shear flow.

The Trouton ratio (Tr) represents the ratio of elongational viscosity to shear viscosity. To create a relationship between $\dot{\gamma}$ and $\dot{\varepsilon}$ and calculate shear and extensional viscosities, Jones et al. [64] introduced a definition for the Trouton ratio as:

$$Tr = \frac{\mu_e(\dot{\varepsilon})}{\mu_s(\dot{\gamma} = \sqrt{3}\dot{\varepsilon})}. \tag{2.10}$$

In the Newtonian case and for all values of $\dot{\varepsilon}$, Tr is equal to three, while in viscoelastic flow, this ratio is only expected to be satisfied in the limit of vanishingly small deformation rate,

$$Tr(\dot{\varepsilon} \to 0) = 3. \tag{2.11}$$

2.3 Mathematical equations and Constitutive models

This section deals with the formulation of the basic equations, in order to predict the behaviour of a flow system. These equations are derived from the basic principle of conservation of mass and momentum. The basic principle of mass conservation must be satisfied at every instant in the type of flow problems considered. This principle is expressed mathematically through the continuity equation (see [36,66,72]),

$$\frac{\partial \rho}{\partial t} + \nabla \cdot (\rho \mathbf{u}) = 0. \tag{2.12}$$

where, ρ is the fluid density, $\mathbf{u}$ the velocity vector and t represents time. For incompressible fluids, ρ is constant; hence equation (2.12) reduces to

$$\nabla \cdot u = 0. \tag{2.13}$$

Newton's second law of motion when applied to a fluid element, states that the change of linear momentum in a system is equal to the sum of the forces acting upon it (also known as the principle of conservation of linear momentum). The forces acting on the system may be of two types: *body* forces acting on the volume of fluid, such as gravitational and electromagnetic forces, and surface forces due to Cauchy stress tensor. Here, if torque is negligible, the Cauchy stress tensor may be considered to be symmetric. In contrast, if torque is applied, the Cauchy stress is unsymmetric as observed by Maxwell [77] and Voigt [132]. In the case of incompressible fluids, the Cauchy stress can be reduced to an isotropic pressure and an extra stress tensor. In differential form, this is given by (see Bird [23]):

$$\rho\left(\frac{\partial u}{\partial t} + u \cdot \nabla u\right) = -\nabla p + \nabla \cdot T + \rho F, \tag{2.14}$$

here p represents the pressure, T the extra stress tensor and F the body forces.

2.3.1 Newtonian modelling

For Newtonian fluids, the extra stress tensor T is defined as

$$T = 2\mu d. \tag{2.15}$$

Correspondingly, the rate of deformation d for general flows is expressed as,

$$d = \frac{1}{2}(\nabla u + [u]^T). \tag{2.16}$$

For an incompressible Newtonian fluid, in the absence of body forces and appealing to equation (2.15) into (2.14), realises the Navier-Stokes equation, which can be written in the form

$$\rho\frac{\partial u}{\partial t} = \mu\nabla^2 u - \rho u \cdot \nabla u - \nabla p. \tag{2.17}$$

2.3.2 Inelastic constitutive modelling

For inelastic (non-Newtonian) case, the extra stress tensor T may be recast as

$$T = 2\mu(\dot{\gamma}, \dot{\varepsilon})d. \tag{2.18}$$

with a shear-rate $\dot{\gamma}$ for simple shear flow, and strain-rate $\dot{\varepsilon}$ for extensional flow, defined generally as

$$\dot{\gamma} = 2\sqrt{II_d}, \tag{2.19}$$

$$\dot{\varepsilon} = 3\frac{III_d}{II_d}. \tag{2.20}$$

Here II_d and III_d represent the second and third invariants of the rate of strain tensor d which, under an axisymmetric coordinate system can be defined as

$$II_d = \frac{1}{2}tr(d^2) = \frac{1}{2}\{(\frac{\partial u_r}{\partial r})^2 + (\frac{\partial u_z}{\partial z})^2 + (\frac{u_r}{r})^2 + \frac{1}{2}(\frac{\partial u_r}{\partial z} + \frac{\partial u_z}{\partial r})^2\}, \tag{2.21}$$

and

$$III_d = \det(d) = \frac{u_r}{r}\{\frac{\partial u_r}{\partial r}\frac{\partial u_z}{\partial z} - \frac{1}{4}(\frac{\partial u_r}{\partial z} + \frac{\partial u_z}{\partial r})^2\}. \tag{2.22}$$

Hence, for incompressible inelastic fluid flows under an isothermal setting, the governing equations may be expressed as:

$$\nabla \cdot u = 0. \tag{2.23}$$

$$\rho\frac{\partial u}{\partial t} = \nabla \cdot (2\mu(\dot{\gamma}, \dot{\varepsilon})d) - \rho u \cdot \nabla u - \nabla p. \tag{2.24}$$

Here, for inelastic fluids the viscosity is a function of combined shear-rate and extension–rate. In contrast, Newtonian fluids are both shear-rate and strain-rate independent, manifesting a constant shear viscosity, zero first normal stress difference, and a constant extensional viscosity.

2.3.2.1 Material modelling considerations

For non-Newtonian fluids, there are many possible inelastic constitutive models to consider. Some of these models describe shear viscous stress response and the others present extensional response. In addition, many materials are non-Newtonian, and exhibit either shear-thinning or shear-thickening behaviour.

The most fundamental constitutive model is that which describes shear viscous stress response of power-law form, which describes shear-thinning or shear-thickening

behaviour. Fluids of this type, originally proposed by Ostwald-de Waele, may be expressed as

$$\tau = (k|\dot{\gamma}|^{m-1})\dot{\gamma} \tag{2.25}$$

where k is a consistency parameter and m is a power-law index. Then, higher k-values are found to exhibit more viscous fluid characteristics. When $m=1$, the Newtonian limiting approximation is recovered, with no shear-rate dependence; shear thinning is gathered for $m<1$ (as applied in this task) and shear-thickening is observed for $m>1$.
In contrast to the foregoing, and specifically to address extensional material properties, consideration is given to further shear-extensional viscous-inelastic models, Fit-I and Fit-II (see Binding et al. [21]). These provide for the following material shear viscosity and extensional viscosity dependence:

(a) Fit-I model

$$\begin{aligned} \mu_s(\dot{\gamma}) &= \mu_0(1+(K\dot{\gamma})^2)^{(m-1)/2} \\ \mu_E(\dot{\varepsilon}) &= 3\mu_0 \cosh(m\lambda\dot{\varepsilon}).(1+3(K\dot{\varepsilon})^2)^{(m-1)/2}, \end{aligned} \tag{2.26}$$

(b) Fit-II model

$$\begin{aligned} \mu_s(\dot{\gamma}) &= \mu_0(1+(K_1\dot{\gamma})^2)^{(m_1-1)/2} \\ \mu_E(\dot{\varepsilon}) &= 3\mu_0(1+3(K_1\dot{\varepsilon})^2)^{(m_1-1)/2}(1+(K_2\dot{\varepsilon})^2)^{(m_2-1)/2}, \end{aligned} \tag{2.27}$$

where, μ_0 is the zero-shear viscosity, and m and K in model Fit-I represent the parameters that describe the shear and extensional components. In addition, in model Fit-II K_1 and K_2 are natural time constants (not related to fluid elasticity), while m_1 and m_2 are power-law indices that control shear and strain rate behaviour, respectively.
In this fashion, we are able to introduce and discuss the concept of the Trouton ratio (ratio of extensional viscosity to shear viscosity), which is likely to have considerable bearing on these polymer melt flows.

2.3.3 Viscoplastic flow modeling

The concept of viscoplastic material was first introduced by Bingham [22] in (1922) when describing several types of paint. Viscoelasticity is the property of materials that exhibit both viscous and elastic characteristics when undergoing

deformation. Viscous materials resist shear flow and deform linearly with time under applied stress. Elastic materials strain instantaneously when stretched, and just as quickly return to their original state once stress is removed. Under this concept the so-called 'yield stress τ_0' is exhibited. The existence of a "yield stress" is traditionally recognised to be responsible for the complicated transition between classical solid-like and liquid-like behaviour (base yield stress factor, equivalent to a Bingham Number, Bn=(τ_y)*($l/\mu_0 U$), with scaling on the dimensional yield stress τ_y). Many materials such as paint, slurries, pastes and some food products have been described by the Bingham model. This model may be expressed through the following equation:

$$\tau = \left(\mu + \frac{\tau_0}{2|II_d|^{\frac{1}{2}}} \right) \dot{\gamma} \text{ for } |\boldsymbol{II}_\tau| > \tau_0^2 \text{ and } \dot{\gamma} = 0 \text{ for } |II_\tau| \le \tau_0^2. \tag{2.28}$$

Since in some complex applications, parts of the material flow, while the reminder behaves as a solid, the Bingham model assumes sufficient generality. In addition, at vanishing shear rates, the apparent viscosity in the Bingham model becomes infinite, leading to discontinuity. To handle such issues, Papanastasiou [102] suggested a modified Bingham model, by introducing a regularization stress growth exponent (m_p) to control the rate of rise in stress. This parameter (m_p) should be sufficiently large to approximate the ideal model without causing further numerical convergence difficulties. Accordingly, as in the present study the visco-plastic stress is expressed in the form:

$$\tau = \varphi(II_d)\dot{\gamma}, \tag{2.29}$$

where the function $\phi(II_d)$ is defined, following expression (2.29), as:

$$\varphi(II_d) = \left(\mu_0 + \frac{\tau_0 (1 - e^{-m_p |II_d|^{1/2}})}{2|II_d|^{1/2}} \right) \tag{2.30}$$

and

$$II_d = \frac{1}{2} trace(d^2). \tag{2.31}$$

2.3.4 Viscoelastic flow modeling

For non-Newtonian viscoelastic fluids, an additional extra-stress term in the momentum equation (2.14) is introduced, giving

$$\rho\frac{\partial u}{\partial t} = \nabla\sigma - \rho u\cdot\nabla u, \tag{2.32}$$

where σ is the Cauchy-stress tensor, defined as

$$\sigma = -pI + T, \tag{2.33}$$

$$T = 2\mu_s d + \tau. \tag{2.34}$$

Hence, from equations (2.32), (2.33) and (2.34), the system of equation represented by continuity and momentum equations for viscoelastic flow can be expressed as:

$$\nabla\cdot u = 0. \tag{2.35}$$

$$\rho\frac{\partial u}{\partial t} = \nabla\cdot(2\mu_s\, d + \tau) - \rho u\cdot\nabla u - \nabla p. \tag{2.36}$$

For the viscoelastic stress term of equation (2.33), an additional constitutive differential equation (stress model) is required. A brief review covering such equations is provided below.

2.3.5 Constitutive equation

Constitutive equations (models) are equations relating suitably defined stress and deformation variables. In the viscoelastic case, an extra stress term in the momentum equation appears that demands an additional differential equation to provide its description. In this context, many constitutive differential equations are used for this purpose [70], as described in the following subsections of this thesis.

2.3.5.1 The Maxwell model

The Maxwell model [78] was introduced as an early model for viscoelastic fluids. The one-dimensional form of this model is obtained through a combination of a Hookean spring and a Newtonian dashpot in series (see Barnes et al. [14]), expressed as

$$T + \frac{\mu_0}{G_0}\frac{\partial}{\partial t}T = 2\mu_0 d, \tag{2.37}$$

where G_0 and μ_0 represent the elastic modulus and the viscosity, respectively; T is an extra stress tensor, and d the rate of deformation tensor. The ratio $\frac{\mu_0}{G_0}$ is equivalent to the relaxation time (λ) for a Maxwell fluid.

2.3.5.2 The Oldroyd-B model

Oldroyd (1950) [100] introduced an alternative non-linear equation by replacing the time-derivative in the Maxwell equation (2.37) by a convected alternative, which led to the non-linear upper-convected Maxwell (UCM) model:

$$T + \lambda_1 \overset{\nabla}{T} = 2\mu_0 d, \tag{2.38}$$

Likewise emerged the lower-convected Maxwell (LCM) form

$$T + \lambda_1 \overset{\Delta}{T} = 2\mu_0 d\,. \tag{2.39}$$

Above, the upper ($\overset{\nabla}{T}$) and lower ($\overset{\Delta}{T}$) convected stress derivatives can be expressed as:

$$\overset{\nabla}{T} = \frac{\partial T}{\partial t} + u\cdot\nabla T - (\nabla u)^T\cdot T - T\cdot\nabla u, \tag{2.40}$$

$$\overset{\Delta}{T} = \frac{\partial T}{\partial t} + u\cdot\nabla T + (\nabla u)^T\cdot T + T\cdot\nabla u. \tag{2.41}$$

The Maxwell model does not contain a term to account for solvent presence (a purely viscous component). To overcome this, a retardation time λ_2 is introduced in equation (2.38):

$$T + \lambda_1 \overset{\nabla}{T} = 2\mu_0\left(d + \lambda_2 \overset{\nabla}{d}\right). \tag{2.42}$$

Equation (2.42) is known as the Oldroyd-B model, where $\overset{\nabla}{d}$ is the upper-convected derivative of the deformation rate tensor. This model, as discussed in Walters [134], is appropriate to represent the behaviour of fluids that have constant shear viscosity, such

as Boger fluids [26]. Additionally, the model is termed an Oldroyd-A model, if the upper-convected derivatives are replaced by the lower-convected derivatives. Since $\overset{\nabla}{d}$ contains second-order derivatives of velocity, a split version of this model is presented: one for the polymeric component and another for the solvent. This representation has the advantage of avoiding direct approximation of higher order derivatives - hence circumventing expoure to larger numerical discretisation errors. Such a split system may be arranged as:

$$T = \tau + 2\mu_s d, \tag{2.43}$$

$$\tau + \lambda_1 \overset{\nabla}{\tau} = 2\mu_p d, \tag{2.44}$$

$$\lambda_1 \frac{\partial \tau}{\partial t} = (2\mu_p d - \tau) - \lambda_1 (u \cdot \nabla \tau - (\nabla u)^T \cdot \tau - \tau \cdot \nabla u). \tag{2.45}$$

Here, μ_p and μ_s are polymeric and solvent viscosity contributions, respectively. The total viscosity μ_0 and relaxation time λ_2 may be recovered through the following relations:

$$\mu_0 = \mu_s + \mu_p \tag{2.46}$$

$$\lambda_2 = \frac{\lambda_1 \mu_s}{\mu_s + \mu_p}, \tag{2.47}$$

where equation (2.42) must satisfy the constraint $\lambda_1 \geq \lambda_2 \geq 0$. When the solvent viscosity component $\mu_s \neq 0$, the Oldroyd-B model is realised.

Unfortunately, the extensional viscosity predicted by the Maxwell and Oldroyd-B models becomes unbounded as the strain-rate approaches $1/2\lambda_1$; additionally, the shear viscosity is constant at every shear-rate and the second normal stress difference is zero (except for the lower-convected Maxwell model which over-predicts N_2). In uniaxial extensional flow, of an Oldroyd-B model, the extensional viscosity can be expressed as a function of extension rate $\dot{\varepsilon}$, viz,

$$\mu_e(\dot{\varepsilon}) = \frac{2\mu_0(1-2\lambda_2\dot{\varepsilon})}{1-2\lambda_1\dot{\varepsilon}} + \frac{\mu_0(1+\lambda_2\dot{\varepsilon})}{1+\lambda_1\dot{\varepsilon}}. \tag{2.48}$$

2.3.5.3 The Phan-Thien/Tanner (PTT) model

Phan-Thien and Tanner [104, 105] introduced a modified version of the Oldroyd-B model, named the PTT model. This model considers the creation and destruction for a framework of network junctions. Shear-thinning and extension-hardening/softening material behaviour are exhibited by this class of models, which is expressed as:

$$T = \tau + 2\mu_s d, \tag{2.49}$$

$$f(\tau)\tau + \lambda_1 \overset{\diamond}{\tau} = 2\mu_p d, \tag{2.50}$$

$$\overset{\diamond}{\tau} = (1-\frac{\xi}{2})\overset{\nabla}{\tau} + \frac{\xi}{2}\overset{\Delta}{\tau} = \overset{\nabla}{\tau} + \xi(d.\tau + \tau.d), \tag{2.51}$$

$$\lambda_1 \frac{\partial \tau}{\partial t} = (2\mu_p d - f(\tau)\tau) - \lambda_1(u\cdot\nabla\tau) + \lambda_1(1-\xi)((\nabla u)^T\cdot\tau + \tau\cdot\nabla u)). \tag{2.52}$$

The extra function $f(\tau)$ is then,

$$f(\tau) = \begin{cases} \exp\left[\dfrac{\varepsilon_{PTT}\lambda_1}{\mu_p} tr(\tau)\right] & \exp onential, \\ 1 + \dfrac{\varepsilon_{PTT}\lambda_1}{\mu_p} tr(\tau) & linear. \end{cases} \tag{2.53}$$

Where ε_{PTT} and ξ are non-dimensional model material parameters, μ_p and μ_s are polymeric and solvent viscosity coefficients, λ_1 is a relaxation time, T is the extra stress tensor, and d is the rate of strain tensor. Here, the Oldroyd-B model may be recovered from the PTT model when $\varepsilon_{PTT} = \xi = 0$. Moreover, one can observe that from a Taylor series expansion of the exponential form, and using truncation that the so-called linear PTT model may be extracted. Both alternative model forms exhibit shear-thinning behaviour and extension-hardening; strain-softening is anticipated for the exponential form, whilst the linear form displays sustained hardening, although, for some extreme values ($\varepsilon_{PTT} \to 1$) moderate softening is also observed. For the PTT model, the shear behaviour is controlled by both parameters ε_{PTT} and ξ; extensional behaviour is affected principally by ε_{PTT}, although ξ does have some limited effect in certain value ranges of ε_{PTT} (appears parameter independent).

2.3.5.4 Pom-pom models

One of the primary problems in constitutive modelling is to derive the desired a correct nonlinear behaviour in both extensional and shear flows, simultaneously. Well-known constitutive models such as Giesekus, Phan-Thien/Tanner (PTT) and Kaye-Bernstein-Kearsley-Zapas (K-BKZ) are unable to overcome this difficulty. Recently, a new constitutive model has been introduced by McLeish and Larson [79] to explain the behaviour of polymer molecular structures (see Figure 2.1), and as such, is considered as a major step forward: the pom-pom model. This model has been developed, mainly, for long chain branched polymers, based on tube theory, in which polymer chains are denoted by a backbone segment with the same number of dangling-arms (q) attached at both extremes of the backbone section. The drag that the melt exerts on these arms causes the backbone to stretch. The presence of branching points slows down the reptation of the backbone. The ends of the arms are free to move and the process of arm-retraction helps the molecule to free the polymer chain from the tube formed by its surroundings. This arm-retraction is triggered when the molecule reaches its maximum stretched state. The arms gradually free from the tube by diffusion. Once the arms have relaxed, the backbone can subsequently relax by moving the branch points. The extension of the polymer chain is represented by the backbone stretch parameter λ, which represents the actual extension of the molecule scaled by its equilibrium length, $\lambda = L_{backbone} / L_{0_{backbone}}$.

A key aspect of this new type of model is the separation of relaxation times, one for stretch and another for orientation. The model consists of two decoupled equations, one for each relaxation process. In the original formulation of the model, the maximum backbone stretch (finite extensibility constraint) introduces a discontinuity in the gradient of the steady-state extensional viscosity. Two drawbacks remain however; the prediction of a zero second normal stress difference, and the unboundedness of the backbone orientation equation at large strain-rates.

Under the multimode approach proposed by Inkson et al. [63], the same deficiencies are apparent with this form of the pom-pom model. By modifying the evolution equation for stretch (λ), Blackwell et al. [24] allowed branch point displacement. This had the effect of attenuating non-smooth peaks in η_e [101], though discontinuities can still be

detected under finite extension. To the same end, Verbeeten et al. [128] introduced the eXtended pom-pom (XPP) model (see additionally [129]). Two different versions of eXtended pom-pom (XPP) model were introduced; the Single and Double Extended forms of the pom–pom model (SXPP and DXPP). In this study, focus is upon the single-equation version of the pom–pom model.

The constitutive equation for the single equation version of the XPP model may be expressed, using the unit tensor (I) and upper convected stress derivatives in the form,

$$f(\tau)\tau + \lambda_1 \overset{\nabla}{\tau} + \frac{\mu_p}{\lambda_1}[g(\tau)]I + \frac{\alpha\lambda_1}{\mu_p}\tau\cdot\tau = 2\mu_p d, \tag{2.54}$$

and $g(\tau) = f(\tau) - 1$

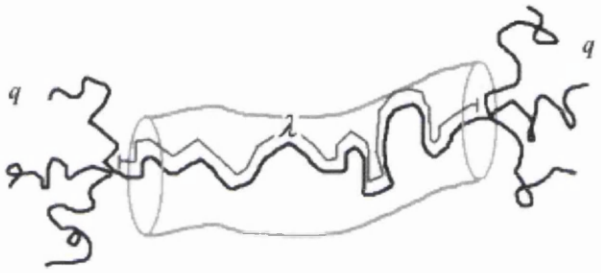

Figure 2.1: Idealized pom-pom molecule

where

$$f(\tau) = \frac{2}{\varepsilon_{SXPP}}\left(1-\frac{1}{\lambda}\right)e^{v(\lambda-1)} + \frac{1}{\lambda^2}\left(1-\left\{\frac{\lambda_1}{\mu_p}\right\}^2\frac{\alpha}{3}tr(\tau\cdot\tau)\right). \tag{2.55}$$

Here $\alpha \geq 0$ is a material parameter defining the degree of anisotropy present. This parameter was incorporated by Verbeeten et al. [128] to represent a non-zero second normal stress difference (N_2) when $\alpha > 0$. The parameter v is taken to be $\frac{2}{q}$, where q represents the number of arms at the end of a chain-segment backbone. Moreover, the parameter ε_{SXPP} can be define as: $\varepsilon_{SXPP} = \frac{\lambda_{0s}}{\lambda_{0b}}$, where λ_{0b} and λ_{0s} are the orientation and backbone stretch relaxation times, respectively. Nevertheless, some 'numerical

defects' have been reported for certain values of α and q with this pom-pom model, as shown by Clemeur et al. [40].

With the SXPP model, the backbone stretch λ is given as

$$\lambda = \sqrt{1+\frac{\lambda_1}{3\mu_p}|tr(\tau)|}\,. \tag{2.56}$$

In equation (2.56), the absolute value function is not included in the original SXPP formulations. Here, this modification is necessary to increase the levels of attainable elasticity by avoiding problems when $tr(\boldsymbol{\tau})<0$ in complex flows (which may only occur under discrete numerical modelling). Finally, the extra-stress tensor may be written as the sum of polymeric and solvent contributions, $T=\tau+2\mu_s d$.

In particular, the Oldroyd-B, LPTT and EPTT model can be recovered from the SXPP model as illustrated in the following Table (for more detail see for example [4,65,118]).

Table 2.1: Characterisation - relationship among Oldroyd-B, LPTT, EPTT and SXPP

model	$f(\tau)$	$g(\tau)$	α
Oldroyd-B	1	0	0
LPTT	$1+\frac{\varepsilon_{PTT}\lambda_1}{\mu_p}tr(\tau)$	0	0
EPTT	$\exp\left[\frac{\varepsilon_{PTT}\lambda_1}{\mu_p}tr(\tau)\right]$	0	0
SXPP	$f(\tau)$	$f(\tau)-1$	α

2.3.6 Viscoelastoplastic flow and viscometric functions

In this study, additional consideration is given to the aspects concerning non-Newtonian visco-elasto-plastic materials and their representation. Here, a combination of viscoelastic and visco-elasto-plastic models is found. The set of equations (2.29)-(2.31) represent the essential basis to incorporate the combination of the Phan-Thien Tanner (EPTT) model with the Papanastasiou-Bingham model. Thereby, the extra stress tensor is defined as:

$$\tau = \tau^{(1)} + \tau^{(2)}, \tag{2.57}$$

$$\tau^{(1)} = 2\phi(II_d)\mu_s d, \tag{2.58}$$

$$f\tau^{(2)} + \lambda_1 \tau^{\nabla(2)} = 2\phi(II_d)\mu_p d \ . \tag{2.59}$$

Under such a description, the Papanastasiou-Exponential Phan-Thien Tanner (Pap-EPTT) material functions may be extracted, as follows:

$$\eta = \frac{1+(1-f)\mu_s}{f}\phi(II_d), \tag{2.60}$$

$$\eta_E = 3\phi(II_d)\mu_s + 3\phi(II_d)\mu_p\left[\frac{f}{f^2 - \lambda_1 f\dot{\varepsilon} - 2(\lambda_1\dot{\varepsilon})^2}\right], \tag{2.61}$$

$$N_1 = \frac{2\phi(II_d)\mu_p\lambda_1\dot{\gamma}^2}{f}. \tag{2.62}$$

These material functions provide the vital background reference to be interpreted against for the anticipated flow response of this model under ideal shear and extensional flow deformation conditions. Hence, one may extend consideration into the context of non-viscometric flow, as manifest in the die-swell problem.

A summary of the various material functions that are used to characterise these non-Newtonian fluids and their model representations is provided in Table 2.2 below.

Table 2.2: Material function expressions for some common models

model	$\mu(\dot{\gamma})$	$\psi_1(\dot{\gamma})$	$\mu(\dot{\varepsilon})$
UCM	μ_0	$2\mu_0\lambda_1\dot{\gamma}^2$	$\frac{2\mu_0}{1-2\lambda_1\dot{\varepsilon}}+\frac{\mu_0}{1+\lambda_1\dot{\varepsilon}}$
LCM	μ_0	$2\mu_0\lambda_1\dot{\gamma}^2$	$\frac{2\mu_0}{1+2\lambda_1\dot{\varepsilon}}+\frac{\mu_0}{1-\lambda_1\dot{\varepsilon}}$
droyd-B	μ_0	$2\mu_0(\lambda_1-\lambda_2)\dot{\gamma}^2$	$\frac{2\mu_0(1-2\lambda_2\dot{\varepsilon})}{1-2\lambda_1\dot{\varepsilon}}+\frac{\mu_0(1+\lambda_2\dot{\varepsilon})}{1+\lambda_1\dot{\varepsilon}}$
EPTT	$\mu_s+\frac{\mu_p f}{f^2+\xi(2-\xi)\lambda_1^2\dot{\gamma}^2}$	$\frac{2\mu_p\lambda_1\dot{\gamma}^2}{f^2+2\xi(2-\xi)\lambda_1\dot{\gamma}^2}$	$3\mu_s+\frac{2\mu_p}{f-2(1-\xi)\lambda_1\dot{\varepsilon}}+\frac{\mu_p}{f+(1-\xi)\lambda_1\dot{\varepsilon}}$
SXPP	$\mu_S+\frac{G_0\lambda_{0b}}{(f(\tau))^2}$	$\frac{2G_0\lambda_{0b}^2}{(f(\tau))^3}$	$3\mu_S+\frac{3G_0}{(\lambda_{0B}\dot{\varepsilon}+f(\tau))(-2\lambda_{0b}\dot{\varepsilon}+f(\tau))}$
p-EPTT	$(\mu_S+\frac{\mu_p}{f(\tau)})\phi(II_d)$	$\frac{2\phi(II_d)\mu_p\lambda_1\dot{\gamma}}{(f(\tau))^2}$	$3\mu_S\phi(II_d)+3\mu_p\phi(II_d)\left[\frac{f}{f^2-\lambda_1 f\dot{\varepsilon}-2\lambda_1{}^2\dot{\varepsilon}^2}\right]$

2.4 Non-dimensional form

The governing equations are expressed in non-dimensional terms via length scale (L, unit length), velocity scale (U), time scale (L/U), and pressure and extra-stress scale of $\mu U/L$. The parameter $\mu=\mu_s+\mu_p$ is the total viscosity, made up from consistent viscosity fractions for solvent and solute.

Here, the dimensionless parameters are introduced in the form of Reynolds number Re, the Weissenberg number We and solvent fraction β, which are given by

$$\mathrm{Re}=\rho\frac{UL}{\mu},\qquad We=\lambda_1\frac{U}{L},\qquad \beta=\frac{\mu_s}{\mu_s+\mu_p}=\frac{\mu_s}{\mu}. \tag{2.63}$$

For Newtonian flow, the system of governing equation can be expressed in non-dimensional form as:

$$\nabla\cdot u=0, \tag{2.64}$$

$$\mathrm{Re}\frac{\partial u}{\partial t}=\mu\nabla^2 u-\mathrm{Re}\,u\cdot\nabla u-\nabla p, \tag{2.65a}$$

and the momentum equation for general Newtonian can be written as

$$\mathrm{Re}\frac{\partial u}{\partial t} = \nabla \cdot (2\mu(\dot{\gamma}, \dot{\varepsilon})d) - \mathrm{Re}u \cdot \nabla u - \nabla p. \tag{2.65b}$$

In contrast, the governing equations for incompressible viscoelastic flow may be express as,

$$\mathrm{Re}\frac{\partial u}{\partial t} = \nabla \cdot (2\beta d + \tau) - \mathrm{Re}u \cdot \nabla u - \nabla p; \tag{2.66}$$

with a constitutive equation of the form

$$We\frac{\partial \tau}{\partial t} = (2(1-\beta)d - f(\tau)\tau) - We(u \cdot \nabla \tau - (1-\xi)((\nabla u)^T \cdot \tau + \tau \cdot \nabla u)). \tag{2.67}$$

Here, the Oldroyd-B model corresponds to setting $f(\tau) = 1$ and $\xi = 0$, while the EPTT model corresponds to setting $f(\tau) = \exp\left[\frac{\varepsilon_{PTT} We}{(1-\beta)} tr(\tau)\right]$ in equation (2.67). In addition, if $\beta = 0$ then the UCM model is recovered.

For the SXPP model, the relaxation time is chosen as λ_{0b}, with the polymeric viscosity defined as $\mu_p = G_0 \lambda_{0b}$, where G_0 is the linear relaxation modulus. With these definitions, the dimensionless parameter, ε_{SXPP} is given by

$$\varepsilon_{SXPP} = \frac{\lambda_{0s}}{\lambda_{0b}}. \tag{2.68}$$

Then, the constitutive equation for the pom-pom model may be expressed in non-dimensional form as

$$We\overset{\nabla}{\tau} + f(\tau)\tau + \frac{\alpha We}{(1-\beta)}\tau \cdot \tau + \frac{(1-\beta)}{We}[f(\tau) - 1]I = 2(1-\beta)d, \tag{2.69}$$

where $f(\boldsymbol{\tau})$ and λ are given by

$$f(\tau) = \frac{2}{\varepsilon_{SXPP}}(1 - \frac{1}{\lambda})e^{\nu(\lambda-1)} + \frac{1}{\lambda^2}\left(1 - \left\{\frac{We}{(1-\beta)}\right\}^2 \frac{\alpha}{3} tr(\tau \cdot \tau)\right), \tag{2.70}$$

and

$$\lambda = \sqrt{1 + \frac{We}{3(1-\beta)} |tr(\tau)|} \,. \tag{2.71}$$

Finally, for viscoelastoplastic flow the constitutive equation (2.59) can be cast in non-dimensional form as:

$$f\tau^{(2)} + We\,\tau^{\nabla(2)} = 2\phi(II_d)(1-\beta)d \,. \tag{2.72}$$

Chapter 3

Numerical Algorithms and Finite element/volume methods

A hybrid method that comprises both the finite element method (FEM) and the finite volume method (FVM) is employed in this thesis to solve sets of differential equations. The method is applied on triangular FE meshes with FV sub-cells, reminiscent of the subelement FE implementation of Marchal and Crochet [76], though that work was on rectangular meshes. The triangular FV approach has been adopted by Morton and co-workers [89,45], Struijs et al. [115] and Tomaich and Roe [123] in the cell-vertex form and by Berzins and Ware [19] in the cell-centred case. Galerkin finite element methods are ideal for discretisation of elliptic operators, and hence may be better suited to solve the field equations, concerned with the momentum and continuity equations (elliptic-parabolic type). In contrast, finite volume technology has advanced considerably over the last decade in its treatment of equations that may be expressed in conservative form such as pure advection equations, hence their application to hyperbolic constitutive equations of first-order in space and time. In particular, our method takes features of both algorithms to

produce a stable high-order finite element/finite volume (*fe/fv*) scheme, see Struijs et al. [115].

3.1 Introduction

Numerical solutions for systems consisting of a very large number of equations have improved with modern developments in computer processors. Nowadays, three numerical methods are used successfully to solve such systems. Widely used discretisation methods include finite difference methods, finite element methods and finite volume methods. The finite difference method discretises a differential equation by approximating the differential operators with difference operators at each (temporal-spatial) point. In the finite element method, the differential equation is multiplied by a weight function and integrated over the entire domain, and then an approximate solution is constructed using shape functions and optimized by requiring that the weighted outcome have a minimum residual. In contrast, the finite volume method integrates the differential equation over each control volume, ensuring that the conservation laws of mass, momentum and energy hold (see [141] for a concise review).

The finite difference method (FDM) was first developed by A. Thom (1961) [126], in the 1920s under the title "the method of squares" to solve nonlinear hydrodynamic equations. This scheme is based upon approximations that permit replacing differential equations by finite difference equations. These finite difference approximations are algebraic in form, and their solutions are related to grid point locations. Thus, a finite difference solution basically involves three steps:

1. Dividing the domain into grids of nodes.
2. Approximating the given differential equation by a finite difference equivalence that relates the solution to grid points.
3. Solving the difference equations subject to the prescribed boundary conditions and/or initial conditions.

The basic ideas behind the finite element method originated from advances in aircraft structural analysis. In 1941, Hrenikoff [60] presented a solution for elasticity problems

using a framework method. Then, this method was developed in 1943 by Courant [42], who utilized the Ritz method of numerical analysis and minimization of variational calculus to obtain approximate solutions to vibration systems. The work of Argyris [7] on energy theorems and matrix methods laid a foundation for further developments in finite element studies. An early book on the finite element method by Zienkiewicz and Cheung was published in 1967 [155]. In the early 1970s, finite element analysis was applied to nonlinear problems and large deformations. Recently, this method has given rise to adaptive techniques (see for example Thompson 1984 [125]) and has become a powerful tool for the numerical solution of a wide range of engineering problems. Applications range from deformation and stress analysis of aircraft, building, and bridge structures to field analysis of heat flux, fluid flow, magnetic flux, seepage and other flow problems.

The literature on finite element methods (FEM) for viscoelastic flows is broad. Some of the more robust schemes of recent years have shown that it is possible to solve for highly elastic, smooth and non-smooth flows [11,36]. This has produced algorithms as in: EVSS [11], space-time/Galerkin least squares with discontinuous stress [8], DEVSS [52] and DEVSS/DG [9] and Taylor-Galerkin types [73]. In addition, FEM uses a complicated system of points, referred to as nodes, which make up a grid (or mesh). This mesh is programmed to contain the material and structural properties which define how the structure will react to certain loading conditions. Nodes are assigned at a certain density throughout the material depending on the anticipated stress levels of a particular area. Regions which will receive large amounts of stress usually have a higher node density than those which experience little or no stress. Points of interest may consist of: fracture points of previously tested material, fillets, corners, complex detail, and high stress areas. The mesh acts like a spider's web in that from each node, there extends a mesh element to each of the adjacent nodes. This web of spatial-vectors is what carries the material properties to the object, creating many elements.

In contrast, the finite volume method allows one to more concisely represent and solve partial differential equations via the form of algebraic equations (see LeVeque [71]). In previous studies, the finite element approach was used broadly for complex differential

equations. Nevertheless, this approach does carry with it a heavy computational penalty in complex flows, with sophisticated numerical strategies dealing with upwinding, accurate representation of velocity gradients, and the coupling of the system. This is an important issue to address, specifically as three-dimensional [12,143] and viscoelastic [9,18] computations are now being undertaken. Through a weighted-residual approach, one may identify FV-methods as those employing a uniform constant (unity) weighting function.

It is for this reason that attention has been devoted to alternative techniques, such as those embodied in FV methodology, that require less memory and CPU time than do their FE counterparts. Similar to the finite difference method or finite element method, values are calculated at discrete points on a meshed geometry. "Finite volume" refers to the control volume surrounding each node point on a mesh. In the finite volume method, volume integrals for a partial differential equation that contain a divergence term (conservation equations) are converted to surface integrals, using the divergence theorem. Commonly, these terms are then evaluated as fluxes at the surfaces of each finite volume. Since the flux entering a given volume is identical to that leaving the adjacent volume, these methods are conservative. Another advantage of the finite volume method is that it is easily formulated to allow for unstructured meshes. The method is used in many computational fluid dynamics software packages, typically those based on conservation equation system (as in aerodynamics).

Under viscoelasticity, hybrid approaches have been developed by Sato and Richardson [110] and Yoo and Na [144]. They employed a time-explicit FE approach for momentum and FV for pressure and stress. A cell-centred FV scheme is solved implicitly in time for stress. In contrast, the present hybrid approach includes a time-stepping procedure that combines a finite element discretisation for continuity and momentum equations, and a cell-vertex finite volume scheme for the constitutive equation. This combination is posed as a fractional-staged formulation based upon each time-step. The positioning of finite volume nodal values and control volumes is such that (in two dimensions) four linear finite volume triangular cells are formed as embedded sub-cells of each parent quadratic finite element triangular cell (see Wapperom and Webster [138]). Here, this is accomplished by

connecting the mid-side nodes of the parent finite element triangular cell. An important aspect is that with stress variables located at the vertices of the finite volume cells, no interpolation is required to recover the finite element nodal stress values. A brief review is provided below on the finite difference method, the Galerkin finite element method, the finite volume method and development of the hybrid finite element/volume method.

3.2 Brief description of numerical methods employed

3.2.1 Description of the Galerkin finite element method

The finite element method deals with splitting a simple or complex domain (geometry) into a number of finite elements (mesh) over which the problem is to be solved. To find an approximate solution for the primary variables in the system of governing equation using the finite element method, a classical trial-solution method is undertaken, with the following summarised steps:

1- Construction of a mesh of N nodes.

2- Interpolating a trial-solution for the primary variables $\tilde{u}(x)$.

3- Implementation of an optimising criterion (variation or weighted residual method) to the primary variables.

4- Approximating the function in the vicinity of each element, to solve the linear/non-linear algebraic system of equations, while at the same time evaluating the accuracy of the solution.

Here, the first and second steps are implemented in tandem. The primary variables can be expressed as a linear combination of basis functions (also known as trial functions). For instance the variable of velocity u, can be written as a finite sum of trial functions:

$$\tilde{u}(x) = \sum_{i=1}^{N} N_{\phi}^{i}(x) u^{i} . \tag{3.1}$$

Here, $N_{\phi}^{i}(x)$ are referred to as the basis (interpolation or shape) functions. The summation extends over all N-nodes (i=1,2,…,N). There are many different forms of shape functions that can be adopted, depending on the applied approximation method. For the finite element

method, the shape functions $N_{\phi}^{i}(x)$ are locally defined as polynomials within each element, and are set equal to zero outside the considered element (local compact support). The parameters u^{i} are the unknown nodal values of the dependent variables u. After preparation of the trial solution $\widetilde{u}(x)$, the governing equations are transformed to finite element equations for all elements by using the weighted residual or variational principles approaches. Then, one brings together the equations for all elements to form a global system of differential or algebraic equations with imposition of proper boundary and/or initial conditions. The solution of this algebraic system represents the parameters u^{i}.

For the weighted residual method the process is to minimise the calculated error of the differential algebraic equation rather than the equation itself. In that context, the following five common implementations are used:

1) The collocation method
2) The sub-domain method
3) The least-squares method
4) The least-squares collocation method
5) The Galerkin method

On the other hand, the variational principle (such as the Rayleigh-Ritz method) requires the minimisation of a physical quantity (energy) encompassed in the global system. Due to the limitation of variational principles, the weighted residual Galerkin approach was employed. As an example, consider the following time independent Poisson equation,

$$\frac{\partial^2 u}{\partial x^2} = f(x). \tag{3.2}$$

Suitable functions (typically polynomial type of first or second order) can be used to interpolate the unknown solution variables. Then, the problem residuals are weighted and applied to each of the finite elements belonging to the original domain.

$$u(x) = \sum_{i}^{nt} \phi_i(x) u_i, \tag{3.3}$$

where $\phi_i(x)$ are the trial functions, u_i are unknown solution nodal values and nt is the number of nodes in an element. Substituting (3.3) in (3.2) and inserting $w_j(x)$ as the weighting functions will yield the following expression,

$$\int_{\Omega_e} \frac{\partial^2}{\partial x^2}\left[\phi_i(x)u_i\right] w_j(x)\mathrm{d}\Omega_e = \int_{\Omega_e} f(x) w_j(x)\mathrm{d}\Omega_e . \tag{3.4}$$

In the Galerkin method, weighting functions and trial functions are from the same space, that is $w_j(x) = \phi_j(x)$. Then, integration by parts results in,

$$\left.\frac{\partial \phi_{i(x)}}{\partial x}\phi_{j(x)}\right|_{\Gamma_e} - u_i \int_{\Omega_e} \frac{\partial \phi_{i(x)}}{\partial x}\frac{\partial \phi_{j(x)}}{\partial x}\mathrm{d}\Omega_e = \int_{\Omega_e} f_{(x)}\phi_{j(x)}\,\mathrm{d}\Omega_e . \tag{3.5}$$

Summation of all element contributions leads to the full system over the geometry ($\Omega = \sum_e \Omega_e$). When the solution values are known at the outer domain boundary, the term determined on the boundary (Γ_e) of the element is set to zero; otherwise, it cancels out on interior elements. In the present study this is the case, as the velocity is typically given on the boundaries.

In matrix notation, the full system of equations resulting from equation (3.5) can be expressed as

$$Ku = b, \tag{3.6}$$

where the nodal values are contained in the column-matrix u, K and b may be evaluated either analytically or numerically, and are defined as follows,

$$K_{ij} = \int_{\Omega} \frac{\partial \phi_i(x)}{\partial x}\frac{\partial \phi_j(x)}{\partial x}\mathrm{d}\Omega, \qquad b_j = \int_{\Omega} f(x)\phi_j(x)\mathrm{d}\Omega . \tag{3.7}$$

Configuration of all single elements and their contributions into a total system must encompass the specified boundary conditions. For instance, since known certain values are imposed in this example on the solution, accordingly nodal values are specified at either

side of the domain (boundary Γ) and may be substituted directly into their corresponding positions in K, b, and deleted from u. Direct or iterative algebraic procedures are required to obtain a solution for equation (3.6), where the degree of complexity depends on the number of elements/nodes and the shape functions.

3.2.2 Description of the finite volume method

Finite volume schemes are quite useful for modelling hyperbolic conservation law. In this method, rather than solving the conservation law differential equation directly, an integral equivalent expression has been considered. This approach may be applied in the differential constitutive equation where one integrates over an *fv*-subdomain. This can be classified as a subclass of the finite element scheme with weighting functions set to unity, $w(x)=1$. Here, the integral form of the conservation law may be expressed as,

$$\frac{\partial}{\partial t}\int_{\Omega}\varsigma\, d\Omega+\int_{\Omega}\nabla\cdot F^{*}=\int_{\Omega}q\, d\Omega. \tag{3.8a}$$

Using the Gauss divergence theorem, equation (3.8a) can be written as

$$\frac{\partial}{\partial t}\int_{\Omega}\varsigma\, d\Omega+\oint_{\Gamma}F^{*}\cdot n\, d\Gamma=\int_{\Omega}q\, d\Omega, \tag{3.8b}$$

where ς represents any quantity to be 'conserved' such as mass, momentum or energy; F^{*} is the flux which consists of two terms diffusive and convective terms; n is the outward pointing unit normal to the domain boundary Γ over a control volume Ω; and q is a body force or source term. In a *fv*-cell, the mean values are defined as,

$$\varsigma_i=\frac{1}{|\Omega_i|}\int_{\Omega_i}\varsigma\, d\Omega_i. \tag{3.9}$$

Using the mean values ς_i and q_i, applying (3.8b) on a single finite volume gives,

$$\frac{\partial}{\partial t}\varsigma_i+\frac{1}{|\Omega_i|}\sum_{k}\oint_{\Gamma_k}F^{*}\cdot n_k\, d\Gamma_k=q_i, \tag{3.10}$$

where k varies over the *fv*-subcell faces, and Γ_k represents the area of those faces. An advantage of the FVM is that natural conservation of the variables arises in integral form on each individual *fv*-cell, and hence, over the entire domain as well.

By applying numerical integration procedures, the mean values may be evaluated,

$$\int_{\Omega_i} \varsigma(x)\,\mathrm{d}\Omega_i \approx \sum_{i=0}^{nc} \varphi_i \varsigma_i(x), \tag{3.11}$$

where nc is the number of nodes and $\varphi_i \geq 0$ are the weights of the integration procedure. Surface integrals can be approximated as,

$$\oint_{\Gamma_k} F^* \cdot n_k \, d\Gamma_k \approx \sum_k F_k^{**} \ . \tag{3.12}$$

F_k^{**} is an approximation of $F^* \cdot n_k$ and k is the number of faces of the *fv*-cell.

Employment of all such approximations over each finite volume, including their assembly to represent the total domain, gives the discretised form of equation (3.8b). Accordingly, a system of algebraic equations is generated similar to that represented by equation (3.6).

3.2.3 Two- step Lax-Wendroff scheme

The Lax–Wendroff method [114], after Peter Lax and Burton Wendroff, is a numerical scheme for the solution of hyperbolic partial differential equations, based on finite differences. Use is made of the Lax–Wendroff time stepping scheme which uses a Taylor series expansion in time resulting in a second order scheme. To explain the two-step Lax-Wendroff scheme, consider a one-dimensional problem of the form,

$$\frac{\partial u}{\partial t} = F(u), \tag{3.13}$$

and using

$$\frac{\partial^2 u}{\partial t^2} = \frac{\partial F}{\partial t} = \frac{\partial F}{\partial u}\frac{\partial u}{\partial t} = \frac{\partial F}{\partial u} F, \tag{3.14}$$

a second-order Taylor expansion of u around t^n results in the following expression

$$u^{n+1} = u^n + \Delta t F^n + \frac{1}{2}(\Delta t)^2 (\frac{\partial F}{\partial u})^n F^n, \tag{3.15}$$

where the superscript n denotes the time level. To obtain an $O(\Delta t^2)$ accurate scheme, and to avoid the explicit evaluation of the Jacobian $\frac{\partial F}{\partial u}$, a two-step approach is used, known as a predictor-corrector scheme. First $u^{n+\frac{1}{2}}$ is approximated with an error of $O(\Delta t^2)$ by an explicit Euler step, and then, the corrector step gives an approximation of u^{n+1} with an error $O(\Delta t^3)$. Therefore, the two-step Lax-Wendroff procedure over split time-step $t \in [t^n, t^{n+\frac{1}{2}}]$ and $t \in [t^n, t^{n+1}]$ is,

$$\begin{aligned} &step1: \quad u^{n+\frac{1}{2}} = u^n + \frac{\Delta t}{2} F^n, \\ &step1: \quad u^{n+1} = u^n + \Delta t F^{n+\frac{1}{2}}. \end{aligned} \tag{3.16}$$

In these equations and in the remainder of the chapter, terms with n indicate evaluation at a specific time step (n).

3.3 Time discretisation

The framework of the current study is based on a Taylor-Galerkin/Pressure-Correction (TGPC) algorithm, as proposed by Townsend and Webster [127]. This algorithm was developed to solve viscous incompressible flows of generalized non-Newtonian and viscoelastic fluids. The basis of this algorithm is a temporal Taylor series expansion and a two-step Lax-Wendroff time-stepping procedure (predictor-corrector) (see section 3.2.3 above. Here, applying a two-step Lax-Wendroff (3.16) to the momentum equation (2.66), gives

$$\begin{aligned} &step\,1a: \quad u^{n+\frac{1}{2}} = u^n + \frac{\Delta t}{2\mathrm{Re}}\left[H(u^n, d^n, \tau^n) - \nabla p^n\right], \\ &step\,1b: \quad u^{n+1} = u^n + \frac{\Delta t}{\mathrm{Re}}\left[H(u^{n+\frac{1}{2}}, d^{n+\frac{1}{2}}, \tau^{n+\frac{1}{2}}) - \nabla p^{n+\frac{1}{2}}\right], \end{aligned} \tag{3.17}$$

where,

$$H(u, d, \tau) = \nabla \cdot (2\beta d + \tau) - \mathrm{Re}\, u \cdot \nabla u. \tag{3.18}$$

For the constitutive equation (2.67), we have also

$$\begin{aligned} &step\,1a: \quad \tau^{n+\frac{1}{2}} = \tau^n + \frac{\Delta t}{2We} G(u^n, \tau^n, \nabla u^n), \\ &step\,1b: \quad \tau^{n+1} = \tau^n + \frac{\Delta t}{We} G(u^{n+\frac{1}{2}}, \tau^{n+\frac{1}{2}}, \nabla u^{n+\frac{1}{2}}), \end{aligned} \tag{3.19}$$

where,

$$G(u, \tau, \nabla u) = (2(1-\beta)d - f(\tau)\tau) - We\, u \cdot \nabla \tau + We(\nabla u \cdot \tau + \tau \cdot (\nabla u)^T). \tag{3.20}$$

The pressure $p^{n+\frac{1}{2}}$ in equation (3.17) is approximated by

$$p^{n+\frac{1}{2}} = \theta p^{n+1} + (1-\theta) p^n, \tag{3.21}$$

which has an error equal to $O(\Delta t^2)$ for $\theta = \frac{1}{2}$ and equal to $O(\Delta t)$ for other values of θ. For second-order accuracy in time, the Crank–Nicolson choice of $\theta = \frac{1}{2}$ is adopted for pressure terms. The equation (3.17b) can be rewritten as

$$u^{n+1} = u^n + \frac{\Delta t}{\mathrm{Re}}\left[H(u^{n+\frac{1}{2}}, d^{n+\frac{1}{2}}, \tau^{n+\frac{1}{2}}) - \theta \nabla p^{n+1} - (1-\theta)\nabla p^n\right]. \tag{3.22}$$

In order to solve equation (3.22) together with the incompressibility constraint (2.64), an intermediate velocity u^* is introduced such that

$$u^* = u^n + \frac{\Delta t}{\mathrm{Re}}\left[H(u^{n+\frac{1}{2}}, d^{n+\frac{1}{2}}, \tau^{n+\frac{1}{2}}) - \nabla p^n \right]. \tag{3.23}$$

Subtracting equation (3.23) from equation (3.22) then gives that u^{n+1} can be computed from

$$u^{n+1} = u^* - \frac{\theta \Delta t}{\mathrm{Re}} \nabla q^{n+1}, \tag{3.24}$$

where, the pressure difference $q^{n+1} = p^{n+1} - p^n$.

Taking the divergence of equation (3.24), and using $\nabla \cdot u^{n+1} = 0$, gives the pressure difference q^{n+1} as function of u^* only:

$$\nabla^2 q^{n+1} = \frac{\mathrm{Re}}{\theta \Delta t} \nabla \cdot u^*. \tag{3.25}$$

To provide a more stable scheme a semi-implicit Crank-Nicolson time-split is adopted for the diffusion term of the momentum equation, whereas an explicit approach is retained for other terms (see Hawken et al. [57]). In this particular case, the diffusion term is incorporated into the left-hand side of equations (3.22) and (3.23). In addition, where boundary conditions are specified, only the term $\nabla \cdot d$ is affected. Here, alongside an incremental pressure-correction (PC) procedure with a constant factor $0 \le \theta_1 \le 1$ and a forward time increment factor $\theta_2 = 1/2$. An incremental pressure-correction procedure ($0 \le \theta_1 \le 1$) is used to solve the momentum-continuity equation system, introducing semi-discrete fractional-staged equations in time prior to spatial discretisation. Then, the fractional-staged formulations within each time-step may be given by

Stage 1a:

$$\frac{2\,\mathrm{Re}}{\Delta t}(u^{n+\frac{1}{2}} - u^n) = [\nabla \cdot (\tau + \mathrm{Re}\, u \cdot \nabla u)]^n + \nabla \cdot \left(2\beta \left[\frac{d^{n+\frac{1}{2}} + d^n}{2} \right] \right) - \nabla (p^n + \theta_1 [p^n - p^{n-1}]), \tag{3.26a}$$

$$\frac{2We}{\Delta t}\left(\tau^{n+1/2}-\tau^{n}\right)=\left[2(1-\beta)d-f\tau-We(u\cdot\nabla\tau-(\nabla u)^{T}\cdot\tau-\tau\cdot\nabla u)\right]^{n}, \tag{3.26b}$$

Stage 1b:

$$\frac{\mathrm{Re}}{\Delta t}(u^{*}-u^{n})=[\nabla\cdot\tau-\mathrm{Re}\,u\cdot\nabla u]^{n+\frac{1}{2}}+\nabla\cdot\left(2\beta\left[\frac{d^{*}+d^{n}}{2}\right]\right)-\nabla(p^{n}+\theta_{1}[p^{n}-p^{n-1}]), \tag{3.26c}$$

$$\frac{We}{\Delta t}(\tau^{n+1}-\tau^{n})=[2(1-\beta)d-f\tau-We(u\cdot\nabla\tau-(\nabla u)^{T}\cdot\tau-\tau\cdot\nabla u)]^{n+\frac{1}{2}}. \tag{3.26d}$$

Here, the time step index over the interval $[n,n+1]$ is denoted by n. The velocity and stress components are calculated at the half time step $(n+\frac{1}{2})$ from data gathered at level n after stage 1a and for stage 1b, the intermediate velocity and stress components are solved for the full time step. Given initial velocity and pressure fields, non-divergence-free $u^{n+\frac{1}{2}}$ and u^{*} fields are calculated via a two-step predictor-corrector procedure with a constant factor $0\le\theta_{1}\le 1$. The corresponding mass matrix equations are solved iteratively by a Jacobi method.

Stage 2:

$$\nabla^{2}q^{n+1}=\frac{\mathrm{Re}}{\theta_{2}\,\Delta t}\nabla\cdot u^{*}, \tag{3.26e}$$

Having solved for u^{*}, here we calculate the pressure difference $(p^{n+1}-p^{n})$ through a Poisson equation by application of a direct Choleski decomposition method with a forward time increment factor $\theta_{2}=1/2$.

Stage 3:

$$\frac{2\,\mathrm{Re}}{\Delta t}(u^{n+1}-u^{*})=-\theta_{2}\nabla q^{n+1}. \tag{3.26f}$$

using u^*, and pressure difference $p^{n+1}-p^n$, determine a divergence free velocity field u^{n+1} by Jacobi iteration.

In the iterative process to solve the system of equations, the equations of motion and the stress constitutive equation are coupled and solved across the three fractional stages TGPC, on a single time step $\Delta t=[t^n,t^{n+1}]$ with initial values $[u^n,\tau^n,p^n,p^{n-1}]$.

3.5 Finite element scheme

In the finite element method, we introduce approximations $u(x,t)$ and $p(x,t)$ to the velocity and pressure respectively over finite dimensional function spaces. Hence we have,

$$u(x,t)=u_j(t)\phi_j(x),\quad j=1,\cdots.6,\qquad p(x,t)=p_k(t)\psi_k(x),\quad k=1,\cdots,3 \tag{3.27}$$

such that $u_j(t)$ and $p_k(t)$ represent the vector of nodal values of velocity and pressure and $\phi_j(x)$, $\psi_k(x)$ are their respective basis (shape or interpolation) functions. Similar forms apply for u^* and q. The domain Ω is partitioned into triangular elements with velocities computed at the vertex and midside nodes, and pressure only at vertex nodes. For the shape functions, $\phi_j(x)$ are selected as piecewise quadratic basis functions and $\psi_k(x)$ as piecewise linear basis functions. The corresponding semi-implicit Taylor-Galerkin/Pressure-Correction (TGPC) form of equations ((3.26a), (3.26c), (3.26e) and (3.26f)) may then be expressed in matrix-form as:

Stage 1a: $$A_u^a(\boldsymbol{U}^{n+\frac{1}{2}}-\boldsymbol{U}^n)=b_u^a(P^n,P^{n-1},\boldsymbol{U}^n,\boldsymbol{T}^n,\boldsymbol{D}^n), \tag{3.28a}$$

Stage 1b: $$A_u^b(\boldsymbol{U}^*-\boldsymbol{U}^n)=b_u^b(P^n,P^{n-1},\boldsymbol{U}^n,\boldsymbol{U}^{n+\frac{1}{2}},\boldsymbol{T}^{n+\frac{1}{2}},\boldsymbol{D}^{n+\frac{1}{2}}), \tag{3.28b}$$

Stage 2: $$K(P^{n+1}-P^n)=b_2(\boldsymbol{U}^*), \tag{3.28c}$$

Stage 3: $$A_1(\boldsymbol{U}^{n+1}-\boldsymbol{U}^*)=b_3(P^n,P^{n+1}). \tag{3.28d}$$

Here the notation is with superscript n denoting the time level, Δt the time step and $\boldsymbol{U}$, $\boldsymbol{U}^*$, p, $\boldsymbol{T}$, $\boldsymbol{D}$ the nodal values of velocity, non-solenoidal velocity, pressure, extra-stress and velocity gradient, respectively. The total stress nodal vector is comprised of its modes

$$(\boldsymbol{T})_j^{\,n} = \sum_{k=1}^{M} (\boldsymbol{T}_k)_j^n \text{ and}$$

$$A_u^a = \frac{2Re}{\Delta t} M + \frac{\beta}{2} S,\ A_u^b = \frac{Re}{\Delta t} M + \frac{\beta}{2} S,\quad A_1 = \frac{2Re}{\Delta t} M, \tag{3.28}$$

where M and S are the consistent mass-matrix and diffusion matrix. The stress matrix A_τ equates to the identity matrix for the FV method, whilst under the finite element implementation would take a mass matrix form. The pressure matrix A_2 is the standard stiffness matrix and A_3 is the mass matrix. The terms b_u^a, b_u^b, b_2 and b_3 are defined as:

$$b_u^a = \{\boldsymbol{F}_1 - [\beta S + ReN(\boldsymbol{U})]\boldsymbol{U} - B\boldsymbol{T}\}^n + L^T\{P^n + \theta_1(P^n - P^{n-1})\}, \tag{3.29}$$

$$b_u^b = \{\boldsymbol{F}_1 - [\beta S + ReN(\boldsymbol{U})]\boldsymbol{U} - B\boldsymbol{T}\}^{n+1/2} + L^T\{P^n + \theta_1(P^n - P^{n-1})\}, \tag{3.30}$$

$$0 \le \theta_1 \le 1,$$

$$b_2 = \frac{Re}{\theta \Delta t} L\boldsymbol{U}^*, \text{ and } b_3 = -\theta_2 L^T(P^{n+1} - P^n), \tag{3.31}$$

where $N(U)$ and L represent the consistent advection and pressure gradient matrices, respectively whilst any body force is included through F_1-term. Utilising implied summation with repeated indicial notation over the problem domain Ω, corresponding matrices are,

$$M_{ij} = \int_\Omega \phi_i \phi_j d\Omega,\ S_{ij} = \int_\Omega \nabla\phi_i \nabla\phi_j d\Omega,\ N(\boldsymbol{U})_{ij} = \int_\Omega \phi_i(\phi_l \boldsymbol{U}_l)\nabla\phi_j d\Omega. \tag{3.32}$$

The pressure stiffness matrix, K, and remaining matrices adopt the forms:

$$K_{ij} = \int_\Omega \nabla\psi_i \nabla\psi_j d\Omega, (L_k)_{ij} = \int_\Omega \psi_i \frac{\partial \phi_j}{\partial x_k} d\Omega, (B)_{ij} = \int_\Omega \nabla\phi_i \phi_j d\Omega. \tag{3.33}$$

The additional stress-related matrices and vectors (A_i^τ and b_τ) are described below, under the fv-context. The scheme becomes implicit (and stable) as approximation of diffusion terms is carried out in the momentum equation, via a Crank-Nicolson discretisation over each time-step. On the parent triangular *fe*-cell, pressure is represented through linear ($\psi_k(\boldsymbol{x})$) interpolation, while that for velocity ($\phi_j(\boldsymbol{x})$) is quadratic. In nodal (*j*) notation, such trial space solutions may be represented, viz.

$$\boldsymbol{u}(\boldsymbol{x},t^n)=\sum_j \phi_j(\boldsymbol{x})\boldsymbol{U}_j^n,\ p(\boldsymbol{x},t^n)=\sum_j \psi_j(\boldsymbol{x})P_j^n\ . \tag{3.34}$$

For the temporal increment of pressure, homogeneous Neumann boundary conditions are imposed, and for u^* the same boundary conditions are imposed as on u^{n+1} , see [57,127,138] for details. The pressure is fixed at the outflow to specify the constant of integration.

3.6 Numerical methods for solving the linear systems

A range of linear/non-linear methods may be considered for the solution of the resultant system of a finite element discretization. Linear methods may involve either direct or iterative methods. By a direct method for solving a system of linear equations one means a method which after a certain finite number of steps gives the exact solution, disregarding rounding error. For the system

$$Ax=b\,, \tag{3.35}$$

where the matrix A is full (that is, most of the elements of A are nonzero), direct elimination methods are almost always the most efficient. However, where A is sparse (that is, a large proportion of the elements of A are zero), iterative methods offer certain advantages, and for some very large sparse system they are indispensable. Iterative methods give a sequence of approximate solutions, converging under a finite number of iterative steps given suitable conditions. They may give useful results with fewer arithmetic operations than direct methods, but this is true only for less stiff systems with particular well-conditioned number properties. Thus, the choice between direct and iterative methods

depends on the proportion and distribution as well as sign and size of the nonzero elements of A. Jacobi-based methods exploit the sparseness of the associated matrices via element by element implementation in right-hand side vector assembly, matrix assembly and solution. This strategy emerges throughout the finite element time-stepping procedure and is taken advantage of here to avoid assembly of complete system matrices.

3.6.1 Consistent mass-matrix iteration

Both *fe* and *fv* discretisation-stencils may be united under a single framework. First, one commences with the generalised weighted-residual form (weighting $w_i(x)$) for the time-terms (lhs) of the stress-equation, subsuming temporal gradient discretisation on the time-step, and linear interpolation over a *fv*-subcell T:

$$\left[\int_{\Omega_T} w_i(x)\psi_j(x)d\Omega_T\right]\frac{\left[\Delta\tau^{n+1}\right]_j}{\Delta t} \quad . \tag{3.36}$$

If one adopts a Galerkin weighting ($w_i(x)=\psi_i(x)$), one extracts the *fe* "consistent mass-matrix" and characteristic cell-matrix expression on a *fv*-subcell, of area Ω_T :

$$\frac{1}{\Delta t}\left[M^T_{fel}\right]_{ij}\left[\Delta\tau^{n+1}\right]_j \text{ , where } M^T_{fel}=\frac{\Omega_T}{12}\begin{bmatrix}2&1&1\\1&2&1\\1&1&2\end{bmatrix}. \tag{3.37a}$$

An alternative form, under *fv* -weighting, $w_i(x)\big]_{i=1}^{3}=\sum_i \psi_i(x)=1$, would yield

$$M^T_{fel/fvl}=\frac{\Omega_T}{3}\begin{bmatrix}1&1&1\\1&1&1\\1&1&1\end{bmatrix}. \tag{3.37b}$$

Under *fv*, singularity is avoided by preconditioning, such as diagonalisation, in row-sum form to enhance iterative conditioning ([140], [15]), yielding,

$$(M^T_{fel})^d = \frac{\Omega_T}{3}\begin{bmatrix}1 & 0 & 0\\ 0 & 1 & 0\\ 0 & 0 & 1\end{bmatrix}, \tag{3.38a}$$

$$(M^T_{fel/fvl})^d = \Omega_T\begin{bmatrix}1 & 0 & 0\\ 0 & 1 & 0\\ 0 & 0 & 1\end{bmatrix}. \tag{3.38b}$$

To enforce nodal updates, one has to assemble the system of equations $\forall\Omega_T$, seeking to invert the mass-matrix. A Jacobi iterative solution procedure is identified to solve the created generalised matrix-vector discrete system.

3.6.2 Extrapolated Jacobi iteration

A general system of the following form emerges

$$Mx = b, \tag{3.39}$$

where M, x and b represent the mass matrix, unknown solution difference vector over the time step $[n,n+1]$ and the right hand side vector containing information, respectively. For velocity and stress in stage 1 and stage 3 a Jacobi Iterative method is used. A Jacobi iterative method for eq. (3.37a) can be written as (see [27,28]):

$$M_d\, x^{k+1} = (M_d - \omega M)x^k + \omega b, \tag{3.40}$$

where M_d is a diagonal matrix of the mass matrix, x^k is unknown vector at iteration k of the Jacobi iteration, and ω is a positive relaxation factor, $\omega > 0$. Convergence of eq. (3.37b) for x yields the matrix equation solution for that particular iteration, as taking into account limits on both sides of (3.37b) gives:

$$M_d\, x = (M_d - \omega M)x + \omega b, \tag{3.41}$$

which is of the required form of the eq. (3.37a). The iteration matrix for the above system will be the iteration matrix $(I - \omega M_d^{-1}M)$, and this provides a method that is symmetrizable. Convergence for each iteration is possible, so long as the spectral radius of

the iteration matrix is less than one. Such a condition is satisfied if the diagonal matrix M_d is the row sum modulus of M :

$$d_{ii} \geq \sum_{j=1}^{m_e} |m_{ij}|. \tag{3.42}$$

An alternative Jacobi iteration technique was suggested by Hawken et al. [57] and Ding et al. [47] where full system matrices can be avoided by a purely vector implementation. The diagonal matrix M_d is stored and the initial iterative starting vector $x^{(0)} = c^{(0)} = 0$ is allocated. For each iteration the system of equations is:

$$\begin{aligned} &M_d\, x^{(r)} = c^{(r)}, \\ &M_d\, x^{(r+1)} = c^{(r)} - \omega(Mx^{(r)} - b), \\ &M_d\, x^{(r+1)} = c^{(r)} - \omega[(\sum_{e=1}^{m_e} L_e^T M_e L_e)x^{(r)} - b)], \\ &M_d\, x^{(r+1)} = c^{(r)} - \omega(\sum_{e=1}^{m_e} L_e^T [M_e x_e^r] - b). \end{aligned} \tag{3.43}$$

3.6.3 Choleski decomposition

After discretisation of the Navier-Stokes equation, describing incompressible fluid flow to its four incremental matrix equations, a Choleski decomposition [28,48] may be implemented to calculate the pressure difference through a Poisson equation (3.28c). The matrix K in stage 2 is symmetric[1] and positive definite[2] with a banded structure, hence it is suitable to apply a direct Choleski approach.

Choleski decomposition constructs a lower triangular matrix L whose transpose L^T can itself serve as the upper triangular part. In other words one uses

$$LL^T = K, \tag{3.44}$$

where the element components of L are provided as:

[1] Symmetric matrix means that $k_{ij} = k_{ji}$ for $i, j = 1, \ldots, N$

[2] Positive definite means that $v^T \cdot K \cdot v > 0$ for all non-zero vector v

$$l_{pq} = 0 \quad \text{if} \quad (q < 0) \; or \; (q > p), \tag{3.45}$$

$$l_{ij} = \frac{1}{L_{ii}}\left(k_{ij} - \sum_{k=i-m_b}^{i-1} l_{ik} l_{jk} \right), \quad j = i - m_b, \cdots, i-1 \tag{3.46}$$

$$l_{ii} = \left(k_{ij} - \sum_{k=i-m_b}^{i-1} l_{ik}^2 \right)^{\frac{1}{2}}. \tag{3.47}$$

Here, m_b the band-width for the non-singular matrix L. Hence, the solution of the system Kx=b can be found by the following steps:

$$Ly = b, \tag{3.48}$$

$$L^T x = y. \tag{3.49}$$

The elements of x and y can be express as:

$$y_i = \frac{1}{l_{ii}}\left(b_i - \sum_{k=i-m_b}^{i-1} l_{ik} y_k \right), \quad i = 1, \cdots, m_{pr} \tag{3.50}$$

$$y_i = \frac{1}{l_{ii}}\left(b_i - \sum_{k=i-m_b}^{i-1} l_{ik} y_k \right), \quad i = 1, \cdots, m_{pr}, \tag{3.51}$$

where, m_{pr} is the total number of pressure nodes in the mesh.

3.7 Strain-rate stabilization (SRS or *D-D*$_c$)

Aspects of 'Strain-Rate Stabilisation (*D-D*$_c$)' are herein investigated to hone the response of the base finite element and hybrid finite element/volume implementations via capture of continuous-discontinuous representation of ∇u. At high Weissenberg number many numerical methods suffer from instabilities and numerical convergence may not be attainable. This is often attributed to the presence of solution singularities due to the geometry or dominant nonlinear terms in the constitutive equation. Accordingly, this scheme is implemented in the present context to investigate, in particular, the impact of

such a stabilisation technique upon free surface problems. Following, the derivational theory of Guènette and Fortin [52] linking to so-called DEVSS-schemes, the rate of deformation tensor D is treated in two forms in the momentum equation, continuous and discontinuous representations (see also 'Strain Rate Stabilisation' in Belblidia et al.[15,16]). Accordingly, the momentum equation (in the weak form) becomes:

$$\int_{\Omega} \mathrm{Re}\,\varphi_i \frac{\partial u}{\partial t} d\Omega = \int_{\Omega} \varphi_i (\nabla.(\tau + 2\beta D) - \mathrm{Re}\, u.\nabla u - \nabla p + \nabla.(2\alpha(D - D_c))\, d\Omega. \tag{3.52}$$

This is achieved by appending the *Galerkin-Least-Squares (GLS)* correction term $2\alpha(D-D_c)$ (see Baaijens [10]; or Walters and Webster [136]), in which D is discontinuous and D_c is continuous; also the parameter α is an auxiliary viscosity factor. Addition terms under the $(D\text{-}D_c)$-scheme are introduced into stages 1a and 1b of the three-stage TGPC structure, and may be expanded in the following form:

Stage 1a: $$A_u^c(\boldsymbol{U}^{n+\frac{1}{2}} - \boldsymbol{U}^n) = b_u^c(P^n, P^{n-1}, \boldsymbol{U}^n, \boldsymbol{T}^n, \boldsymbol{D}^n), \tag{3.53a}$$

Stage 1b: $$A_u^d(\boldsymbol{U}^* - \boldsymbol{U}^n) = b_u^d(P^n, P^{n-1}, \boldsymbol{U}^n, \boldsymbol{U}^{n+\frac{1}{2}}, \boldsymbol{T}^{n+\frac{1}{2}}, \boldsymbol{D}^{n+\frac{1}{2}}), \tag{3.53b}$$

where

$$A_u^c = \frac{2Re}{\Delta t} M + \frac{\beta}{2}(S + S_{SRS}),\ A_u^d = \frac{Re}{\Delta t} M + \frac{\beta}{2}(S + S_{SRS}), \tag{3.54}$$

and

$$b_u^c = \{\boldsymbol{F}_1 - [\beta(S + S_{SRS}) + ReN(\boldsymbol{U})]\boldsymbol{U} - B\boldsymbol{T}\}^n + L^T\{P^n + \theta_1(P^n - P^{n-1})\}, \tag{3.55}$$

$$b_u^d = \{\boldsymbol{F}_1 - [\beta(S + S_{SRS}) + ReN(\boldsymbol{U})]\boldsymbol{U} - B\boldsymbol{T}\}^{n+1/2} + L^T\{P^n + \theta_1(P^n - P^{n-1})\}. \tag{3.56}$$

One emphasizes here three aspects of detail (Belblidia et al.[15,16]): first, the crucial role of the localized capture of velocity gradients in D_c over global approximations (as used in conventional DEVSS-based schemes, often prone to solution degradation); second, the high solution accuracy available, via superconvergence properties afforded; third, the consistent and localized diffusive role played by such stabilisation terms, with properties of non-

dissipative and thus highly-localized capture of sharp solution features (hence, importantly, gradient capture). One may comment that such stabilisation procedures may be used in the context of non-smooth flows (as here), to approximate solution singularity (in stress, strain-rates), or in fact more generally, to constrain the development of the numerical solution via its gradients (hence, indirectly, via the constitutive equation itself and its various dependencies).

In the above equations, the strain-rate stabilisation term (SRS-term) arises, but only once spatial discretization and integral weighting has been introduced. The difference factor term D-D_c takes the form

$$\int_{\Omega} \varphi_i \, 2\hat{\alpha}\beta \nabla \cdot (D - D_c)^n \, d\Omega, \tag{3.57}$$

over the domain Ω with weighting functions $\varphi_i(x)$. Here, $\hat{\alpha}$ is a stabilisation parameter, D represents the discontinuous rate of deformation tensor under *fe*-approximation (across element interfaces), and D_c its recovered equivalent based on localized velocity-gradient recovery [73]. Nodal stress values are computed at the vertices of each fv-sub-cell, details of which are outlined below.

3.8 Finite-volume cell-vertex for stress

The finite volume methodology is utilised here, for the hyperbolic constitutive stress equations. The concepts and rationale for application of cell-vertex finite volume techniques in this viscoelastic context are presented elsewhere ([137,138]). Concisely, by rewriting the constitutive model such as equation (2.67), with flux term ($R = u \cdot \nabla \tau$) and upon absorbing remaining terms under the source (Q), one may obtain:

$$\frac{\partial \tau}{\partial t} + R = Q, \tag{3.58}$$

with expressions for the source (Q) of

$$Q = \frac{1}{We}[2\mu_p d - f(\tau)\tau] + (1-\xi)[(\nabla u)^T \cdot \tau + \tau \cdot \nabla u)]. \tag{3.59}$$

Then, cell-vertex *fv*-schemes are applied to this differential equation utilising fluctuation distribution as the upwinding technique, to distribute control volume residuals and furnish nodal solution updates (Wapperom and Webster, [137]). Now, consider each scalar stress component, τ, acting on an arbitrary volume $\Omega = \sum_l \Omega_l$, whose variation is controlled through corresponding fluctuation components of flux (R) and source (Q),

$$\frac{\partial}{\partial t}\int_{\Omega_l} \tau d\Omega = -\int_{\Omega_l} R d\Omega + \int_{\Omega_l} Q d\Omega . \tag{3.60}$$

Such integral flux and source variations are evaluated over each finite volume triangle (Ω_l), and are allocated proportionally by the selected cell-vertex distribution (upwinding) scheme to its three vertices. The nodal update is obtained, by summing all contributions from its control volume Ω_l, composed of all *fv*-triangles surrounding node (l) as in Figure 3.1(a,b). In addition, these flux and source residuals may be evaluated over two separate control volumes associated with a given node (l) within the *fv*-cell T, generating two contributions, one upwinded and governed over the *fv*-triangle T, (R_T, Q_T), and a second area-averaged and subtended over the median-dual-cell zone, (R_{mdc}, Q_{mdc}). For reasons of temporal accuracy, this procedure demands appropriate area-weighting to maintain consistency, with extension to time-terms likewise. In this manner, a generalized *fv*-nodal update equation has been derived per stress component [140], by separate treatment of individual time derivative, flux and source terms, and integration over associated control volumes, yields,

$$\left[\sum_{\forall T_l} \delta_T \alpha_l^T \Omega_T + \sum_{\forall MDC_l} (1-\delta_T)\hat{\Omega}_l^T\right]\frac{\Delta\tau_l^{n+1}}{\Delta t} = \sum_{\forall T_l} \delta_T \alpha_l^T b^T + \sum_{\forall MDC_l} (1-\delta_T) b_l^{MDC} \quad , \tag{3.61}$$

where $b^T = (-R_T + Q_T)$, $b_l^{MDC} = (-R_{MDC} + Q_{MDC})^l$, Ω_T is the area of the *fv*-triangle T, and $\hat{\Omega}_l^T$ is the area of its median-dual-cell (*MDC*). The weighting parameter, $0 \le \delta_T \le 1$, controls the balance taken between the contributions from the median-dual-cell and the *fv*-triangle T. The discrete stencil (3.61) identifies the fluctuation distribution and median dual cell contributions, area weighting and upwinding factors (α_l^T -scheme dependent). The

interconnectivity of the *fv*-triangular cells (T_i) surrounding the sample node (l), the blue-shaded zone of *mdc*, the parent triangular *fe*-cell are all features illustrated in Wapperom and Webster [137]. In addition, a brief review on the fluctuation distribution (*fv*-upwinding) parameters (α_i^T), for $i = l, j, k$ on each *fv*-cell, is described in section 3.8.1 below.

3.8.1 Fluctuation distribution schemes- choice of parameters (α_i^T)

The finite volume scheme utilised in the present study is based on various Fluctuation Distribution (FD) approaches. These are compact-stencil upwinding schemes, which update the solution in a triangular cell, by splitting flux variations to its vertices according to a prescribed strategy, see Figure 3.1a. Here, for the flux R_i in node i, we have

$$R_i = \sum_T \alpha_i^T R_T \,. \tag{3.62}$$

$\sum_T$ being the summation over all triangles that contain i as a vertex, in case of the triangles $T_1, \cdots, T_6$ see Figure 3.1b. The α_i^T are weights which determine the distribution of the flux R_T to vertex i of triangles T.

The criteria for the appropriate choice of α_i^T are

(a) Conservation: Conservation gives the requirement that the sum of the coefficients α_i over the vertices i of each triangle T equals:

$$\sum_i \alpha_i^T = 1. \tag{3.63}$$

(b) Positivity: that is associated with accuracy in the transient evolution, prohibiting the incidence of false extrema in the solution. Particular attention must be paid to the issue of dealing with sources, as these may lead to physical extrema that should not be suppressed artificially by imposing positivity.

(c) Linearity preservation: that is related to second-order accuracy at steady state.

Furthermore, FD approaches may be divided into linear and non-linear classes. Non-linear methods can be both linearity preserving and positive; alternatively, linear schemes may

only possess one such property. Due to present interest in viscoelastic flows where sources can be dominant, the Low Diffusion B (LDB) scheme is selected. Based on the previous studies this scheme is performed an accuracy grounds, compared to those that satisfied positivity instead (see for example [137]). This is a linear scheme with linearity preserving properties, which has proven efficient in dealing with model problems, as well as some complex flows [137, 138]. The LDB distribution coefficients α_i^T can be defined per cell node *i* according to the angles γ_1 and γ_2 in the fv triangle *T*, subtended on both sides of the cell advection velocity *a* (see Figure 3.1c). The LDB coefficients are defined as:

$$\alpha_i^T = \frac{\sin\gamma_1 \cos\gamma_2}{\sin(\gamma_1+\gamma_2)}, \tag{3.64}$$

$$\alpha_j^T = \frac{\sin\gamma_2 \cos\gamma_1}{\sin(\gamma_1+\gamma_2)}, \tag{3.65}$$

$$\alpha_k^T = 0. \tag{3.66}$$

The closer the advection velocity *a* is to being parallel to one of the cell boundaries, the larger the contribution to the downstream node at that boundary, hence minimising the introduction of spurious numerical diffusion.

To avoid interpolation when recovering the stress nodal values for the momentum equation, the finite volume tessellation is constructed from the finite element grid by connecting the mid-side nodes. This generates four triangular fv sub-cells per fe parent triangle, as indicated in Figure 3.1a. Then, MDC zones are defined per central node *l* as indicated in Figure 3.1b

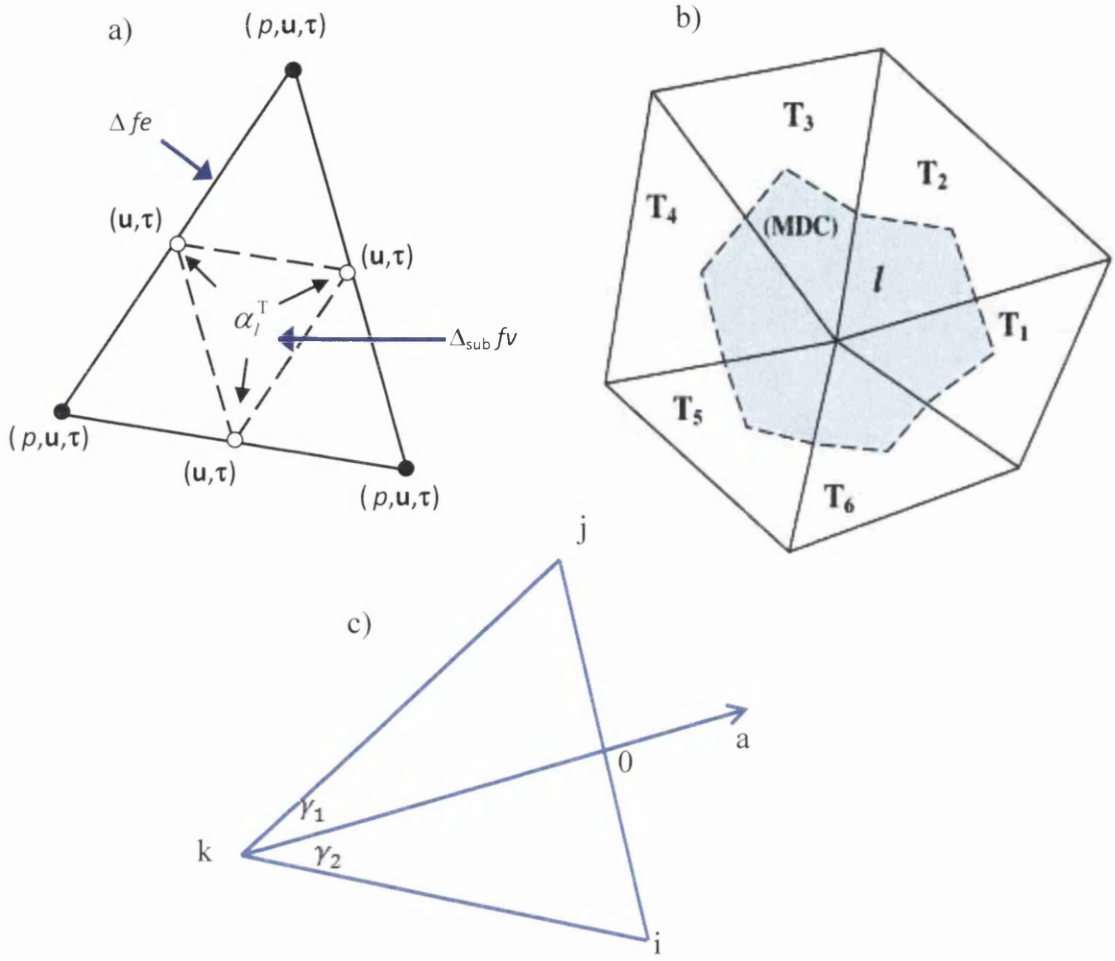

Figure 3.1: a) *fe* parent triangle and *fv* subcells, b) Control volume about node *l*, with median dual cell (MDC), c) LDB-scheme, defining γ_1 and γ_2 in fv cell.

3.9 Free surface modelling

A free-surface can be defined as an interface between a fluid 1 and fluid 2 having to be found as part of the solution. The reason for the free designation arises from the large difference in the densities of the fluid 1 and fluid 2. A low fluid 1 density means that its inertia can generally be ignored compared to that of the liquid. Therefore, the fluid 2 movement is independent with respect to the fluid 1. The only influence of the fluid 1 is through the pressure applied to the fluid 2 surface. Modelling free surface flows is a multi-disciplinary challenge comprising fluid mechanics, mathematics, rheology, wetting, spreading, interfacial phenomena and heat transfer. A numerical model incorporating all

these phenomena is highly complex to conceive. In that context regardless of the method employed, there are two essential features needed to properly model a free surface:

1. A scheme (or algorithm) needs to describe the shape and location of a surface.
2. Boundary conditions applied to the free-surface.

3.9.1 Time dependent free-surface prediction method

This time dependent prediction method, which is termed Phan-Thien (dh/dt) scheme, has been selected for the current implementation, to compute free-surface movement. In this method, to determine the eventual position of the free-surface (stage 4), after the TGPC fractional stages, the following kinematic boundary equation is enforced (see [111,145,37]):

$$\frac{DF}{Dt} = \frac{\partial F}{\partial t} + v_z \frac{\partial F}{\partial z} + u_r \frac{\partial F}{\partial r} = 0. \tag{3.67}$$

Where in cylindrical coordinates $F(r,z,t) \equiv [h(z,t) - r]$ is a function that defines the free surface position at time t, u_r is the radial velocity component, v_z is the axial velocity component and $h = h(z,t)$ is the radial height see Figure 3.2. Thus, by differentiating F with respect to r, z and t, one obtains:

$$\frac{\partial h}{\partial t} + v_z \frac{\partial h}{\partial z} - u_r = 0. \tag{3.68}$$

Conceptually, the free-surface location of the height function, $h(x,t)$, is determined via the solution of the equation (3.68). In addition, the new position of each node on the free surface is computed using equation (3.68). Remeshing must be performed after each time-step to avoid excessive distortion of elements in the boundary zones.

In brief, the algorithm involved to compute the free-surface position in time is:

(i) Update the kinematic fields (velocity) on the shifted domain (t_{n+1}), solving fractional-stages with dynamic boundary conditions.

(ii) Calculate the new position (h^{n+1},z) of each node on the free-surface using:

$$\frac{\partial h^{n+1}}{\partial t} = (u_r - v_z \frac{\partial h}{\partial z})^n \quad \text{(on the time step } [t^n, t^{n+1}]\text{)}. \tag{3.69}$$

(iii) Remesh after each time-step to readjust the boundary zones.

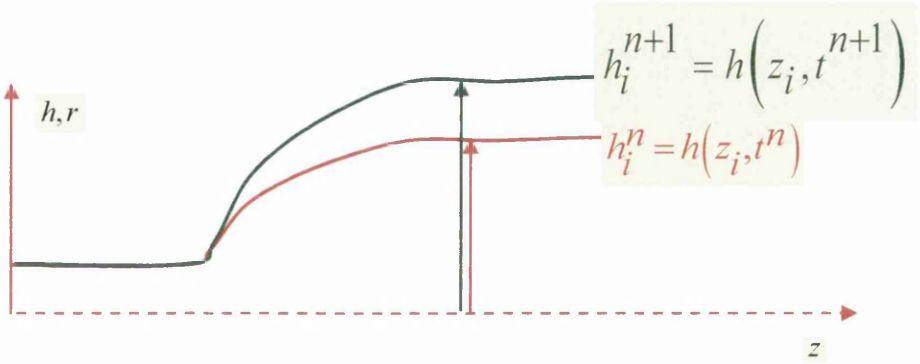

Figure 3.2: Time dependent free-surface predictions

3.9.2 Theoretical prediction

Tanner [119,120] reviewed the position on die-swell solutions with updated predictive theory for a wide class of constitutive equations, including Phan-Thien Tanner (PTT), pom-pom and general network type models. According to Tanner, for the PTT family of models and from a theoretical viewpoint, the extrudate swelling ratio of an elastic fluid may be predicted as:

$$\chi = \frac{R}{R_0} = \left[1 + \frac{1}{2}\left(\frac{N_1}{2\tau}\right)_w^2\right]^{\frac{1}{6}} + 0.13. \tag{3.70}$$

Where, N_1 is the first normal stress difference, τ is the shear stress, R_0 is the diameter of the tube and R is the diameter of the extrudate emerging from the tube. This classical theory functionally relates the swell to the ratio between N_1 and τ_w at the die-wall (w) in fully developed shear flow.

Tanner (1970) [119] established the swell ratio relationship as:

$$\left(\frac{R}{R_0}\right)^6 = \frac{\int_0^{\tau_w} 2\tau^2/N_1[1+(N_1/2\tau)^2]d(\tau^2)}{\int_0^{\tau_w}(2\tau^2/N_1)d(\tau^2)}. \tag{3.71}$$

Although N_1 is often closely proportional to τ^2, it is often even closer to

$$N_1 = k\tau^m. \tag{3.72}$$

If one uses (3.71) and (3.70) one gathers accordingly, the correction:

$$\chi = \frac{R}{R_0} = \left[1+\left(\frac{4-m}{m+2}\right)\left(\frac{N_1}{2\tau}\right)_w^2\right]^{\frac{1}{6}} + 0.13, \tag{3.73}$$

which agrees with (3.70) in the limiting case $m \to 2$.

The swell ratio is then defined as $\chi = R/R_o$, where R is the limiting external radius of the extrudate jet and R_o is the die radius (see Figure 3.3).

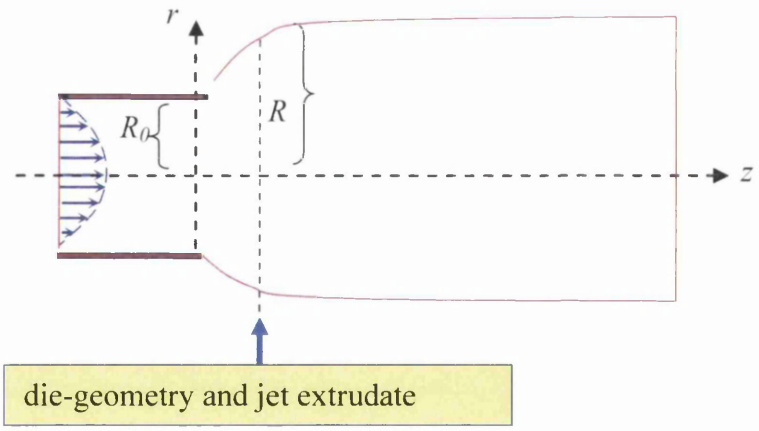

Figure 3.3: Die-swell geometry

3.9.3 Surface solution reprojection

To compensate for free-surface (lie-segment) adjustment and to satisfy the zero normal velocity free-surface boundary condition, nodal coordinates after the die-exit are modified. Consequently, the velocity solution must be projected onto the new surface position.

Therefore, if (r_1, z_1) and (r_2, z_2) are two sampling points selected from the new surface position, then the updated velocity components are divided through the projection:

$$\begin{aligned} v_z &= V_{total}\cos(\theta) \\ v_r &= V_{total}\sin(\theta) \end{aligned}, \tag{3.74}$$

where, V_{total} is the velocity magnitude on an element that takes the form:

$$V_{total} = \sqrt{v_z^2 + v_r^2}\ . \tag{3.75}$$

For the new free-surface position, the angle θ between the boundary and horizontal z (see Figure 3.4) is:

$$\theta = \tan^{-1}\left(\frac{r_2 - r_1}{z_2 - z_2}\right). \tag{3.76}$$

This procedure happens only at the end of each time step.

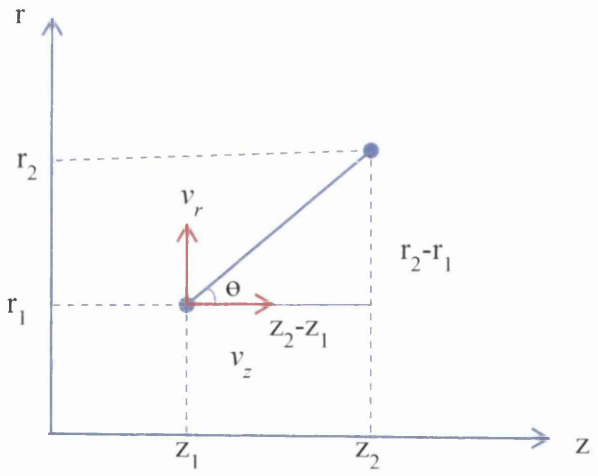

Figure 3.4: Coordinate

3.10 Monitoring the solution

To monitor the solution process one needs a criterion to calculate error estimation for the hybrid finite element/volume scheme to achieve a convergence tolerance threshold. An error estimation criterion $\|E(x)\|_r$ is given by:

$$\left\|E(x)\right\|_r = \frac{\left\|x^{n+1} - x^n\right\|_r}{\Delta t \left\|x^{n+1}\right\|_r} \leq \varepsilon, \tag{3.77}$$

where x^n is a solution vector at time step n and relative increment norms are applied $\| \ \|_r$, over least square (r=2) or infinity (r=∞) norm measures. In addition, ε is a small convergence tolerance value representing the degree of error, while Δt is the associated time step, $\Delta t = t^{n+1} - t^n$.

For non-zero Reynolds number (*Re*) and Weissenberg number (*We*), such convergence criteria (3.77) may be relatively scaled, in the form:

for velocities:-

$$\frac{\alpha_1 \mathrm{Re}\left\|x^{n+1} - x^n\right\|_r}{\Delta t \left\|x^{n+1}\right\|_r} \leq \varepsilon_v \quad \alpha_1 = \frac{1}{\mathrm{Re}} \text{ conventional, } \alpha_1 \neq \frac{1}{\mathrm{Re}} \text{ scaled} \tag{3.78}$$

for stress:-

$$\frac{\alpha_2 We\left\|x^{n+1} - x^n\right\|_r}{\Delta t \left\|x^{n+1}\right\|_r} \leq \varepsilon_s \quad \alpha_2 = \frac{1}{We} \text{ conventional, } \alpha_2 \neq \frac{1}{We} \text{ scaled} \tag{3.79}$$

3.11 Free-surface tolerance monitoring and convergence criteria

In order to analyse the evaluation of free-surface position and its movement, with respect to its accuracy and stability in deformation, it is necessary to monitor its temporal relative increment norms (in L_2 and L_∞ measures). Here, an error estimation criterion $\left\|E(r)\right\|_\alpha$ is defined as a relative increment norm factor:

$$\left\|E(r)\right\|_\alpha = \frac{\left\|r^{n+1} - r^n\right\|_\alpha}{\left\|r^{n+1}\right\|_\alpha} \leq TOL\_C, \tag{3-80}$$

where r^n is the free-surface radial coordinate of the vector at time step n. Again, norms may be taken over L_2 and L_∞ measures. Here, the L_2 norm, for $\alpha = 2$, is a root mean

square measure; correspondingly L_∞ (where $\alpha \to \infty$) represents a maximum norm measure over the numerical solution vector. Then, TOL_C is a predefined level of tolerance to invariance in reaching steady-state convergence and is taken of the order of $10^{-5} \le TOL\_C \le 10^{-3}$.

Chapter 4

Numerical Simulation of Viscoelastic and Viscoelastoplastic Die swell flow[†]

In this chapter one focuses on the modelling of viscoelastic and viscoelastoplastic fluid flow in steady free-surface die swell situations. This common benchmark problem introduces a discontinuity at the die-exit extrusion plane and the shape of the free-surface must be determined apriori. In this context, some novel algorithmic approaches associated with strain-rate stabilisation are introduced to incorporate the die-exit singularity into the problem, and alternative dynamic free-surface location strategies are investigated.

The momentum and continuity flow equations are solved by a semi-implicit time-stepping Taylor-Galerkin/pressure-correction finite element method, whilst the constitutive equation is dealt with by a cell-vertex finite volume (*cv/fv*) algorithm. This hybrid scheme is performed in a coupled fashion on the nonlinear differential equation system using

[†] Material of the present chapter is based on that submitted under "Simulation of Viscoelastic and Viscoelastoplastic Die swell flow", by A. Al-Muslimawi, H.R. Tamaddon-Jahromi and M.F. Webster, Journal of Non-Newtonian Fluid Mechanics.

discrete subcell technology on a triangular tesselation. The hyperbolic aspects of the constitutive equation are addressed discretely through upwind Fluctuation Distribution techniques.

The study explores both viscous Newtonian and non-Newtonian flow response. Viscoelasticity is introduced through the network class of models, of exponential Phan-Thien Tanner (EPTT) type; shear-thinning, strain-hardening/softening, moderate-high Trouton ratios. Initially, the influence of variation in Weissenberg number on swelling ratio is investigated. The analysis is then extended into viscoelastoplasticity through the viscous-limiting Papanastasiou approximation, coupling this with the Phan-Thien Tanner model. There, the representation and tracking of yield front movement is pertinent. Findings reveal there is significant impact on swelling ratio and exit pressure correction due to variation in yield stress levels and viscoelasticity, with viscoplastic influences countering those due to elasticity, and vice versa.

4.1. Introduction

This chapter is concerned with solving the extrusion problem under visco-elasto-plastic material response, which is of particular importance in industrial polymer melt processing. The dynamic free-surface, swell and exit pressure losses generated are the key solution features. Early viscoelastic solutions for die-swell and a Maxwell fluid appeared in Tanner [119]; followed by generalized Maxwell fluid studies by Chang et al. [39] on slit and circular die swell flows with Collocation and Galerkin methods. The upper limits of Weissenberg number ($We = \lambda\dot{\gamma}$, λ characteristic relaxation time, $\dot{\gamma}$ based on mean flow rate) reached in [39] were We=0.05 for slit and We=0.2 for circular dies, limitation being attributed to the Maxwellian lack of finite extensibility at finite deformation rates. In contrast, Caswell and Viriyayuthakorn [33] employed backtracking techniques and a single integral Maxwell model for viscoelastic calculations, to reach a Deborah number of 1.0 ($De = \lambda\dot{\gamma}_w$, λ characteristic relaxation time, $\dot{\gamma}_w$ downstream wall shear-rate). Subsequently, Crochet and Keunings [44] addressed the extrudate swell problem, with Oldroyd-B fluids

and a mixed Galerkin formulation, applied to slit, circular and annular dies; a limiting Deborah number (De_{crit} based on wall shear-rate) of 4.5 was reported for the circular case. Bush et al. [29] also conducted investigations, using both finite element and boundary integral methods, for planar and axisymmetric extrusion with Maxwell fluids. Under the finite element implementation, the De_{crit} achieved was 1.5, whilst boundary integral solutions offered a lower limit, De_{crit}=0.75. Bush [30] also reported polymer concentration effects (solvent β-factor) on swell ratio for Oldroyd-B and circular free jets. At any given Weissenberg number, findings revealed that swell ratio was particularly sensitive to high polymer concentration (*i.e. low* β). Clermont and Normandin [41] likewise applied the stream-tube method to Oldroyd-B fluids for several values of polymer concentration, $0.01 \leq \beta \leq 1.0$. Similarly, Ngamaramvaranggul and Webster [94] established semi-implicit Taylor-Galerkin/Pressure-correction procedures for such extrudate problems, therein appealing to a streamline-based free-surface detection technique.

More recently, Tanner [120] reviewed the position on die-swell solutions with updated predictive theory for a wide class of constitutive equations, including Phan-Thien Tanner (PTT), pom-pom and general network type models. Bringing citation to the present date, more recently Ganvir et al. [50] used the Arbitrary Lagrangian-Eulerian (ALE) technique to simulate extrudate swell for PTT model fluids, with comparison to previously published numerical and experimental studies for LLDPE and HDPE melts. The simulated extrudate swell profiles for long and short dies were found to be in good agreement with reported experiments. Considering dilute polymer solutions representative of Boger fluids, Mitsoulis [82] determined extrudate swell factors and exit corrections for capillary and slit dies whilst employing a multi-mode integral constitutive equation. With respect to the pom-pom model solutions for branched polymer melts, Oishi et al. [99] reported on the influence on swelling ratio of the various parameters of the eXtended pom-Pom model (XPP), investigating such issues as anisotropy, solvent fraction, entanglement, dangling molecular arms and Weissenberg number. There, free surface movement was determined by a Marker and Cell (MAC) particle tracking technique using virtual marker-particles and an Euler tracking method. Earlier Tomé et al. [124] developed these free-surface numerical methods

to simulate the free-surface flows of viscoelastic Oldroyd-B fluids. This method was applied to simulate extrudate swell for various Weissenberg numbers, and a qualitative comparison was made with those obtained by Tanner [119] and Crochet and Keunings [44], showing greater swelling ratios than those obtained by both these comparative studies.

In more recent years, simulations have been extended to the consideration of viscoplastic flow with yield stress, to represent materials such as paints, slurries, pastes and some food products, in so-called Bingham fluid modeling [22]. To computationally handle low shear-rate limiting behaviour effectively, Papanastasiou [102] suggested the inclusion of a regularization stress growth exponent (m_P) to control the initial rate of rise in stress. Subsequently, such a modified model has found wide appeal and been applied to several types of flow problems, as in: one-dimensional channel flow, two-dimensional boundary layer flow, and two-dimensional extrusion flow (Papanastasiou, [102]). Ellwood et al. [49] used the Papanastasiou model to study steady and transient jets from circular and slit nozzles, noting the influence of yield stress on the resulting extrudate. Likewise, Abdali et al. [2] solved entry and exit flows of Bingham plastics through planar and axisymmetric 4:1 contractions to determine extrudate swell factors. This demonstrated that extrudate swell decreases as yield stress (τ_0) increases. In addition by using an extra stress based cut-off criterion for exceeding the yield stress, yield fronts were accurately determined, revealing the extent of the yielded and unyielded flow regions.

Beverly and Tanner [20] proposed a suitable model for viscoelastoplastic response, in simulating some experiments on plastic-propellant dough [32]. These authors [20] employed a Herschel-Bulkley model for plasticity, alongside a linearised viscoelastic Phan-Thien/Tanner model (LPTT). Such a LPTT model, of shear-thinning, sustained strain-hardening quality, is held suitable to represent the material properties of some common polymer-solutions. Subsequently, these results were reproduced for an extended range of apparent shear rates by Mitsoulis et al. [81] with the addition of the Papanastasiou model to the CEF viscoelastic model. On extrudate swell behaviour, these visco-plastic-elastic solutions demonstrated close agreement with experiments. Moreover, Belblidia et al. [17] also applied a Papanastasiou-Oldroyd approximation to the 4:1:4 contraction-expansion

flow problem using a hybrid finite element-finite volume subcell scheme. The present chapter advances upon this position by considering the dynamics of free-surface die-swell flow, whilst also introducing a richer rheological dimension, with the properties of shear-thinning, strain-hardening/softening, and moderate-high Trouton ratios. This goal is achieved by combining the viscoplastic Papanastasiou-Bingham model with the viscoelastic Phan-Thien Tanner (EPTT) model, suitable for typical *polymer melt* response. Thus, a systematic study is undertaken on swelling ratio, exit pressure loss and flow response, as a consequence of viscous, plastic and viscoelastic material behaviour. In particular, investigation follows variation in solvent fraction (polymer concentration), EPTT strain-hardening and yield stress. This leads to identifying principal differences and root causes for swell effects due to viscoplastic and viscoelastic response, extent and shape of yielded-unyielded flow regions generated, and determination of yield fronts.

4.2 Governing equations and numerical scheme

Under viscoelastic incompressible isothermal flow conditions, the relevant mass conservation and momentum equations are introduced in non dimensional terms, in equations (2.64) and (2.66) respectively. In addition, the constitutive equation for the exponential Phan-Thien Tanner (EPTT) model is given in equation (2.67).

The hybrid finite element/volume method is employed in the present study to provide solutions to the relevant governing field equations. Features of the current hybrid approach include a time-stepping procedure that combines a finite element discretisation (semi-implicit Taylor-Galerkin/Pressure-Correction) for continuity and momentum equations, and a cell-vertex finite volume scheme for the constitutive equation (see Webster et al. [140]; Wapperom et al. [137]; Walters and Webster [136]; Matallah et al. [73]). Background detail on this scheme was introduced in chapter 3. A combination of the viscoplastic Papanastasiou-Bingham model with the viscoelastic Phan-Thien Tanner-(EPTT) model is achieved in this study (see section 2.3.6). In this context, a minor change in the governing equation lead on to a modification in the numerical algorithm. No change occurs in stage 2

(equation 3.26e) and stage 3 (equation 3.26f) of Taylor-Galerkin/Pressure-Correction fractional stages. The main modification is apparent in stages 1a and 1b, which express in the following form:

Stage 1a:

$$\frac{2\,\mathrm{Re}}{\Delta t}(u^{n+\frac{1}{2}}-u^{n})=[\nabla\cdot(\tau+\mathrm{Re}\,u\cdot\nabla u]^{n}+\nabla\cdot\left(2\beta\varphi(II_d)\left[\frac{d^{n+\frac{1}{2}}+d^{n}}{2}\right]\right)-\nabla(p^{n}+\theta_1[p^{n}-p^{n-1}]), \tag{4.1a}$$

$$\frac{2We}{\Delta t}\left(\tau^{n+1/2}-\tau^{n}\right)=\left[2(1-\beta)\varphi(II_d)d-f\tau-We(u\cdot\nabla\tau-(\nabla u)^{T}\cdot\tau-\tau\cdot\nabla u)\right]^{n}, \tag{4.1b}$$

Stage 1b:

$$\frac{\mathrm{Re}}{\Delta t}(u^{*}-u^{n})=[\nabla\cdot\tau-\mathrm{Re}\,u\cdot\nabla u]^{n+\frac{1}{2}}+\nabla\cdot\left(2\beta\varphi(II_d)\left[\frac{d^{*}+d^{n}}{2}\right]\right)-\nabla(p^{n}+\theta_1[p^{n}-p^{n-1}]), \tag{4.1c}$$

$$\frac{We}{\Delta t}(\tau^{n+1}-\tau^{n})=[2(1-\beta)\varphi(II_d)d-f\tau-We(u\cdot\nabla\tau-(\nabla u)^{T}\cdot\tau-\tau\cdot\nabla u]^{n+\frac{1}{2}}. \tag{4.1d}$$

The extra term $\phi(II_d)$ is defined in equation (2.30) in chapter 2.

4.3 Problem specification

4.3.1 Boundary and free surface location

The die-swell problem may be subdivided into two flow regions, each of different character, the shear flow within the die and the free jet flow beyond the die. Each region has its unique set of boundary conditions and for reasons of symmetry, it is only necessary to consider half of the domain, that above the central axis of symmetry. To solve the governing system of partial differential equations for the EPTT model it is necessary to impose suitable boundary conditions. EPTT/Pap-EPTT inlet stress solutions are set by solving the corresponding set of nodal-pointwise ODEs. The inlet velocity profile (pressure-driven pure shear flow) at the equivalent set flow-rate, is initially adopted for a

fully-developed analytic Oldroyd-B form (of constant viscosity), but subsequently is iteratively corrected to that of EPTT/Pap-EPTT, using feedback from the internal field solution (shear-thinning). This procedure is equivalent to solving the one-dimensional equivalent shear flow problem. Fully developed boundary conditions are established at the outflow ensuring a constant streamwise velocity component v_z and a vanishing crossstream component u_r. In addition, no-slip boundary conditions are imposed along the stationary die-channel walls. Along the free surface, slip conditions are imposed, surface tension may be neglected and the normal velocity component vanishes.

In order to detect the free surface evolution, the time dependent prediction scheme (dh/dt), which is presented by Phan-Thien has been selected for the current implementation. In this approach, equation (3.68) is utilised to compute the new position of each node on the free surface following the stages of section (3.9.1).

Moreover, an important feature of this study is the extrudate shape, which is termed as the swell ratio. This ratio is defined as $\chi = R/R_o$, where R and R_o are the final extrudate radial and die radius, respectively. Additionally, in the present study a finite small value of the Reynolds number is assumed, $Re=10^{-4}$ and the time-stepping procedure is monitored for convergence to a steady state via relative solution increment norms, subject to satisfaction of a suitable tolerance criteria, taken here as 10^{-8} with typical Δt set as $O(10^{-4})$. The initial mesh for the study is illustrated in Figure 4.1. Mesh refinement has also been performed across a series of three meshes (see Table 4.1), from which we observe mesh convergence. Here, close agreement has been observed between the computed solutions, with variance less than 0.1% between coarse-medium-fine meshes. Hence, solutions are reported on the medium meshing option. Furthermore to confirm the issue of independence of findings re extent of fully developed flow regions, we have doubled the length of the upstream and downstream sections, and detect no significant difference in the plotted patterns between our standard and longer meshes.

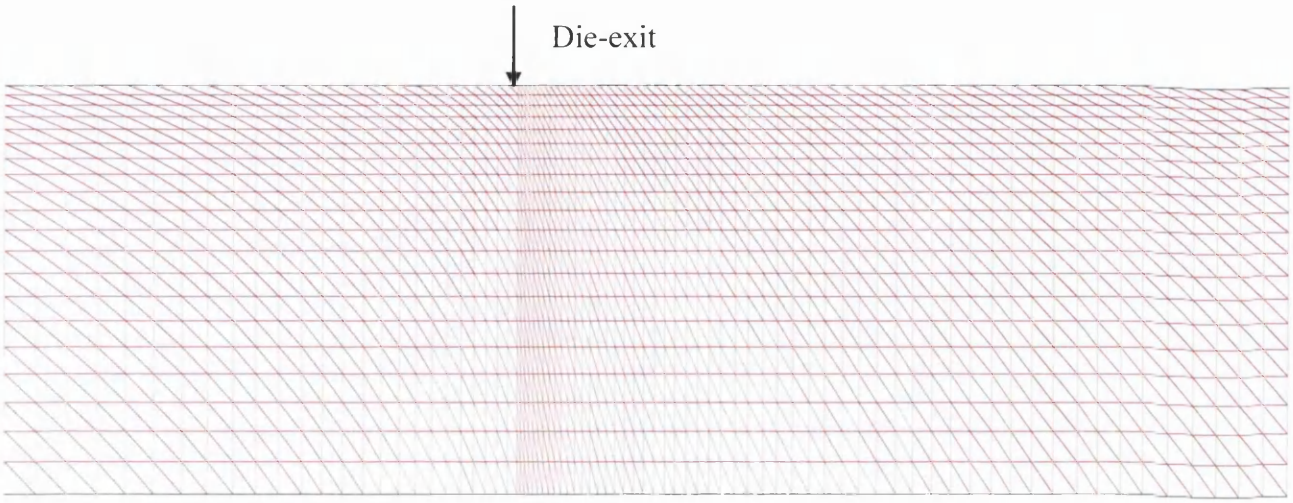

Figure 4.1: Medium mesh patterns, die length 4, jet length 6

Table 4.1: Mesh characteristic parameters

Meshes	**Elements**	**Nodes**	**Degrees of freedom (u,p, τ)**
Coarse	1994	4033	25243
Medium	3200	6601	41307
Refined	6000	12261	76697

To construct the essential basis for solution and internal starting conditions, the problem is first resolved for viscoelastic fluid properties, using the exponential Phan-Thien Tanner (EPTT) representation. Various parameter settings have been chosen for the EPTT model, namely with $\{\beta=0.9, \varepsilon=0.25\}$ - high solvent fraction, low Trouton ratio, and with $\{\beta=1/9, \varepsilon=0.25\}$ - highly-polymeric, low Trouton ratio. A switch to $\varepsilon=0.02$ yields high Trouton ratio comparisons. Then, from this position, the viscoelastoplastic problem is initiated with additional viscoplastic parameters of yield stress (τ_o) and exponent (m_p). Throughout such solution phases, there was no change in boundary condition settings necessary.

Finally, aspects of 'Strain-Rate Stabilisation (D-D_c)' are investigated for this Pap-EPTT constitutive equation. As stated in section (3.7) an extra terms (D-D_c) is applied to avoid the instabilities and numerical divergence may be attainable.

4.4 Papanastasiou-Exponential Phan-Thien Tanner (Pap-EPTT) - Rheological properties

Here, one describes the rheological properties of the Papanastasiou-Exponential Phan-Thien Tanner (Pap-EPTT) model with respect to the model parameters in question. In particular, one presents steady-state shear (η) and extensional (η_E) viscosities, the shear stress (τ_{rz}) and the first normal stress difference (N_1) (see section 2.3.6).

***τ_o variation*:** Figure 4.2 shows these rheological functions for this shear-thinning Pap-EPTT model when the level of yield stress (τ_o) is varied. Here, the solvent fraction is (β=0.9) and ε=0.25 at fixed m_p-value of 10^2. The shear viscosity plot (Figure 4.2(a)) reflects the elevation in zero-shear rate value through τ_o=(0.01,0.1,0.5,1.0) of (1.5,6,25,50). From Figures 4.2b (legend as in Figure 4.2(a)), one detects the lower limit of extensional viscosity (τ_o=0.01) and upper limit (τ_o=1.0), with rising limiting zero-deformation rate extensional viscosity of three time that in shear. The insert expands the plot to show the limited strain-hardening achieved around the deformation rate of unity. Increasing the τ_o-level has a significant impact upon shear stress, as in Figure 4.2(c), which appears at deformation rates less than unity, while there is insignificant change at deformation rates greater than unity. Data in Figure 4.2(d) infer a strengthening of N_1 for shear-rates lower than 10^1. At the larger extremes of τ_o (τ_o ~ unity), further contributions to N_1 appear; yet, the influence of τ_o-variation on the first normal difference becomes negligible at shear-rates larger than ~10^1.

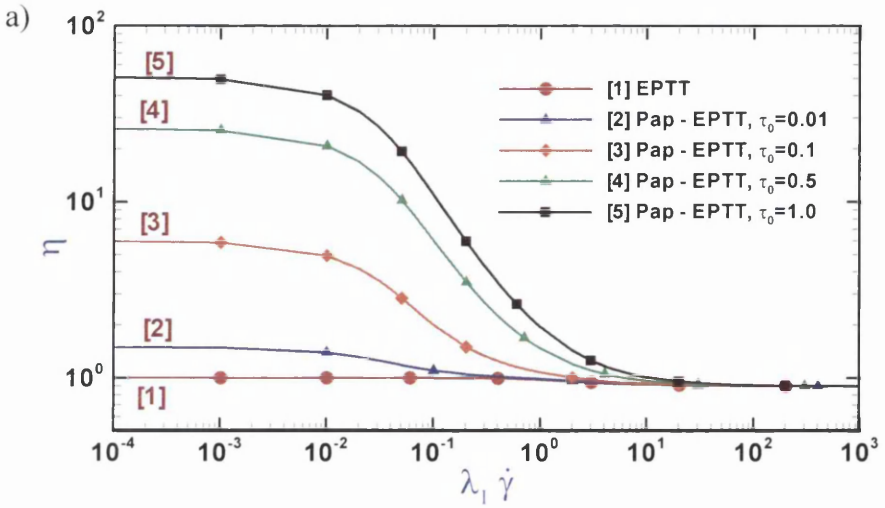

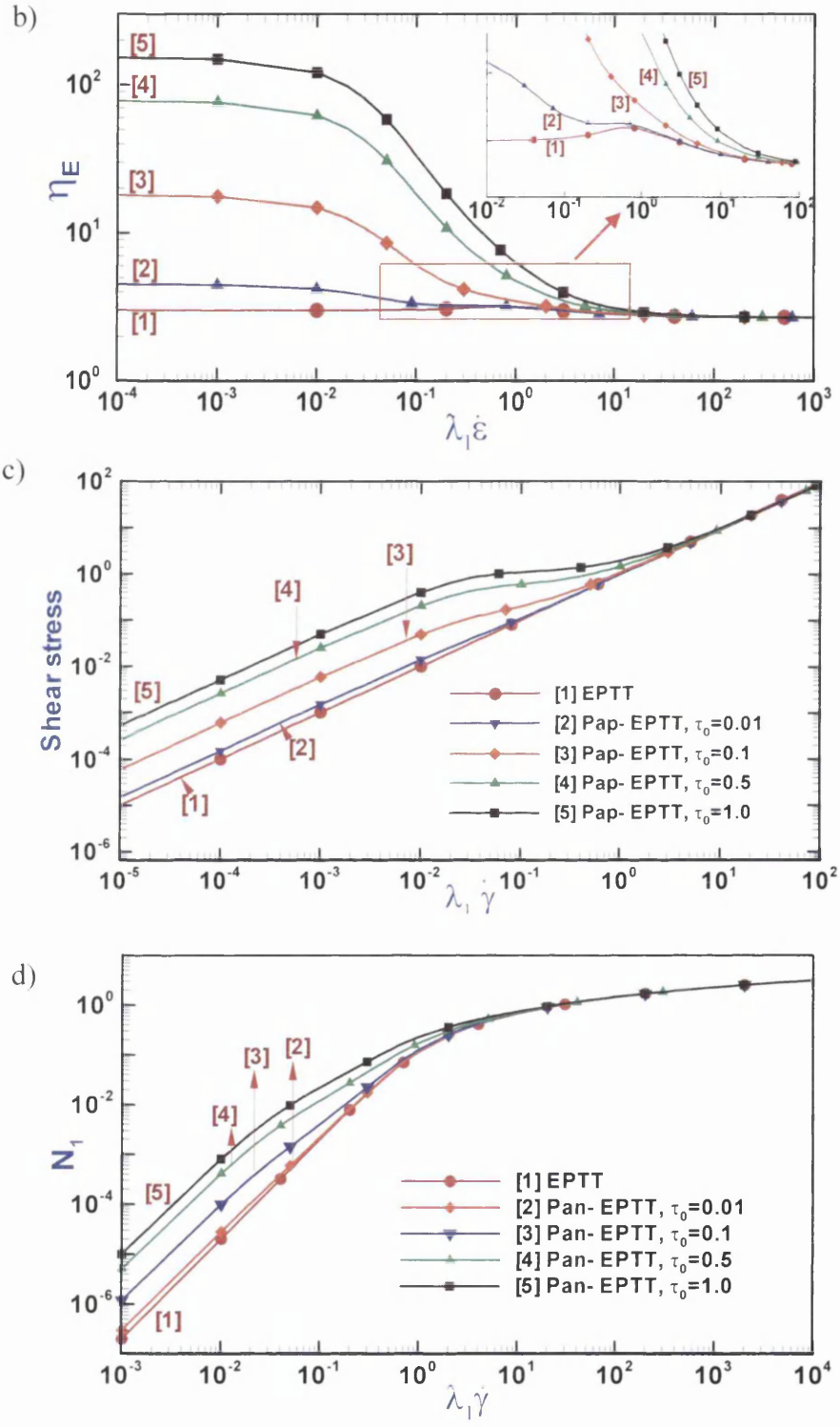

Figure 4.2: a) Shear viscosity, b) extensional viscosity, c) shear stress, d) first normal stress: EPTT, Pap-EPTT, τ_0 variation, $m_p=10^2$, $\beta=0.9$, $\varepsilon=0.25$

β, ε}-variation: Two pairings of these parameters are considered, ε={0.02, 0.25} and β={0.9, 1/9}, at fixed τ_o-value (τ_o=0.01) and m_p-value of 10^3 (elevation in m_p to amplify yield stress effects), as seen in Figure 4.3. These choices are made to reflect: (i) in ε–parameter, high and low Trouton ratios (extensional viscosities), and (ii) in β–parameter, high and low solvent fraction, respectively. The base choice is that of {ε, β}={0.25, 0.9}. The Pap-EPTT response for β=0.9 and two different ε-values (ε={0.02, 0.25}), is closely matched in both shear viscosity and first normal stress difference, Figure 4.3(a,c). While, in extensional viscosity of Figure 4.3(b), noted differences arise over the deformation rate range from 10^{-1} to 10^1; and likewise in N_1 at low rates less than 10^{-2}. Significant differences are observed in all three functions under the highly-mobile state of β=1/9, apparent in shear above rates of 10^0 and in extension above 10^{-1}. Here, {ε, β}={0.25, 1/9} is the more shear-thinning of the two ε={0.02, 0.25} cases, which is also reflected therefore in N_1. Hence, when {ε, β}={0.25, 1/9}, extensional response is clearly more complex, rich in variation and rate dependent: displaying first strain-hardening[1] in the rate-range 10^{-1} to 10^0, prior to softening[2] in the rate-range 10^0 to 10^4. Peaks and limiting high-rate plateaux of η_E vary from case to case: reaching peaks of 5 units for {ε, β}={0.25, 1/9}, 7 units for {ε, β}={0.02, 09}and 30 units for {ε, β}={0.02, 1/9}; and plateaux at {rates, levels} of {10^3,4*10^{-1}} for {ε, β}={0.25, 1/9}, {10^2,2*10^0} for {ε, β}={0.02, 0.9}and {10^4,4*10^{-1}} for {ε, β}={0.02, 1/9}.

[1] In this range, shear viscosity is fairly constant, so Trouton ratio (Tr) is dictated by extensional viscosity alone

[2] In this extended range, decline in shear viscosity strongly contributes to a first rise in Tr (up to unity in shear viscosity), dropping thereafter.

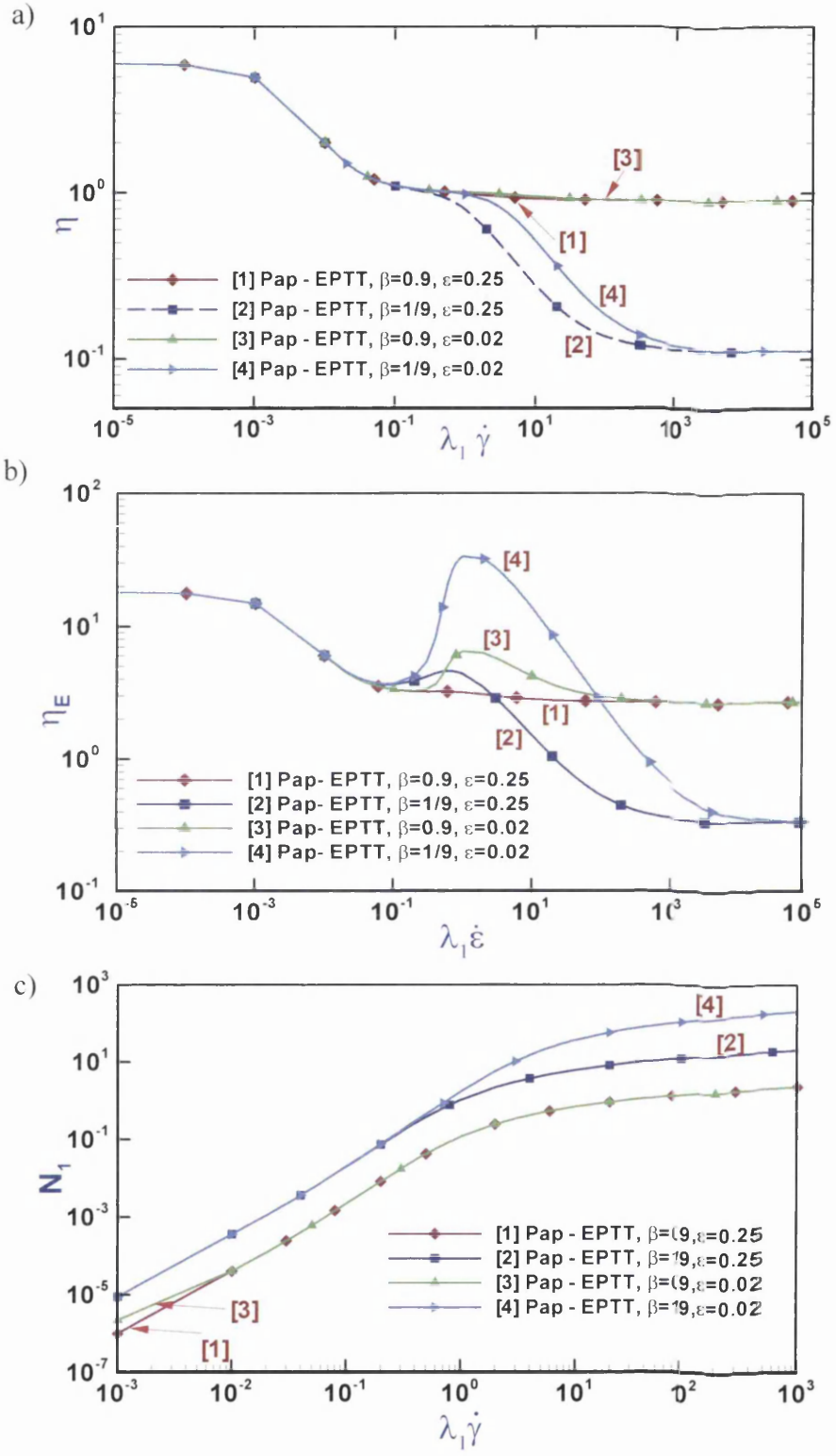

Figure 4.3: a) Shear viscosity, b) extensional viscosity c) first normal stress: Pap-EPTT, $m_p=10^3$, $\tau_0=0.01$

4.5 Numerical results and discussion

4.5.1 Swelling ratio and exit pressure correction

***τ_o variation*:** Figure 4.4(a) demonstrates swell profiles as a function of τ_0, corresponding to the free surface location over the jet region at Weissenberg number, *We*=5. Findings for swell reveal, as shown by others (Beverly and Tanner 1989 [20]), that viscoplastic influences counter those due to elasticity, with *elevation* in *plasticity suppressing swell* whilst *rise* in *elasticity stimulates swell*. Hence, the jet swelling is observed to diminish as yield stress level (τ_0) rises (akin to inertial over viscous response, governed by zero shear-rate viscosity), so that, the minimum swell corresponds to the instance with the largest yield stress (τ_0=0.1). From Mitsoulis [83], it is clear that a Bingham response reduces swelling from about 13% to zero as the yield stress increases, and similar considerations apply here with a more complex model. Results on swelling ratio are charted in Figure 4.4(b) for *We*={1,5} and $m_p=10^2$, with *We*=1 data showing a quadratic decline from the purely viscous level initially up to τ_0=0.02, followed by an almost linear fall-off thereafter, noted up to τ_0=0.5. The *We*=5 data, tends to suppress this early quadratic decline in swell at low-τ_0, but ceases to have any further influence beyond the τ_0-level of 0.1, where after the viscoplastic influence dominates. In this low-τ_0 regime, the evidence at *We*=1 points to a strong influence of shear viscosity and shear-thinning causing the swelling ratio to diminish with rising yield-stress (τ_0). That is, with shear-thinning taken with reference to the equivalent Newtonian level of that for the largest yield-stress considered. At *We*=5 and in comparison with *We*=1, the difference in levels of shear viscosity and shear-thinning are much less prominent for different values of τ_0, so there is less relative change observed in swelling ratio as τ_0 increases.

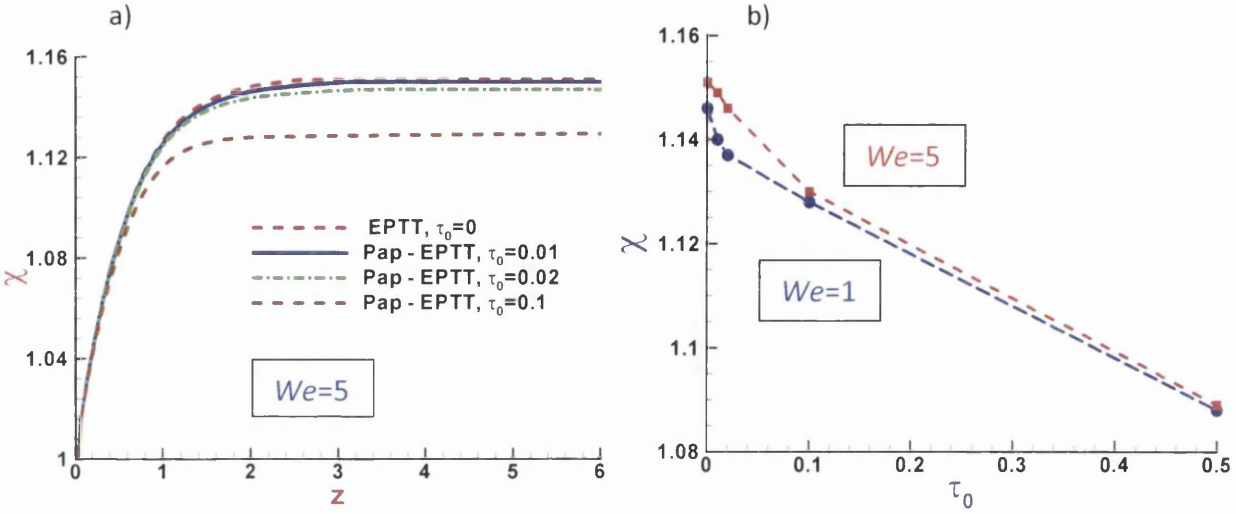

Figure 4.4: a) Swell profiles, *We* =5; b) swelling ratio vs τ_0, *We* =1, 5: τ_0 variation, m_p=10^2, β=0.9

Exit pressure correction results are presented in two forms: normalised with respect to wall shear stress, n_{ex}^{wall}, and normalised against the purely viscoelastic fluid, with definitions:

$$n_{ex}^{wall} = \frac{\Delta p - \Delta p_o}{2\tau_{w,0}}, \tag{4.2}$$

$$n_{ex}^{Eptt} = \frac{(\Delta p - \Delta p_o)_{Pap-Eptt}}{(\Delta p - \Delta p_o)_{Eptt}}, \tag{4.3}$$

where Δp is the overall inlet-exit pressure drop in the system, Δp_o is the pressure drop based on the fully developed channel flow and $\tau_{w,0}$ is its wall shear stress. The n_{ex}^{wall} correction taken against the wall shear stress reflects the standard form, as taken under a *'Couette Correction'*, accounting for wall shear and viscoelasticity. That taken against EPTT, n_{ex}^{EPTT}, bases the comparison on the incremental difference due to yield stress alone. Figure 4.5(a) shows the corresponding findings for n_{ex}^{wall} for *We*={1,5} as a function of yield stress τ_0, which increases linearly according to τ_0 rise: with a relative difference rise in n_{ex}^{wall} over τ_0 =[0.01,0.5] of approximately 6% at *We*=1, elevating to nearer 15% at *We*=5.

Effectively, *less swell*, is compensated by a *larger exit pressure correction*. A supplementary linear increase in exit correction measure n_{ex}^{Eptt} is observed in Figure 4.5(b) on *We*=5 data, when normalised against EPTT(*We*=5); this reaches around 30% above the unit-base EPTT reference line when τ_0=0.5. This finding is replicated for correspondingly-scaled *We*=1 data (not shown, noting base-line shift in levels), and is unequivocally attributable to the viscoplastic contribution alone.

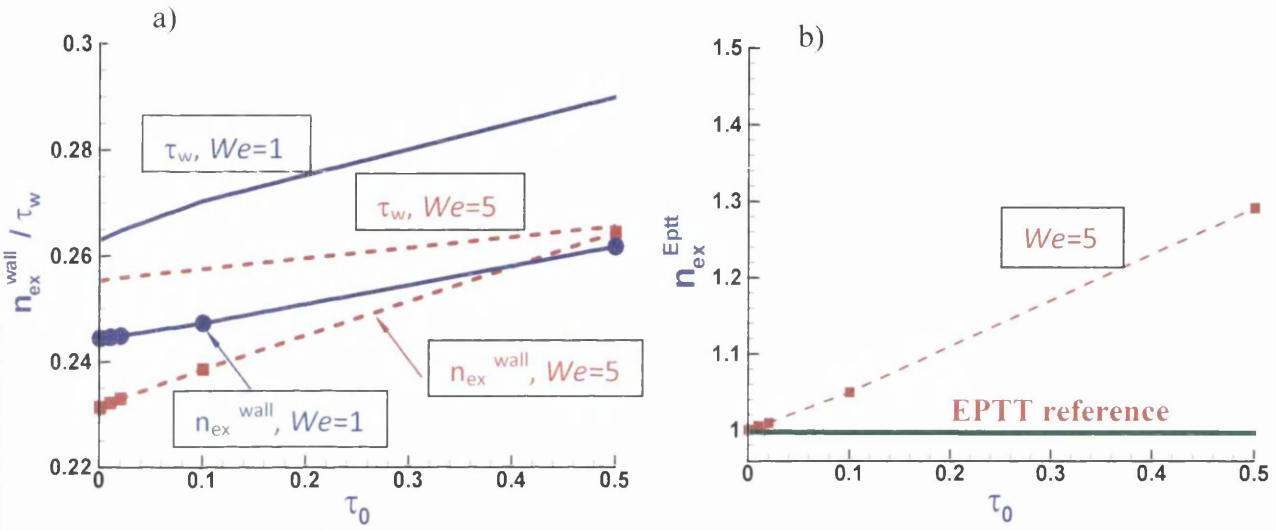

Figure 4.5: a) exit correction n_{ex} and τ_w scaled by 7*τ_0, *We* =1, 5, b) exit correction n_{ex} normalised by EPTT(*We* =5): τ_0 variation, m_p=10^2, β=0.9

We variation: In contrast to the foregoing; we next consider swell profile results through variation in *We* at fixed τ_0-value (τ_0 =0.01) and m_p-value (m_p=10^2), as in Figure 4.6(a,b) for EPTT and Pap-EPTT models. Here, findings oppose those observed under τ_0 rise, in that *larger elasticity* provokes *greater swell* and *lesser exit correction*. Hence, there is rise in swell according to increase in *We*, where maximum swell is observed at the largest *We* for both cases of EPTT and Pap-EPTT models: at *We*=5, swell reaches levels of 1.151 for the viscoelastic EPTT model, and slightly less in 1.149 for the viscoelastoplastic Pap-EPTT model.

The pressure distribution along the axis of symmetry with rising *We*, is also included in Figure 4.6(c-d). For each *We*, one observes a consistent linear decline in pressure throughout the channel, after which the pressure reduction declines quadratically to zero,

achieved locally at a distance around one unit beyond the die-exit. With a rise in *We*, there is a fall in channel pressure-drop (reduction of gradient), as apparent in the zoomed-insert of Figure 4.6(c). The zoomed representation for the die-exit zone alone of Figure 4.6d would also indicate a minor undershoot and recovery occurs in the pressure distribution at the centre of the flow, before taking up jet-flow conditions by around 3 units from the die-exit.

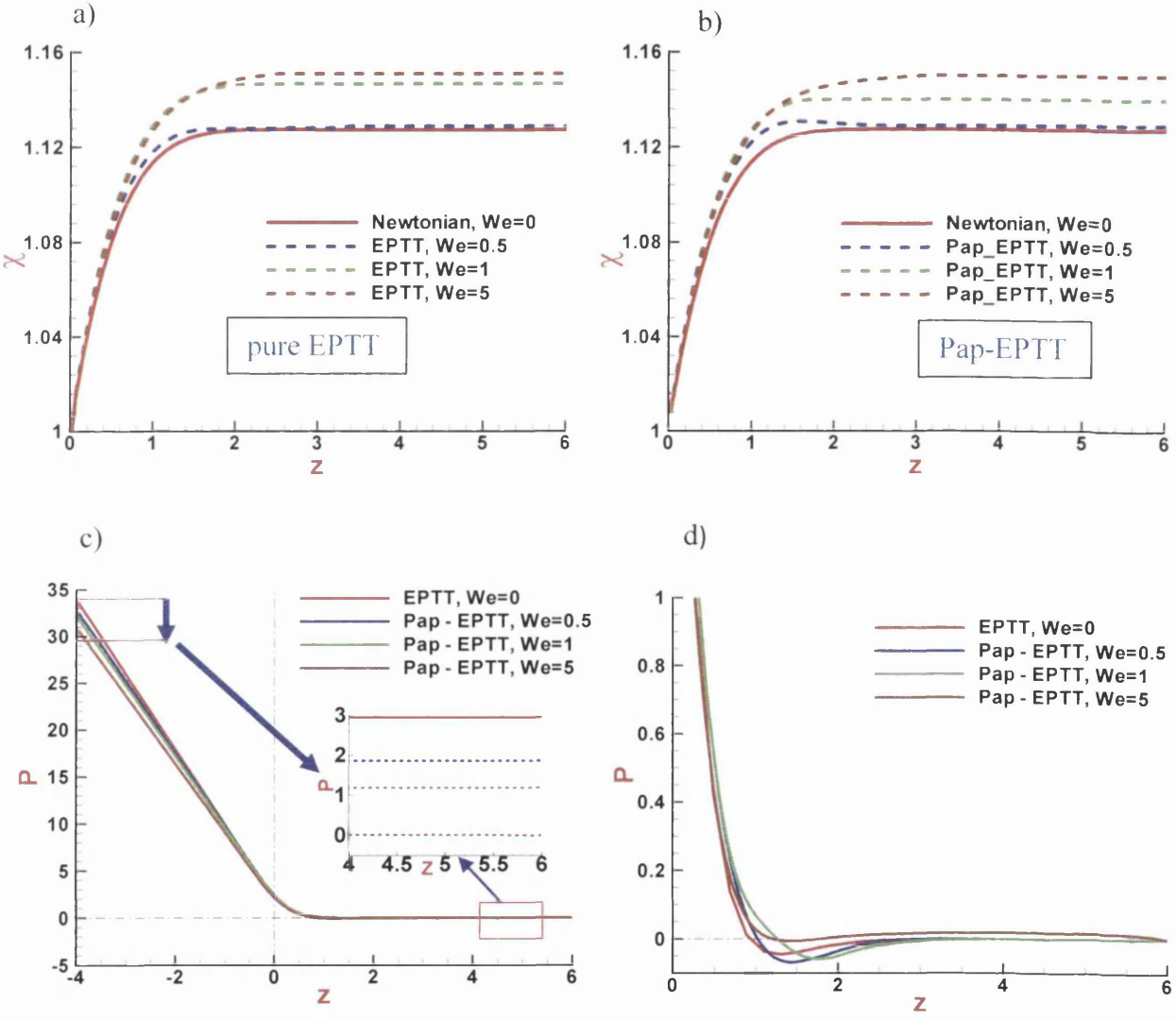

Figure 4.6: Swell profiles, a) EPTT, (b) Pap-EPTT; c) pressure profiles on symmetry-axis, d) zoom of pressure drop in jet region: *We*-variation, τ_0=0.01, m_p=10^2, β=0.9

For further clarification, swelling ratio is drawn as a function of *We*, as depicted in Figure 4.7. From this data a parametric functional relationship may be established between swelling ratio and *We* for *We*>1, rising from 1.14 when *We*=1 to around 1.153 when *We*=10. For *We* greater than 6, there is gradual relaxation in swelling, approaching an ultimate plateau at larger *We*.

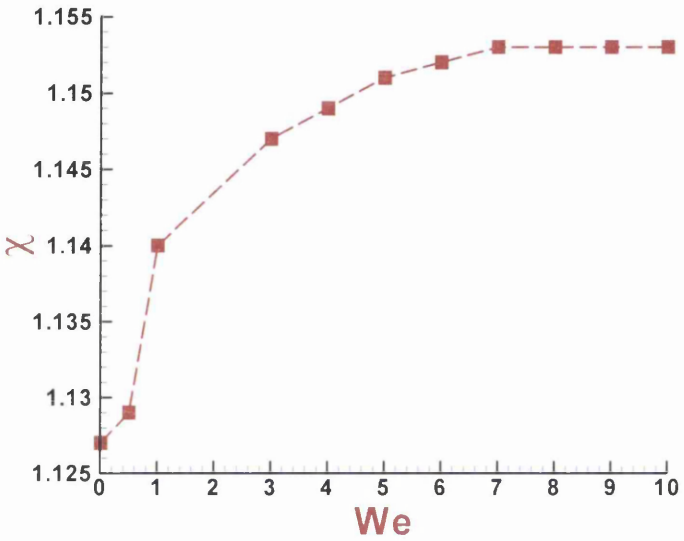

Figure 4.7: Swelling ratio as a function of *We*: Pap_EPTT τ_0=0.01, m=10^2, β=0.9

At a larger scale in Figure 4.8(a), these swell results may be charted against the elastic theory, as expounded by Tanner [120] and given in equation (4.4)

$$\chi = 0.13 + \left[1 + \left(\frac{4 - m_T}{2 + m_T}\right)\left(\frac{N_1}{2\tau}\right)_w^2\right]^{\frac{1}{6}}, \tag{4.4}$$

with various choices of factor m_T and accuracy of approximation discussed therein. This classical theory, based on single relaxation-time elastic recoil with sudden removal of tube-walls in a shearing flow, functionally relates the extrudate swell to the ratio between N_1 and τ_w at the die-wall in fully-developed flow. Note from equation (4.4), that a Newtonian swelling ratio of 0.13 is gathered with m_T=4 and vanishing pre-factor; with $\{m_T = 1, 2, 3\}$ the pre-factor equals {1, 1/2, 1/5}, respectively. In Figure 4.8(a) with $2 \le m_T \le 4$, the base

choice of exponent from the theory is m_T=2 (derived according to the commonly applicable, quadratic relationship between N_1 and τ, $N_1 = \tau^{m_T}$), which provides an over-strong elastic-theory swell estimate; whilst a reasonable fit is extracted with m_T=3.8 (relevant for these more highly solvent concentration ranges, β=0.9). This concurs with comments in Tanner [120] on common realistic fluid behaviour, that quotes "often $N_1 = \tau^2$ in proportionality, yet even more often, $N_1 = \tau^{m_T}$, m_T>2". Hence, it is not surprising that m_T=2 fitting provides a theoretical overestimate, and clearly therefore, with reference to common occurrence, the range of deformation rate considered must also be an issue.

Moreover, the results on exit correction as a function of *We* are given in Figure 4.8(b), when normalised with wall shear stress n_{ex}^{wall}. Hence with both viscoelastic and viscoplastic contributions accounted for, monotonic decline is observed in n_{ex}^{wall} with minima around 0.227 units at *We*=10. Noting channel pressure-drop declines with *We*-rise, still a dominant factor in the declining n_{ex}^{wall}, is the falling wall shear-stress (τ_w). In contrast, the trend in exit correction is non-monotonic when normalised against the equivalent EPTT model (n_{ex}^{Eptt} data not shown), when only the yield stress contribution is differentiated. The relative reference may be taken at variable EPTT(*We*), so that both the EPTT elastic and shear-thinning effects are suppressed. When this is the case, a decrease in exit correction is reported in the extended range $2 < We < 9$; yet, there is a slight increase detected in the initial range $0 \le We \le 2$.

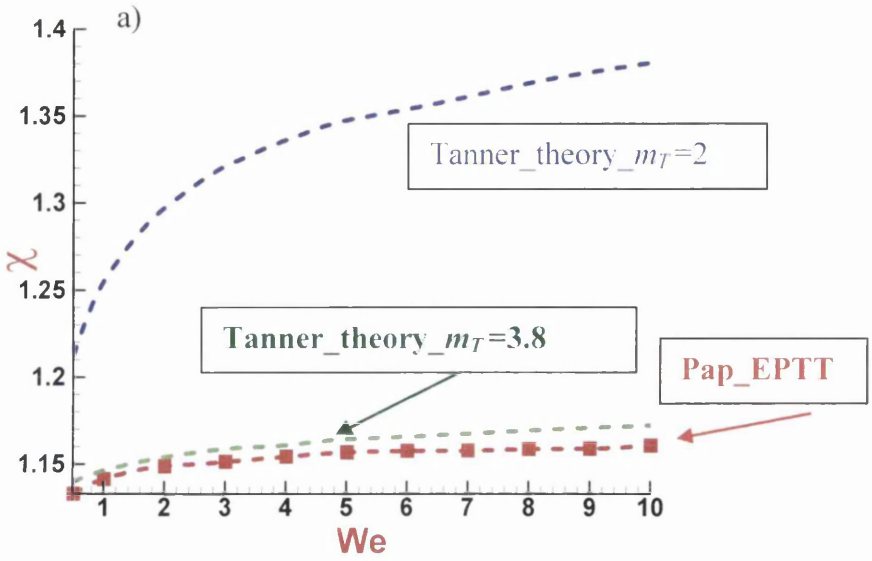

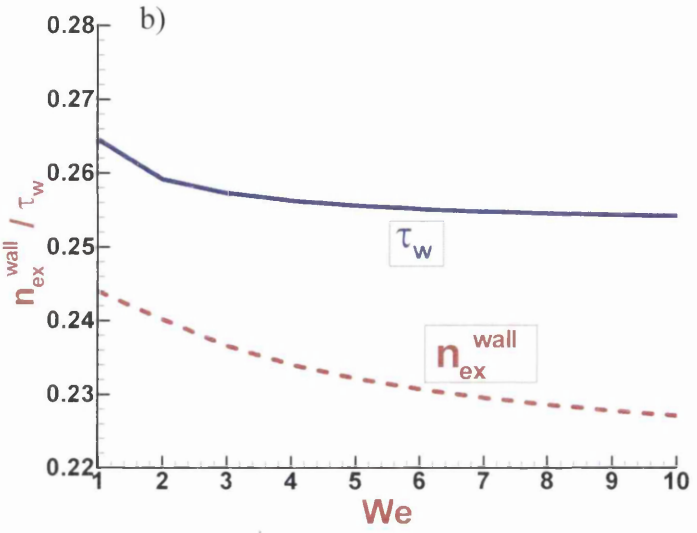

Figure 4.8: Swelling ratio, a) Tanner theory (2005), *We*-variation, b) exit correction n_{ex} and τ_w scaled by 7* τ_0, τ_0=0.01, m_p=10^2, β=0.9

β variation: At fixed ε=0.25, significant swelling may be observed with β=1/9 (increased slope), when compared to that with β=0.9, bar in the range 0<*We*<0.5 and as illustrated in Figure 4.9(a,b). At any given value of *We*, the swelling ratio is larger with less solvent concentration, as concluded by Bush [30]. To quantify and at *We*=7 for example, the swelling ratio is only 14% with β=0.9 but 22% for β=1/9. Additionally for β=0.9, final swelling is practically insensitive to change beyond *We*=2; in contrast at β=1/9, swelling is continually rising from *We*=1 to *We*=7, showing increase of almost 8%. Full swell profiles of Figure 4.9(b) reveal that at the extreme of low β=1/9 and high *We*=7, a prominent solution feature is the overshoot that occurs at a distance of around unity from the die (curve-[4]). This is an important result and one that is rationalized as primarily due to N_1 influence, as follows. From *We*=1 data (lower deformation rate), some minor enhanced swell is detected in the {β=1/9, ε=0.25; curve-[2]} solution compared to {β=0.9} solutions (curves-[1,3]) – this is the region of extensional viscosity domination (see Figure 4.3b). Alternatively, from *We*=7 data (larger deformation rate), much larger enhanced swell is observed in the {β=1/9}-solution above that for the {β=0.9}-solution (curve-[4] vs curve-[3]) – this is the region in which extensional viscosity is softening (so reducing), and where

differential in $\{N_1, \beta=1/9\}$ is captured; that is, with N_1 weakening upon rise in deformation rate, displaying an order of magnitude increasing shift at fixed rate from levels for $\varepsilon=0.25$ to $\varepsilon=0.02$ (see Figure 4.3c). Here, we are able to absorb the rheological benefit of the EPTT selection above that of the sustained hardening LPPT model-hence rationale for selection.

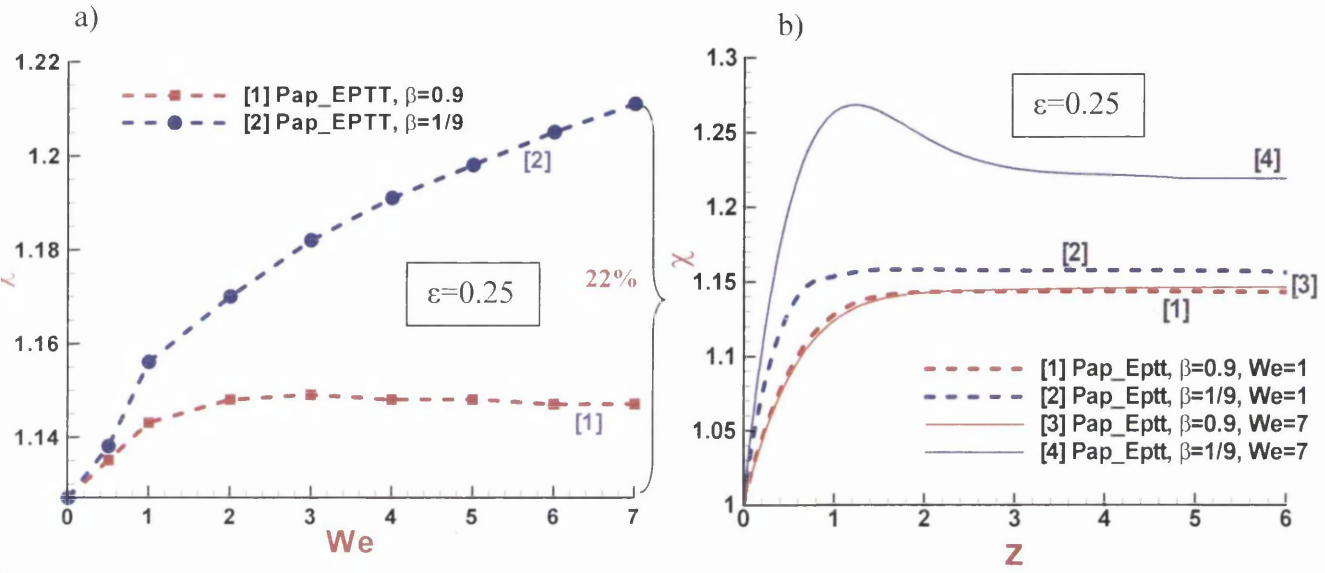

Figure 4.9: Swelling ratio, $\{\beta, \varepsilon\}$-variation, *We*–variation and position: $\tau_0=0.01$, $m_p=10^3$, $\beta=0.9, 1/9$; $\varepsilon=0.25$

ε variation: At fixed $\beta=0.9$ and shown in Figure 4.10(a) as a function of *We*, there is evidence of relatively large final swell increase observed at $\varepsilon=0.02$ and $We=7$; characteristically, some 33% in curve-[2] above the unity value. Similarly, one may account for the effect of β and ε variation together. From Figure 4.10(a) data, one may infer the impact of ε-change on the swelling is stronger than that due to β-parameter adjustment. By way of example, swelling ratio reaches 1.33 in value for $\{We=7, \beta=0.9, \varepsilon=0.02\}$, in contrast only reaching 1.14 for $\{We=7, \beta=0.9, \varepsilon=0.25\}$; a rise noted of some 19%. On the other hand, this ratio reaches 1.21 for $\{We=7, \beta=1/9, \varepsilon=0.25\}$, substantiating only a rise of some 7% (curve-[3]) above the $\{We=7, \beta=0.9, \varepsilon=0.25\}$ solution (curve-[1]). The data for the combination $\{\beta=1/9, \varepsilon=0.02\}$ of curve-[4], follows the same pattern of combined trends, displaying extreme behaviour in highly prominent swelling ratio, but remains

tractable to a convergence level of $We \approx 0.5$. This one attributes to the excessively strong extensional response for the $\{\beta=1/9, \varepsilon=0.02\}$ fluid model, which is larger at $We \approx 0.5$ with $\{\beta=1/9, \varepsilon=0.02\}$ than for $We=7$ with $\{\beta=1/9, \varepsilon=0.25\}$. Moreover, in Figure 4.10(b) for swell profiles, there is no evidence here of swell overshoot with $\beta=0.9$ data; which was apparent in the data for $\beta=1/9$ at higher elasticity $We=7$ (only attainable with $\varepsilon=0.25$). Hence, the lower elasticity solution of $\{We=0.5, \beta=1/9, \varepsilon=0.02\}$ does not reflect this overshoot either, but does achieve a most significant final swell value of 1.4, practically 40% of the initial jet-channel width (curve-[5]). The data of Figure 4.10(b) reveal relative change in final swell achieved with ε-shift from $\varepsilon=0.25$ to $\varepsilon=0.02$ at fixed $\{We, \beta=0.9\}$-level, being: 9% increase (from 13% to 22%) at $We=1$ (curves noted [1] to [2]); and some 19% (from 14% to 33%) at $We=7$ (curves noted [3] to [4], as in Figure 4.10(a)). The extra data provided in this plot for $\{We=0.5, \beta=1/9, \varepsilon=0.02\}$, show an additional increment in the final swell value of some 7%, (from 33% to 40%) above and beyond that gathered for $\{We=7, \beta=0.9, \varepsilon=0.02\}$ Here, it is the β-shift that is the most significant factor prevailing. One suspects that some overshoot in swell profile would appear around this latter parameter setting of $\{We=0.5, \beta=1/9, \varepsilon=0.02\}$ but this has proven elusive to resolve thus far in our parameter search.

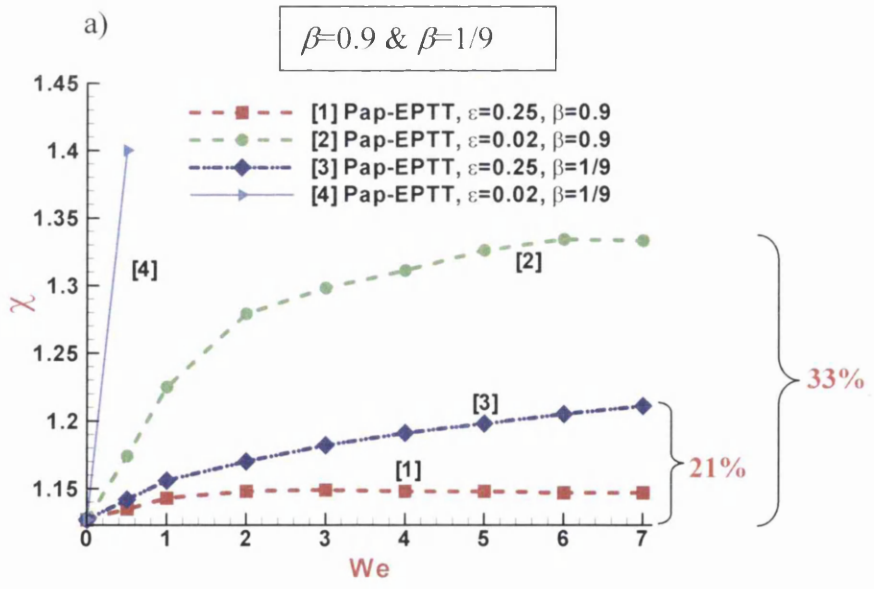

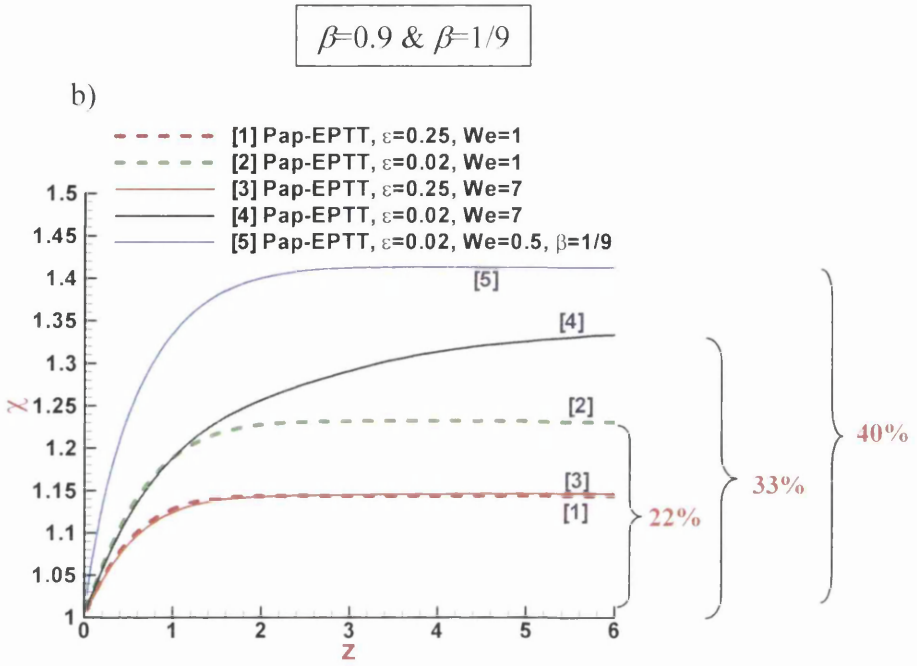

Figure 4.10: Swelling ratio, $\{\beta, \varepsilon\}$-variation, *We*–variation and position: τ_0=0.01, m_p=10^3, β=0.9, 1/9; ε=0.25, 0.02

ξ variation: The effect of second normal stress differences (N_2) in swelling ratio is also analysed, in addition to the dominant effect of the first normal stress difference (N_1). Note that in pure shear flow and with the PTT model, an increase in ξ proportionally reduces N_1 and increases N_2, $[N_2 = -(\xi/2)N_1]$. Therefore, one may anticipate that an increase in parameter ξ would reduce the swelling ratio. In Figure 4.11 and at fixed {*We*=1 and ε_{EPTT}=0.25, β =0.9 and 0.1}, the profile-shape of the free-surface can be interrogated for two different ξ_{EPTT}-values of ξ_{EPTT} =0.0 and 0.2. Here, one can detect a relative decrease of almost 3% and 1.6% in swelling ratio from ξ_{EPTT} =0.2 to ξ_{EPTT} =0.0 (from 1.16 to 1.13 and from 1.146 to 1.127) for β =0.9 and β =0.1 respectively. Values of ξ_{EPTT} larger than 0.2 (N_2/N_1=20%) lead to numerical convergence difficulties, being subject to onset of the well-known Gordon-Schowalter instability.

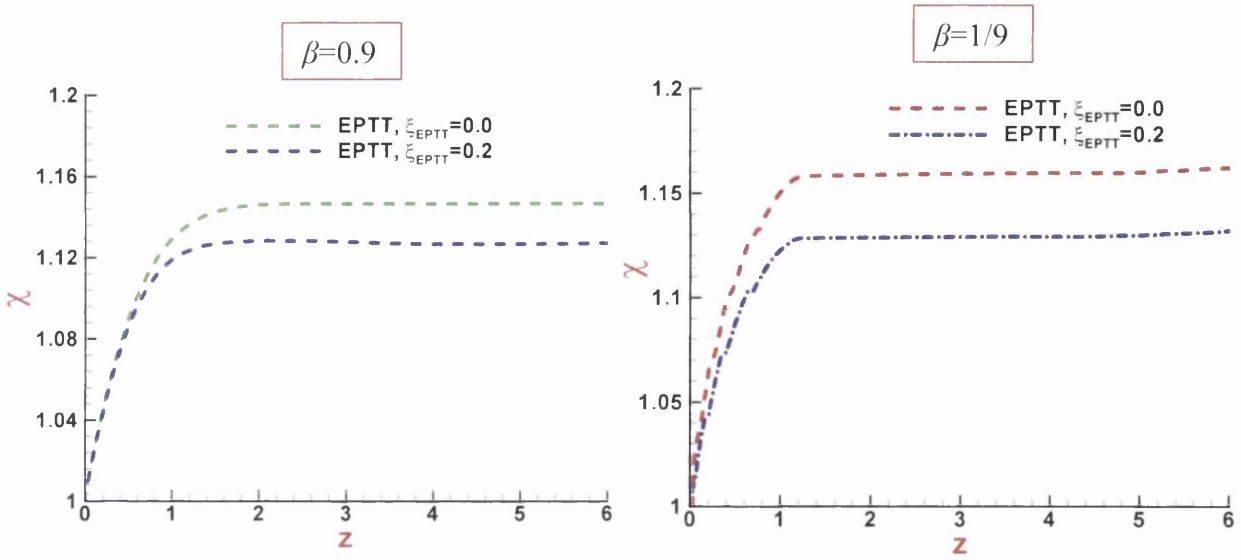

Figure 4.11: Swell profiles, EPTT: ξ_{EPTT}-variation, *We*=1, β=0.9, β=1/9; ε=0.25

4.5.2 Velocity profiles

Cross-channel velocity profiles in radial and axial component forms are provided in Figure 4.12 at fixed τ_o (τ_o=0.01) and m_p (m_p=10^2). The axial velocity profile shows parabolic flow structure for z≤0; then the magnitude diminishes as it approaches the die exit (over z≥0) and gradually adjusts to a plug flow over this zone. Along the radial span 0≤r≤1, the radial velocity increases initially, up to z=0.1, after which it drops away with gradual decrease observed through the free surface region (z≥0). Maxima at z≤0 reduce by almost half from U_r of 0.3 at z=-0.1 to 0.15 at z=0.1.

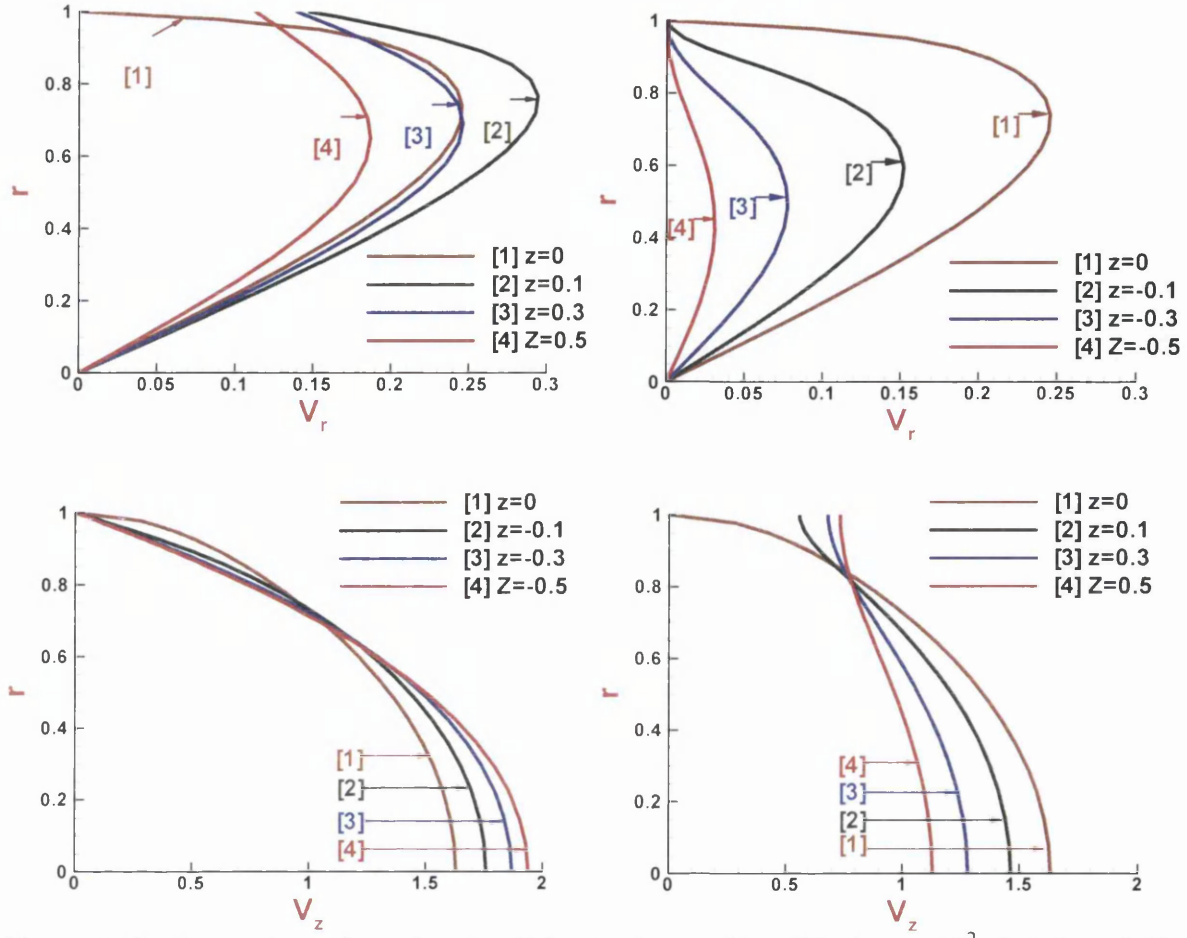

Figure 4.12: Cross-channel axial and radial velocity profiles: We=1, m_p=10^2, β=0.9,τ_0=0.01

4.5.3 Stress profiles

τ_o variation: The radial stress τ_{rr} profiles, first normal stress difference (N_1), and normal stress (τ_{zz}) along the *axis of symmetry* are plotted in Figure 4.13(a,c,d) at fixed {We=1, m_p =10^2, β=0.9, ε=0.25} under τ_0 variation (see additional comparative data in Table 4.2 for We=1,5; shear-rate $\dot{\gamma}$ (gamma) and strain-rate Σ (sigma)). In all cases, shear-rate, strain-rate and stress peaks are observed in the singular region at the die-exit plane (z=0), with some relaxation apparent over the jet region and where there is relatively insignificant influence of yield stress τ_0 on deformation rates (data withheld). Shear-rate peaks rise near the contact point as τ_0 increases, with maxima occurring around 17.76 units at τ_0=0.1; a

strictly localized effect on the *top surface*. In Figures 4.13(a,c), one can observe a relative increase of almost 52% in τ_{π} and 38% in τ_{zz} peak magnitudes, as τ_0 increases from zero (EPTT) to 0.1. Noting from Figure 4.4(b) that the swelling ratio declines with such increase in τ_0; hence one notes an opposing trend in normal stress from that in swell. Moreover, with rising τ_0 between τ_0=0.02 to 0.1, both τ_{π} and τ_{zz} profiles reveal trends of downstream shift and amplification. In contrast, viewing the τ_{rz} data on the top surface (see Figure 4.13(b)), an opposing declining trend from shear-rate data occurs at the die-exit singular peak with a gradually falling peak as τ_0 rises (attributable to viscous effects); in the die itself (confined shear flow), the shear stress increases in magnitude with τ_0 rise (see exit correction above, due to τ_0 rise). In extensional data, strain-rate peaks adjust with τ_0 rise as in shear-rates, being strictly localised to the die-exit and top surface (extrema -1.26 units for τ_0=0.1). Most significant solution shifts are detected in N_1 (normal stress, $\tau_{zz} - \tau_{rr}$) along the symmetry-axis in Figure 4.13(d) (vs Figures 4.13(a,c)); this is clearly conspicuous in τ_0=0.1 data, displaying both increased magnitude in the singular zone (doubles τ_0=0 (EPTT) level, with downstream shift) and undershoot/overshoot in pre- and post-die-exit regions. Notably, the trend here is of *increasing N_1 maxima with rising τ_o* (see below, to contrast against that under rising *We*).

Table 4.2: Die-swell flow: Stress, shear-rate, and strain-rate as a function of τ_0, Pap-EPTT, We =1, m_p=10^2, β=0.9

solutions	*We*=1			*We*=5		
	τ_o			τ_o		
	0	0.02	0.1	0	0.02	0.1
τ_{rr}	Max= 0.086 Min= -0.051	Max= 0.067 Min= -0.051	Max= 0.088 Min= -0.053	Max= 0.049 Min= -0.010	Max= 0.055 Min= -0.011	Max= 0.035 Min= -0.011
τ_{rz}	Max= 0.268 Min= -0.253	Max= 0.267 Min= -0.254	Max= 0.264 Min= -0.309	Max= 0.094 Min= -0.076	Max= 0.094 Min= -0.076	Max= 0.093 Min= -0.076
τ_{zz}	Max= 1.020 Min= -0.068	Max= 1.024 Min= -0.063	Max= 1.044 Min= -0.074	Max= 0.321 Min= -0.028	Max= 0.322 Min= -0.034	Max= 0.327 Min= -0.023
τ_{qq}	Max= 0.086 Min= 0.0	Max= 0.067 Min= 0.0	Max= 0.087 Min= 0.004	Max= 0.049 Min= 0.0	Max= 0.055 Min= 0.003	Max= 0.035 Min= 0.004
$\dot{\gamma}$	Max= 17.16	Max= 17.28	Max= 17.76	Max= 16.95	Max= 17.07	Max= 17.54
Σ	Max= 0.027 Min= -1.258	Max= 0.027 Min= -1.259	Max= 0.370 Min= -1.264	Max= 0.029 Min= -1.258	Max= 0.030 Min= -1.259	Max= 0.319 Min= -1.264
N_1	Max= 1.002 Min= -0.154	Max= 1.01 Min= -0.12	Max= 1.03 Min= -0.16	Max= 0.304 Min= -0.074	Max= 0.306 Min= -0.089	Max= 0.311 Min= -0.058
N_2	Max= 0.058 Min= -0.064	Max= 0.057 Min= -0.065	Max= 0.057 Min= -0.067	Max= 0.017 Min= -0.017	Max= 0.017 Min= -0.017	Max= 0.016 Min= -0.018

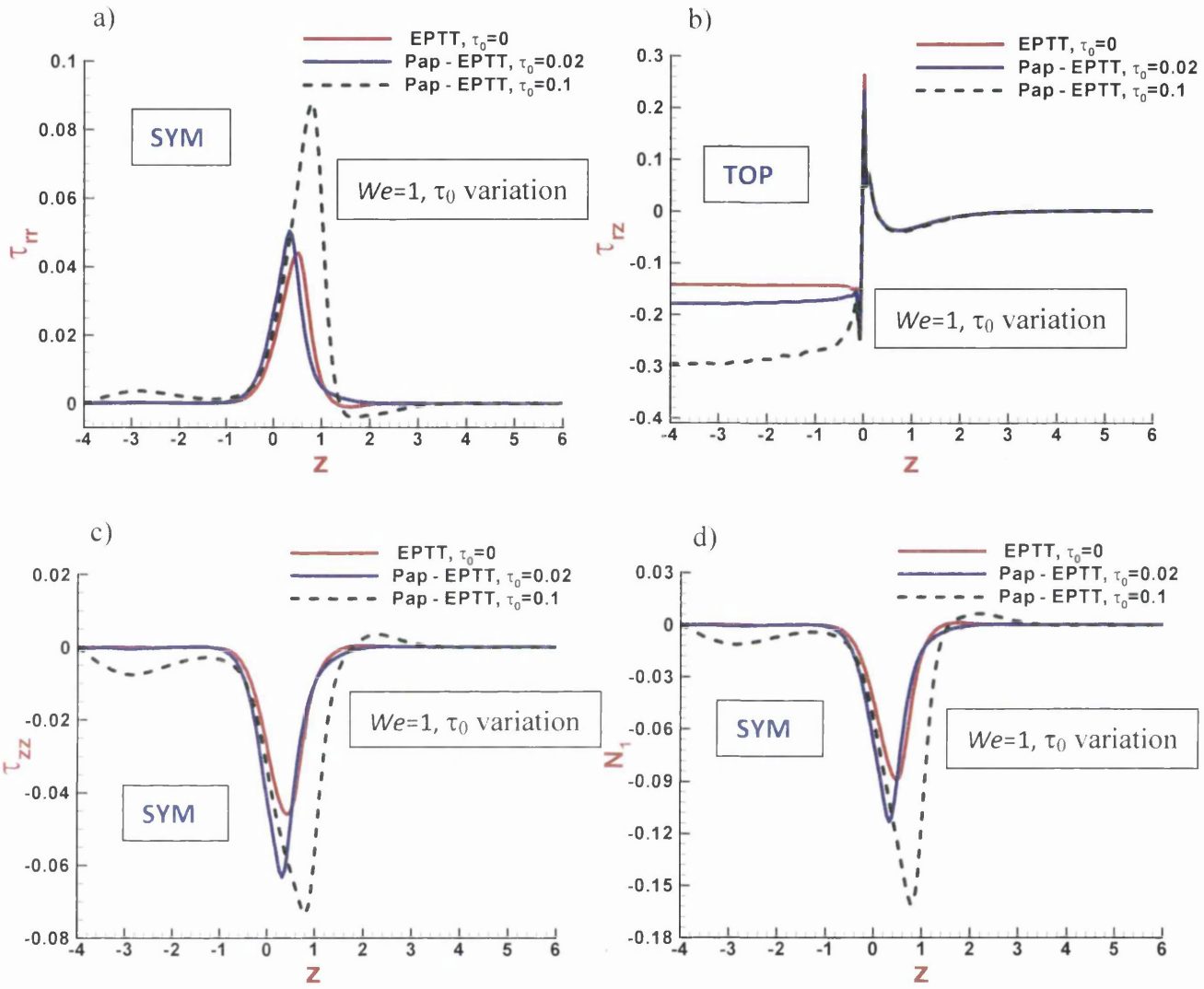

Figure 4.13: Stress profiles along symmetry-axis and top surface; τ_0 variation, a) τ_{rr}, b) τ_{rz} c) τ_{zz}, d) N_1; Pap-EPTT, $m_p=10^2$, $\beta=0.9$

We variation: In contrast to the above, Figure 4.14(a,c,d) plots illustrate change with *We* in the radial stress (τ_{rr}), first normal stress difference (N_1), and normal stress (τ_{zz}) at fixed {$\tau_0=0.01$, $m_p=10^2$, $\beta=0.9$, $\varepsilon=0.25$}. One also gives consideration to shear stress along the top surface (τ_{rz}, Figure 4.14(b)). Through the radial component τ_{rr}, one observes slight increase in its magnitude with increasing *We*, as illustrated in Figure 4.14(a); comparably, the converse is true (with decline) in first normal stress N_1 and normal stress τ_{zz}. One may

interrogate this rich extensional stress data in Figure 4.14(a,c,d) together, which reveals that normal stress effects are highly significant in this flow with rising *We*. N_1-peaks shift downstream and now *reduces by about 30% from We=0.5 to 5* (from around -0.12 to -0.08 units); *downstream overshoot* is also apparent. To explain such trends through individually segregated stress components, one identifies that radial stress amplifies (0.04 to 0.06), whilst axial stress magnitude declines (0.06 to 0.03) with rising *We*, both displaying *strong downstream shift*: from *We*=0.5 to 5: τ_{zz} reduces by about 43%, whilst τ_{rr} increases by about 21%. This implies that second normal stress effects (via τ_{rr}) adopt a significant role in this benchmark problem, and contribute strongly to reduction in first normal stress difference levels. Thus, in contrast to the above findings under rising τ_0 (yield stress influence), the trend now *with rising We* (viscoelastic influence) is one of *declining* N_1 *maxima*; a completely opposite finding, and one that correlates the opposing results observed on swell. These comments apply to the isolated window of extensional deformation on the axis of symmetry, pre and post die-exit. In addition in shear deformation on the top surface and Figure 4.13(b), and Figure 4.14(b), one may comment on shear stress (and N_1) trends, where once more yield stress and elasticity effects act in opposing directions. From such die-wall shear stress data, one can conclude that shear viscosity declines with rising *We* (relatively thinning) and increases with rising τ_0 (relatively thickening); this trend is replicated therefore in N_1 along the die-wall. Consistently, at the die-exit singularity, shear stress (and N_1) peaks are observed to decline with rising *We*, following trends within the die; yet are barely influenced by rising τ_0. The shear stress profile just beyond the die, displays undershoot damping with rising *We* (elastic response), yet is unaffected by rising τ_0 (viscoplastic response).

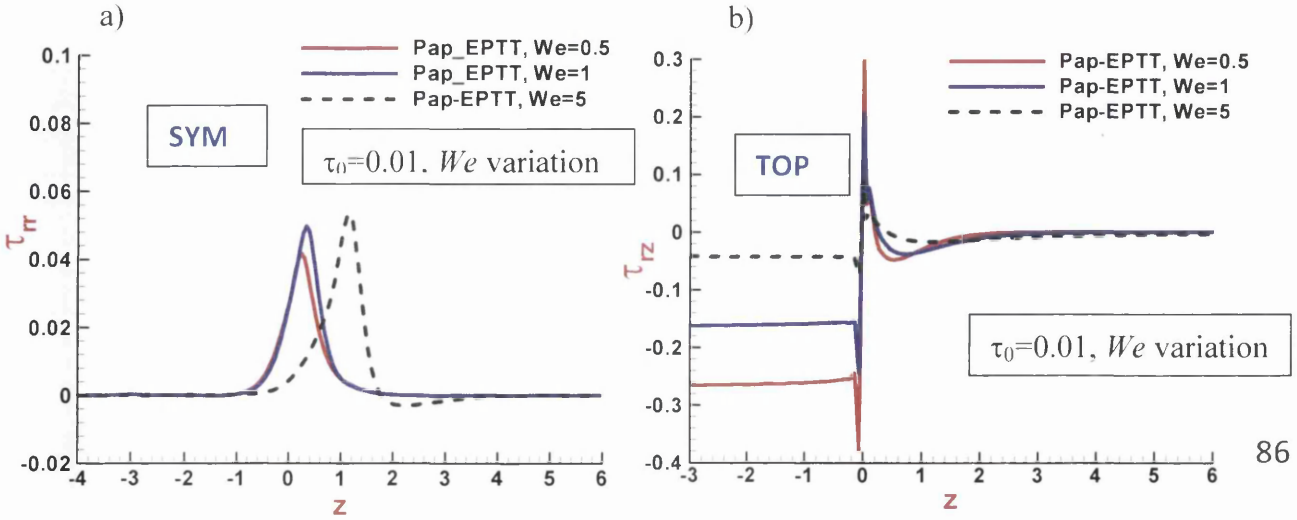

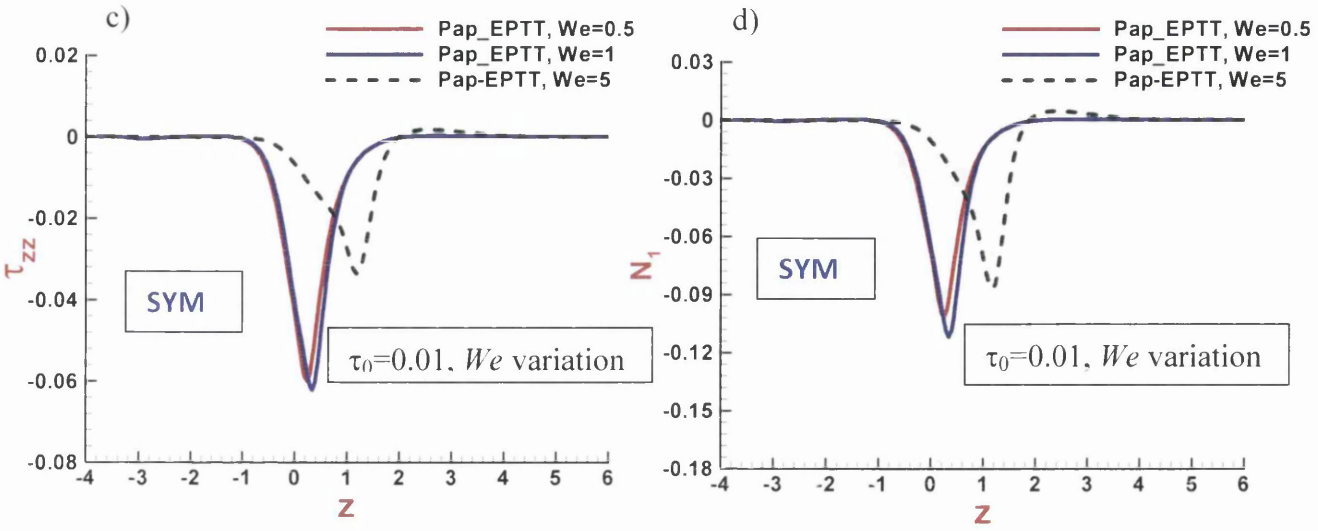

Figure 4.14: Stress profiles along symmetry-axis and top surface; *We*-variation, a) τ_{rr}, b) τ_{rz}, c) τ_{zz}, d) N_1, Pap-EPTT, $m_p=10^2$, $\beta=0.9$

4.5.4 Stress fields-yielded and unyielded regions

With regard to normal stress effects, the field structures in first and second normal stress, axial normal stress τ_{zz} and radial normal stress τ_{rr} are displayed in Figure 4.15, 4.16 and 4.17. From N_1, N_2 and τ_{zz} the maxima are focused near the zone of the singularity. Whilst, for the radial stress τ_{rr} maxima arise around the symmetry–axis, see Figure 4.17. N_1 influence at *We*=1, see Figure 4.15 shows a rise in N_1 with increase τ_0 around the singular point (z=0). Similar trends in τ_{zz} are observed, with maxima of 1.04 units reached at $\tau_0=0.1$

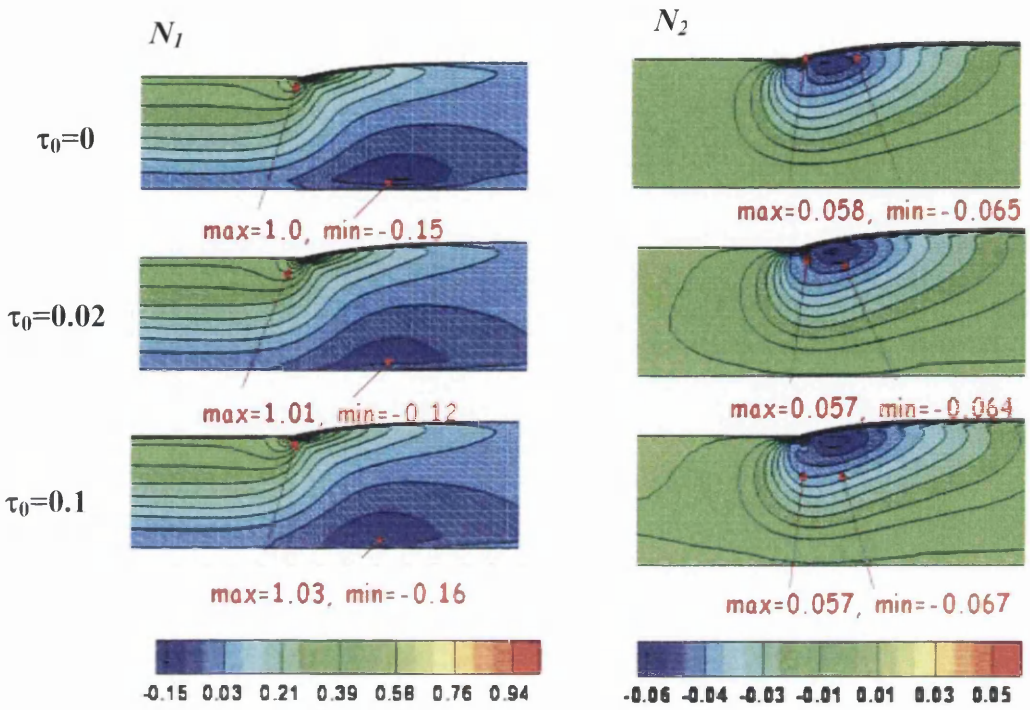

Figure 4.15: First normal stress difference (N_1), second normal stress difference (N_2): Pap-EPTT,τ_0 variation We =1, m_p=10^2, β=0.9

In contrast, there is clear influence of We rise on τ_{zz} maxima, which reduces by 30% from We=1 to We=5. Additionally, τ_{rr} maxima reduce by 50% from We=1 to We=5

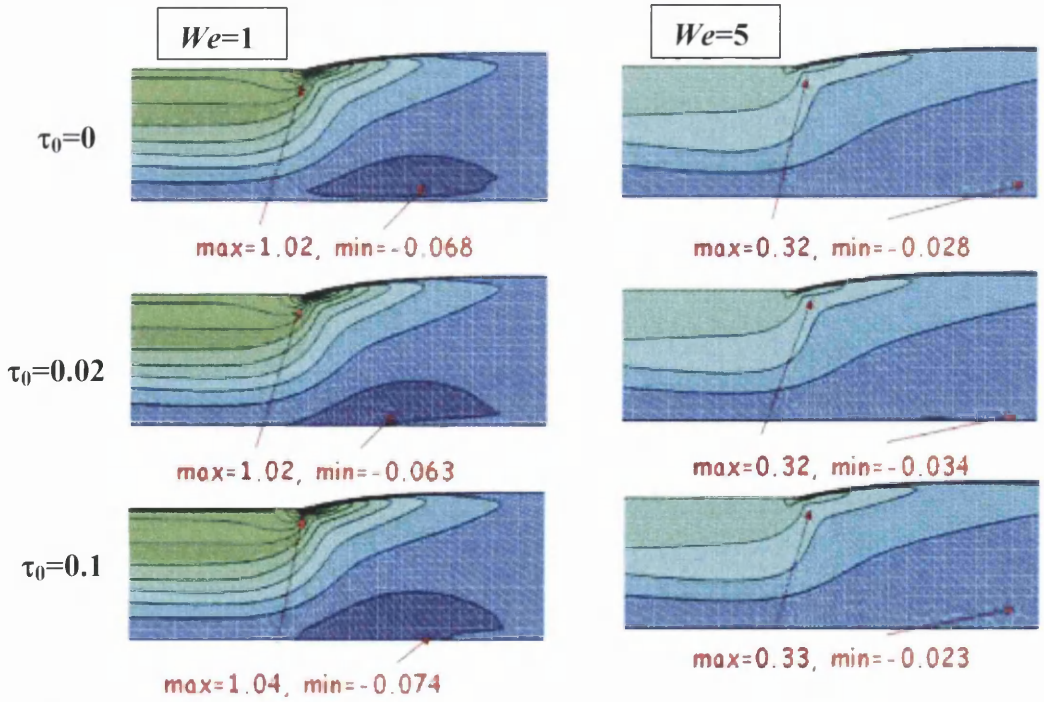

Figure 4.16: Axial normal stress (τ_{zz}): Pap-EPTT,τ_0 variation, We =1,5, m_p=10^2, β=0.9

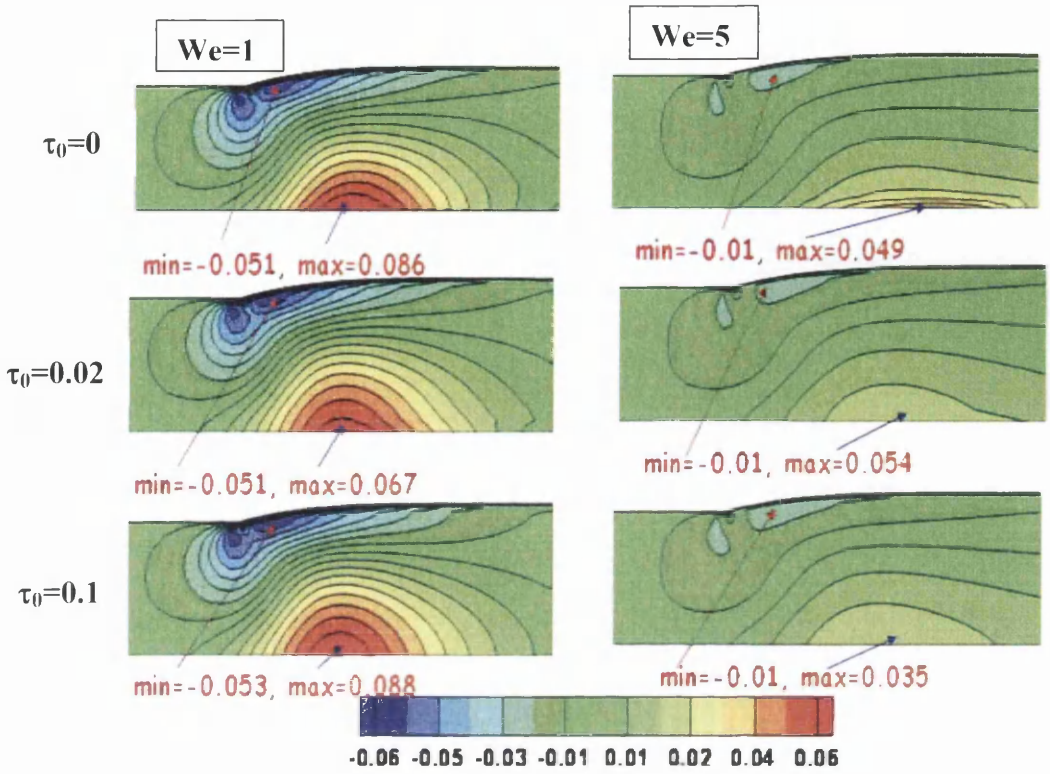

Figure 4.17: Radial normal stress (τ_{rr}): Pap-EPTT,τ_0 variation, *We* =1,5, m_p=10^2, β=0.9

Considering yield stress effects, it is informative to interrogate the yielded and unyielded regions, according to various τ_0 at fixed m_p (m_p=10^2), as depicted in Figure 4.18. With this Pap-EPTT model, the cut-off locations between the yielded and unyielded regions are based on the second rate-of-strain invariant criterion. In all cases and with larger τ_0 values, there is a slight growth apparent in the unyielded zones. The unyielded material is observed to extend over the jet region, where the relatively yielded (greater flow deformation, red) region for τ_0 =0.01 occupies the zones within the channel and one-third of the jet region. At the same time, one can gather that the unyielded (plug-like, less flow deformation, blue) region extends through to the free surface itself. Sharp adjustment is noted in the yield front shape towards the free-surface at the low level of τ_0 =0.01. As the level of yield stress τ_0 increases, no significant change is detected between τ_0 =0.02 and τ_0 =0.01. With further rise in τ_0 to 0.1, the unyielded zones expand and a narrow zone appears on the symmetry-axis in

the die; yield fronts are now relatively smooth. Upon further amplification of τ_0 to 0.5, the unyielded material now occupies practically all the jet region, and also broadens on the axis of symmetry. As τ_0 increases, the progressive growth of the unyielded regions is quite apparent, which is entirely consistent with findings reported by others (Zisis and Mitsoulis [156]; Mitsoulis and Huilgol [84]; Belblidia et al. [17])

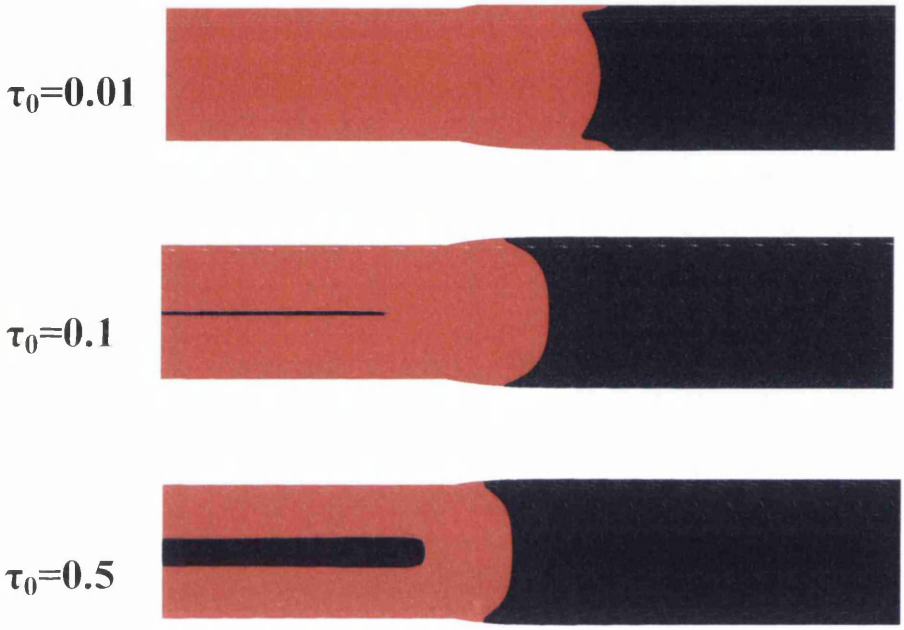

Figure 4.18: Growth of unyielded region (blue): Pap-EPTT model, τ_0 variation, second invariant of rate-of-strain criterion; τ_0 variation, We =1, m_p=10^2, β=0.9

4.6 Strain-rate stabilization (SRS) (*D-Dc*)

Here, results are described for the Pap-EPTT model with β=0.9 and ε=0.25, when appealing to the singularity capturing and stabilisation technique, referred to earlier as '*Strain-Rate Stabilisation (SRS) (D-D$_c$)* (for more details, see section 3.7). In this regard, the focused interest lies in identifying the effective discrete handling of the die-exit swell singularity, for which we present steady-state stress solutions and swelling ratios at selected We-levels. See also, the pertinent work of Georgiou et al. [51], which captured solution

singularity by applying a singular finite element method to accelerate convergence for sudden-expansion and die-well problems.

4.6.1 Swelling ratio

The corresponding swelling ratio data is provided in Figure 4.19, at the two different values of the Weissenberg number (We=1,5), with fixed (τ_0=0.01, m_p=10^2). According to these findings, a lower level of swelling is observed when the singularity is directly represented through (D-Dc) realisation. One may report that the relative difference in swelling ratio with and without (D-D_c) decreases from 0.85% at We=1 to 0.43% (almost half) at We=5. This is firm evidence of the strongly localized nature of the die-exit singularity and the consequent impact that this can have on the extrudate solution; in particular, the swell captured varies with the degree of elasticity in the flow. Hence, the dominance of such localized effects shifts and the challenge is to sharply capture such solution features with minimum numerical dispersion (akin to shock capturing).

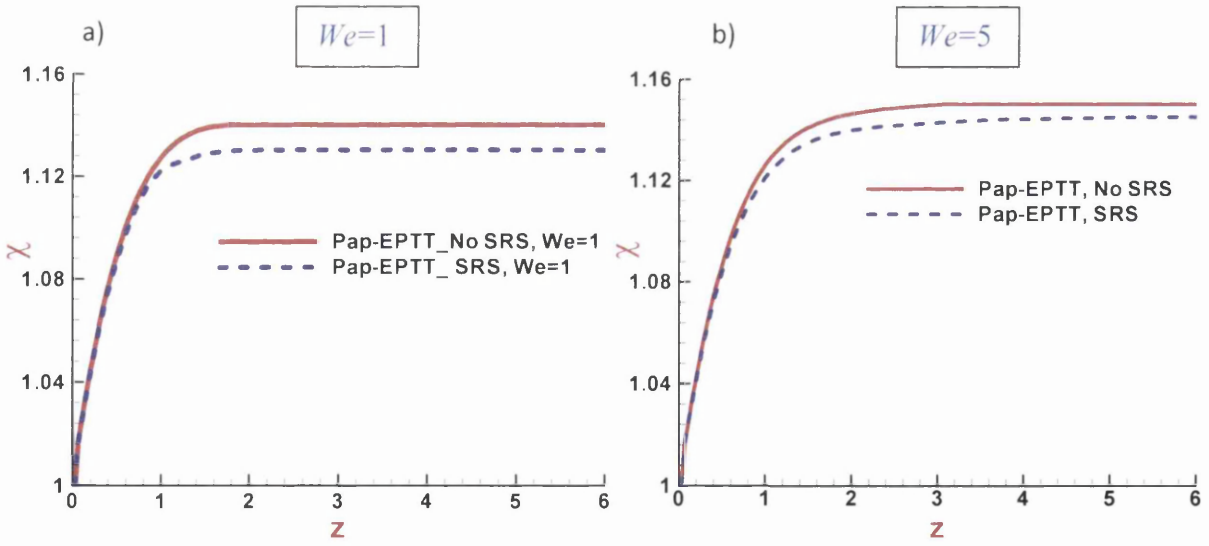

Figure 4.19: Swelling ratio with D-Dc, a) We =1, b) We =5: Pap-EPTT,τ_0 =0.01, m_p=10^2, β=0.9

4.6.2 Stress profiles

Stress and strain-rate profiles are illustrated in Figure 4.20 and 4.21 through We=1, 5 at fixed τ_0-value (τ_0=0.01) and m_p-value (m_p=10^2). In Figure 20(a,b) at We=1 and under strain-

rate stabilization, there is decrease in shear-rate and τ_{rz} –stress peaks compared to that without (*D-Dc*) treatment. This pattern is repeated with elevation in elasticity to *We*=5, as displayed in Figure 21(a,b). These plots reflect the highly-localised influence of the (*D-Dc*) correction, particularly at the singular plane (z=0). Elsewhere, away from the singularity and along the symmetry axis, there is little effect appearing in strain-rate under (*D-Dc*) treatment; whilst τ_{zz} stress shows a slight downstream shift, with magnitude reduction as *We* rises from 1 to 5.

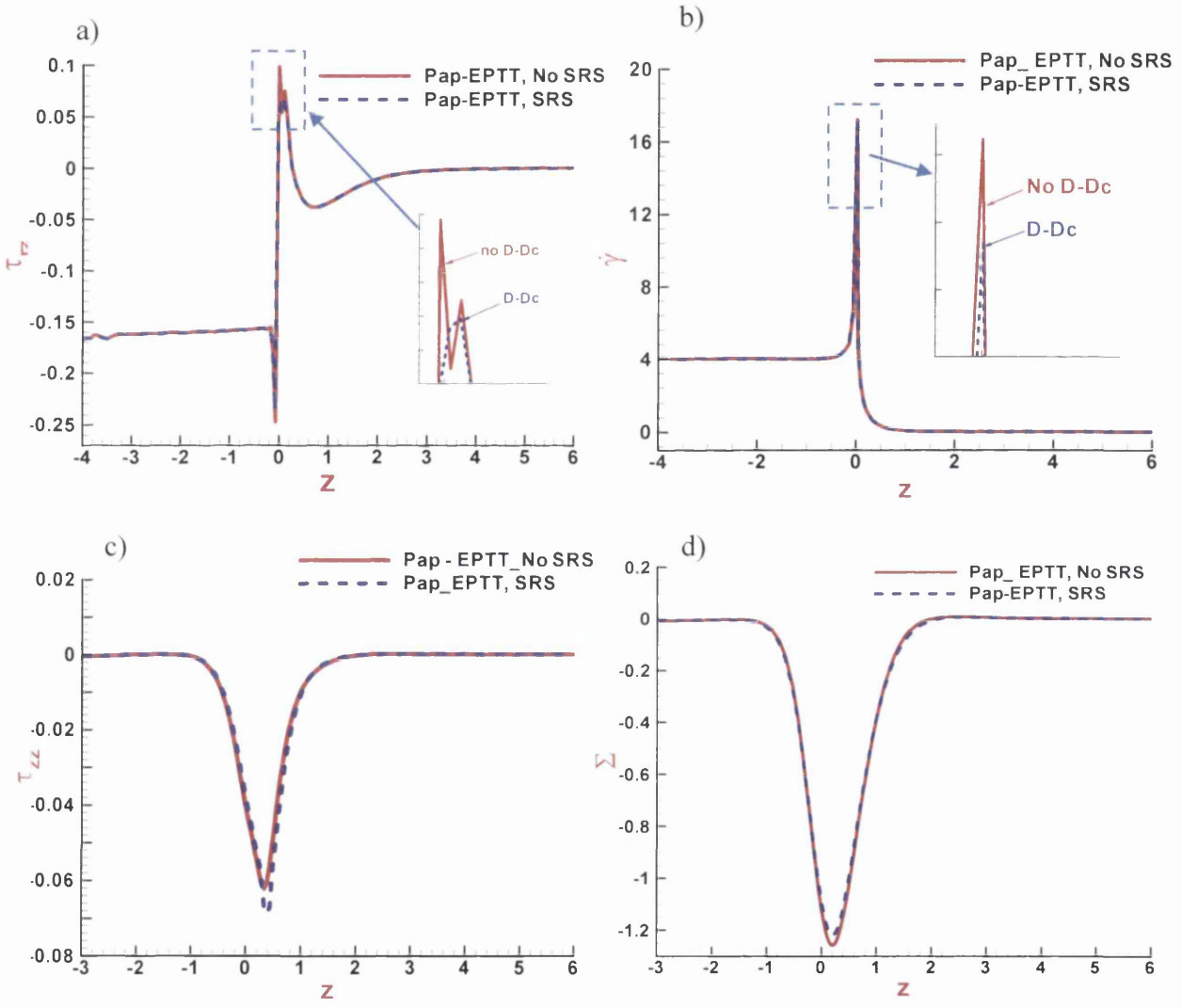

Figure 4.20: Stresses with *D-Dc* (SRS), (1) along top surface a), shear stress, b) shear-rate, (2) along axis of symmetry, c) normal stress, d) strain-ratr : Pap-EPTT, *We* =1, τ_0=0.01, m_p=10^2, β=0.9

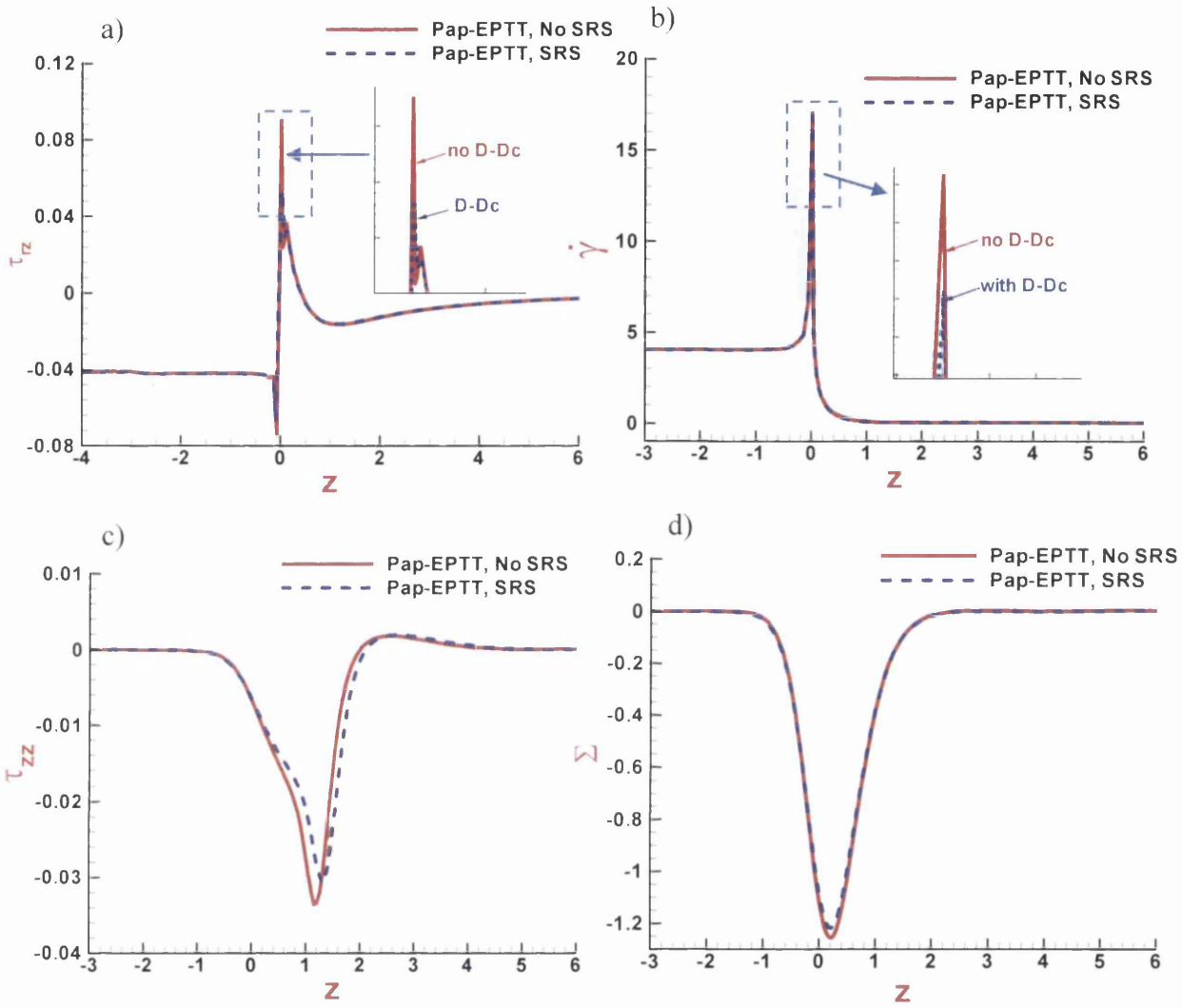

Figure 4.21: Stresses with *D-Dc*, (1) along top surface a), shear stress, b) shear-rate, (2) along axis of symmetry, c) normal stress, d) strain-rate : Pap-EPTT, We =5, τ_0=0.01, m_p=10^2, β=0.9

Moreover, this position is further supported with the additional stress profile data of Figure 4.22 along the top surface alone, which allows one to directly contrast findings between the individual components for the two algorithm settings. The dominance of the axial component in τ_{zz} is clear and this is strictly localisied to the corner singularity plane. Note that the azimuthal τ_{qq} component also indicates a downstream shift with elasticity increase.

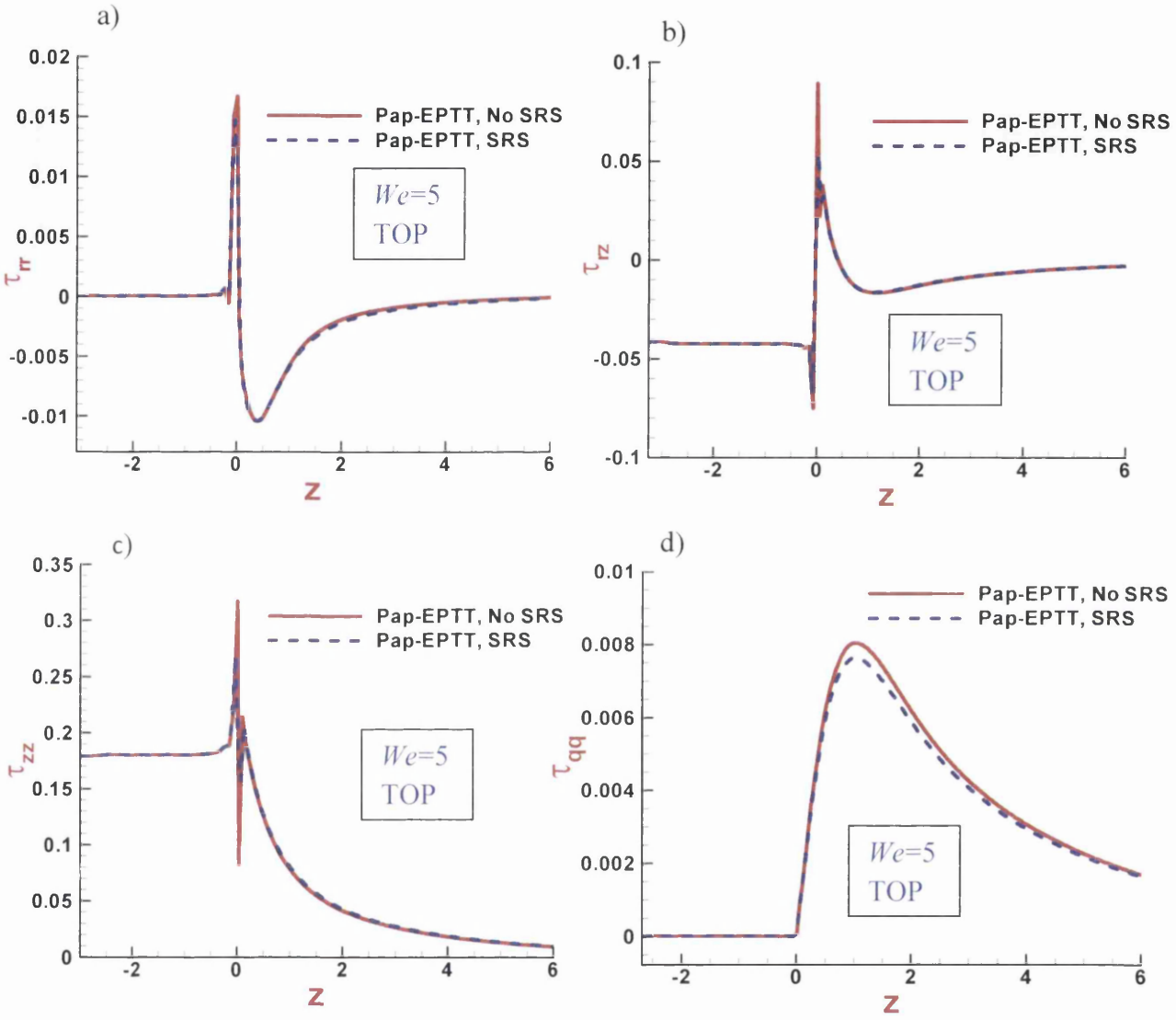

Figure 4.22: Stresses with *D-Dc*, along top surface a) τ_{rr} b) τ_{rz}, (c) τ_{qq}, d) τ_{zz}: Pap-EPTT, We =5, τ_0=0.01, m_p=10^2, β=0.9

Finally, a steady-state three-dimensional plot of the *D-Dc* term is provided in Figure 4.23 at We=5. This figure exposes the localised nature of the stabilisation term (compact support for singularity capturing, dispersion restricted), which is strongly constrained to act around the die-wall exit/jet-entry position. A comment in passing is that such a deferred

correction term is observed to principally affect the subsequent accurate capture of the jet free-surface position.

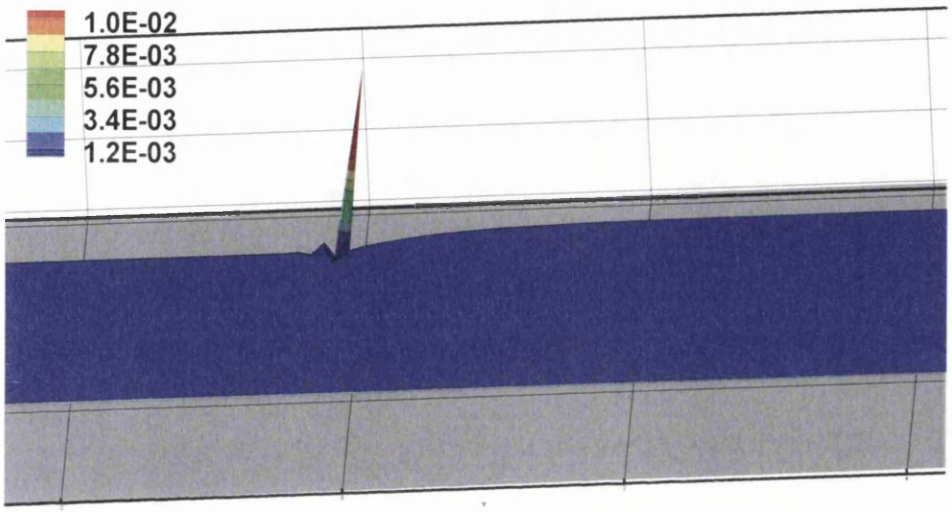

Figure 4.23: 3D plot of steady-state (D-Dc) field; SRS-scheme, Pap-EPTT, We =5, τ_0=0.01 m_p=10^2, β=0.9

4.7 Conclusion

In this chapter, an analysis has been presented of steady free-surface flows for the viscoelastic EPTT fluid and extended this into viscoelastoplasticity via viscous-regularisation, and the Papanastasiou-EPTT fluid model. Two pairings of {β, ε}-parameters are investigated, ε={0.02, 0.25} and β={0.9, 1/9}, at fixed yield stress setting {τ_o, m}; to reflect (i) in ε–parameter, high and low Trouton ratios (extensional viscosities), and (ii) in β–parameter, high and low solvent fraction. With the selected set of parameters, the study began with a fluid of high solvent fraction β=0.9 and ε=0.25, after which comparison is extended to instances with β=1/9 (highly polymeric) and ε=0.02 (highly dynamic). Thereby, significant impact has been reported on swelling ratio and exit pressure correction due to variation in yield stress parameter τ_o, Weissenberg number (We), viscosity parameter β and Trouton ratio parameter ε.

Findings ***on swell*** reveal that viscoplastic influences counter those due to elasticity, with *elevation* in *plasticity suppressing swell* whilst *rise* in *elasticity stimulates swell (due to normal stress effects, see below)*. Hence, under yield stress parameter ***τ_o-variation*** and fixed elasticity, the swelling decreases (whilst *exit correction rises*). The *We*=1 swell data reveal a quadratic decline from the purely viscous level initially up to τ_0=0.02, followed by an almost linear fall-off thereafter. At a larger elasticity level of *We*=5, the tendency is to suppress this early quadratic decline in swell at low-τ_0, but beyond the τ_0-level of 0.1, the viscoplastic influence completely dominates. In the low-τ_0 regime, the evidence at *We*=1 points to a strong influence of shear viscosity and shear-thinning causing swelling ratio to diminish with rising yield-stress (τ_0). In contrast and as explained through the respective material functions, there is little impact on swelling ratio under m variation (yield stress growth exponent). Findings ***under fixed yield stress*** and with ***We*-variation** oppose those observed under τ_0 rise, in that *larger elasticity* provokes *greater swell* and *lesser exit correction*. Classical elastic theory relates the swell versus *We* to the ratio between N_1 and τ_w at the die-wall in fully developed flow, from which the standard exponent m_T =2, clearly provides an overestimated swell prediction, whilst a reasonable fit is extracted with m_T =3.8.

In the case of **{β, ε} variation with** *We*, at fixed τ_0=0.01 and m_p=10^3, swelling ratio is found to rise with increasing *We*, reaching the high percentage ranges of 14% with {β=0.9, ε=0.25}, 21% with {β=1/9, ε=0.25} and 33% with {β=0.9, ε=0.02}. At fixed ε=0.25 and under ***β* variation**, significant swelling may be observed with β=1/9, when compared to that with β=0.9, bar in the low range 0<*We*<0.5. At any given value of *We* and as concluded by others, swelling ratio is larger with less solvent concentration. Full swell profiles at the extreme of low β=1/9 and high *We*=7, reveal a prominent solution overshoot that occurs at a distance of one unit from the die. One may argue comparatively that this is primarily due to N_1 weakening, as extensional viscosity is softening in the associated parameter ranges. At fixed β=0.9 and under **ε variation**, there is evidence of a relatively large final swell increase observed at ε=0.02 and *We*=7; characteristically, some 19% above the reference

level for {β=0.9, ε=0.25}. Taken together, one may infer the impact of ε-change (Trouton ratio) on swell is much stronger than that due to β-adjustment (solvent fraction).

With respect to ***exit pressure correction***, a consistent rise is observed with increasing *We* and τ_0. ***Under τ_o variation***, the exit correction increases linearly by some 30% above the unity EPTT reference line at τ_0=0.5, when m_p=10^2 and *We*=1. Effectively, *less swell*, is compensated by *larger exit pressure correction*, and in this regime viscoplastic influence dominates. Whereas for exit pressure correction ***under We variation***, and with both viscoelastic and viscoplastic contributions accounted for, monotonic decline is observed in n_{ex}^{wall} with minima around 0.227 units at *We*=10. Noting the decline in channel pressure-drop with *We*-rise, still a dominant factor in the declining n_{ex}^{wall}, is the falling wall shear-stress (τ_w). In contrast, the trend is non-monotonic in n_{ex}^{Eptt} data, when only the yield stress contribution is differentiated (with EPTT elastic and shear-thinning effects suppressed). Then, a gradual decline in exit correction is reported in the extended range $2 < We < 9$; yet, there is a slight increase to a maximum seen in the initial range $0 \le We \le 2$. Taken on the basis of comparison re n_{ex}^{Pap} data, whereupon yield stress influence is nullified, findings again reveal monotonic decline in exit correction due to the viscoelastic contribution.

On stress data, under *We* increase at fixed yield stress level, it is notable that radial stress strongly amplifies, whilst axial stress declines with rising *We*, both displaying significant *downstream shift;* resulting in N_1 decline. In contrast, under τ_o increase N_1 rises, and this may be attributed to rise in both τ_{rr} and τ_{zz} components. This implies that second normal stress effects (τ_{rr}) are vitally important in this problem, which have major impact on first normal stress difference levels and swell damping amplification.

Present findings demonstrate that the extent and shape of the yielded and unyielded regions depend on the level of yield stress imposed (level of τ_0 or Bingham number). The unyielded zone begins to appear first in the jet region, and then expands with further increase in τ_0 to gradually emerge around the symmetry axis, simultaneously retreating further back within the die. Once more, these results are consistent with the findings of others.

Finally, *strain-rate stabilisation* has also been investigated for this problem to interrogate the influence of singularity capturing on the die-exit solution. In this respect, there is successful demonstration that such treatment can have a significant impact on peak stress and strain rates exiting the die. In turn this has been shown to influence the accurate determination of the free-surface profile, where such variation has been detected in swell ratio at selected Weissenberg numbers and yield stress levels.

Chapter 5

Numerical study of the Finite element method for tube-tooling cable-coating flow: Newtonian and inelastic fluids

5.1 Introduction

In this chapter, a numerical analysis of Newtonian and inelastic fluids is performed with a semi-implicit time-stepping Taylor-Galerkin Pressure-Correction finite element (TGPC) algorithm as mentioned in chapter 3. The momentum and continuity equations that govern the Newtonian and general Newtonian fluids are elliptic partial differential equations. In this instance, the Galerkin discretisation represents an optimal selection to solve this type of equation. Briefly, this algorithm is based upon two phases. The first phase is a Taylor-Galerkin approach expressed through a two-step Lax-Wondroff time stepping procedure (see section 3.2). The second phase involves a pressure-correction method which provides second-order accuracy in time.

This investigation addresses the tube-tooling extrusion coating problem, where steady solutions to this free surface flow problem are obtained through a transient finite element procedure. Here, free-surface movement is accommodated via a particle-tracking/surface height-function technique (*dh/dt)*, developed by Phan-Thien [103]. Two

scenarios are considered to resolve the flow dynamics and determine a suitable shape for the extrudate swell. Initially, a solution is obtained when free surface movement is suppressed, and a domain-interior solution is generated. Then, at the second stage, the solution to the free surface problem is resolved commencing from this interior solution, using coupled and decoupled free-surface approaches. In the coupled technique, the problem is solved with freedom of movement on both the top and bottom surfaces of the draw-down conduit. In contrast, the decoupled method subdivides itself into two phases of analysis. The first phase permits movement of the bottom surface of the draw-down section alone; hence with fixed top surface position. Then, the second phase is used to solve the equivalent top-surface movement alone.

Cable coating procedures play an important role in the modern industrial process setting. This process involves the extension of a molten polymer over a moving cable, and typically requires a cable preheater, an extruder with a cross-head shaped die, a cooling trough for the extruded cable, and a take-up and payoff device ([93,85,86]). There are two main types of annular extrusion coating designs: namely tube-tooling, used for wide-bore coating, and pressure-tooling, associated with narrow gauge wires/cables ([56]). For pressure-tooling the coating is delivered directly to the coating substrate/carcass from the die, whilst for tube-tooling, there is an air-gap beyond the die. Here, the molten polymer is drawn down onto the cable-carcass by virtue of the additional drag flow component induced by the motion of the cable. Since contact between the polymer coating and the cable occurs beyond the die for tube-tooling, the control and shape of the extrudate is of considerable importance in the process.

Numerically, the subject matter of cable-coating, with dual free-surface location, die-swell and slip, dynamic contact point singularity and influence of vacuum effects, remains a significant challenge, yet despite its commercial importance, relatively little tube-tooling cable-coating research has been reported in the literature. The finite element method has become a powerful tool for the numerical solution of free surface cable coating problems. A finite element analysis of tube-coating for a power law fluid was presented by Caswell and Tanner [34]. In this study, finite element approximation was able to accommodate complex shaped geometries and non-Newtonian fluid properties in a realistic manner, and produce streamline and stress patterns within the die. Sun et al. [117] analysed the expansion of a thick tube between a pipe die and a sizing sleeve employing an integral viscoelastic fluid model. This problem resembles

tube-coating, except that the tube expands instead of contracting. Kuyl ([68], [69]) reported predictions for both isothermal and non-isothermal high-speed tube-coating melt flow using a finite element method. He concluded that various parameters influence the melt cone shape and stability; also, predicting the distance from the die exit to the contact-point. Under isothermal analysis, Kuyl [68] demonstrated that applying vacuum both shortens and stabilizes the contact length. In his non-isothermaal study, Kuyl [69] showed that cooling the melt cone extends the contact length; but also cone cooling destabilizes the cone length.

Theoretically, Slattery et al. [112] derived an analytic solution for cable-coating draw-down of an extruded annular melt. Their analysis was for Newtonian, power-law and Noll simple fluids, and excluded the effects of vacuum. In this study, the solution was developed with the assumption that pressures inside and outside the film (coating) are equilibrated (balanced and equal); a process in which these pressures differ, such as a vacuum inside the film, was treated as a limiting case. Moreover, Webster and Ngamaramvaranggul [95] used a semi-implicit Taylor Galerkin/pressure-correction finite element scheme (STGFEM) to solve annular incompressible coating flows for Newtonian fluids, associated with coatings of wire and cable, fibre-optic cables or glass-rovings. Both annular tube-tooling and pressure-tooling type extrusion-drag flows were investigated for viscous fluids. A modified free surface location technique was employed to determine the shape of the die extrudate. This method involved remeshing and a three-stage iterative cycle, using appropriate convergence criterion. Moreover, the effects of die walls Navier slip conditions on the stress singularities at the die exit were considered throughout this study. Similarly, Hade and Giacomin [54] presented analysis for isothermal power-law tube-coating flow, under vacuum or with an externally applied pressure. This study was concerned with the effect of shear-thinning on the drawing force and contact-length of the melt-cone. These authors found that, shear-thinning properties tend to increase the drawing force, and for power-law index $m>0.5$, only slightly affect the contact-length. In addition, an analytic solution was also derived by Hade and Giacomin [55] for the reduced problem, of isothermal Newtonian conduit coating-drawing flow, under vacuum but devoid of extrudate swell, and under a set of prescribed flow assumptions. This result established the melt cone shape as the solution of a Boundary Value Problem (BVP), composed of a system of two coupled ordinary differential equations, from which and by iteration, various draw-down ratios and

balances may be established. This result has been found useful in providing a starting point for the conduit-cone free-surface initial positioning. Moreover, with a view to viscoplastic analysis, Mitsoulis and Kotsos [87] studied the wire-coating flow of non-Newtonian pseudoplastic and viscoplastic fluids using a Herschel-Bulkley model and finite element approximation. These authors observed that yielded/unyielded zones exist only beyond the die-exit, where the coating fluid moves on the wire as a rigid body.
In brief, the present finite element study covers a steady isothermal analysis for the full and combined tube-tooling/draw-down annular flow – hence, a predominately die shear-flow to a draw-coating flow. This includes practical considerations of dual inner-outer free-surfaces (dynamic location), extrudate swell and slip, dynamic contact point representation (melt-to-cable) and effects of vacuum imposition. Initially, a Newtonian analysis has been conducted to construct an essential kinematic basis and steady, zero-vacuum solution, under prescribed flow-rate and cable-speed process conditions. This may then be utilised as a base-flow state and internal starting condition for the time-stepping algorithm to explore other flow scenarios, encompassing vacuum imposition and viscous inelastic melt flow representations.

5.2 Problem specification

In this study, consideration is given to tube-tooling flow with special design as displayed in Figure 5.1a. In this Figure, a schematic representation for the whole geometry with zoomed die section, draw-down section and cable region is presented. In addition, sectional details are provided in zoomed form in Figure 5.1b for the finite element mesh. In contrast, the finite element mesh for the draw-down section and cable region is shown in Figure 5.1c, and the free surface of this position is observed with zooming for the critical region near the corners in the draw-down exit. Moreover, the relative dimensions are given in Table 5.1. Mesh refinement has been performed throughout across a series of three meshes, from which mesh convergence is observed.

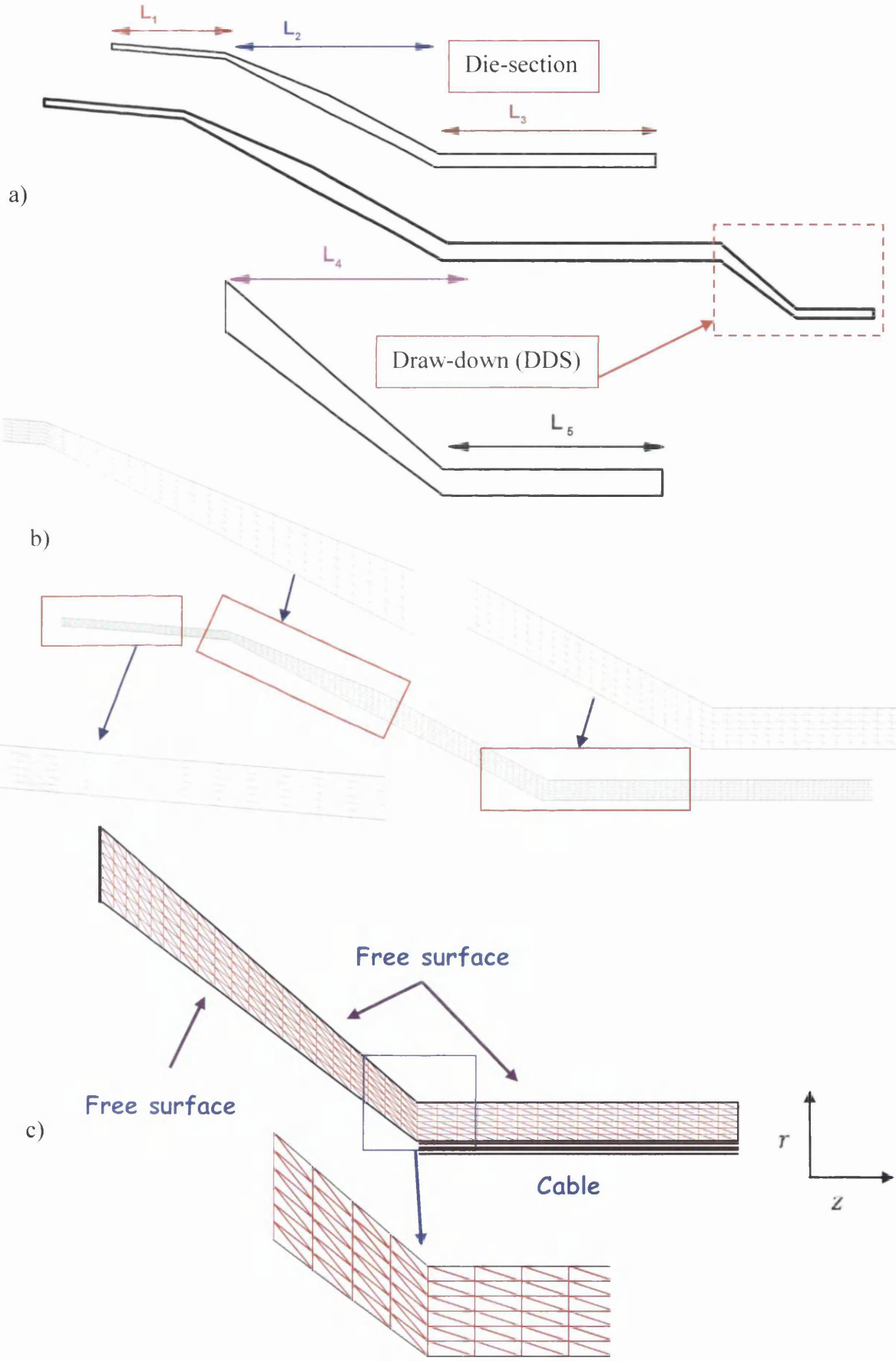

Figure 5.1: Schematic diagram for; a) die section, b) draw down section and cable region *c) mesh pattern for draw down section and cable region*

Typical finite element mesh characteristics are included in Table 5.2, following notation *M-r4, M-r6, M-r8*, which implies four, six, and eight element widths, respectively, across the die inlet. From this selection and subject to satisfaction of sufficient accuracy criterion (less than 1% change in sampled solution values), the middle mesh design is highlighted and chosen for computations.

Table 5.1: Geometry non-dimensions measurements

Die-inlet (L_1)	Converging section (L_2)	Land section (L_3)	Draw-down length (L_4)	Cable region (L_5)
1.0	1.88395	1.93384	0.542299	0.542301

Table 5.2: Mesh characteristic parameters

Mesh	Elements	Nodes	Degrees of freedom (u, p)
M_r4	1024	2313	5271
M_r6	1536	3341	7585
M_r8	2048	4369	9899

Boundary conditions are taken as no-slip applied at the die walls prior to die exit. For the draw-down section and cable region the boundary conditions read as follow: at the top free surface section tractions vanish, free velocity with zero pressure; at the outflow a plug flow is imposed travelling with the moving cable; the lower domain boundary corresponds to the moving cable. Furthermore, all results pertain to Newtonian and Inelastic flows at minimal levels of inertia, equating to $Re=10^{-5}$. In addition, to construct the essential basis for our solution and internal starting conditions, the problem is first solved for Newtonian fluid properties. Then, from this solution position, the inelastic problem is initiated. Throughout such solution phases, there was no change in boundary condition settings necessary.

5.2.1 Free-surface procedure

A free-surface location method is employed as a modified iterative technique by which the shape of the die extrudate is derived. In this section, the time dependent prediction method, which is named the Phan-Thien (*dh/dt*) method, has been selected to

compute the new position of the boundary nodes of the free surface zone. To avoid excessive distortion of elements in the boundary zones, an updating of the free surface must be performed in time, by starting from suitable initial conditions and applying the stages in section (3.9.1).

5.2.2 Dynamic contact point adjustment

In this study an important factor to take into consideration throughout the coating process is the approximation of the dynamic contact point solution, where the melt interfaces meet the cable with the moving substrate surface. Here, the dynamic contact point (line) is allowed freedom of movement under slippage, through wetting or peeling of adjacent surface sections, onto or off the moving cable-carcass. In this manner, the contact point is traversed relatively smoothly, so that, when the contact angle (θ) is adjusted, as subtended by the adjacent free-surface line-segment (linear straight-sided surface element approximation), any node on that bottom free-surface line-segment (see for example, nodes 3, 2, and 1 in Figure 5.2) which makes contact with the cable is assumed to wet the cable boundary. Thereupon, cable conditions then apply to such segments and nodes. Under such a procedure and due to the sucking-drawing down of the polymer melt onto the cable, the horizontal distance between the die-exit of the tube and the contact-point on the cable slightly reduces throughout the coating process.

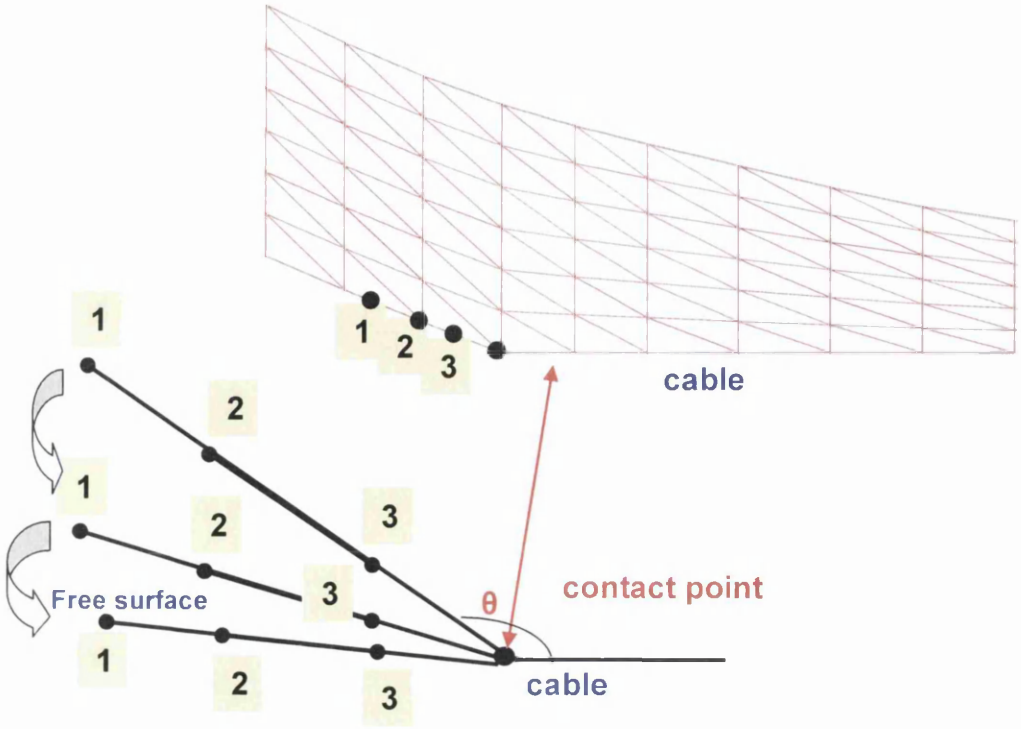

Figure 5.2: Dynamic contact point

5.2.3 Slip conditions on the die-wall

A further factor to consider relates to the influence of slip boundary conditions, as pertaining to and applied at the die-wall location. Based on a momentum balance at the wall, it can be shown that the slip velocity may be taken as a function of the velocity gradient at the wall:

$$u_{slip} = \hat{\beta}_{slip}\, \tau_{rz} \tag{5.1}$$

where $\hat{\beta}_{slip}$ is the slip coefficient and τ_{rz} is the shear stress. So, for example with Newtonian fluids, u_{slip} is given by:

$$u_{slip} = \delta \frac{\partial u}{\partial r} \tag{5.2}$$

where, δ is referred to as the slip-length and $\partial u/\partial r$ is the die-wall shear velocity-gradient. This is the basis employed and reported upon below under a selection of sampled results.

5.3 Governing equations and mathematical modelling

The system of governing equations for Newtonian and non-Newtonian inelastic flows under isothermal setting are stated in chapter 2. This system consists of the continuity and momentum equations with constant viscosity for Newtonian case and variable viscosity in the inelastic case (see Equations (2.64), (2.65a), (2.65b)). Moreover, two different inelastic shear-extensional viscosity model fits to experimental data are proposed, namely Fit-I and Fit-II (see section 2.3.2.1). Each offers its own individual quality of match to the data.

5.4 Numerical scheme

To solve the momentum equation (2.65), together with the continuity equation (2.64), a semi-implicit time-stepping procedure, namely Taylor-Galerkin/pressure-correction finite element scheme is employed. This scheme is based on a fractional-step method, utilising semi-discretisation in the temporal domain, through a Taylor series expansion in time and a pressure correction procedure, to extract a time stepping

scheme of second order accuracy. For the Newtonian case, the polymer stress is zero, then T=0 and $\mu_s = 1$ in equation (3.28a) and (3.28b), allowing for the reduction of these equations (step 1a and 1b), viz

$$\text{Step 1a: } [\frac{2\text{Re}}{\Delta t}M + \frac{1}{2}S](U^{n+\frac{1}{2}} - U^n) = \{-[S + \text{Re}\,N(U)]U + L^T P\}^n \tag{5-3a}$$

$$\text{Step 1b: } [\frac{\text{Re}}{\Delta t}M + \frac{1}{2}S](U^* - U^n) = \{-SU + L^T p\}^n - \text{Re}[N(U)U]^{n+\frac{1}{2}} \tag{5-3b}$$

In contrast, for the inelastic case $\mu_s = \mu(\dot{\gamma}, \dot{\varepsilon})$, with a shear-rate $\dot{\gamma}$ for simple shear flow, and strain-rate $\dot{\varepsilon}$ for extensional flow. Hence, the step 1a and 1b can be written as:

$$\text{Step 1a: } [\frac{2\text{Re}}{\Delta t}M + \frac{\mu(\dot{\gamma}, \dot{\varepsilon})}{2}S](U^{n+\frac{1}{2}} - U^n) = \{-[\mu(\dot{\gamma}, \dot{\varepsilon})S + \text{Re}\,N(U)]U + L^T P\}^n \tag{5-4a}$$

$$\text{Step 1b: } [\frac{\text{Re}}{\Delta t}M + \frac{\mu(\dot{\gamma}, \dot{\varepsilon})}{2}S](U^* - U^n) = \{-\mu(\dot{\gamma}, \dot{\varepsilon})S_u U + L^T p\}^n - \text{Re}[N(U)U]^{n+\frac{1}{2}} \tag{5-4b}$$

The pressure and velocity equations (stage 2 and 3) are identical among Newtonian, inelastic and viscoelastic case.

As shown in chapter 3, the Taylor-Galerkin Pressure-Correction Scheme has three distinct fractional stages per time step:

Stage1: Given initial velocity and pressure fields, non-divergence-free $u^{n+\frac{1}{2}}$ and u^* fields are calculated via a two-step predictor-corrector procedure (step 1a and 1b). The corresponding mass matrix governed equations are solved iteratively by a Jacobi method.

Stage 2: Having solved for u^*, here one calculates the pressure difference $p^{n+1} - p^n$ through a Poisson equation.

Stage 3: using u^*, and pressure difference $p^{n+1} - p^n$, determine a divergence free velocity field u^{n+1} by Jacobi iteration (for more details see Hawken [57]).

5.5 Stability and convergence of numerical computations

5.5.1 Strain-Rate Stabilization (SRS)

Considering the numerical oscillations and poor stability response, once spatial discretisation has been established, localised singularity capturing for die-swell and contact-point solution, and may be invoked stabilisation methodologies. This may be introduced through the *Strain-Rate Stabilisation* (*D-Dc*) approach. Background detail on the *Strain-Rate Stabilisation* scheme and it implementation are provided in section 3.7.

5.5.2 Numerical stability and treatment of the momentum diffusive matrix (S-Matrix)

Under the present temporal schema, the generalised diffusion terms in the momentum equation are treated in a semi-implicit manner in order to enhance temporal stability. Hence, by adopting a Crank-Nicolson representation for such inelastic diffusion terms at stage 1 of TGPC fractional-stages, the following fully-discretised equations may be derived (see Hawken [57]):

Stage 1a:

$$[\frac{2\mathrm{Re}}{\Delta t}M+\frac{1}{2}\bar{\bar{S}}](U^{n+\frac{1}{2}}-U^{n})=\{-[\bar{\bar{S}}U+\mathrm{Re}\,N(u)U]+L^{T}P\}^{n}, \tag{5.5}$$

Stage 1b:

$$[\frac{\mathrm{Re}}{\Delta t}M+\frac{1}{2}\bar{\bar{S}}](U^{*}-U^{n})=[-\bar{\bar{S}}U+L^{T}p]^{n}-\mathrm{Re}[N(u)U]^{n+\frac{1}{2}}, \tag{5.6}$$

where S represents the symmetric positive semi-definite momentum diffusive matrix (positive definite augmented mass-matrix), defined under axisymmetric frame of reference, as:

$$S=\begin{bmatrix}S_{rr} & S_{rz}\\ S_{zr} & S_{zz}\end{bmatrix},$$

$$S_{rr}=\int_{\Omega}\mu\left[2\frac{\partial\phi_i}{\partial r}\frac{\partial\phi_j}{\partial r}+\frac{\partial\phi_i}{\partial z}\frac{\partial\phi_j}{\partial z}+2\frac{\phi_i\phi_j}{r^2}\right]r\,d\Omega,$$

$$S_{rz}=\int_{\Omega}\mu\left[\frac{\partial\phi_i}{\partial r}\frac{\partial\phi_j}{\partial z}\right]r\,d\Omega, \tag{5.7}$$

$$S_{zr} = \int_{\Omega} \mu \left[\frac{\partial \phi_i}{\partial z} \frac{\partial \phi_j}{\partial r} \right] r \, d\Omega ,$$

$$S_{zz} = \int_{\Omega} \mu \left[\frac{\partial \phi_i}{\partial r} \frac{\partial \phi_j}{\partial r} + 2 \frac{\partial \phi_i}{\partial z} \frac{\partial \phi_j}{\partial z} \right] r \, d\Omega .$$

To enhance numerical stability under iteration for low solvent-viscosity levels and inelastic settings (as with melts), and hence to determine optimal scheme configuration for time-stepping and iterative convergence, different system-matrix filters have been investigated. This has lead to five alternative scheme approaches being considered (see below), when applied to the diffusive matrix (*S*) component of the augmented mass-matrix on the left-hand side (*lhs*) of Stage-1, equations (5.5) and (5.6). Under free-surface problem numerical solution, this is particularly important for low solvent fractions ($\beta<10^{-2}$), and indeed for more severe problem settings of low power-law index ($m<0.5$) or stronger vacuum level settings ($\Delta P<-80$). These schematic approaches may be summarised as:

Approach 1 (Full-*S*-matrix): the diffusive matrix (*lhs-S*) remains unaltered, as in equation (15).

Approach 2 (Full-*S*-matrix_r(lhs)=1): Here, the radial-factor (r) is replaced by unity in the integrand components of *lhs-S* alone (as in Cartesian reference).

Approach 3 (Diag-S-matrix_r(lhs)=1): As Approach 2, by discarding off-diagonal S_{rz}-matrix component terms but also diagonalised lhs-S with r=1.

Approach 4: (Newtonian *S*-matrix_r(lhs)=1): Here, a Newtonian approximation is adopted on the *lhs-S*-matrix with r=1. This diagonalises the *lhs-S*-matrix, by application of continuity and the chain-rule to off-diagonal S_{rz}-matrix component terms.

Approach 5: (Full-*S*-matrix_Gauss_Samp): As Approach 1, but with varying quadrature points (GQP) for numerical integration per element.

In addition, a single Jacobi-iteration version under each of the above approaches, yields a resultant diagonalised system-matrix (via the corresponding iteration matrix, see Ding et al. 1992 [47]). Furthermore, a single Gauss-Quadrature point approximation for the integrands per element renders piecewise-constant viscosity approximation, as in a constant Newtonian level viscosity per *fe*-triangle (parent) control volume. Findings on the application of each of these individual scheme variants are discussed below.

5.6 Material functions

Here, the rheological properties are described of Fit-I and Fit-II (shear-extensional viscous-inelastic) models with respect to the model parameters in question. In this context, Fit-I offers a single power-index response, identical in shear and extension; this is generalized under Fit-II, with independent choice of power-indices, $\{m_1, m_2\}$. These may be evaluated by fitting to the experimental data, as shown in Figure 5.3(a,b). Fit-I introduces the extension-rate dependence via cosh-functionality, so that large and early rise in extensional viscosity data may be accommodated. Under inelastic Fit-I, the model parameters taken are m=0.5, λ=1, and K=1; whilst under inelastic Fit-II, the parameter choice is m_1=0.3, m_2=0.4, K_1=20 and K_1=0.45 (see Eq(2.26), (2.27)). This model selection permits a three-way comparison between: Newtonian, Fit-I and Fit-II models; also exposing the attractive independent shear-extensional fitting under Fit-II, not realized within Fit-I. Note, the order of magnitude difference in extrapolated levels of zero shear-rate viscosity for the two model fits. Here, the common basis of zero shear-rate viscosity is taken as the constant Newtonian value (same as that based on Fit-I), so that the comparison of Fit-I and Fit-II is meaningful.

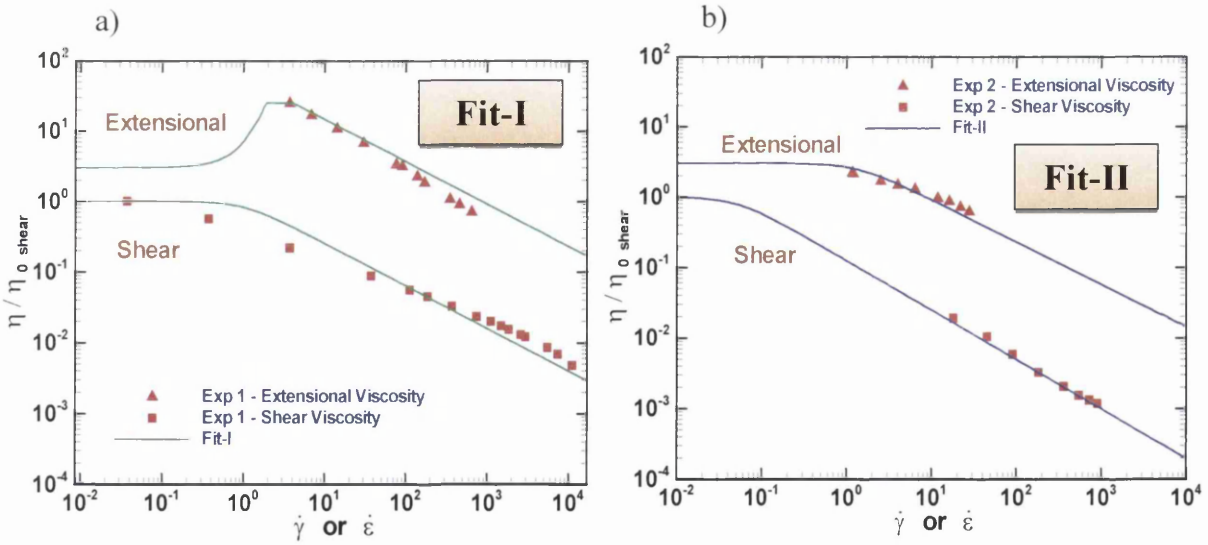

Figure 5.3: Experimental viscosity data: Inelastic; a) Fit-I, b) Fit-II

5.7 Computational predictions for Newtonian and inelastic model fits

5.7.1 Surface friction effects

With specific attention paid to surface slip for viscous flows, the influence of slip onset ($\hat{\beta}$ =40%), as opposed to no-slip conditions within the die, is examined. Pure slip is defined as 100% slippage on the die-walls (at full slip velocity, defined on the steady mean velocity in the die, consistent with a plug-flow approximation and vanishing deformation rates), total friction equates to 0% slippage (no-slip) and the 40% slip condition implies that 40% of the slip velocity is imposed. The impact of imposing such slip conditions on pressure profiles is to generate almost 12% reduction in pressure-maxima (at die-entry, hence, in pressure-drop), see Figure 5.4a. The maximum velocity attained at the land-region reduces correspondingly by around 20%. In Figure 5.4b, a plug flow is seen to be reached by the middle of the land-region and sustained beyond. Over the land die-region, and on both top and bottom surfaces, as observed in Figure 5.4c, there is around 70% decrease in exposure to shear-deformation (Γ) with the selected slip-BC imposed. This translates to bottom surface shear rates of 15.5 units without slip, and to 4.7 units with slip. Slip imposition also impacts on deformation about the complex zone of land-entry. In addition, central streamwise profile results reveal slight reduction in the generalised measure of extensional deformation (not shown). The shear stress levels and distribution in Figure 5.4d, are held to be consistent with these deformation rate profiles.

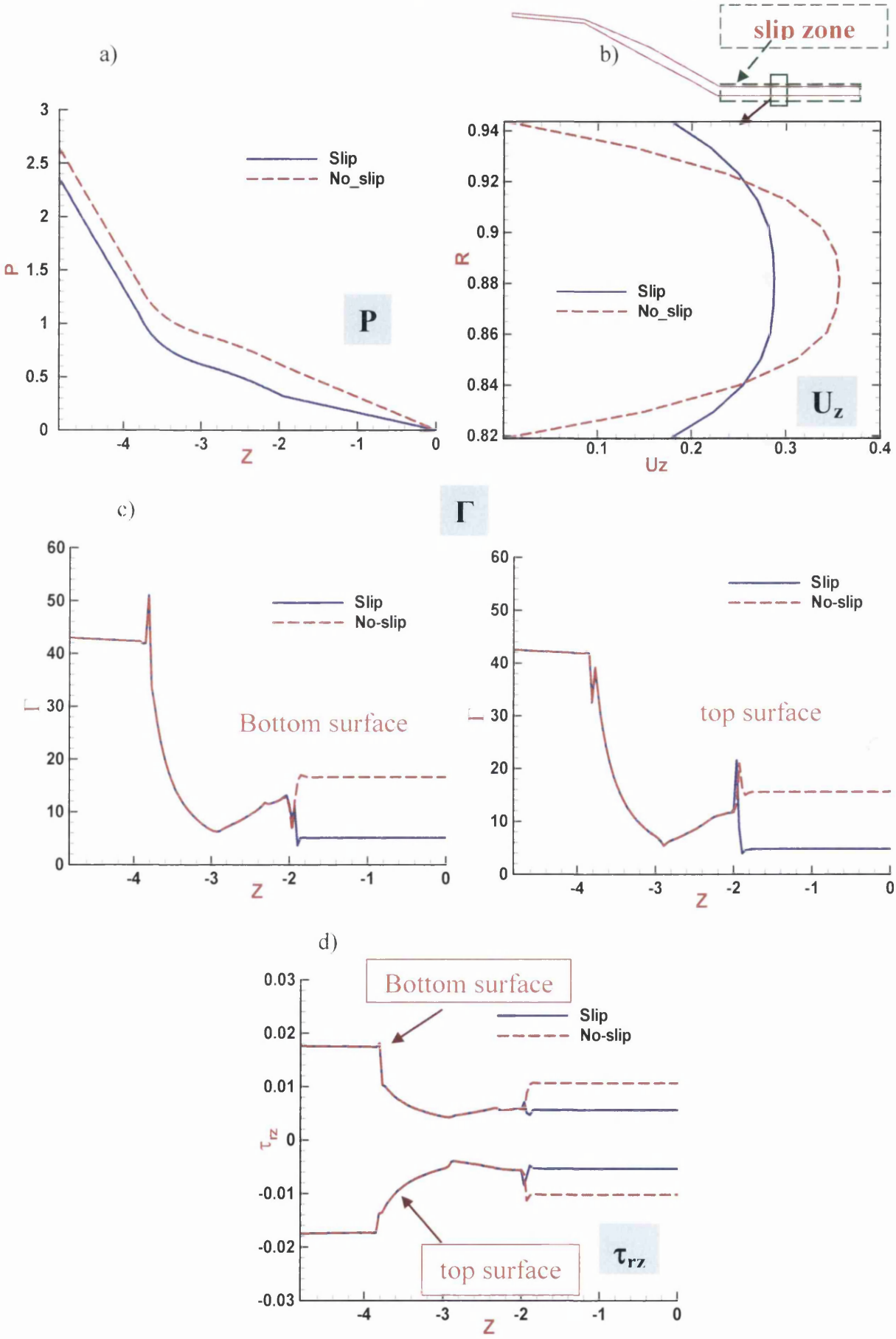

Figure 5.4: Surface friction effects, a) pressure, b) velocity, c) shear-rate, d) shear-stress profiles, inelastic (m=0.5)

5.7.2 Coupled free-surface tracking, Newtonian solutions

The present study documents the application of the free surface location methodology, to determine the free surface evaluation. A coupled (dependent) method is used in the free-surface calculation commencing from a fixed position interior solution. In this process, the problem is solved with freedom of movement on both top and bottom surfaces of the draw-down conduit for Newtonian and inelastic fluids. The shape is determined from only vertical node-movement, interpreted in terms of change in the radial direction only; then new r-coordinates are calculated, depending on the radial and axial velocity components, and governed by the equations (3.68). The temporal development free surface of draw down section alongside axial velocity fields is presented for the Newtonian case in Figure 5.5 for $0.05 \leq t \leq 200$. From this Figure, one is clearly able to detect the evolution of both top and bottom free surface profiles through the calculation process.

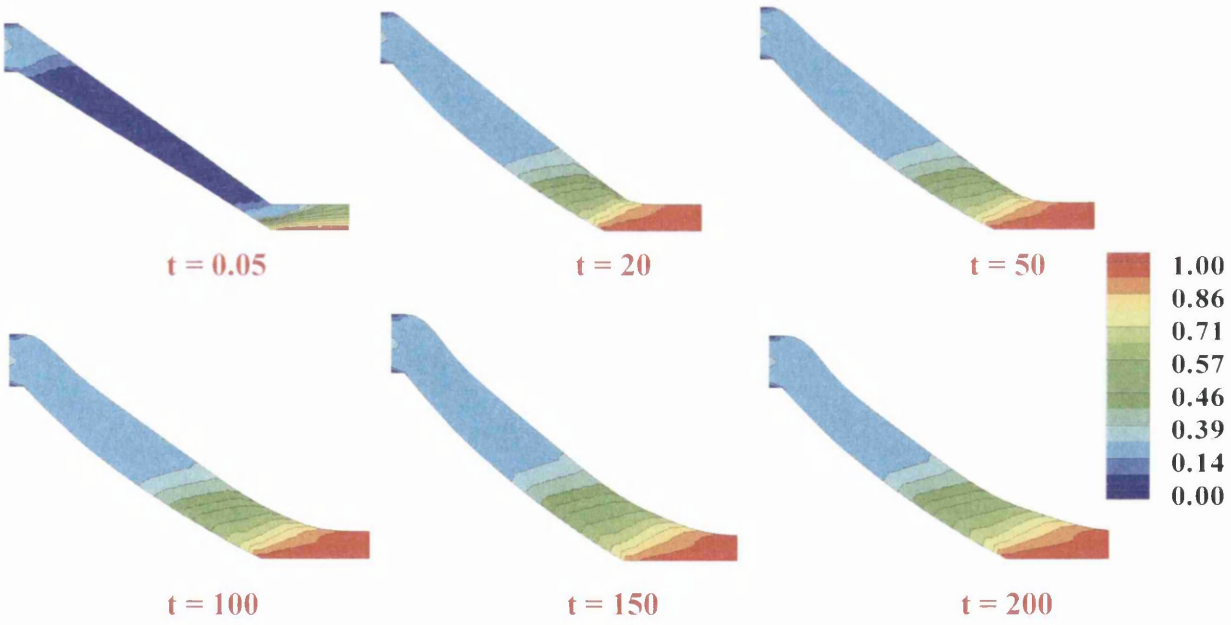

Figure 5.5: Time-frame evolution through surface development process, top and bottom zone movement, axial velocity field

5.7.2.1 Pressure drop

Figure 5.6 with zoomed draw-down, provides comparisons for pressure fields between Newtonian, inelastic Fit-I and Fit-II solutions. Findings reveal that, pressure-drop (essentially that across the die) decreases significantly from the Newtonian

position for inelastic shear-extensional models, with an overall minimum level taken up by Fit-I of 554 units. The Newtonian field prediction suggests that in relative terms, large pressures are endured throughout much of the die, only significantly declining over the land region. In contrast, Figure 5.7 provides comparison in pressure-drop between purely-viscous approximations in Newtonian, inelastic Fit-I and Fit-II solutions. At the die-inlet and for Newtonian solutions, an overall maximum of 2260 units is observed, while for inelastic Fit-I model this peak is *reduced by about a factor of four, and with Fit-II model by about one-half.* Furthermore over the draw-down section, similar trends at the die-exit are detected across all three solutions, whilst Fit-II provides the most significant solution features (in size, negative in value, at -3 units) at the cable-melt contact zone.

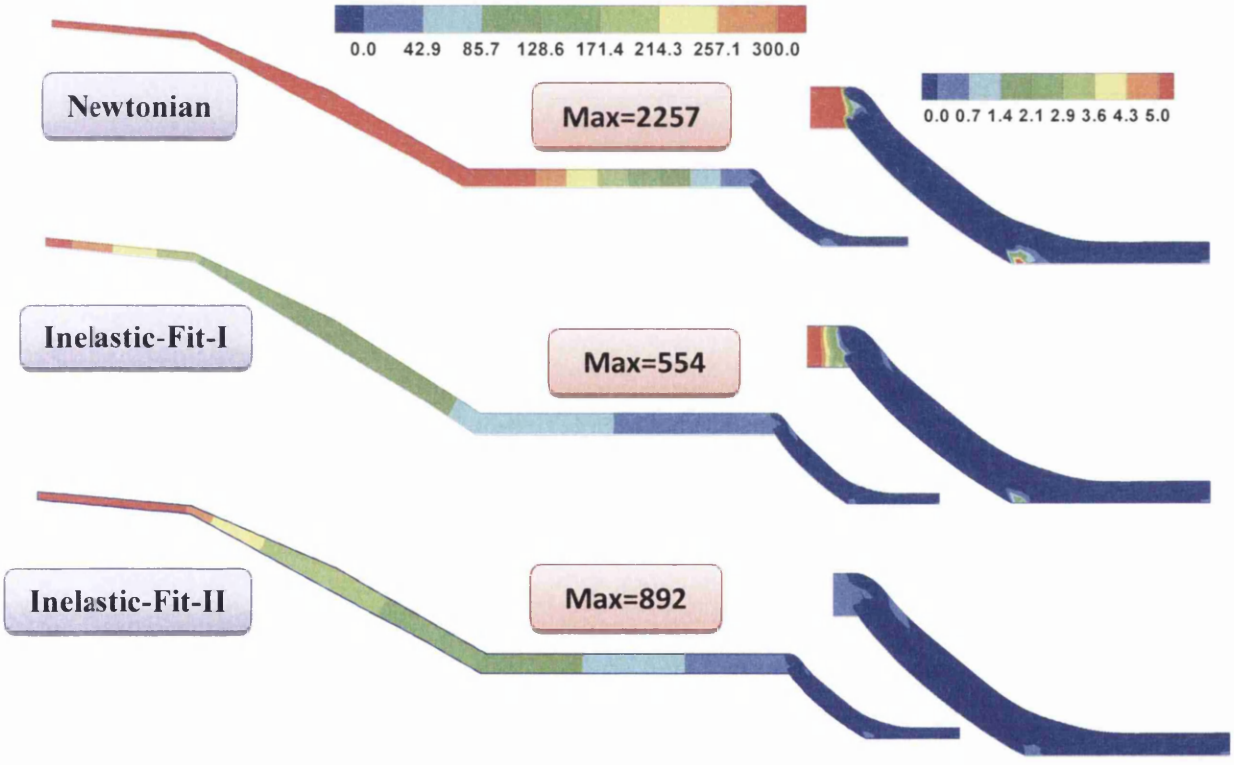

Figure 5.6: Pressure fields: full geometry, draw-down section, Newtonian, Fit-I and Fit-II

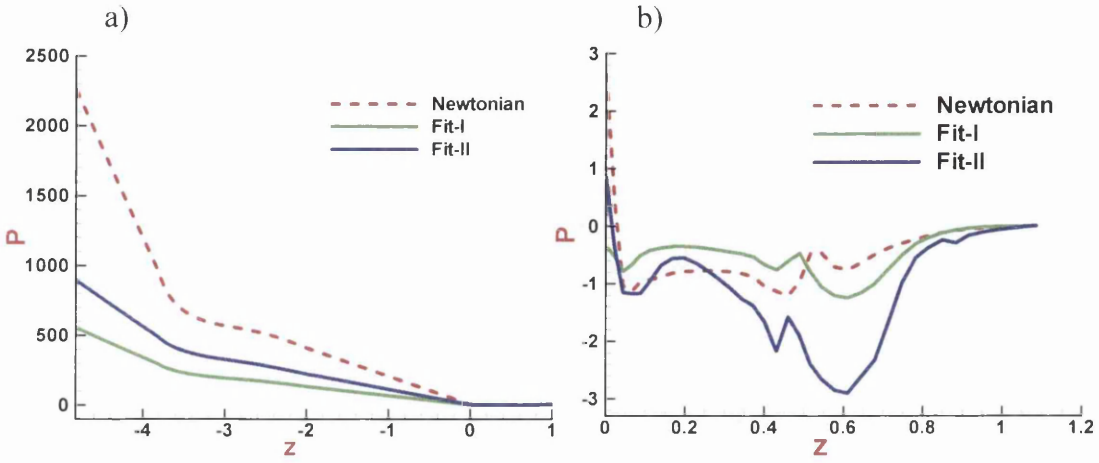

Figure 5.7: Pressure drop, along centreline: a) full geometry, b) draw-down section, Newtonian, Fit-I and Fit-II

5.7.2.2 Stress profiles

Figure 5.8 (a,b) provides associated three-way sampled and localised profiles in shear stress (τ_{rz}) and shear-rate (Γ), with reference to top and bottom surface locations. In shear stress, a constant level is observed at the tube-inlet (reflecting pure shear), with maxima in magnitude of 36 units for the Newtonian solution and switch in sign in τ_{rz} observed between both top and bottom surfaces. Over the converging section on either surface, τ_{rz} decreases in absolute value. Once more throughout the land section, pure-shear is established in all three cases. Close levels are upheld for inelastic fluids that are notably reduced from the Newtonian solution; manifesting a *five-fold decrease with Fit-I and 3.5-fold decrease with Fit-II*. Over the draw-down section, melt-cable contact-point peaks are observed, of absolute value 28 units for Newtonian solutions; these are held at levels much reduced from Newtonian but comparable for inelastic solutions (4 units). These effects are more exaggerated on the inner-surface, but are also reflected onto the top surface beyond the termination of the draw-down region. Comparing shear-rate (Γ) over top and bottom surfaces, similar but sign-reflected features are observed. At the end of the die-inlet bottom surface, Fit-II generates the largest maximum Γ-level of 60 units, which *explains the larger stress levels amongst the inelastic solutions*. Throughout the converging section, there is a sharp drop at its start, reaching a minimum over its middle section, with a rise over its latter section. Through the land region, the degree of shearing rises to a constant plateau once more. First, this is

manifest with a sharp localized peak at its start on the top surface, rising to a maximum. In contrast and on the bottom surface, there is a corresponding initial sharp decline followed by an obvious increase. Subsequently, at the inlet of the draw-down cone, there is a dramatic sharp drop and oscillation in shear-rate. On the top-surface and for the Newtonian solution, the shear-rate peak around the melt-cable contact-point observes a local maximum of 28 units; whereas, on the bottom-surface the largest apparent peak lies with Fit-II at 34 units. In all cases and as anticipated with viscous solutions, stress fully dissipates over the cable region.

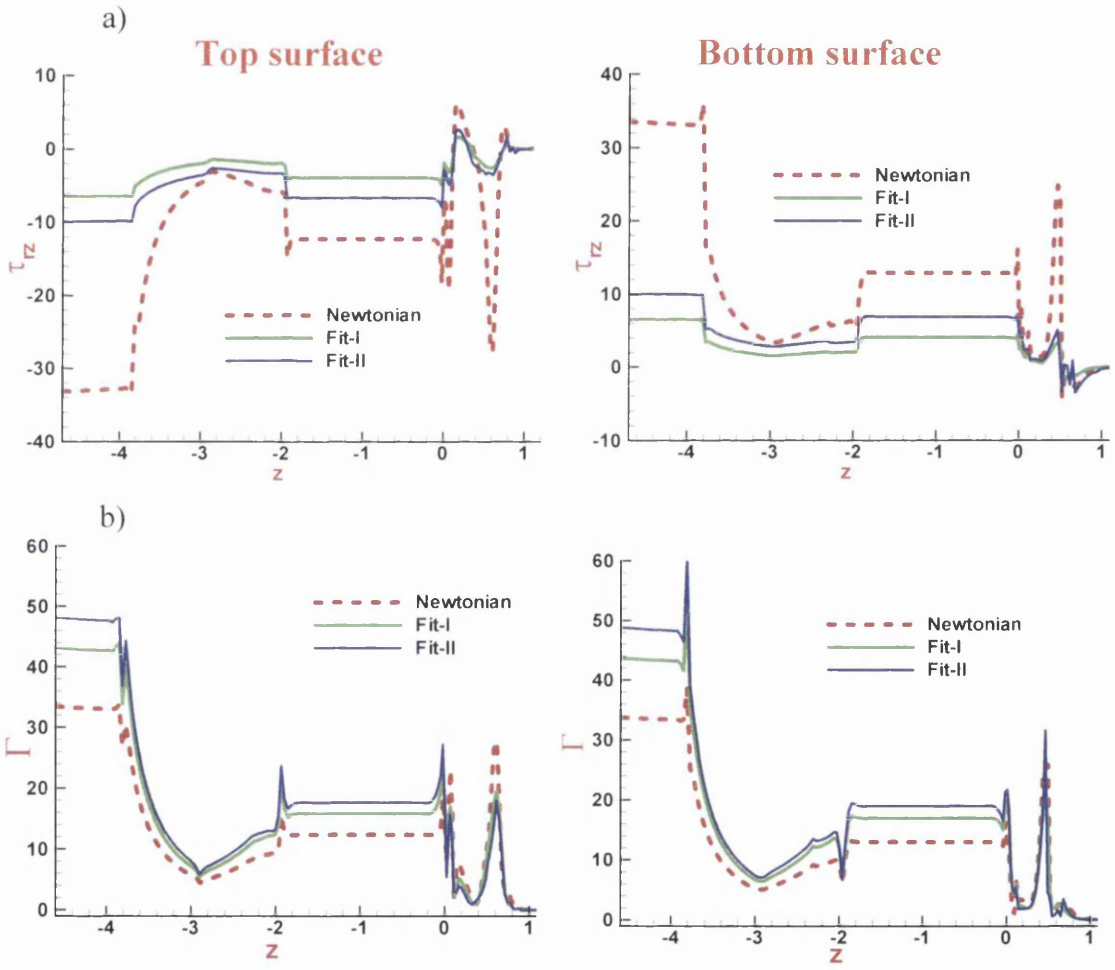

Figure 5.8: Stresses along top and bottom surfaces: a) shear stress, b) shear-rate, Newtonian, Fit-I and Fit-II

In contrast, centreline profiles of normal stress (τ_{zz}) and strain-rate (Σ) are plotted in Figure 5.9 for Newtonian, Fit-I and Fit-II solutions. The τ_{zz}-profiles amply illustrate sharp solution changes at geometry intersections. This is an important feature to observe with the largest peak corresponding to the Newtonian die-exit value of -4 units, whilst

throughout the die, τ_{zz} for Fit-II solution is the largest. In contrast and taken over the draw-down section, Newtonian and Fit-I solutions provide close results in τ_{zz}, whilst Fit-II generates a slightly lower level (see zoomed insert). Similar trends and variations (peaks, troughs) are observed in the strain-rate across the whole flow-domain for each of the three fluid approximations. In contrast and throughout the draw-down section, maxima in strain-rate are observed near the melt-cable contact-point for the Newtonian solution (~2 units); whilst minima correspond to Fit-II in this same location (around -0.4 units).

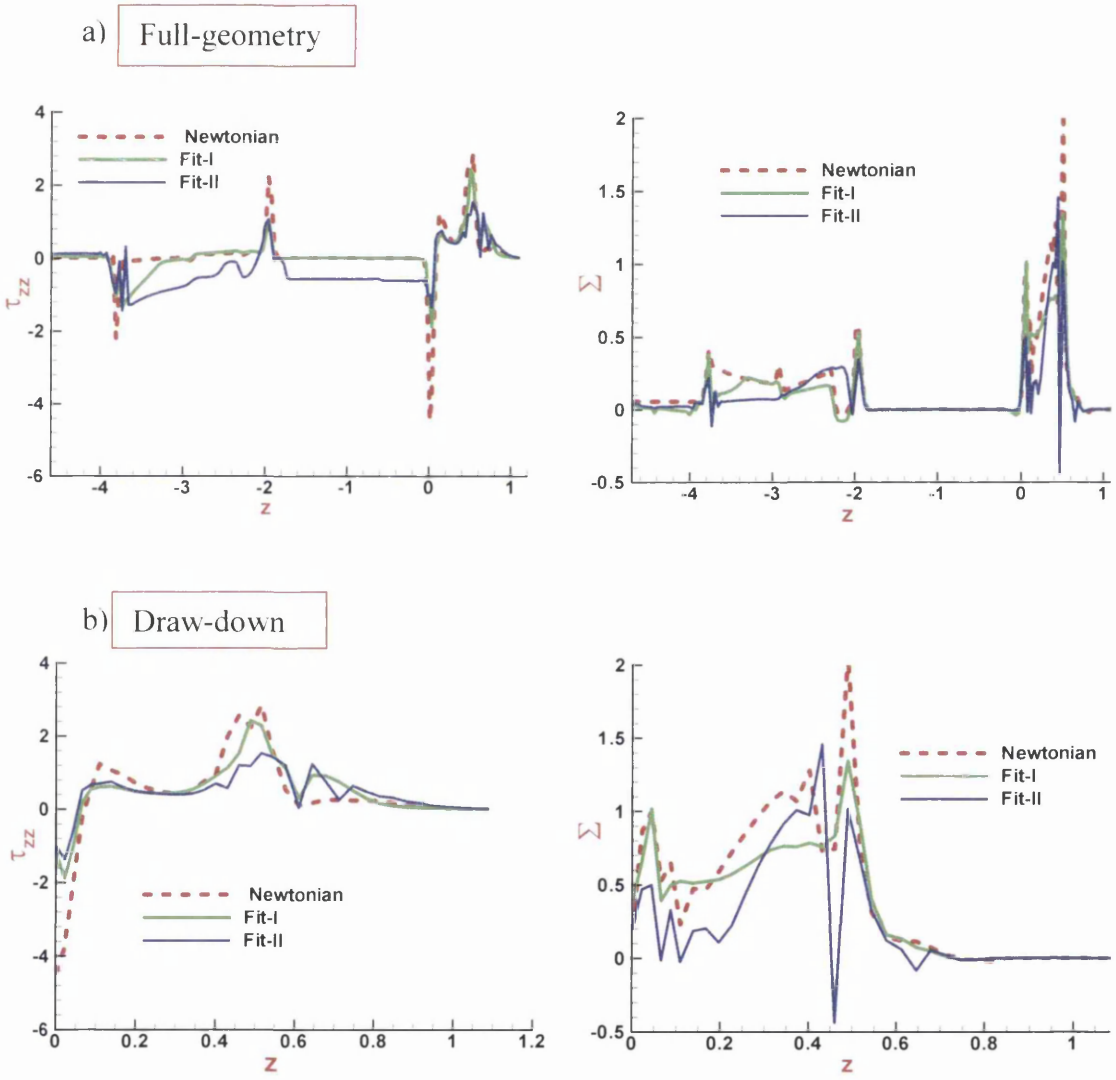

Figure 5.9: Normal stress and strain-rate along centreline: a) full geometry, b) draw-down section, Newtonian, Fit-I and Fit-II

5.7.2.3 Strain-Rate Stabilization (SRS)

Here, the problem is solved by appealing to singularity capturing and stabilization techniques, referred to earlier as '*Strain-Rate Stabilization (SRS) (D-D_c)*. Two choices of stabilization factor {α=0.25, α=0.5} have been trialled. In this regard, the focused interest lies in the effects of such strategies upon the die-exit stress singularity and resulting swell. According to these findings, a smaller level of swelling is observed (not shown) when the singularity is additionally accounted for through the (*D-D_c*) realisation. Moreover, one can extract the effects of (*D-D_c*) treatment on the dynamic contact point solution, which follows slower movement under singularity capturing (i.e. the distance from the die-exit to contact point is greater under (*D-D_c*) treatment). In Figure 5.10 with and without strain-rate stabilization (*D-D_c*), shear-rate (Γ) and shear stress (τ_{rz}) profiles along the top and bottom surfaces and strain-rate (Σ) and normal stress (τ_{zz}) along draw-down centre are presented for the Newtonian fluid. From these profiles, notable reduction is displayed in shear-rate (Γ), shear stress (τ_{rz}) at the top surface, and strain-rate (Σ) along the draw-down centre (almost 60% reduction in shear-rate peak with *D-D_c*). Therefore, this technique is observed to have a significant impact on the capture of peak stress and strain rates exiting the die on the top surface (though note, there is little influence from the variation in level of constant factor α). Alternatively, on the bottom surface, there are insignificant variations observed in Γ and τ_{rz} with α=0.5; while for α=0.25, there is notable change near the contact point, with reduction in its magnitude. In the normal stress τ_{zz} profile, one can note change only near the contact-point region, where a larger normal stress is noted under (*D-D_c*) treatment: lying around 4 units with *D-D_c* and 2.5 units without *D-D_c*. These findings are anticipated to remain localised within this viscous approximation.

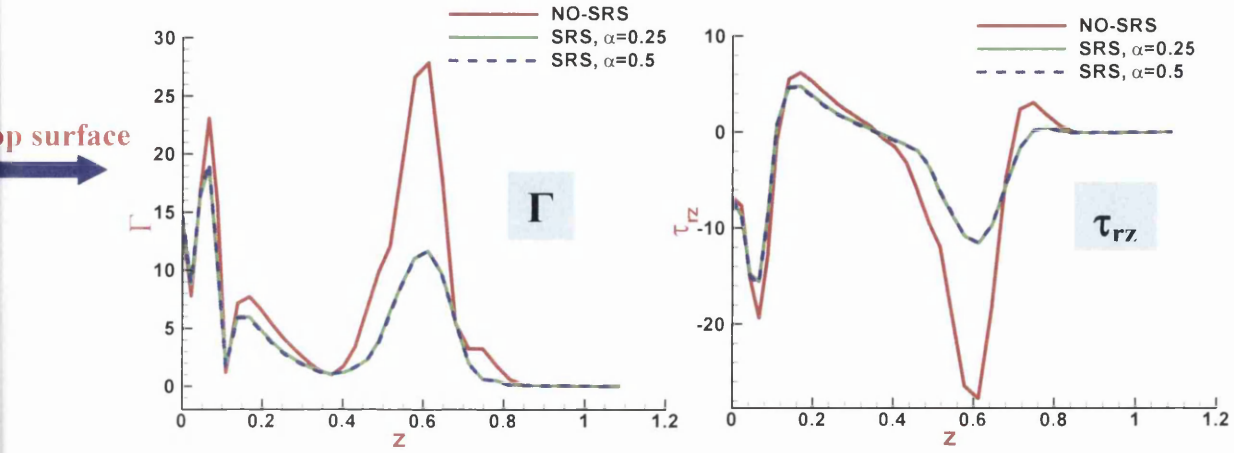

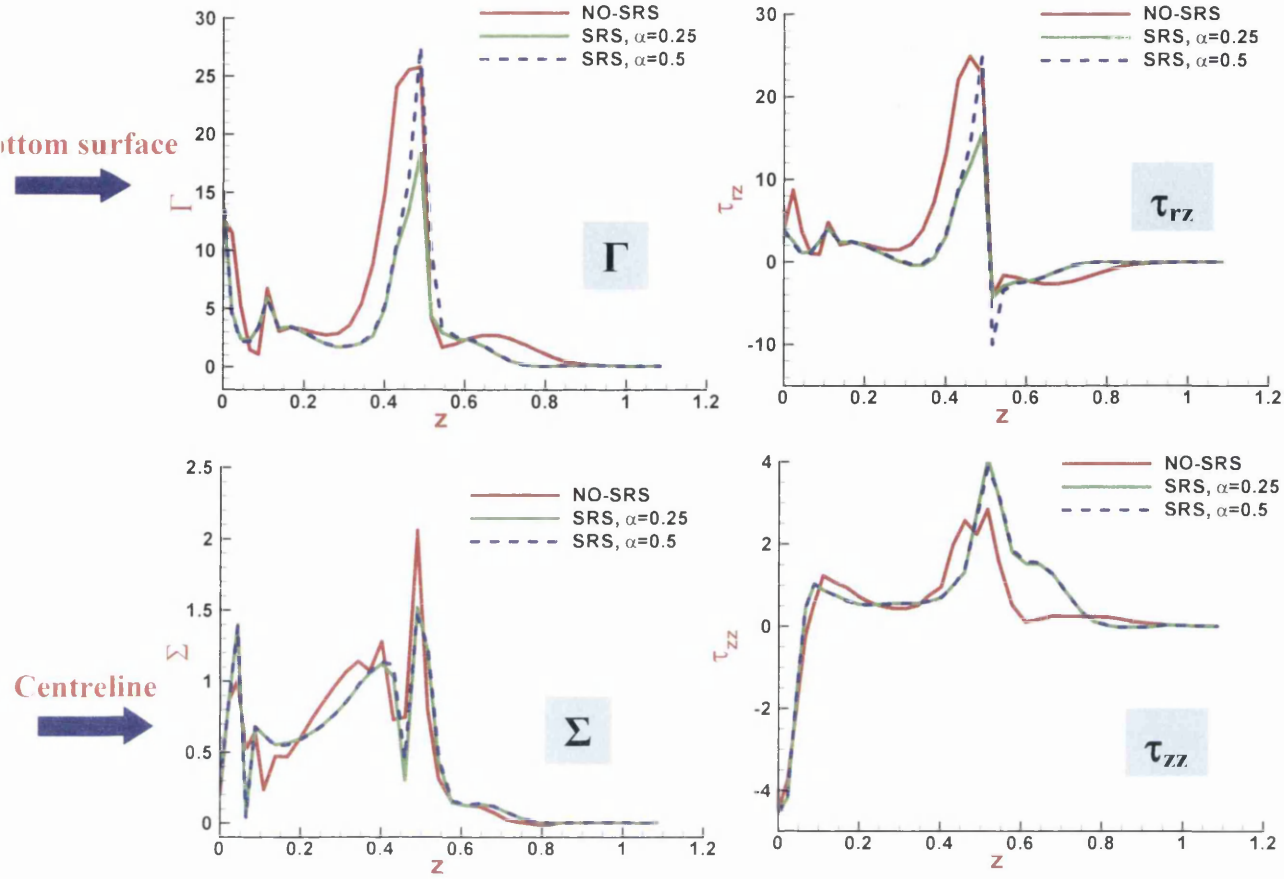

Figure 5.10: Γ, Σ, τ_{rz} and τ_{zz} profiles: SRS scheme, α=0.25 and 0.5; Newtonian

5.7.2.4 Free-surface line-segment mid-side node calculation-coupled schemes

Furthermore, the coupled method has been tested with two different *free-surface location line-segment oriented* schemes, in order to more accurately capture the temporal-update positions of the nodes that lie on the dynamic free-surface. Firstly, from the prevailing velocity field, nodal temporal-updates (h_i^{n+1}) are computed via equation (3.68). In the vertex-node oriented scheme this provides the raw data on nodal position for vertex nodes, so that mid-side node positions are determined by linear interpolation along each straight-line surface-segment (Vertex Node FS Cal). Secondly and by way of alternative, a similar strategy is adopted by appealing to equation (3.68) computation, but with solution retained primarily on mid-side nodes (Mid-Side Nodes FS Cal), instead of vertex-nodes. In this form, the average of each pair of surrounding mid-side node heights is employed to determine the height of the common-connected vertex nodes. The principle behind such an alternative is that surface dynamics is better controlled by surface segments (and not nodal-points), and in addition mid-side node data (shared by maximum of two interior *fe*-elements) is often of superior quality to

vertex node data (potentially unlimited sharing between *fe*-elements on irregular meshing; see [57] for superconvergence properties, *fe*-interpolation on tessellations and solution sampling). The corresponding temporal-history profiles of the relative error increment norms in nodal surface height, velocity and pressure are illustrated in Figure 5.11 for both vertex and mid-side node-based procedures. From these profiles, one can detect similar trends and levels of convergence in all variables and under both strategies up to time (t^n=10 units) beyond which faster convergence is clearly apparent under the mid-side node strategy (equivalently, O(50%) less compared to that enjoyed under the vertex-node strategy). Hence, the mid-side node strategy is selected as the superior free-surface location scheme of choice.

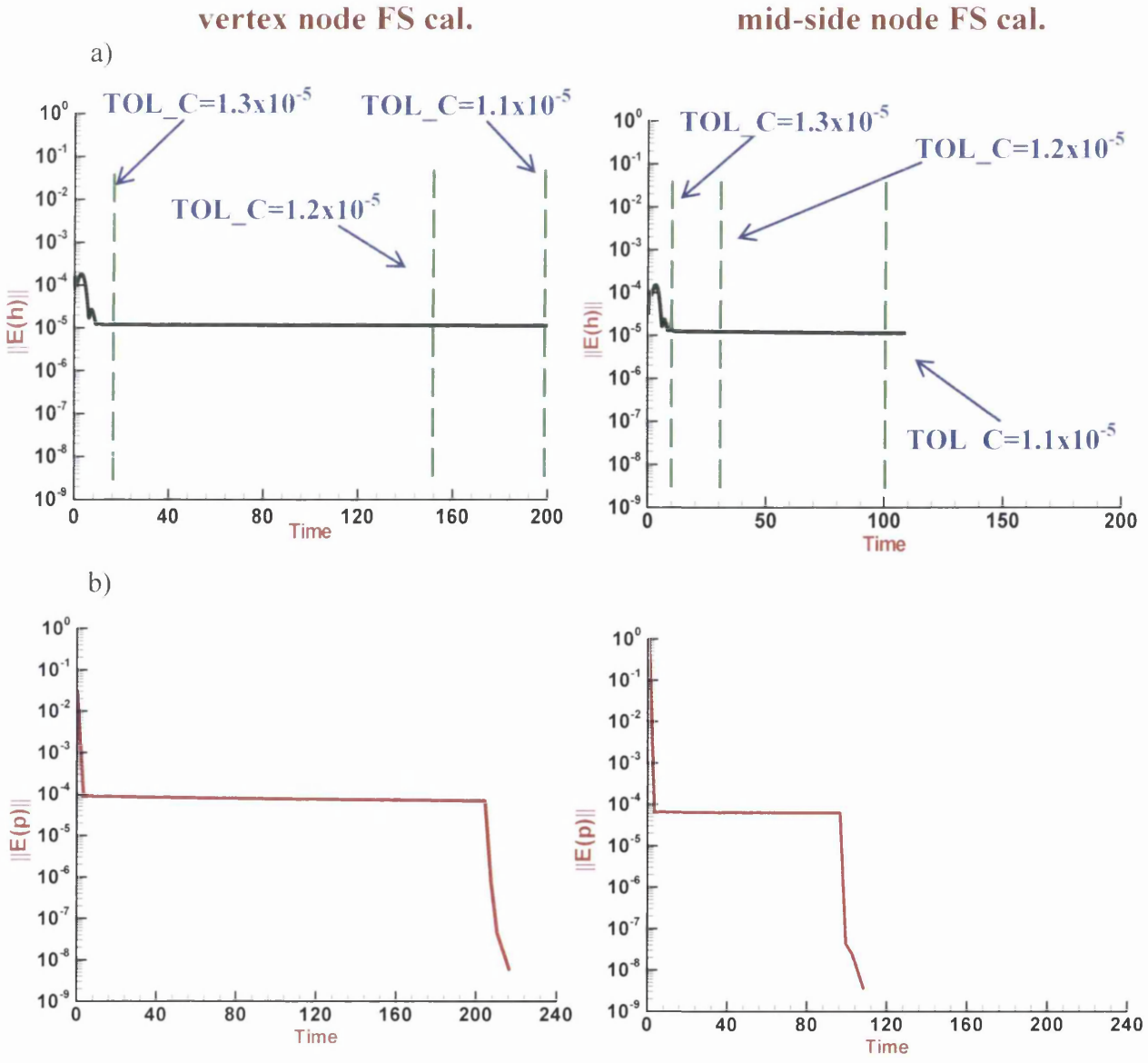

c)

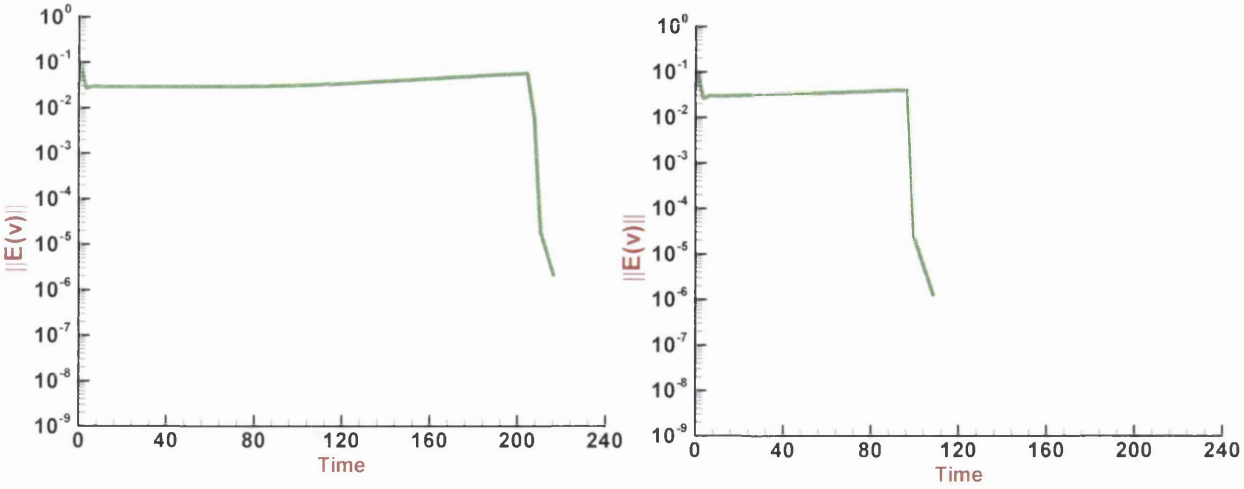

Figure 5.11: History of convergence, a) free-surface height, b) pressure, and c) velocity, vertex node free-surface calculation vs mid-side node free-surface calculation

5.7.2.5 Momentum diffusive matrix (S-Matrix) treatments

History plots of the relative error increment norms in velocity and pressure are provided in Figure 5.12 for the four different temporal-iterative approaches described above. These results reflect a higher rate of convergence for the two Approaches (2 and 4) under *lhs*-*S*-matrix with r=1, as compared to that extracted under Approach 1 with the full *lhs*-*S*-matrix. As a consequence, larger time-steps are required under Approach 1 (with *full*-*S*-matrix – rendering more constraint on its time-stepping capability), as opposed to with the alternative approaches. Note, almost the same rate of time-stepping convergence is observed for Approaches 2 and 4 (*Full*-*S*-matrix_r(lhs)=1 and Newtonian *S*-matrix_r(lhs)=1). Hence, Approach-2 is the preferred choice here. Table 5.3 presents the findings in direct mode of comparison on the rates of convergence observed, when employing different numbers of Jacobi mass-iterations of 1, 3, and 5. Likewise and under Approach-5, the rates of convergence are also displayed in Table 5.3 for different Gauss-Quadrature point approximations of GQP=1, 4, and 7 (equivalent to exact piecewise-constant, linear, quadratic integrand function approximations). Reduced integration is implied for GQP<7. Here, findings reveal that numerical solutions are stable for GQP=4, and GQP=7; whilst numerical instability is encountered under the piecewise-constant function approximations of GQP=1. This result would indicate that reduced integration is not a favourable option here, and that Newtonian constant-viscosity approximation at the element level would demand much further mesh refinement to offer any advantage.

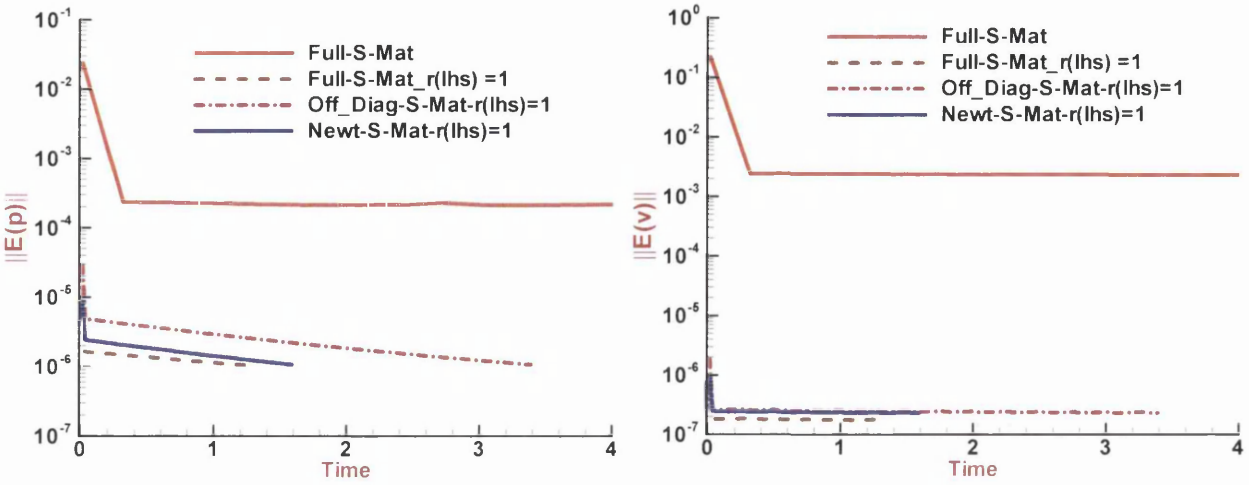

Figure 5.12: History of the relative error increment norms in pressure and velocity, mint=3

Table 5.3: Rate of convergence (time Units) with different numbers of mass-iterations, Approaches 1-5, GQP=7

Approach	No. of mass iteration	Convergence Rate (Time Units)
1)Full-S-Mat	1	20
	3	20
	5	Not stable
2)Full-S-Mat_r(lhs)=1	1	0.002
	3	1.3
	5	1.5
3)Diag-S-Mat_r(lhs)=1	1	3.5
	3	3.4
	5	2.9
4)Newtonian S-Mat_r(lhs)=1	1	0.002
	3	1.6
	5	1.6
5)Full-S-Mat_Gauss_samp (mint=1)	1 (GQP=1)	Not stable
	1 (GQP=4)	20
	1 (GQP=7)	20

5.7.2.6 Pressure vacuum imposition

To explain the influence of different factors on the cable coating process, the Newtonian problem is first resolved with negative pressure (vacuum) on the bottom surface of the draw-down section and by appealing to a coupled free-surface solution strategy. This has the effect of imposing an inward sucking force on the conduit, drawing it down upon the cable carcass. Then, in practice, the top free-surface boundary

conditions may still be retained for the draw-down conduit perimeter, with various selected values of negative pressure-differential being imposed on its inner (bottom) surface. The effect of negative pressure-differential on the contact-point position may be observed in Figure 5.13a for alternative settings of imposed negative pressure vacuums {ΔP=0,-10,-30,-80,-200}. There is insignificant adjustment in contact-point position for ΔP=0 up to ΔP=-30; but this state adjusts with further amplification of vacuum pressure level. The results reveal that relative to a zero vacuum conduit state (ΔP=0), there is between 2% and 5% change in contact-point position for pressure vacuum changes from ΔP=-80 to ΔP=-200, respectively. The relationship between imposed negative pressure-differential and uptake of contact-point position is clearly apparent in the profile plot of Figure 5.13a. From this profile, one can anticipate a reduction in draw-down length as the pressure vacuum level rises. In addition, the pressure along the centreline of the draw-down section is displayed in Figure 5.13b for various settings of inner-surface negative pressure. Findings reflect that, as vacuum levels rise (inner pressure falls), undershoot occurs near the die-exit and overshoot around middle of the die.

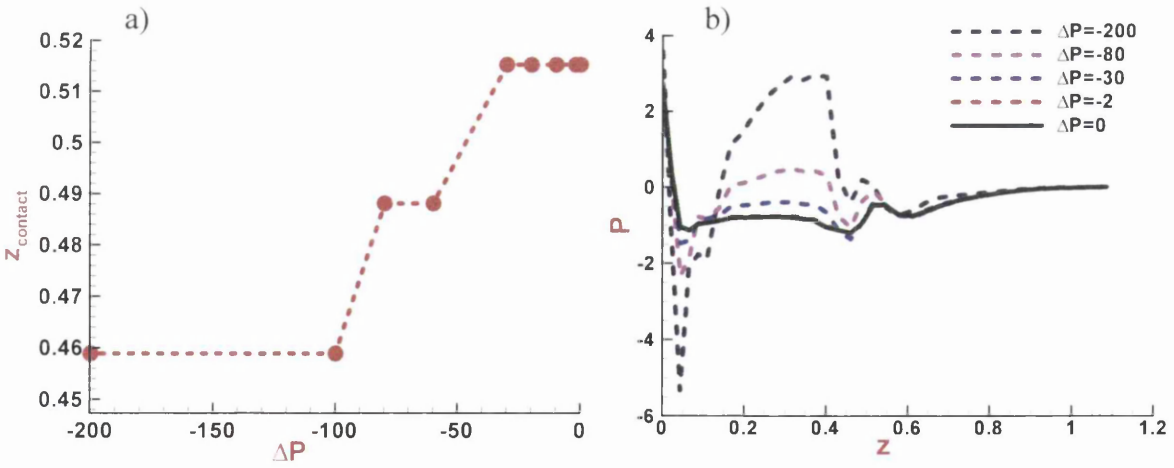

Figure 5.13: a) Contact point position, b) pressure drop along centreline, c) coupled free-surface solutions, vacuum effects, Newtonian

Newtonian and Inelastic Fit-II for m_I=0.9 solution pressure fields are displayed in Figure 5.14a, for two various alternative settings of imposed negative pressure-differential {ΔP=-60, -80}. Here, it is also relevant to show direct contrast between coupled and decoupled free-surface strategy solutions (see later), to expose the positive benefits of the decoupled approach whilst more severity is introduced into the problem

through vacuum pressure elevation (see arrow added in Figure 5.14). From these fields, one can observe a distinct impact on conduit shape with increase of vacuum pressure level (inward sucking pressure rises in magnitude). For stable steady inelastic solutions, a critical vacuum pressure level of $\Delta P \approx -80$ is achieved for Fit-II (see $\Delta P=-60$ stable solution), which occurs considerably sooner in vacuum pressure elevation than under Newtonian rheology ($\Delta P \approx -200$). Findings reflect that the outer conduit top-surface shape is majorly affected for $\Delta P \leq -20$, whilst the inner surface shape remains relatively unaltered. There is also significant downstream shift in contact point location, between inelastic solutions with $\Delta P=-60$ and $\Delta P=-80$, approaching critical conditions. Describing extrema in top-surface shape change for the largest vacuum level imposed ($\Delta P=-80$), there is greater concavity experienced in the swell region post-die-exit, the conduit surface is more wavy throughout its length, and there is obvious pinching in the vicinity of the melt-cable contact-point. This structure represents a dramatic change when compared to the Newtonian solution position, which showed a prominent corresponding decrease in draw-down length. Taking into account the variability in critical vacuum pressure levels between Newtonian and inelastic representations, it is quite apparent that inelastic solutions are more sensitive to contact-point conditions and Newtonian solutions to die-swell conditions. This contrast is drawn out in Figure 5.14a and Figure 5.14b. Hence, to overcome this drawback the decoupled free-surface strategy is implemented. This technique has been successfully trialled for Newtonian, inelastic and vacuum pressure scenarios as illustrate below.

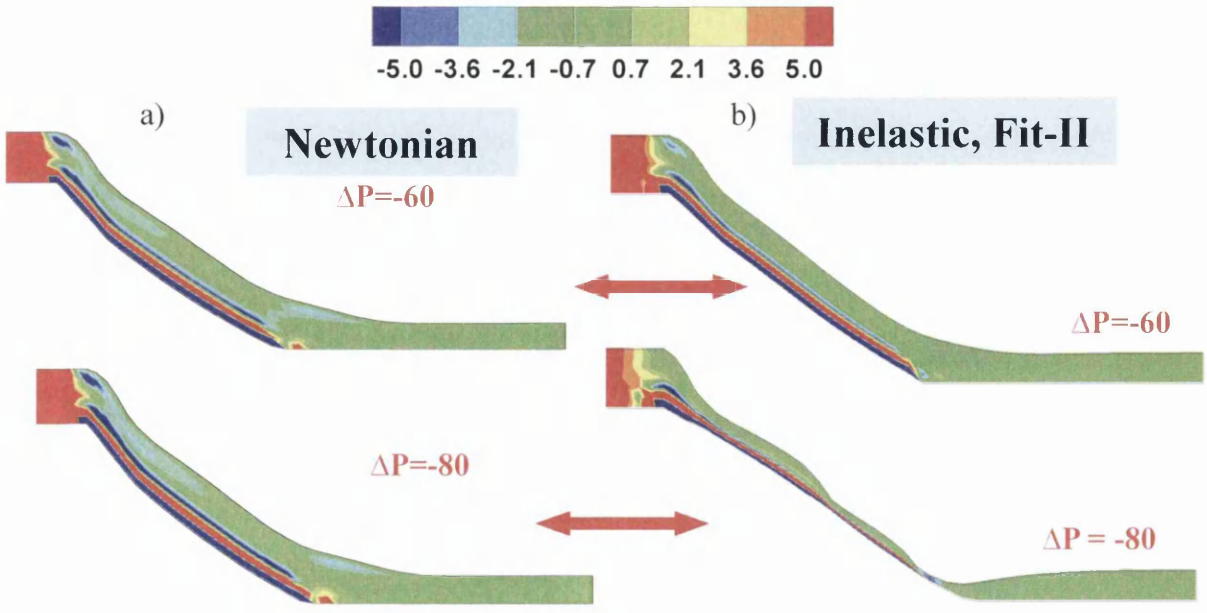

Figure 5.14: a) Newtonian, b) Inelastic, Fit-II: coupled free-surface solutions, vacuum effects, m_I=0.9

5. 7.3 Decoupled free-surface techniques

This aspect of the study documents the application of a new robust free-surface location technique, utilising a decoupled (independent) approach in calculations between top and bottom conduit surfaces. In this process, two solution sub-phases are considered. The first, seeks a solution when free-surface movement is suppressed, and a domain-interior solution is generated. Here, internal solution variables of velocity and pressure are determined, without boundary movement. Then, at a second phase, the draw-down section is subdivided into three sub-sections: (i) top-surface A - including the whole draw-down conduit and half of the coating region (surface-A); (ii) bottom-surface B of the draw-down conduit (surface-B); and (iii) second/final half C of the coating region (surface-C). Accordingly, the double free-surface problem may be tackled by commencing from a fixed position interior solution (step 1), subdivided itself into *four stages of analysis*. The *first stage* (i) permits only lower conduit surface-B movement, with fixed surface-A and surface-C (B free; A, C fixed). The cable velocity is imposed at the moving cable surface, and the contact point location itself is to be determined as part of the problem. The *second stage* (ii) is then to solve with independent top-surface A movement alone, that is with fixed surface-B (of the draw-down conduit) and surface-C (of the coating region) (labelled A free; B,C fixed). The procedure may terminate at this point, as the *third and fourth stages* constitute consistency checks. The *third stage* (iii) reassesses surface-B movement, as a consequence of repositioning of surfaces-A (labelled B free; A,C refixed). Finally the *fourth stage* (iv), the double free-surface solution may be checked in two ways: (a) with recoupling surface-A and surface-B simultaneously (labelled A, B free; C fixed); and (b) rechecking surface-A movement alone, after B-movement in stage (iii) (labelled A free; B,C refixed). This systematic approach allows for separate interpretation of free-surface degrees of freedom in the problem, and their relative strength of impact on the process.

Experience would indicate that, each of the above intermediate steps yields a solution to a specified level of solution invariance, when commencing from a previous solution. It is also apparent that perturbation to one or either of the free-surfaces will influence the other, and that some sufficient conditions are demanded to seek steady-solutions. To this end, tolerance monitoring on the free-surface location has been instigated, both as a

guide to error estimation and assessment of suitable convergence criteria across the sequence of time steps (see section 3.11 of chapter 3).

5.7.3.1 Decoupled free-surface tracking, Newtonian solutions

Through the time-stepping solution procedure to update the free-surface location, first the solution commences from initial conditions of the previously derived Newtonian solution satisfying a fixed surface position. Then, the temporal equations for the free-surface are integrated through time to solve for a steady solution position using the specific tolerance for the radial coordinate to satisfy sufficiency in free-surface convergence over the time-step sequence. In order to present findings with clarity, this task is reported upon as segregated into four solution phases:

Stage (i) – To seek the solution under free-surface B movement, applied to the bottom surface alone (surface-B)

Stage (ii) – To seek the solution under free-surface A conditions, permitting only top surface of draw-down conduit movement (surface-A)

Stage (iii) – To re-assess the solution under free-surface B movement alone, following resettlement of surface-A

Stage (iv) – To re-assess the solution under free-surface movement for:

(a) both top and bottom surfaces combined (surface-A and surface-B)

(b) top surface of draw-down conduit alone (surface-A)

5.7.3.1.1 Decoupled free-surface, bottom zone movement (surface-B) - Stage (i)

Here, only the bottom-part of the draw-down conduit (surface-B) is permitted to move (free-surface and mesh nodes), whereas the other surfaces remained fixed. The shape is determined from vertical node-movement, interpreted in terms of change in the radial direction only. New r-coordinates are then calculated, dependent on the radial and axial velocity components. Two different tolerance levels have been utilised to assess trends in temporal development and convergence of the lower conduit surface-B {TOL_C=5×10^{-5}, 10^{-5}}. The temporal radial coordinate evolution increment is plotted in Figure 5.15(a,b) by tracking two different points on the lower surface-B, one near the die-exit and the other near the contact point, respectively (two central plots). Findings reveal that, under TOL_C=10^{-5}, free-surface B convergence occurs rather quickly, and meets the tolerance at n-step=10000 (time=10 units) (see Figure 5.15c). The solution

location-point near the contact-point takes nearly twice as long to settle down to an invariant state, as the location-point near the die-exit. Further evidence on time-trace and development of the lower surface-B lies in the profile (Figure 5.15d), which indicates that this solution is invariant over further time (*20).

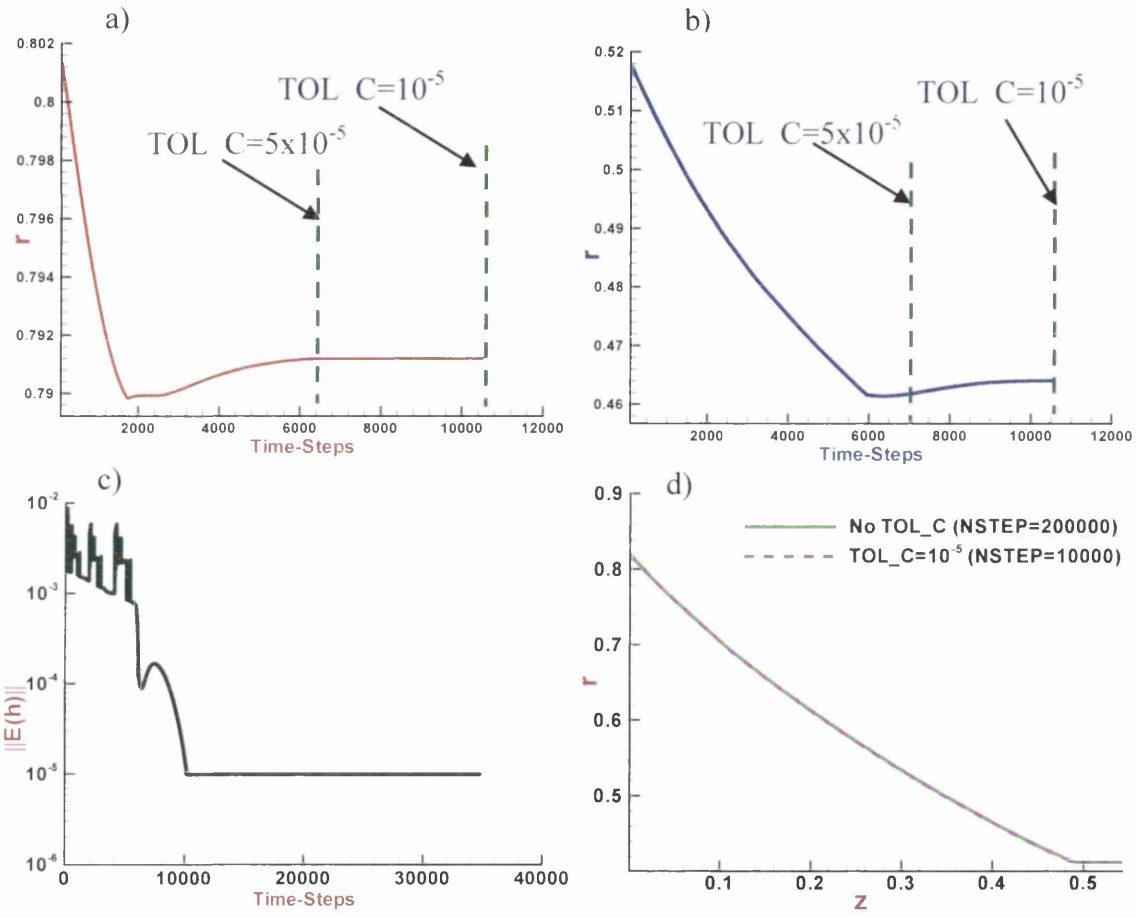

Figure 5.15: Convergence of bottom free-surface B position, Newtonian

5.7.3.1.2 Decoupled free-surface, top surface movement (surface-A) - Stage (ii)

Here, the same techniques are applied once more as in the previous subtask, with the distinction that, now, only the top free-surface of the draw-down conduit (surface-A) is unrestricted in movement. Likewise as in Figure 5.16(a,b), the results of free-surface convergence are considered through tracking two different points on surface-A, one near the die-exit and the other above/close to the contact point region. In addition, the tolerance history and full profile of the top surface are also displayed in Figure 5.16c. Convergence rates are clearly slower for the point located above the dynamic contact point than that near the die-exit. From the profile of tolerance histories one detects that,

the top free-surface in stage (ii) demands appreciably more time to reach this stringent convergence criteria TOL_C=1.1x10^{-5}; n-step=200000 (time=200); which represents twenty times more than is required for the bottom free-surface B of stage (i). One concludes that, the convergence of the top surface requires much longer computation times compared to the bottom surface. Moreover, comparative data are presented on top-surface solutions derived from both the coupled scheme (previous method) and this decoupled method (current method) (see Figure 5.16d). These profiles reflect that, there is practically no difference observed between the top-surface shapes for the two separate solutions.

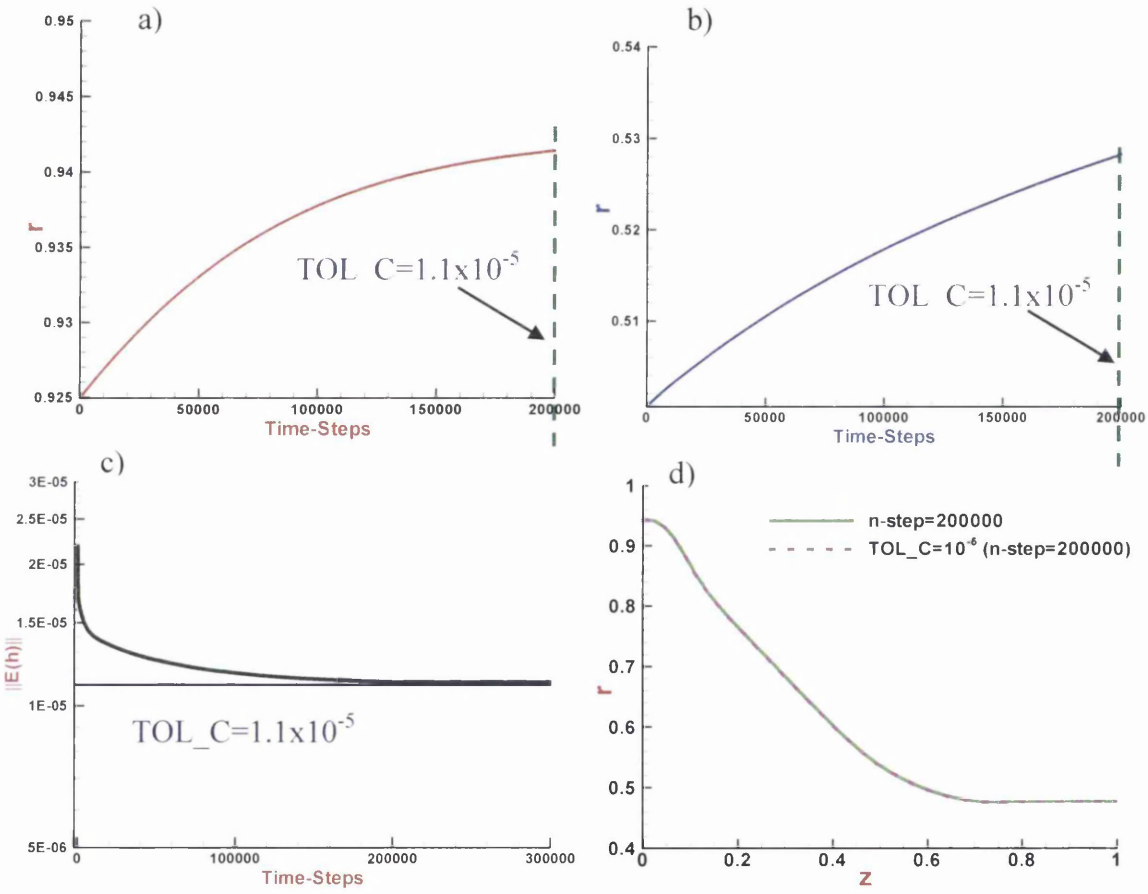

Figure 5.16: Convergence of top-free-surface A position, Newtonian

5.7.3.1.3 Decoupled free-surface, bottom zone repositioning (surface-B) – Stage (iii)

This stage constitutes a consistency check, where free-surface movement is re-applied to the lower conduit surface (surface-B), once surface-A has been located, again with other parts fixed. Findings reveal that, convergence is relatively quick for the

setting TOL_C=10^{-5}, noted in the early time (n-step=6200; time=6.2) when compared with stages (i) and (ii) (not shown). There is practically no readjustment necessary for surface-B from the result in stage (i).

5.7.3.1.4 Final consistency check with decoupled free-surface movement - Stage (iv)

(a) Top and bottom (surface-A and surface-B) - coupled

Here, the combination of section A and section B free-surfaces is considered (interacting, coupled) while, section C is held in a fixed position. A number of different tolerance levels have been monitored over the time-stepping sequence to assess their attainment {TOL_C=1.3x10^{-5}, 1.25x10^{-5}, 1.2x10^{-5}, 1.1x10^{-5}}, surface interaction and convergence trends (see Figure 5.17). The history profiles in Figure 5.17a demonstrate that, an appropriate level of tolerance lies between 1.3x10^{-5} and 1.2x10^{-5}; there is no significant change observed beyond these ranges. In addition, the predicted shapes for the draw-down sections illustrate that one cannot enforce both free surface-A and surface-B simultaneously to long times, without stimulating long-term dissipation (see Figure 5.17b for solution drifting). This ultimately tends to violate mass conservation across the radial cross-section. Hence, the decoupled free-surface solution approach is advocated to avoid this issue (see below).

a)

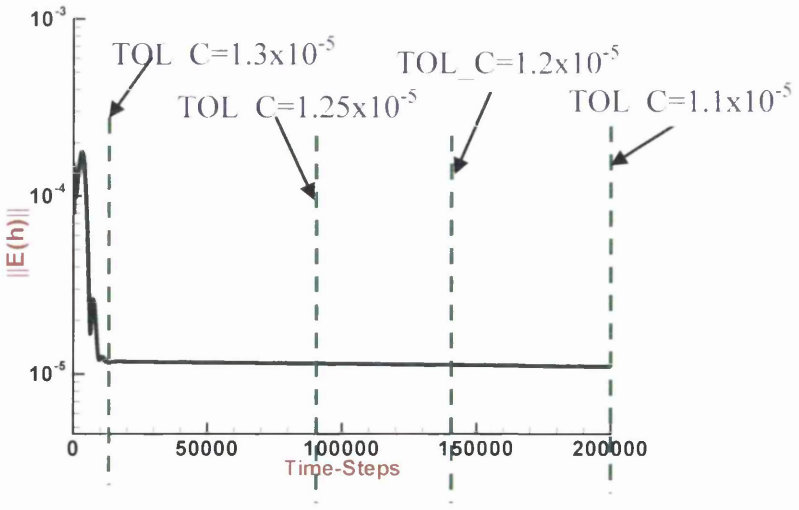

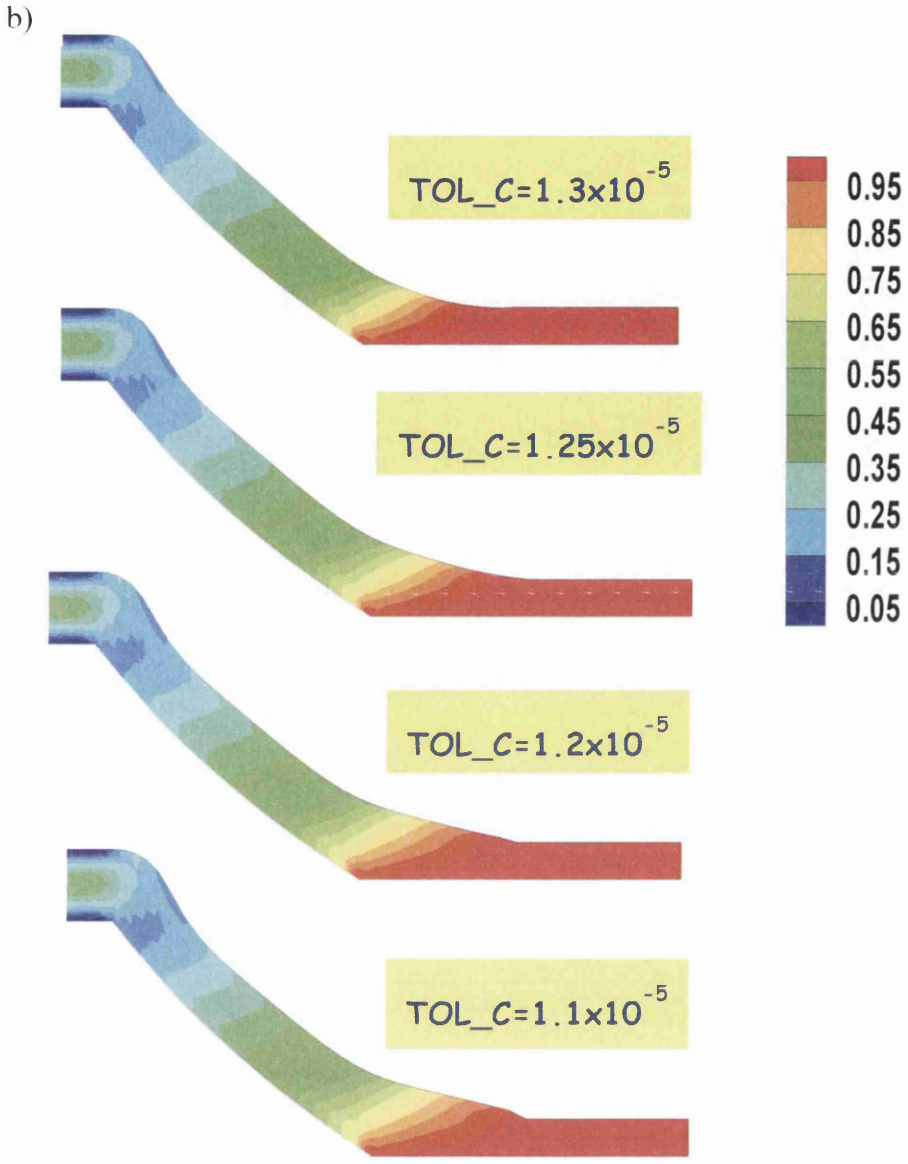

Figure 5.17: Convergence of top & bottom free-surface A&B positions, Newtonian

(b) Top surface of draw-down zone re-movement (surface-A) - decoupled

The profile of the tolerance history is displayed in Figure 5.18a to an appropriate tolerance (TOL_C=1.3x10^{-5}), providing a direct comparison between coupled (free surface-A and surface-B simultaneously) and decoupled solutions (free surface-A alone). Convergence is relatively rapid for stage (iv)-b: 730 time-steps, time=0.73; whilst in contrast is considerably protracted under stage (iv)-a: 12000 time-steps, time=12. In terms of conduit shape, insignificant change occurs under both scenarios at this tolerance setting (pre long-term dissipation) as illustrated in Figure 5.18b.

Consequently, both to reduce computational cost and to avoid solution drifting, the decoupled approach is pursued under the more severe scenarios of interest (inelastic rheology, imposed vacuum pressures).

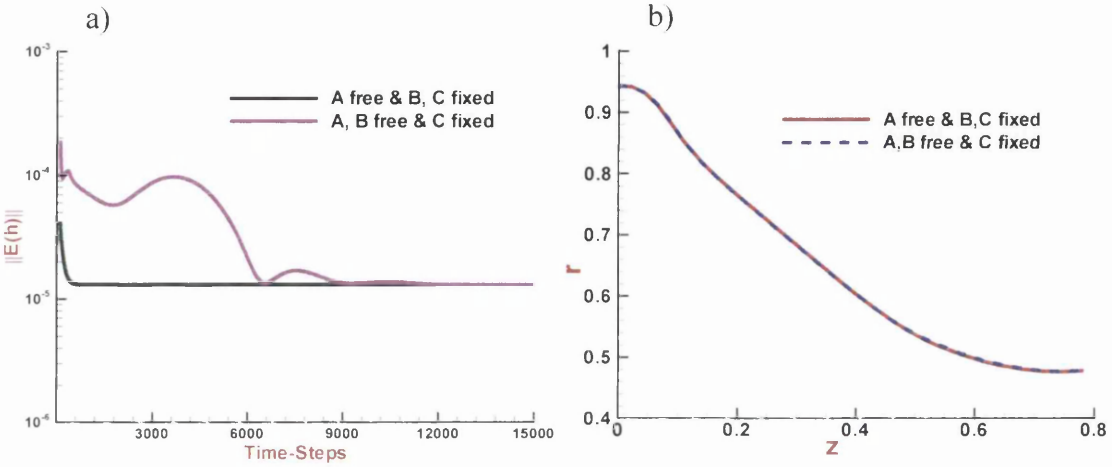

Figure 5.18: Convergence of top & bottom free-surface A&B positions vs Convergence of top free-surface A position, Newtonian

5.7.3.2 Decoupled free-surface tracking for inelastic solutions

5.7.3..2.1 Results without vacuum pressure applied

For the inelastic Fit-II model and the decoupled strategy outlined above, whilst incrementing between different levels of power-indices, m_I, and this task is segregated into the following three phases:

i- Seek the *internal field* inelastic solution (current m_I) under *frozen free-surface* movement

ii- Seek the solution under free-surface movement applied to the conduit bottom surface alone (*surface-B*)

iii- Seek the solution under free-surface conditions permitting only conduit top surface movement (*surface-A*)

As above and to commence the time-stepping procedure, the initial conditions (and shape) are adopted from the previous solution (Newtonian). The corresponding results with different power-index settings (m_I= {0.9, 0.8, 0.7, 0.5}) are shown in Figure 5.19, using an appropriate tolerance extracted as (TOL_C=1.3x10^{-5}). Findings indicate that in surface readjustment (shape), there is insignificant change, apparent over all phases, with power-index variation (not shown). In addition comparative tolerance histories are

presented on free-surface convergence for stage (ii)-B and stage (iii)-A with four different m_1-values. Overall, the results reflect that quick convergence is noted for both top and bottom surfaces, and to the same tolerance the bottom surface converges considerably quicker (10*). In addition and for all cases, one observes the consistent trend of an increase in time to convergence with decreasing m_1 (with increased relative thinning).

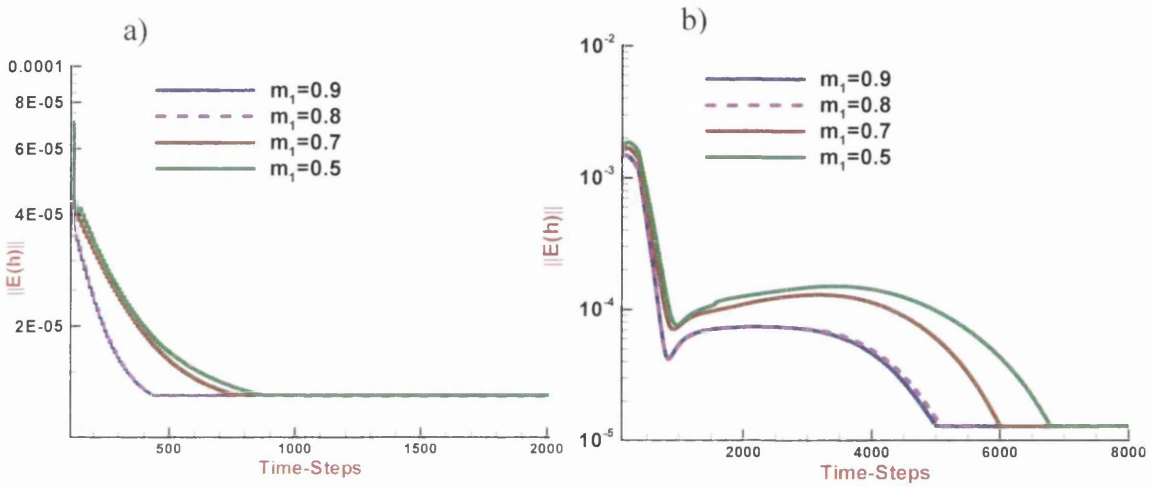

Figure 5.19: tolerance histories for convergence of top & bottom free-surface, Fit-II, m_1 variation

5.7.3.2.2 Vacuum effects & inelastic solutions

As discussed above, a decoupled free-surface approach has also been introduced when required to improve the numerical capture of the conduit surface shape (see for example, the degradation in solution quality as shown in Figure 5.14a with ΔP=-80 at m_1=0.9 and gathered under the coupled free-surface approach). Here, improved solution quality is accessible with the decoupled free-surface approach, as noted in Figure 5.20b, ΔP=-80, where significant improvement in free-surface shape is observed. This free-surface location technique utilises a decoupled (independent) approach in calculation between the two independent surface sections, top and bottom conduit surfaces. This technique has been successfully trialled for Newtonian, inelastic and vacuum pressure scenarios. With respect to bottom (inner) conduit free-surface zone movement, findings reveal that convergence occurs relatively rapidly to meet the specified convergence tolerances. The solution point-location near the contact-point takes nearly twice as long to settle down to an invariant state, as does the point-location near the die-exit. On convergence to steady state of the top (outer) free-surface of the conduit, one concludes

that much longer computation times are required here, when compared to those for the bottom surface. In Figure 5.20b, and under this decoupled approach, a solution for ΔP=-100 is also obtained, whilst for the coupled approach, this was not computationally possible (divergence ensued). Overall, the results reflect that rapid convergence is noted for both top and bottom surfaces with the decoupled free-surface approach in comparison to that for the coupled approach. In addition, one observes a consistent trend of an increase in time to achieve a common convergence threshold upon decreasing m_I further away from unity (notably, with increased relative thinning effects).

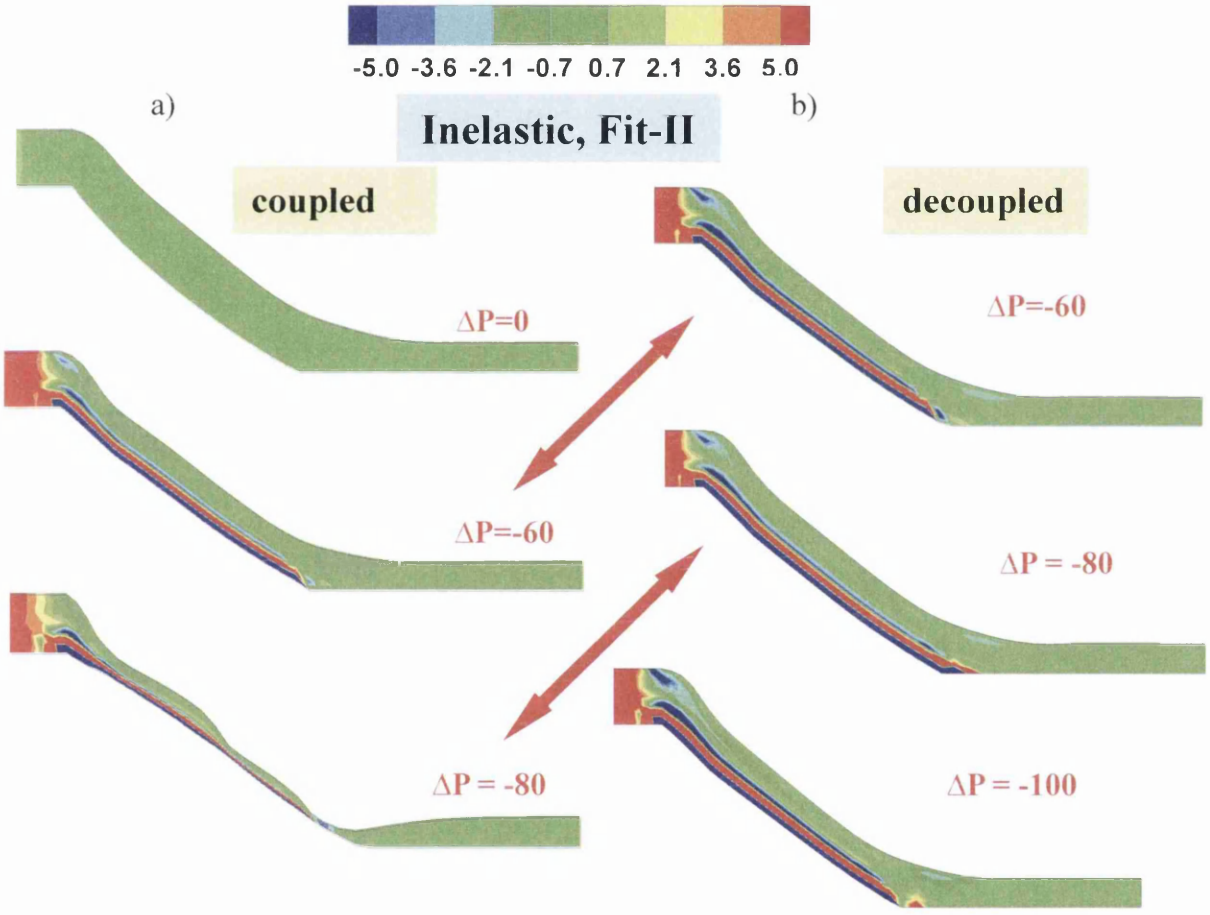

Figure 5.20: a) Coupled b) decoupled free-surface solutions, vacuum effects, Fit-II, m_I=0.9

Figure 5.21 provides the development of the pressure fields under vacuum variation {ΔP= -60, -80, -100} for two sample values of power-index {m_I=0.9, 0.8} with the corresponding tolerance history profiles; Figure 5.22 gives the corresponding data for fluids with power-index {m_I=0.7, 0.5}. From this information, one is able to detect the consequence of *greater vacuum influence on the ensuing melt cone shape - which*

causes the top free-surface of the conduit to be sucked inwards. In contrast, the effect of *reducing* m_1 is also clear, in that it also reduces the critical level of *vacuum pressure* that may be sustained. In this context the results reflect that, for m_1=0.9 the limit of vacuum was ΔP=-120 (not shown), ΔP=-100 for m_1=0.8, ΔP=-20 for m_1=0.7 (not shown), while for m_1=0.5 it was ΔP=-15. In all cases, at larger levels of vacuum pressure, there is significant indentation in top surface shape, when observed in comparison to the lower surface, with a *pinching effect just beyond the die-swell region and a ramping bulge opposite the cable contact-point location*. Moreover, pressure layers arise along and inside the inner free-surface of the draw-down conduit, and eventually inside the upper surface just beyond the die-exit. An isolated pressure peak also occurs just beyond the contact-point. In addition and from history profiles, one notes an increase in tolerance estimation criterion as the pressure vacuum level rises at fixed m_1-level; likewise, there is an increase in tolerance criterion as m_1 decreases at fixed vacuum pressure level. Accordingly, one can predict an appropriate convergence tolerance for each level of vacuum and power-index. Here one can conclude the larger levels of tolerance necessary to capture accuracy and convergence as m_1-declines in value.

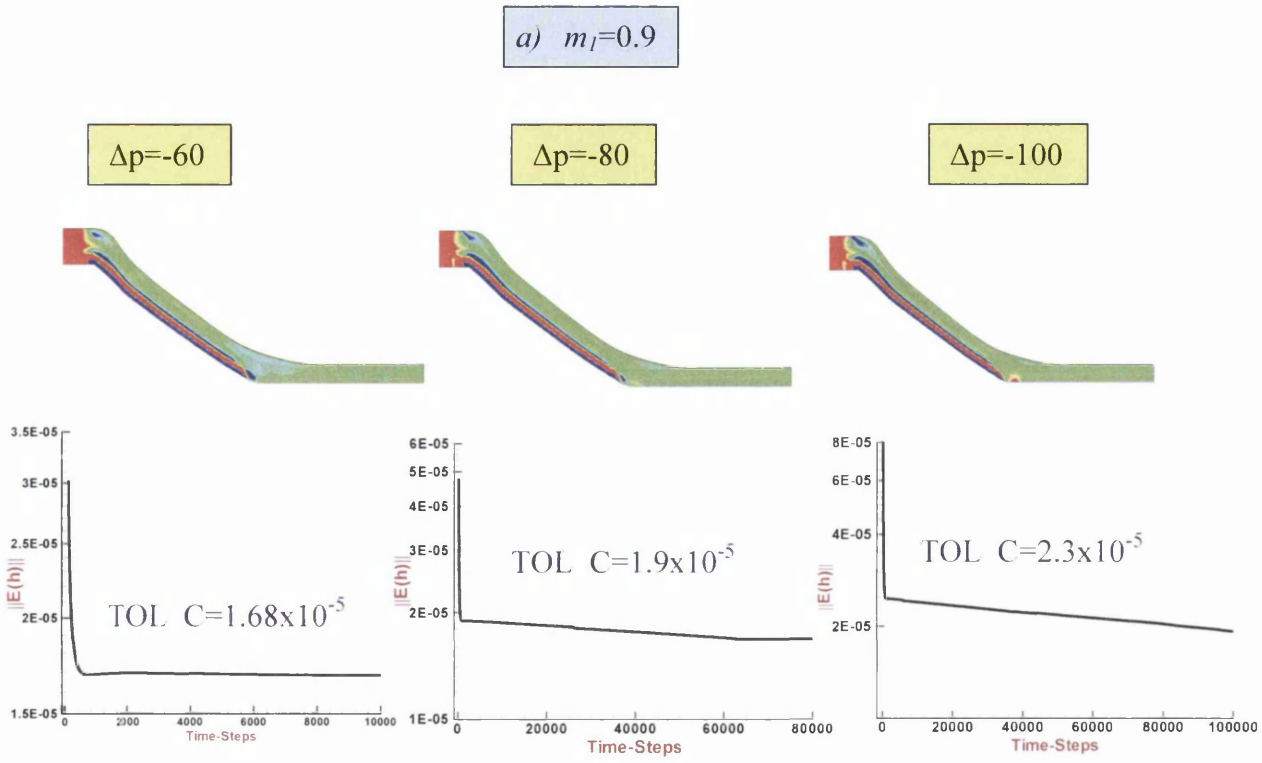

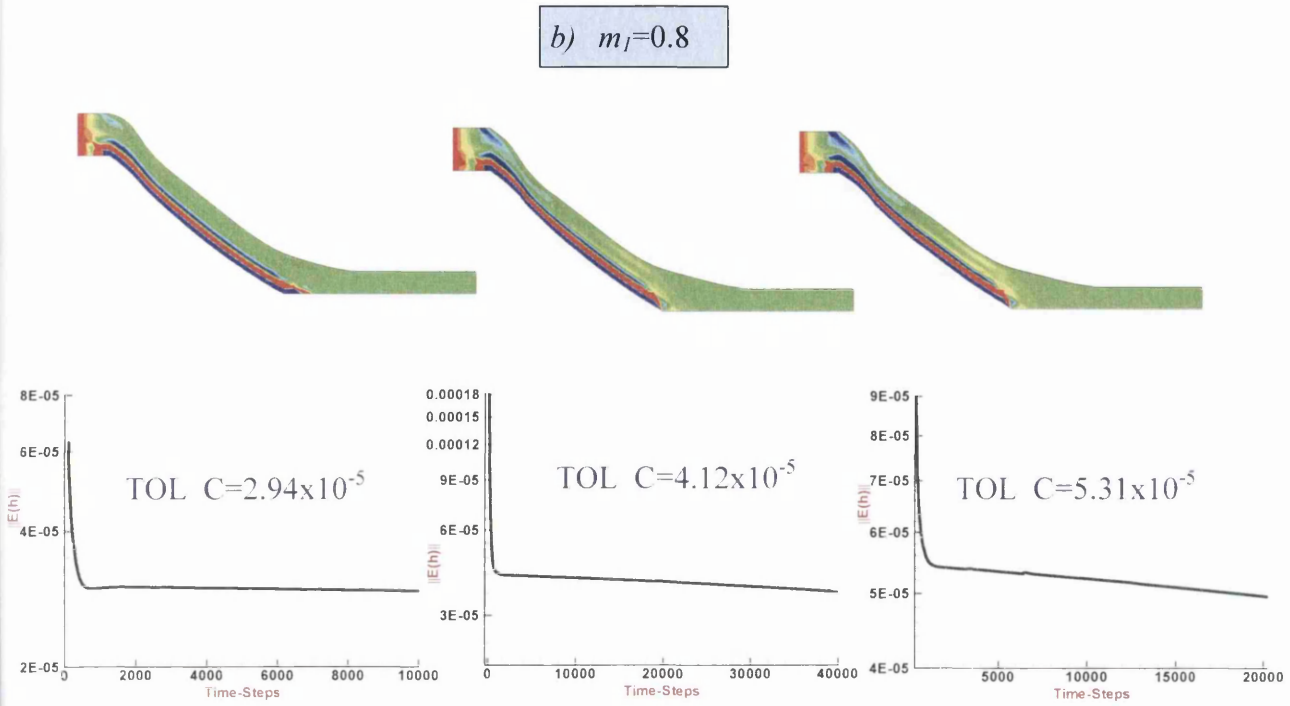

Figure 5.21: Evolution of shape and tolerance histories for convergence of top free-surface, vacuum variation, Fit-II, a) m_1=0.9, b) m_1=0.8

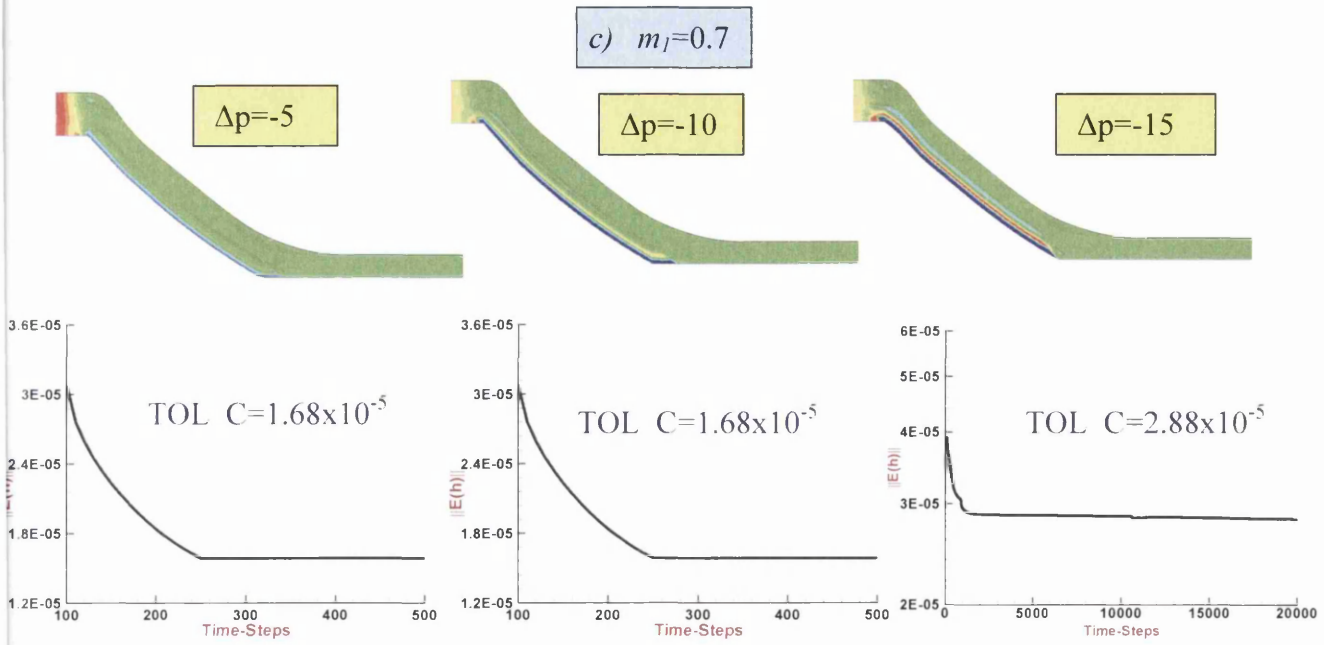

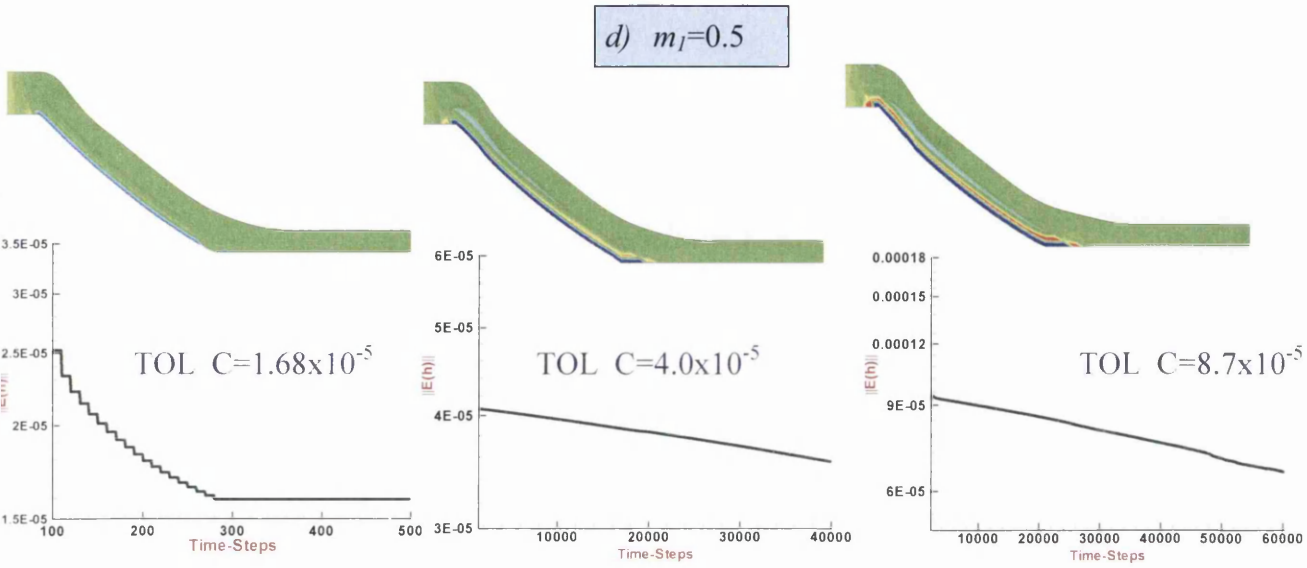

Figure 5.22: Evolution of shape and tolerance histories for convergence of top free-surface, vacuum variation, Fit-II, a) m_1=0.7, b) m_1=0.5

5.8 Conclusion

This chapter has investigated the numerical solution of Newtonian and viscous inelastic flows for the combined tube-tooling/draw down flow. Many factors that have a bearing upon the process as a whole have been investigated – including those of surface friction; vacuum pressure applied across the conduit; aspects of dynamic contact-point and die-exit singularity capturing, via localised shock-capturing; coupled and decoupled free-surface solution. Regarding the effects of surface friction, one can gather that slip is a mechanism to significantly reduce pressure-drops in the die-section of the flow-process. In addition, computational predictions for inelastic model fits show die-inlet pressure-maxima, or pressure-drops, reduce from Newtonian levels by about a *factor of four with Fit-I, and by about one-half with Fit-II* model. Over the draw-down section, Fit-II provides the largest solution changes around the cable-melt contact zone. Shear stress maxima manifest a *five-fold decrease with Fit-I* from Newtonian levels, and *3.5-fold decrease with Fit-II*. This is borne out in shear-rate adjustment likewise. Fit-II generates the largest shear-rate maxima, *which explains the larger stress levels amongst the inelastic solutions*, and on the bottom-surface, the largest peak over the contact

point. On tensile stress, there is plenty of evidence for the impact and clear consequence of viscosity variation; thinning from Newtonian, but hardening of Fit-II compared to Fit-I. Throughout the draw-down section, maxima in strain-rate are observed near the melt-cable contact-point for the Newtonian solution; whilst minima correspond to Fit-II in this same location.

The influence of singularity capturing on the die-exit solution has been explored successfully using the *strain-rate stabilization* (*D-Dc*) technique. In this respect, it has been demonstrated that such treatment can have a significant impact on peak stress and strain rates exiting the die, which themselves influence the levels of die-swell encountered. Throughout the study, some additional numerical convergence aspects have also been addressed, specifically pertaining to temporal solution stability for these free-surface problems, and as solvent fractions diminish, power-indices lower or vacuum pressures rise. Moreover, a new free-surface location technique has been established, utilizing a decoupled (independent) approach in calculation between top and bottom (outer and inner) conduit surfaces. This technique has been successfully trialled for Newtonian, inelastic and vacuum pressure scenarios. Further improvements in free-surface procedures are also documented through mid-side node/line-segment oriented approximations. In addition, taking into account the variability in critical vacuum pressure levels between purely-viscous Newtonian and inelastic representations, it is quite apparent that inelastic solutions are more sensitive to contact-point conditions and Newtonian solutions to die-swell conditions.

CHAPTER 6

Numerical study of the hybrid finite element/volume method for tube-tooling cable-coating flow: with EPTT viscoelastic differential model

This study investigates the numerical solution of viscoelastic flows for tube-tooling die-extrusion coating using a hybrid finite element/finite volume discretisation (*fe/fv*). The finite volume scheme is used for hyperbolic constitutive equation, introduced here of an exponential Phan-Thien Tanner (EPTT) model. The continuity/ momentum equations are solved through a semi-implicit fractional staged/pressure correction finite element scheme. The corresponding non-dimensional momentum-continuity deferential equations and constitutive deferential equations are provided in chapter 2.

6.1 Introduction

The modelling of cable coating with free surface location for axisymmetric and annular systems remains popular topic, which has provoked many studies (see for examples [93], [85], [88], [56]). In addition, there have been a number of studies that have addressed the modeling of wire coating for tube-tooling; see for example Gunter et al. [53], Mutlu et al. [90, 91]. These have provided some progress within the inelastic, non-isothermal and viscoelastic regimes. In their work, viscoelastic coating flows were simulated as with a PTT model and solved with a finite element technique. Based on, a time-stepping Taylor-Galerkin/pressure-correction finite element framework [31], tube

tooling extrusion coating with a low density polymer melt has been analysed by Mutlu et al. [92]. In this study, both decoupled on velocity and stress and coupled numerical approaches were employed with the EPTT model. There, the decoupled method was used to overcome the numerical convergence difficulties when solvent contributions were minimal. Again, Matallah et al. [74] used the finite element method to simulate viscoelastic wire-coating employing coupled and decoupled schemes. There, a multi-mode EPTT model was used to emphasise the influence of die-design on optimal process settings. The draw-down residence time, which dictates the dominance of certain modes within the relaxation time spectrum, was found to be a major factor in the decay of residual stressing in the coating. Further work was conducted by Matallah et al. [75] to include a comparison of both single and multi-mode viscoelastic analysis for such wire-coating flows using the same numerical approach. There it was shown that the differences in findings appeared minimal from single to multi-mode modelling, specifically in the draw-down and coating regions. Similarly, Baloch et al. [13] conducted a comparative study of annular wire-coating flows with polymer melt materials using a single EPTT model. Additionally, Ngamaramaramvaranggul and Webster [96, 97] used a semi-implicit Taylor Galerkin/pressure-correction finite element scheme (STGFEM) to solve annular incompressible coating flows with the EPTT model. The authors showed that the EPTT model presents a better fit for viscoelastic fluids than other models due to its ability to accommodate the high elasticity regime (to the comparison curve), see for example the text of Tanner[121].

Most earlier studies on tube-tooling coatings has been performed through finite element implementations. In contrast, this study advocates a hybrid finite-element/finite-volume approach, which consists of a Taylor–Galerkin finite element discretisation for momentum-continuity-surface calculation, and a cell-vertex fluctuation-distribution finite volume approach for stress. This is an amenable choice made to meet differential equation-typing demands, being of parabolic-elliptic form for the momentum-continuity sub-system, whilst of hyperbolic form for the first-order space-time tensorial constitutive equation ([140]) (also see section 3.9 for more details).

This chapter covers the application of viscoelastic analysis for the tube-tooling cable-coating using the network class of models, of exponential Phan-Thien Tanner (EPTT) type; shear-thinning, strain-hardening/softening, moderate-high Trouton ratios. Initially

and under chapter 5, Newtonian and viscous inelastic coating fluids models have been introduced into the simulations. It is well known that viscoelastic fluids, as opposed to Newtonian and inelastic fluids, exhibit a non-zero first normal stress difference (N_1), hence requiring description of fluid memory and indeed a constitutive equation of state for stress (governing viscoelastic stress, see chapter 2). Here, instances of ideal flow deformation, as in simple shear and uniaxial flows, are used to identify the PTT parameter set (ε_{EPTT}, ξ), for which a close fit to the experimental data is sought. Throughout the study influences of variation in Weissenberg number (We), polymeric viscosity and second normal stress difference (N_2) are analysed, whilst considering the impact of variation in shear-thinning properties. To gain some insight into residual stressing, close attention is paid to cross-stream stress profiles in the coating and its extended zones, necessary to accommodate the various relaxation modes involved.

6.2 Numerical algorithm

To solve the related governing equations, a hybrid finite element/volume discretisation scheme is performed for both coupled and decoupled procedures (across the sub-stages within a time-step)), where the results are found to be comparable (see for example Mutlu et al. [92]). Coupled (u, τ, p, h) solutions are considered only for moderate levels of solvent-fraction [β=O(10^{-1})-O(10^{-2})], where relatively large Weissenberg number solutions may be obtained without difficulty. This method involves solving for kinematics and stress simultaneously using the fractional stages (3.26a)-(3.26f) in chapter 3. However, for pragmatic stabilisation reasons and relative simplicity, a decoupled scheme, which allows for frozen kinematics within the viscoelastic solver, has also been deployed, suitable for smaller levels of solvent-fraction [β=O(10^{-3}), high polymer concentrations]. Hence, with the decoupled approach, the calculation of the viscoelastic extra-stress (τ) is performed separately from the flow kinematics and surface adjustment (u, p, h) using stages (3.26b) and (3.26d). Thus, from anchored velocity and pressure fields, one resolves the extra-stress; then, the kinematics is updated by solving the conservation equations for a given extra-stress employing fractional stages (3.26a), (3.26c), (3.26e) and (3.26f). This strategy is supported by the fact that in many flows the kinematics themselves do not vary significantly with

material variation. In such a decoupled procedure and through *We*-solution incrementation, the surface position (h) may itself be fixed, at say, the initial conditions of the previously derived coupled viscoelastic solution, or remain free to be determined alongside (u, p) kinematics.

6.3 Problem specification

Two schematic diagrams (short and long meshes) for the complete geometry are provided in Figure 6.1. The difference between the short and long meshes lies within the cable-coating region (L5-section), where the long mesh is almost four times more extended (see Table 6.1). In this study and due to the demands of long-range memory effects (see on), solutions are reported principally on the long mesh. Mesh characteristics are provided in Table 6.2 for both meshes, detailing numbers of finite elements, nodes and total numbers of degrees of freedom. Element distribution per region is also shown in Table 6.3. In addition, the relevant finite element mesh structure for the long-mesh is presented with sectional details, both to larger scale and zoomed, inclusive of detailed geometric design features of the draw-down section (DDS), free surface position, and cable-coating region.

Boundary conditions are taken as no-slip, and applied to the annular die-wall prior to the die-exit. For the draw-down section and cable-coating region the following boundary conditions are accepted: along the top and bottom (outer and inner) free surface sections, traction vanishes (natural conditions apply, at atmospheric pressure); along the free surfaces in the cable-coating region, the velocity components are defined assuming a plug-like velocity profile and a constant flow-rate per cross-sectional area; at the outflow, a plug flow is imposed that travels with the moving cable; along the lower domain boundary in contact with the cable, velocity conditions match those of the moving cable surface. The characteristic velocity and length respectively, are taken of (U) cable speed, and (L) the length of the draw-down section.

Table 6.1: Geometry dimensions

Cases	L_1	L_2	L_3	L_4	L_5	R_{int1}	R_{int2}	R_3	R_4	R_5	R_6
S-M	1	1.8839	1.9338	0.5423	0.5423	1.9648	1.9134	0.9436	0.8189	0.4772	0.4122
L-M	1	1.8839	1.9338	0.5423	2.4577	1.9648	1.9134	0.9436	0.8189	0.4772	0.4122

Table 6.2: Mesh characteristic parameters per region

Sections	S-M	L-M
	Elements	
Inlet tube	312	312
Converging section	612	612
Land region	528	528
DD section	240	240
Cable region	312	912
Total	2004	2604

Table 6.3: Mesh characteristic parameters

Mesh	Elements	Nodes	Degree of freedom (u,p,τ)
S-M	2004	4355	27306
L-M	2508	5447	34152

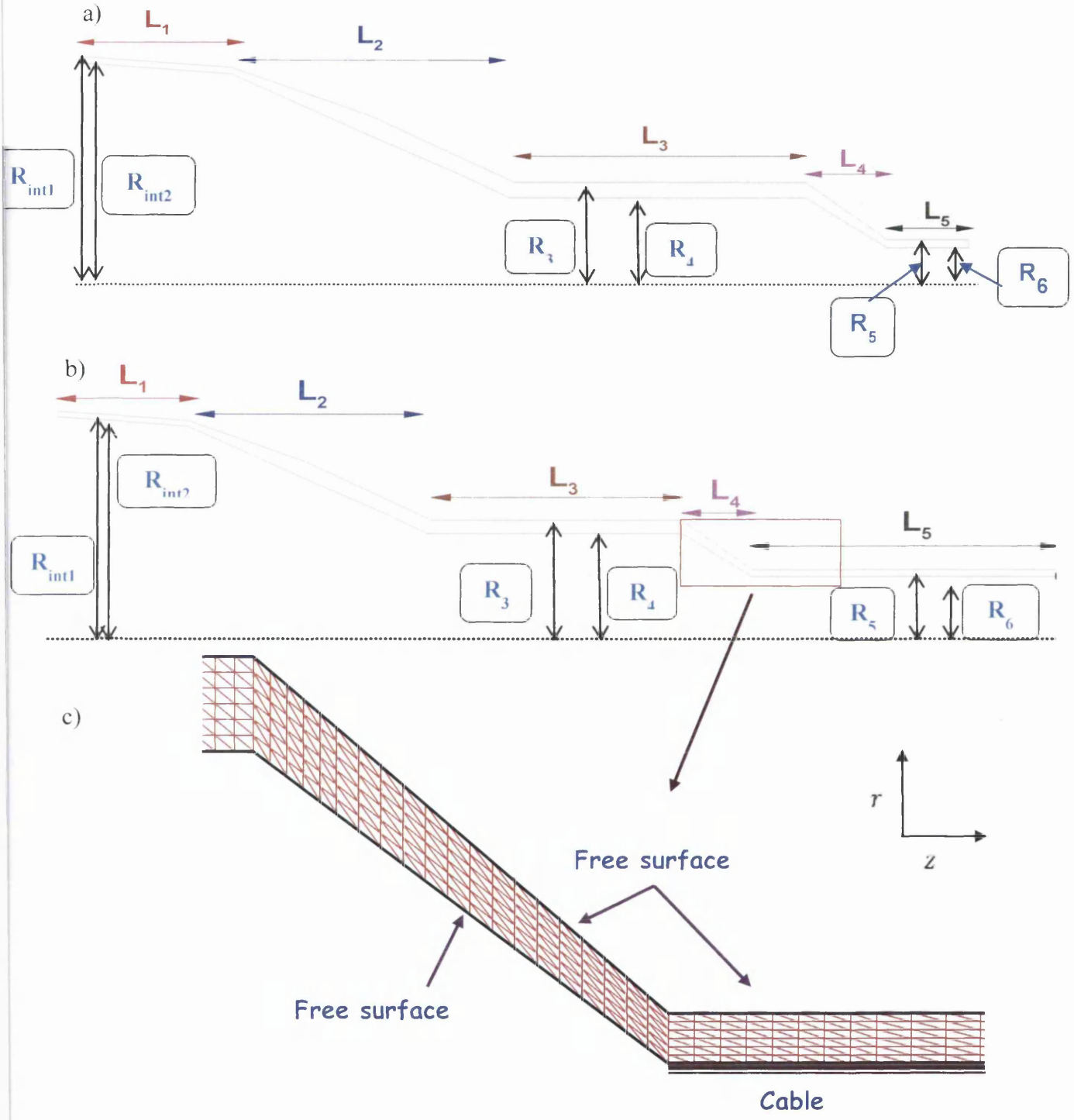

Figure 6.1: Schematic diagram for tube-tooling domain: a) short mesh (S-M), b) long mesh (L-M), c) Finite element mesh for draw-down section

6.4 Material functions

The material properties for the polymer melt exhibit shear-thinning and strain-softening, as illustrated in Figure 6.2. A suitable model to employ in matching this experimental data is an exponential Phan-Thien Tanner (EPTT) viscoelastic model, as this may display a suitable form in its shear-thinning and strain-softening properties. The functionality in the EPTT model provides the following shear viscosity (η_s), extensional viscosity (η_e), first (N_1) and second (N_2) normal stress-difference dependence:

$$\eta_s = \eta_0\beta + \frac{\eta_0(1-\beta)f}{f^2 + (\lambda_1\dot{\gamma})^2\xi(2-\xi)}, \tag{6.1}$$

$$\eta_e = 3\eta_0\beta + \frac{2\eta_0(1-\beta)}{f - 2\lambda_1\dot{\varepsilon}(1-\xi)} + \frac{\eta_0(1-\beta)}{f + \lambda_1\dot{\varepsilon}(1-\xi)}, \tag{6.2}$$

$$N_1 = \frac{2\eta_0(1-\beta)\lambda_1\dot{\gamma}^2}{f^2 + (\lambda_1\dot{\gamma})^2\xi(2-\xi)}, \quad N_2 = -\frac{\xi}{2}N_1. \tag{6.3}$$

Here, λ_1 may be interpreted as a principal relaxation time, $\beta = \mu_s/(\mu_e + \mu_s)$ as a solvent fraction, and μ_e and μ_s represent polymeric and solvent viscosity component fractions, respectively. Then, the zero-shear viscosity $\mu_0 = \mu_e + \mu_s$. Model constants ε and ξ are additional scale-less constitutive law parameters, ε governing the non-linear function f, ξ the combination of upper and lower convected material derivatives (Gordon-Schowalter). The second normal stress difference, N_2, may be expressed via ξ dependency on N_1. In this form, it may be observed that as ξ tends to zero, then so does N_2. This PTT model displays a slight increase of the extensional viscosity at extension rates less than unity, before decreasing to a high strain-rate limiting plateau. We observe from Figure 6.2 (a,b,c), the elongational viscosity fits provide appropriate trends in general behaviour, but at higher strain-rates, yield slightly lower estimated values than the limited set of experimental data provide. With regard to shear viscosity, the EPTT model provides acceptable fits to the experimental data, throughout a wide range of shear-rate. This is achieved by adjusting the ξ parameter to match the industrial characterisation data for any isolated shear rate extreme. At low rates ($\dot{\gamma} < 10^2$), a better fit for the shear-data is attained with EPTT ($\xi = 0.2$, $\varepsilon_{EPTT} = 0.5$, $\beta = 10^{-3}$). At higher rates

of ($\dot{\gamma} > 10^{2}$), EPTT (ξ =0.15, ε_{EPTT}=0.5, β=10^{-3}) provides a near-optimal least squares fit across the complete range of shear rates displayed (see Figure 6.2d). Note that, the elongational viscosity is unaffected by adjustment in the ξ-parameter.

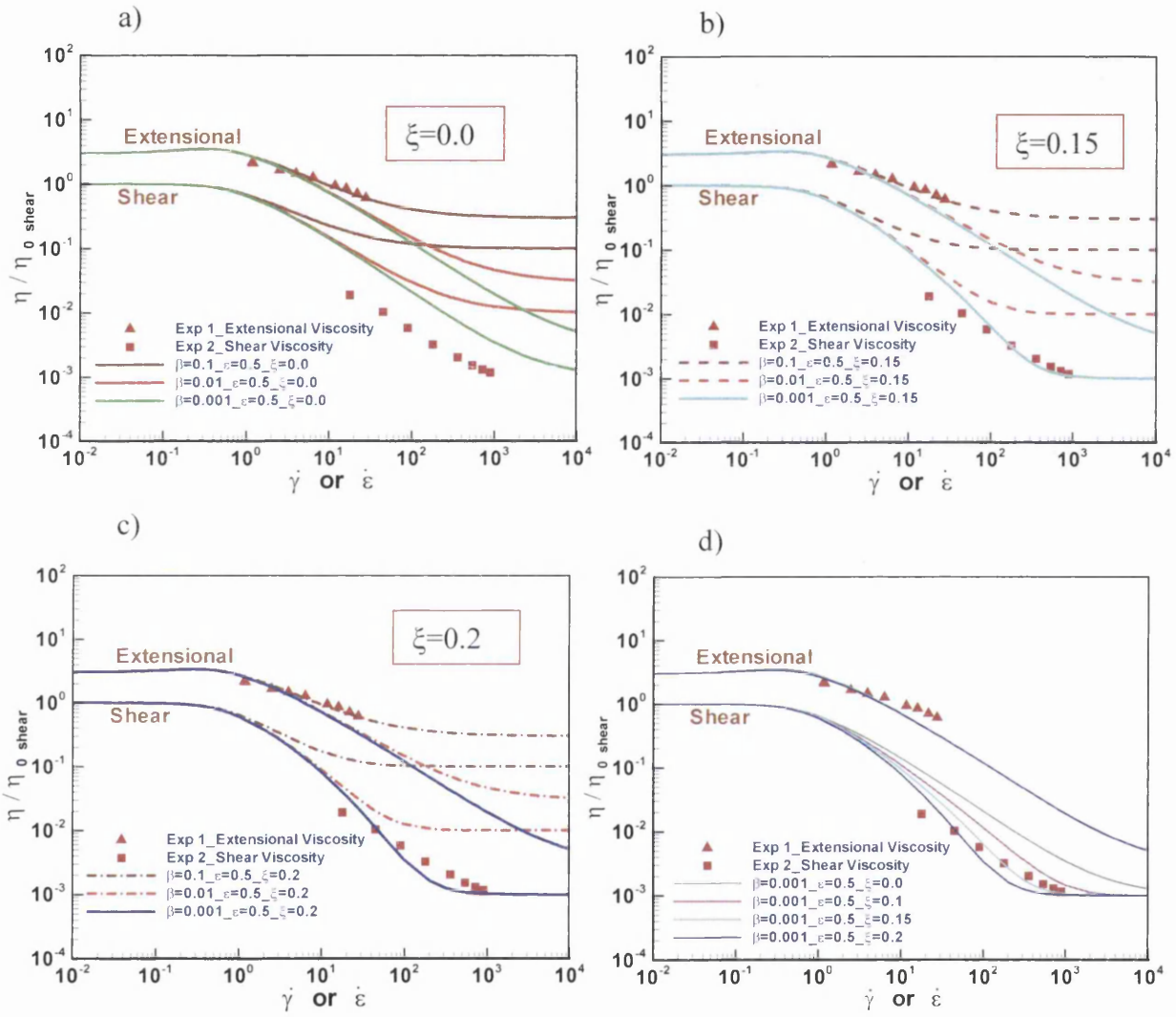

Figure 6.2: shear and extensional viscosity fits: (1) β-variation, ε_{EPTT}=0.5: a) ξ =0.0, b) ξ=0.15, c) ξ=0.2, (2), d) ξ-variation, ε_{EPTT}=0.5, β=10^{-3}

At low rates ($\dot{\gamma} < 10^{2}$), this is also true for the first normal stress difference (N_1), see Figure 6.3. However, as the shear rate increases somewhat further, and with increasing parameter ξ, the dependence of N_1 on $\dot{\gamma}$ becomes weaker (tending to cap N_1). Second normal stress-difference (N_2) is also given in absolute terms and comparative form in Figure 6.3, where N_2 departure from N_1 ($N_2 = -\frac{\xi}{2} N_1$) is clearly apparent at all rates.

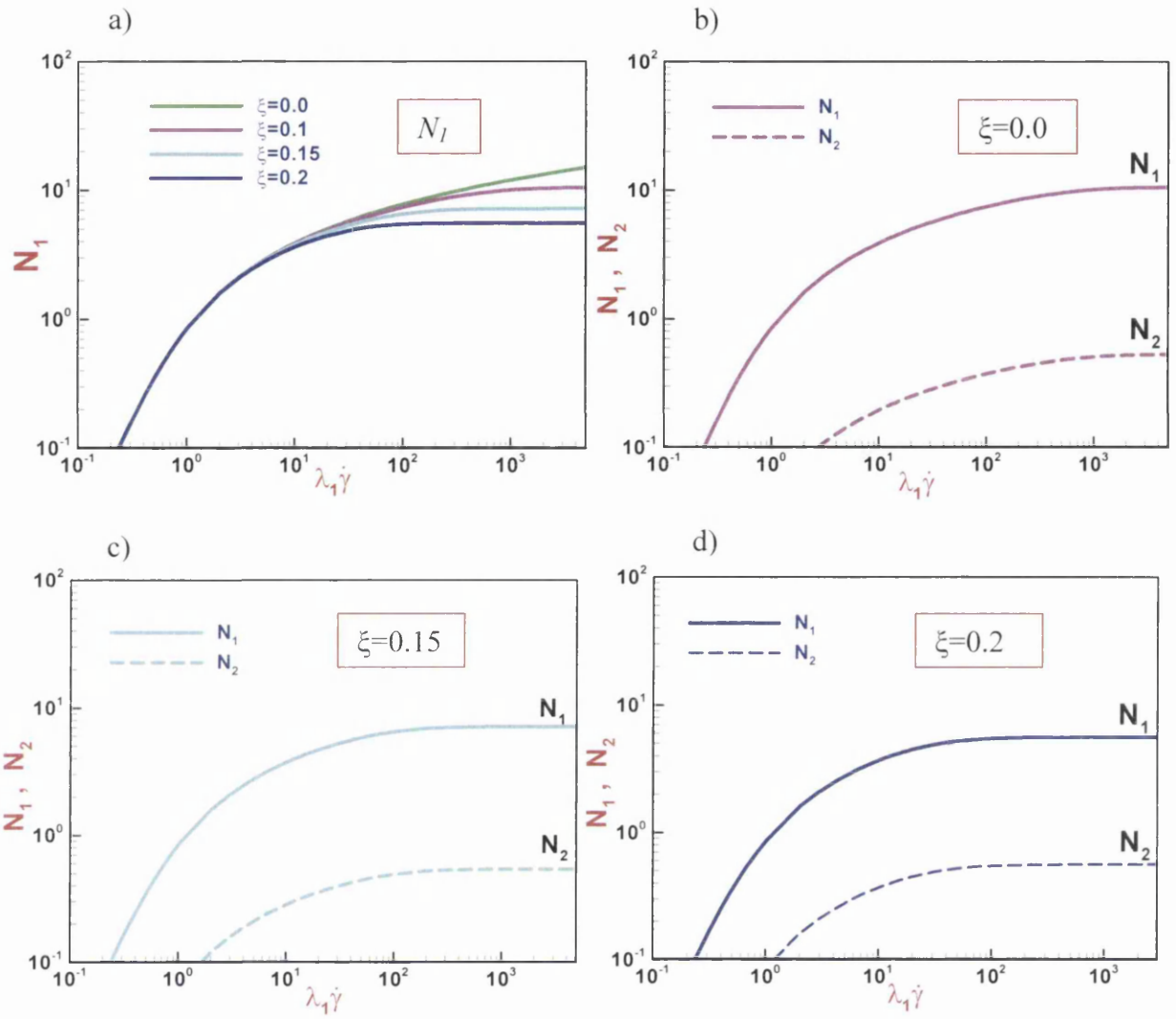

Figure 6.3: First (N_1) and second (N_2) normal stress differences: EPTT, $\xi=\{0,0.1,0.15,0.2\}$, $\beta=10^{-3}$, $\varepsilon_{EPTT}=0.5$

In Figure 6.4, the impact of increasing ε_{EPTT} is also considered, at constant values of (β, ξ). In steady shear flow and at lower rates, the viscosity marginally decreases with an increase of ε_{EPTT}. At moderate and higher rates, a best fit for shear-viscosity (in a least-squares sense, averaged through the data and range) emerges for shear rate ranges, $10^1 < \dot{\gamma} < 4*10^1$ with $\varepsilon_{EPTT}=0.7$, $4*10^1 < \dot{\gamma} < 3*10^2$ with $\varepsilon_{EPTT}=0.5$, and $\dot{\gamma} > 3*10^2$ with $\varepsilon_{EPTT}=0.3$. Here, the range and ε_{EPTT}-setting of $\varepsilon_{EPTT}=0.5$, is held to be most representative (hence, such a selection below). Furthermore, in uniaxial extension, a reducing trend is observed in elongational viscosity with increase in ε_{EPTT}. Extensional viscosity values predicted, at low-rates ($\dot{\varepsilon} \le 10^0$) for ε_{EPTT} =0.7, and medium-rates $\dot{\varepsilon} \le 10^1$ for ε_{EPTT} =0.5, lie closer to the experimental data; whilst for ε_{EPTT} =0.3, the

theoretical values provide a better match at higher rates $\dot{\varepsilon} \leq 10^2$. Intercepts with the experimental data shift through increasingly larger rates as the ε_{EPTT}-parameter is decreased. Overall, an optimal match to the experimental data, in a least-squares sense, and covering both shear and extensional viscosity data, is achieved with $\varepsilon_{EPTT} = 0.5$.

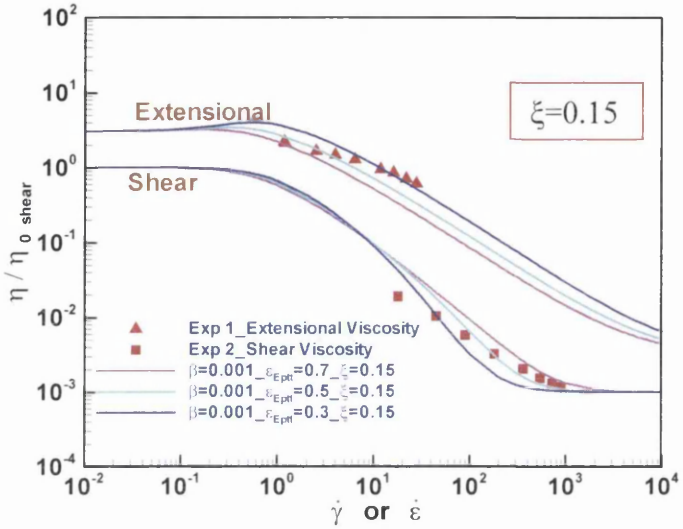

Figure 6.4: Shear and extensional viscosity, EPTT, ε_{EPTT} variation, $\beta = 10^{-3}$, $\xi = 0.15$

6.5 Computational Predictions

6.5.1 ξ=0 (zero N2), Variation in β and We

6.5.1.1 Geometry adjustment

To begin consistency is first confirmed in solution trends through the short and long mesh options. In this respect, one considers shear stress (τ_{rz}) profiles along the top (outer-annular) and bottom (inner-annular) surfaces, and normal stress (τ_{zz}) and first normal stress difference (N_1) profiles along the axial direction for the particular instance, selecting We=1, β=10^{-2}, ε_{EPTT} = 0.5 and ξ=0.0, (see Figure 6.5). Clearly and with two different cable lengths considered, there is little difference detected in these solution patterns throughout the die. In contrast, the changes observed are significant over the cable region and between solutions for the short and long coating sections. Significant stress relaxation occurs throughout the cable coating region, and resolution demands approximation with the long mesh (see use below). As such, a plug-flow state with vanishing shear stress (τ_{rz}), normal stress (τ_{zz}), and first normal stress difference N_1 is only appreciably realised throughout the cable section when using the long mesh.

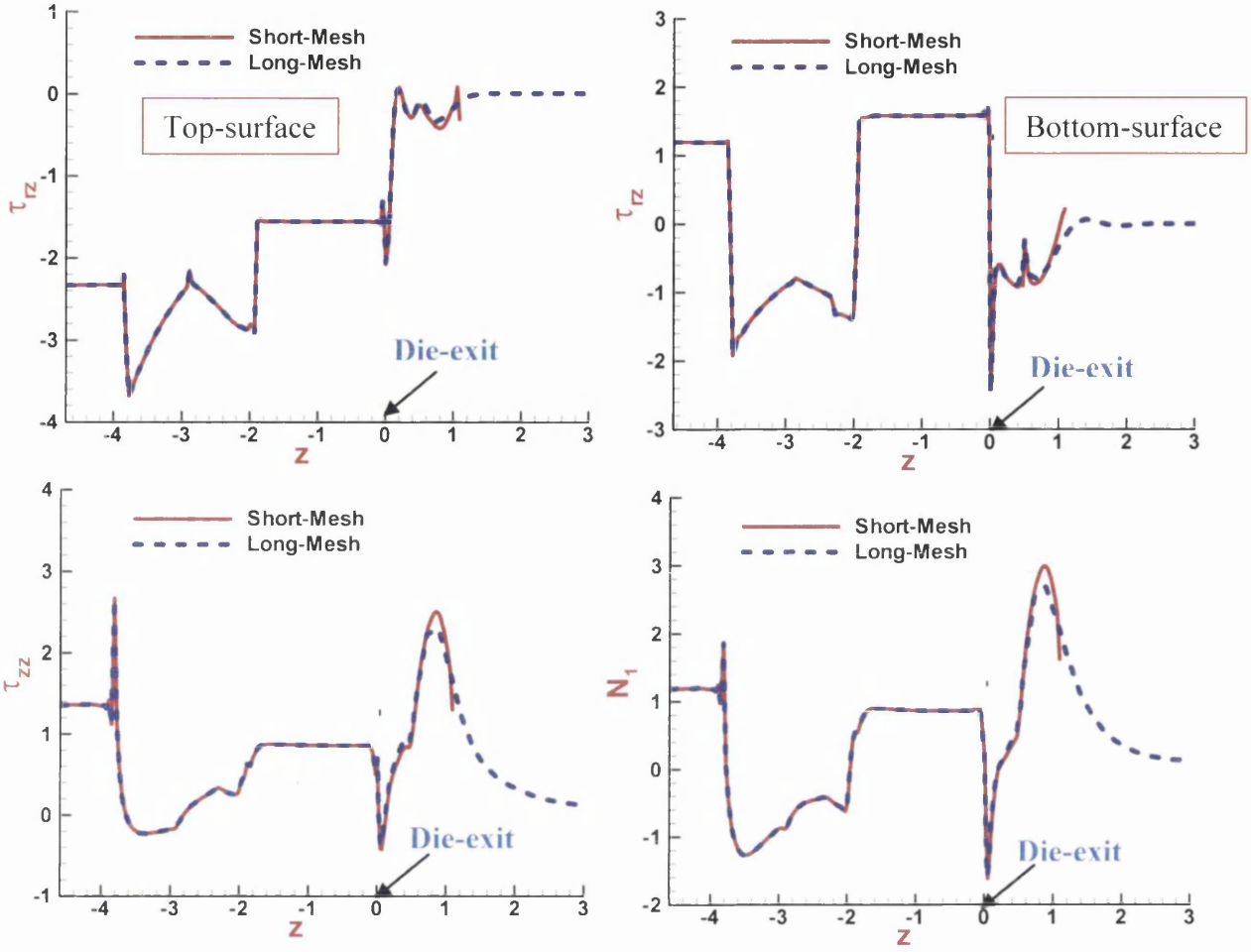

Figure 6.5: τ_{rz}, τ_{zz} and N_1, Short mesh vs Long mesh, EPTT, β=10^{-2}, We=1.0 ε_{EPTT}=0.5, ξ=0.0

6.5.1.2 Pressure-drop profiles

Pressure profiles along the centreline for the EPTT model with different settings of β={10^{-1}, 10^{-2}, 10^{-3}} for We={1,5,10,20} at fixed ε_{EPTT}-value (ε_{EPTT}=0.5) are displayed in Figure 6.6 and Table 6.4.

Table 6.4: Total pressure-drop in units, EPTT, variation in β and We, ξ=0.0

We \ β	10^{-1}	10^{-2}	10^{-3}
1	456.3	233.7	228.1
5	305.8	103.3	66.8
10	281.0	77.5	42.2
20	267.2	62.8	28.5

The pressure profiles reveal a linear decline in pressure throughout the die-inlet section; after which the pressure declines non-linearly over the converging die-section. Subsequently, the pressure falls away linearly within the land region. The shear-thinning behaviour of the EPTT model, with increasing elasticity (*We*) and decreasing solvent-fraction (β), generates a decline in the pressure-drop. As shown in Table 6.4 and for solvent-fraction of $\beta=10^{-3}$, the total pressure-drop reduces nearly by a factor of eight from *We*=1 to *We*=20 (from 228.1 units to 28.5 units). The corresponding reduction factor is almost 3.7 for $\beta=10^{-2}$ (from 233.7 units to 62.8 units), and 1.7 for $\beta=10^{-1}$ (from 456.3 units to 267.2 units). Theoretically in steady shear flow (see Figure 6.2a), by decreasing the solvent-fraction (β) and keeping (ε_{EPTT}, ξ) fixed, the EPTT model thins at high shear-rates and accordingly, will provide a decline in pressure-drop. This is clearly apparent in Table 6.4 at different levels of $\beta=\{10^{-1}, 10^{-2}, 10^{-3}\}$ for any given value of *We*.

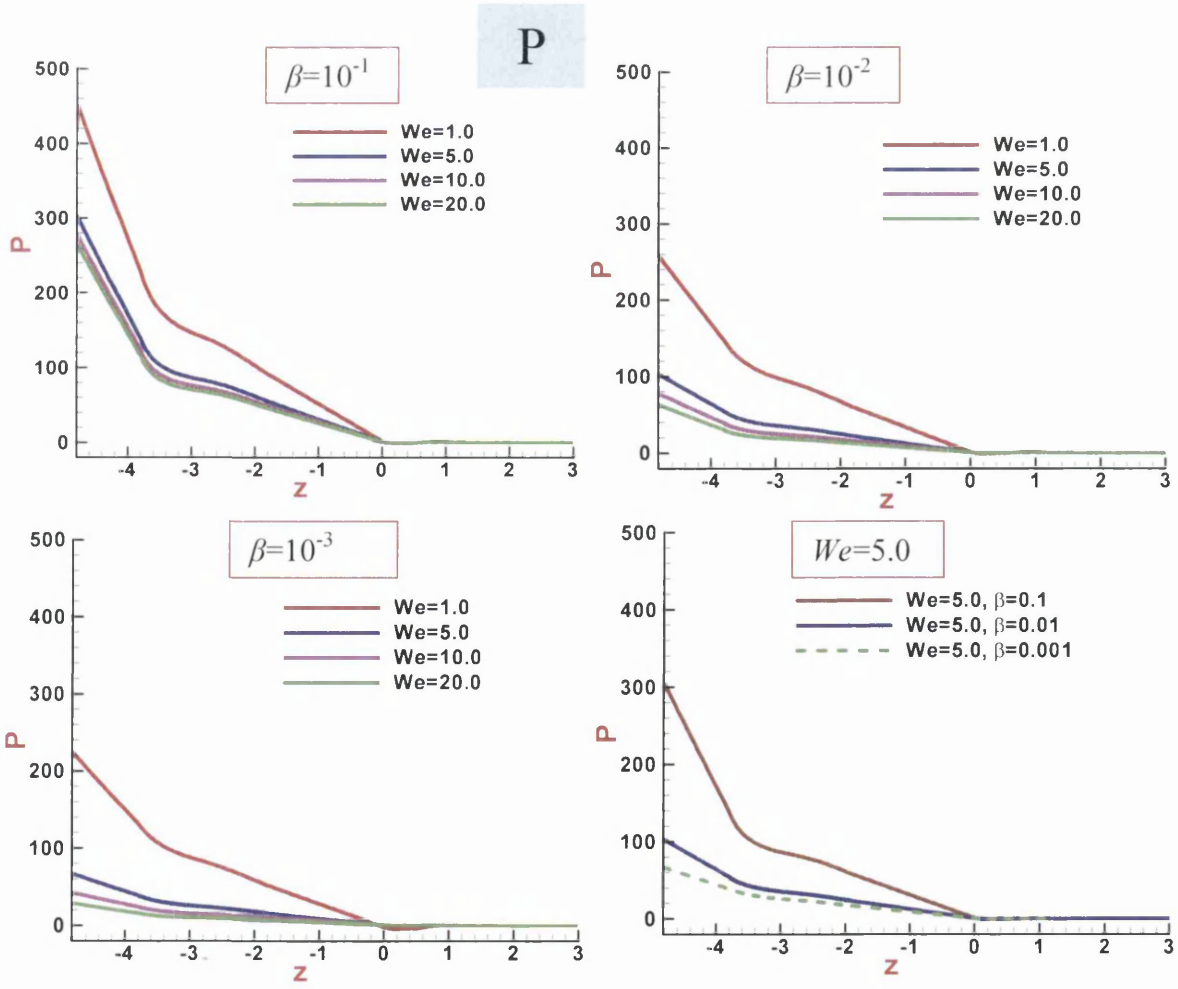

Figure 6.6: Pressure-P, EPTT: β, *We* variation, ε_{EPTT}=0.5, ξ=0.0

6.5.1.3 Stress profiles

Normal stress (τ_{zz}) and first normal stress difference (N_1) profiles along the centreline are plotted in Figure 6.7 for different settings of We=1, 5, 10, 20 and β={10^{-1}, 10^{-2}, 10^{-3}} at fixed ε_{EPTT}-value (ε_{EPTT}=0.5) and ξ=0.0. Here, the general trends and patterns in τ_{zz} and N_1 profiles exhibit a constant value along the inlet-tube followed by a sudden change in normal stress and first normal stress differences with each adjustment in geometry. Subsequently, and as the polymer departs from the die to enter the draw-down section, a sharp decrease within the draw-down is generated. A smaller level of stressing is established with larger values of We, at any given solvent-fraction (β), due to the dominant influence of shear-thinning. Maxima in normal stress (τ_{zz}) and first normal difference (N_1) are located over the draw-down section around the contact point for all values of solvent-viscosity (β) at We=1. Note that, the relative and more significant decrease in τ_{zz} and N_1, is noted as We rises from 1 to 5. There is nearly O(60%) decrease in N_1, when comparing peak draw-down zone values between We=1 to We=5 at the solvent-fraction level of β=10^{-3}, and O(59%) and O(58%) for β=10^{-2} and β=10^{-1}, respectively. The reduction in peak draw-down zone value in N_1 is about O(39%) from We=5 to We=10, and O(37%) from We=10 to We=20 at β=10^{-3}. Once more, this reduction in N_1 is associated with the shear-thinning behaviour of the EPTT model choice and with respect to decreasing the solvent-fraction (β). A further point for discussion, new to this memory fluid approximation, is the stress relaxation phenomenon. Relaxation in tensile stress occurs in the coating flow on the cable and is linked to the relaxation time, for a fixed process time-scale. The rapid decay of normal first normal difference (N_1) for the smaller value of We (shorter relaxation-time) is much more marked, indicating that the stress gradient is much greater in its early spatial development. Here, an increasing value of We from 5 to 10, and 20, has the effect of inhibiting stress decay. The implication is that for larger values of We, longer times (hence, distances) will be required for the stress to decay to an acceptable minimal level.

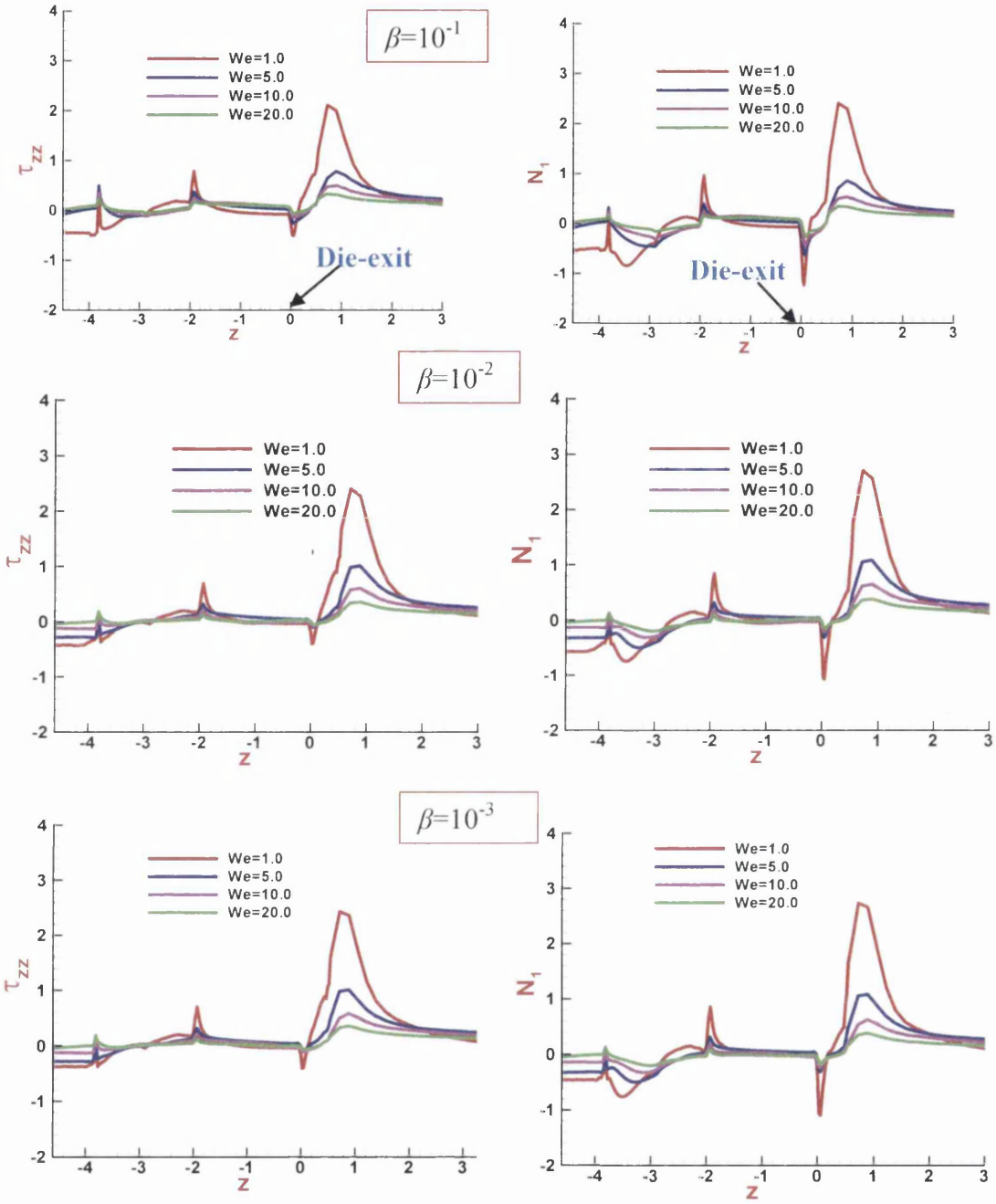

Figure 6.7: τ_{zz} and N_1, EPTT: β, *We* variation, ε_{EPTT}=0.5, ξ=0.0

Tensile normal stresses (τ_{zz} and τ_{rr}) and first normal difference (N_1) profiles are provided in Figure 6.8, again with zoomed draw-down extracts. The effect of τ_{rr} in N_1 is barely significant. From τ_{zz} and τ_{rr} profiles, one may observe that the maximum τ_{zz} value is almost five times larger than the τ_{rr} level. This is clearly apparent in the N_1 profiles, where these follow the same trend as displayed for τ_{zz}.

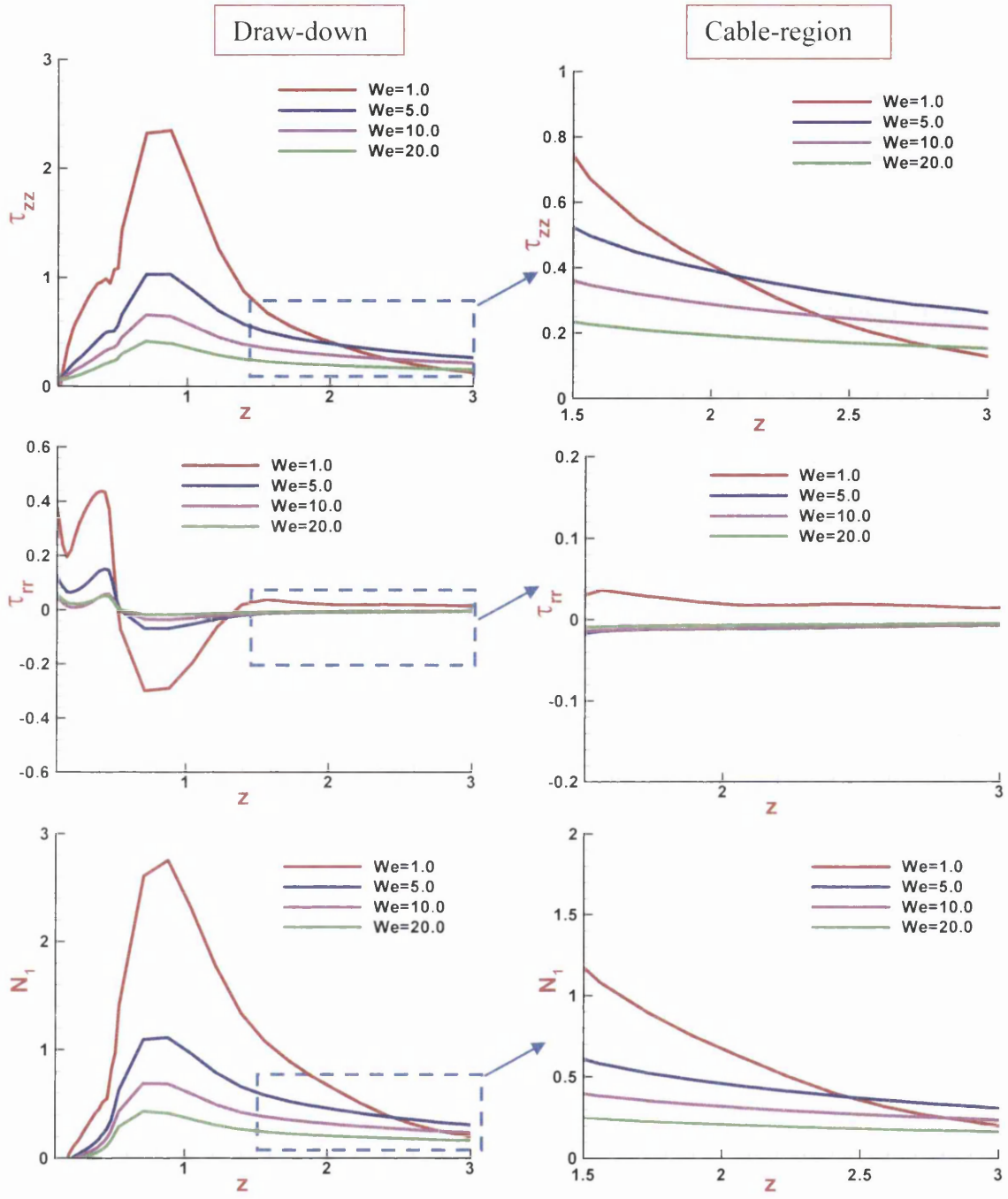

Figure 6.8: τ_{zz},τ_{rr} and N_1, EPTT: *We* variation, β=10^{-3}, ε_{EPTT}=0.5 , ξ =0.0

The influence of solvent-fraction (β) on profiles of normal stress (τ_{zz}) and first normal stress-difference (N_1) is shown in Figure 6.9, covering different levels of elasticity. In all such instances, the dominance of shear-thinning leads to a stress-ratio decrease as the Weissenberg number (*We*) increases (the levels of draw-down zone peaks for τ_{zz} profiles are 2.3, 1.0, 0.7, and 0.4 units for *We*=1, 5, 10, and 20, respectively). In addition, larger values of τ_{zz} and N_1 in the die-section are generated for

β=10^{-1}, in comparison to β=10^{-2} and 10^{-3}. One also notes that β=10^{-1} exhibits slightly smaller values for τ_{zz} and N_1 in the draw-down section after the contact point.

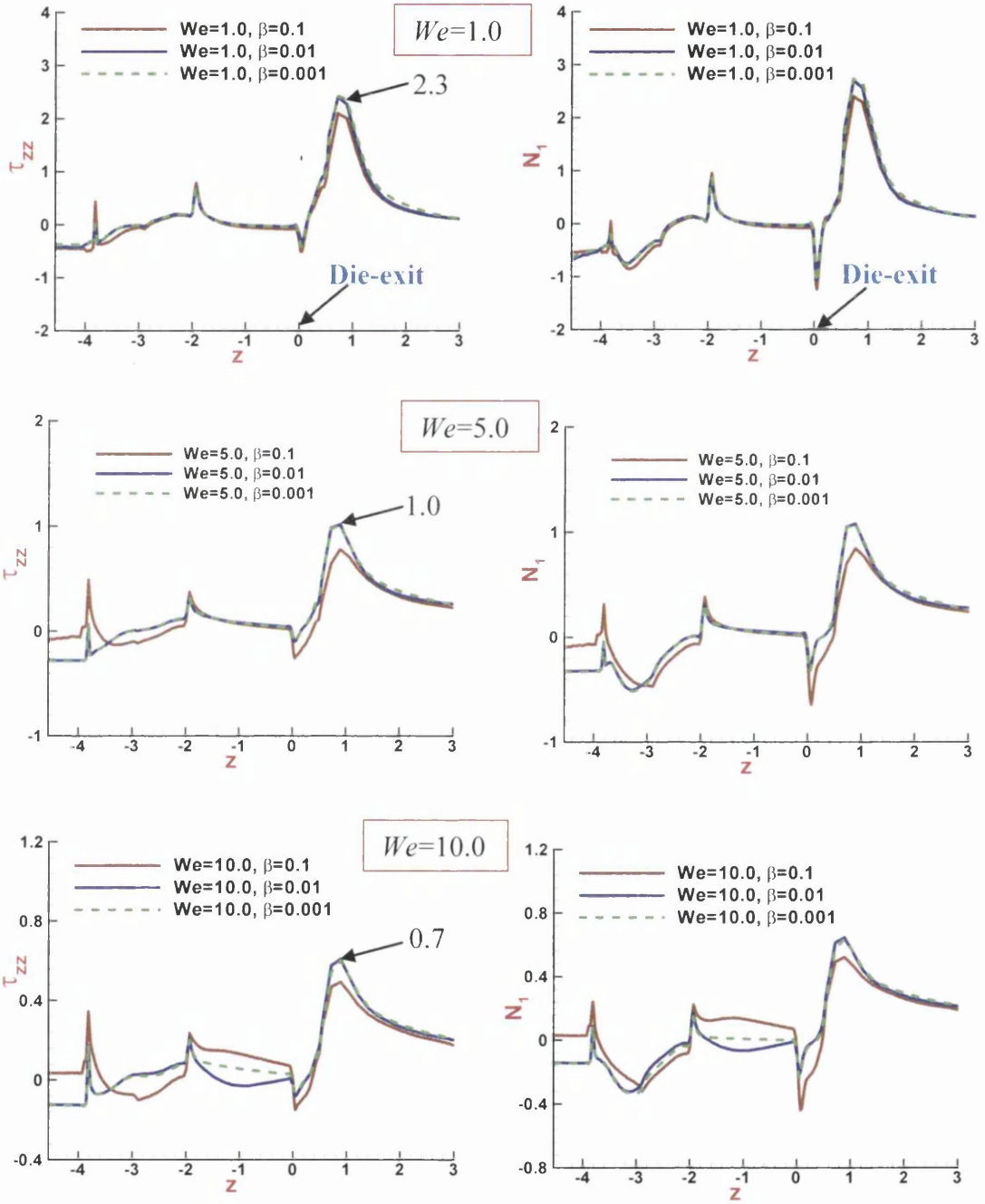

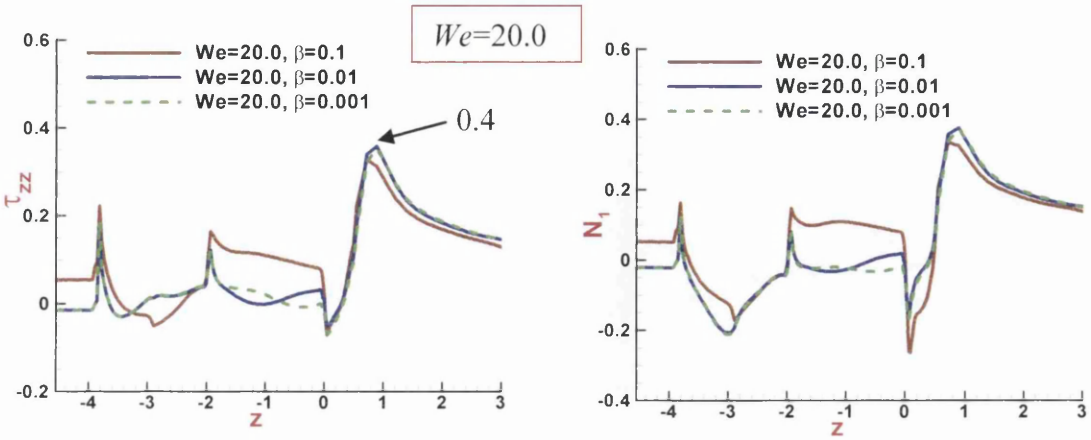

Figure 6.9: τ_{zz} and N_1, EPTT: β, We variation, ε_{EPTT}=0.5, ξ=0.0

Furthermore to consider the shear flow zones, component shear stress (τ_{rz}) profiles along the top (outer) and bottom (inner) surfaces are provided, at the same settings as normal stress (τ_{zz}) above. Here again, sudden change occurs in shear stress with each adjustment in geometry, noticeably for We=1 (see Figure 6.10). There are changes of sign in τ_{rz} observed between both top and bottom surfaces. The bottom-surface shear-stress profile demonstrates most clearly, the localised effect of the die-exit point discontinuity. A violent jump in shear stress is observed over the land region. These are held at levels that much reduce across the elasticity values of We=1 to We=5, 10, and 20. One may observe that the maximum positive level of shear stress (about 3 units) is attained for We=1 on the inner-wall around the contact point. For We=5, 10, and 20, some slight shearing arises over the draw-down region (extrudate). An acceptable plug flow then emerges over the cable region, where the shear stress is practically fully relaxed at all parameter settings.

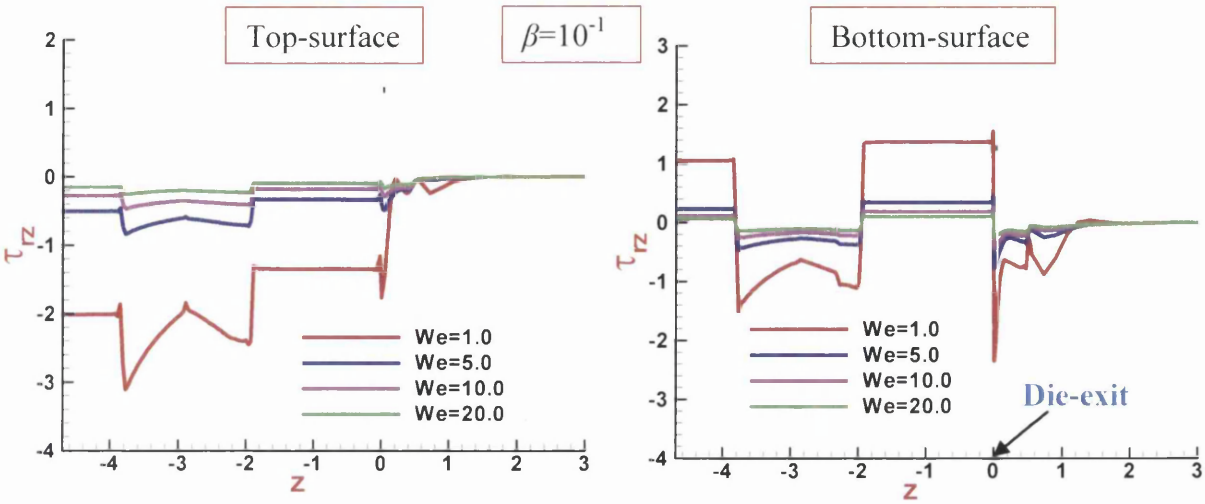

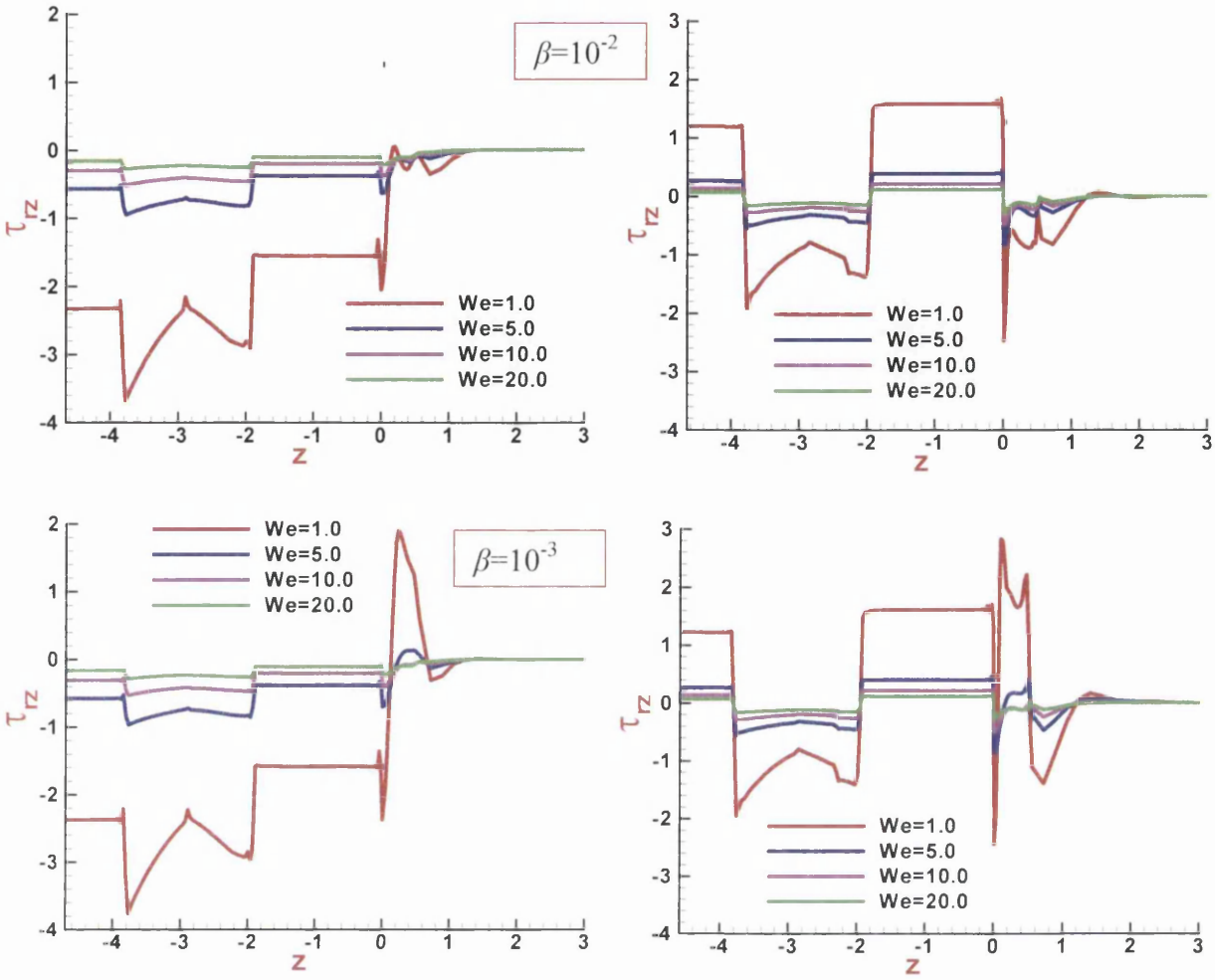

Figure 6.10: Shear stress-τ_{rz}, EPTT: β, *We* variation, ε_{Eptt}=0.5, ξ=0.0

6.5.1.4 Shear and strain-rate profiles

In addition, shear-rate (gamma) (Γ) profiles along the top and bottom surfaces, are shown in the axial direction (Figure 6.11) for different solvent-fraction (β) and elasticity (*We*). Shear and strain-rates are important measurable quantities that describe the state of flow deformation and, according to the ranges encountered, may explain the polymeric response under the different flow scenarios. Throughout the converging section, there is a sharp drop in shear-rate, reaching a minimum over its middle section. Beyond the die-exit, once entering the draw-down flow, a sharp drop in shear-rate is noted. Similar behaviour is observed in both top and bottom surface shear-rate profiles. There is only a gradual decrease in shear-rate over the draw-down section, followed by a sharp decline when the polymer meets the cable. Travelling with the cable, the rate of decrease in shear-rates is minimal. Through the land region, the degree of shearing adopts a constant plateau. At the end of the die-inlet, solvent-fractions $\beta=10^{-2}$ and $\beta=10^{-3}$

generate the largest maximum Γ-level of about 62 and 53 units for bottom and top surfaces, respectively. For β=10^{-1}, a similar trend is observed as with β=10^{-2} and β=10^{-3}, in both top and bottom surface shear-rate profiles throughout the die-section, but observing lower shear-rate values. This is true for all Weissenberg number (*We*), although the level of shear-rate declines as *We* increases from *We*=1 to 5, and 20, again due to dominant shear-thinning.

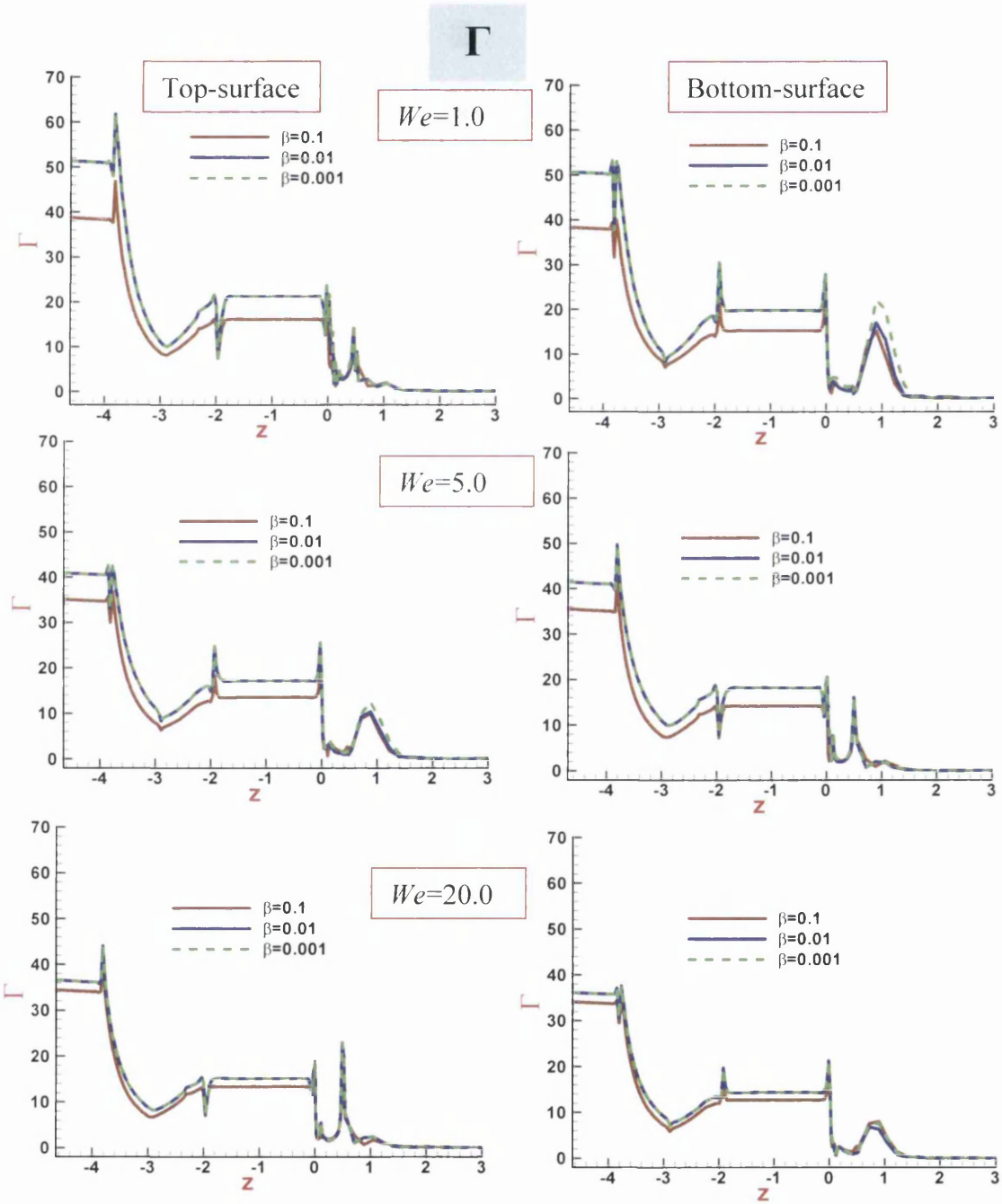

Figure 6.11: Shear-rate (Γ) profiles: EPTT, β variation, ε_{EPTT}=0.5; *We*=1,5, 20, ξ=0.0

For contrast, flow-centreline profiles of strain-rate (Σ) are shown in Figure 6.12 (see Figure 6.9 for corresponding normal stress, τ_{zz}). The profiles for Σ along the axial direction show sharp adjustments as the flow negotiates transition throughout the geometry. Maxima in the strain-rate are observed near the melt-cable contact-point for the various levels of solvent-fraction (β) and elasticity (We). Strain-rates reached in the die-section are about 0.5 units, almost half of that observed in the draw-down section.

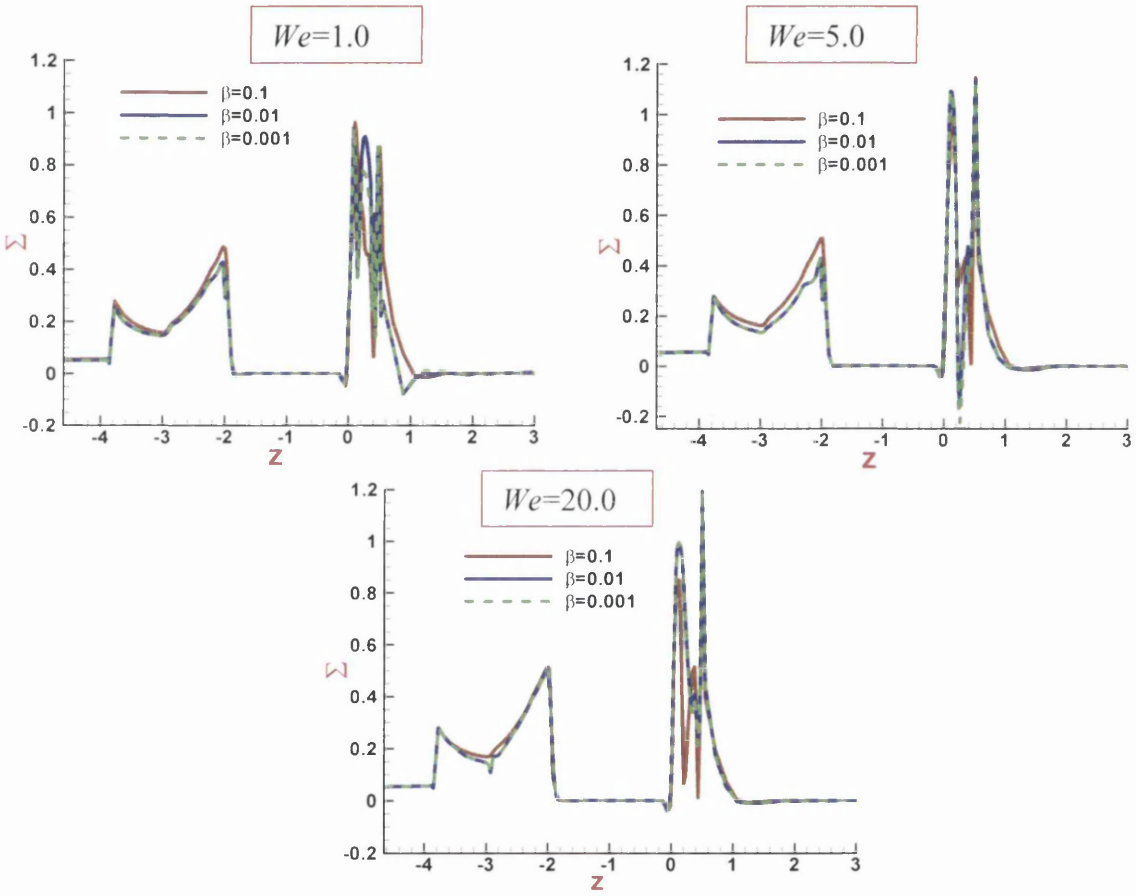

Figure 6.12: Strain-rate (Σ) profiles: EPTT, β variation, ε_{EPTT} =0.5; We=1,5,20, ξ=0.0

6.5.1.5 Field plots, pressure (p), normal stress (τ_{zz}), and shear stress (τ_{rz})

Comparative pressure fields are provided in Figure 6.13, over the whole domain for three different levels of solvent-fraction β=10^{-1}, 10^{-2}, and 10^{-3} at We=5. Here, greatest concentration of pressure drop is noted across the die-entry section (narrowest width of die). At the draw-down and coating regions, the pressure holds to an ambient level. The most important rate of change in pressure-drop arises across the land-region (see also pressure-drop profiles in Figure 6.6). As to be anticipated, the pressure-drop is most prominent across the tube-die. From these fields, one can observe a distinct level of

pressure rise along the inlet-tube with increase of solvent-fractions (maximum pressure level of $O(306)$, $O(103)$, and $O(67)$ for $\beta=10^{-1}$, 10^{-2}, and 10^{-3}, respectively).

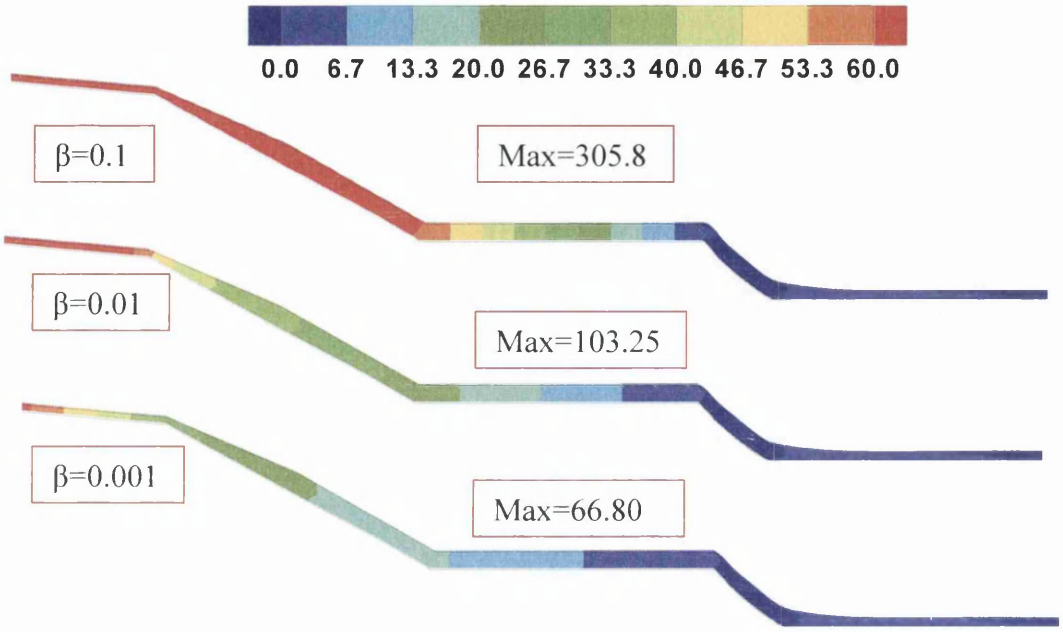

Figure 6.13: Pressure-P, EPTT: β variation, fixed We=5 and ε_{EPTT}=0.5, ξ=0.0

Field plots on the normal stress component for We= 1, 5, 10, and 20 at fixed ε_{EPTT}-value (ε_{EPTT}=0.5) and $\beta=10^{-3}$ of Figure 6.14 illustrate the shear-thinning behaviour of the EPTT model, that (τ_{zz}, We=1) in maxima is almost 3.7, 6.7, and 12.5 times larger than the (τ_{zz}, We=5), (τ_{zz}, We=10), (τ_{zz}, We=20), respectively. In this annular flow, the maximum value of the normal stress emerges at the lower and upper die-wall boundaries. The maximum τ_{zz}-value in draw-down and cable-coating flow sections for We=1 is in the order of 2.1, 3.3, and 5.6 times larger than the τ_{zz}-values for We=5, 10, and 20, respectively.

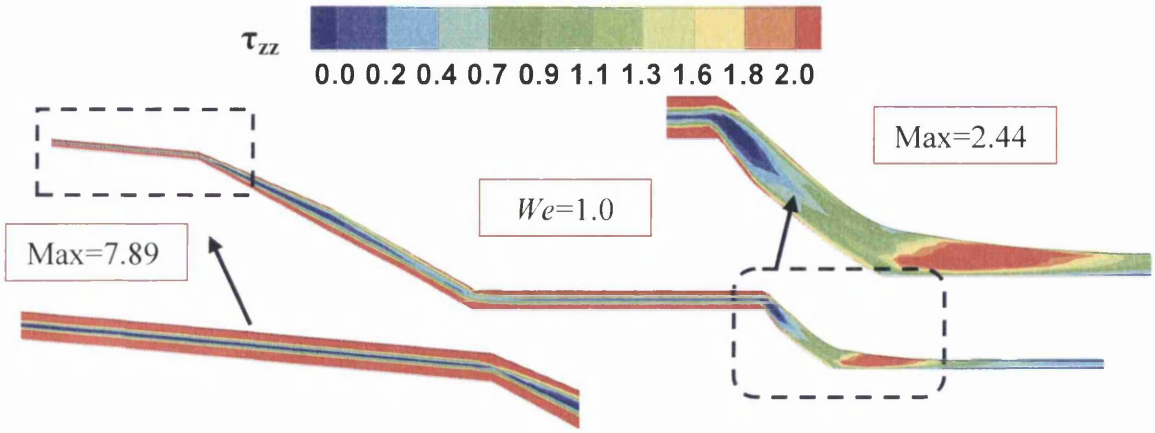

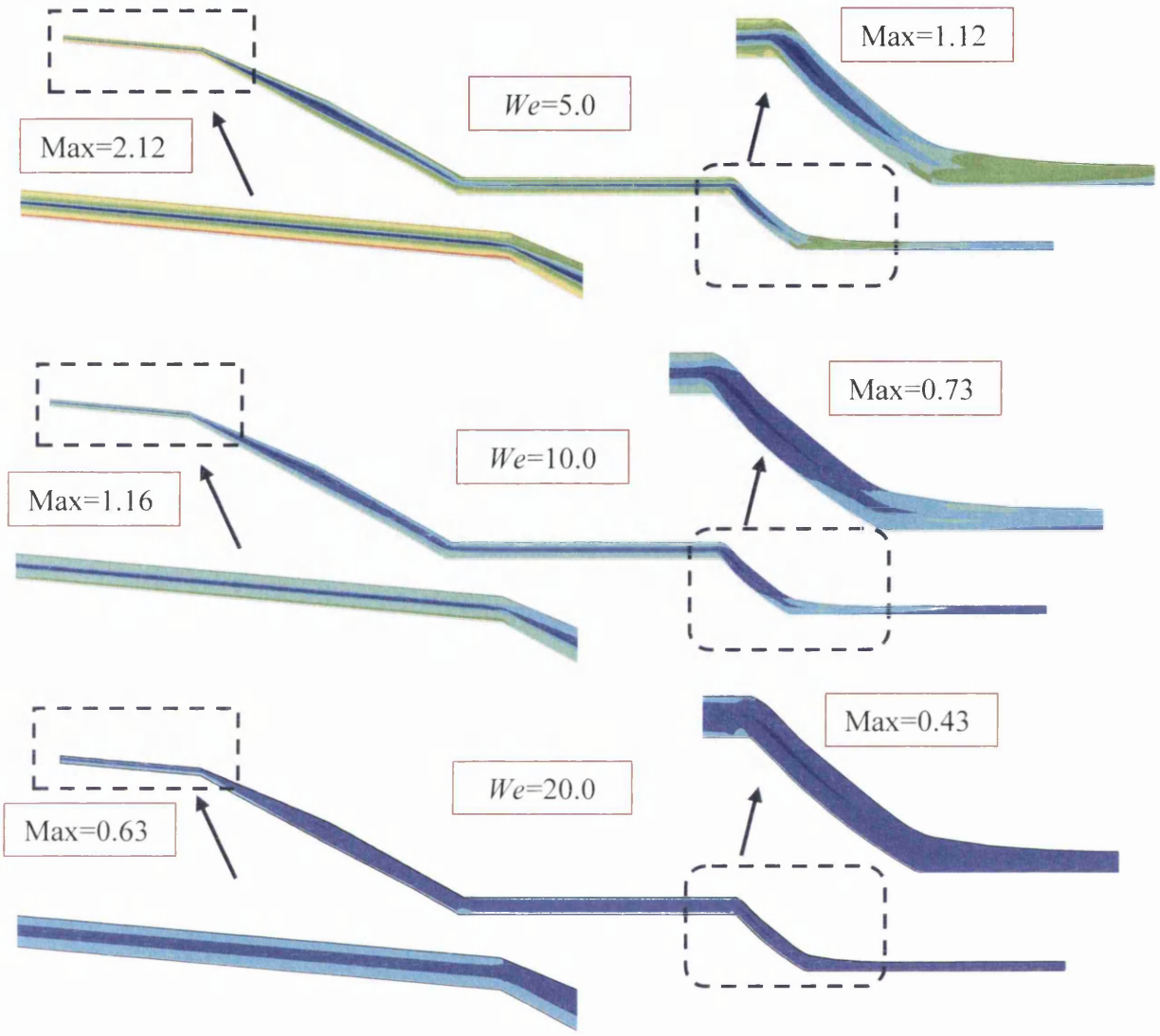

Figure 6.14: Normal stress-τ_{zz}, EPTT: *We* variation, fixed $\beta=10^{-3}$,$\varepsilon_{EPTT}=0.5$, $\xi=0.0$

In comparison, shear-stress τ_{rz} field plots are presented in Figure 6.15. Again, the maximum shear-stress level attained is shown to decrease with increasing *We*. Increasing the level of elasticity (*We*) has had less impact on shear-stress (τ_{rz}) levels than on normal stress (τ_{zz}) levels. A quantitative summary of data-maxima is provided in tabular form in Table 6.5, covering values of pressure (P), normal stresses (τ_{rr}, τ_{zz}), and shear-stress (τ_{rz}) components for different levels of solvent-fraction ($\beta=10^{-1}$, 10^{-2}, 10^{-3}) and elasticity (*We*=1, 5, 10, 20). This comparative data emphasizes the major stress solution shifts between *We*=1 and *We*={5, 10, 20}; also the minor adjustments apparent with β-shift over $\{10^{-2}, 10^{-3}\}$.

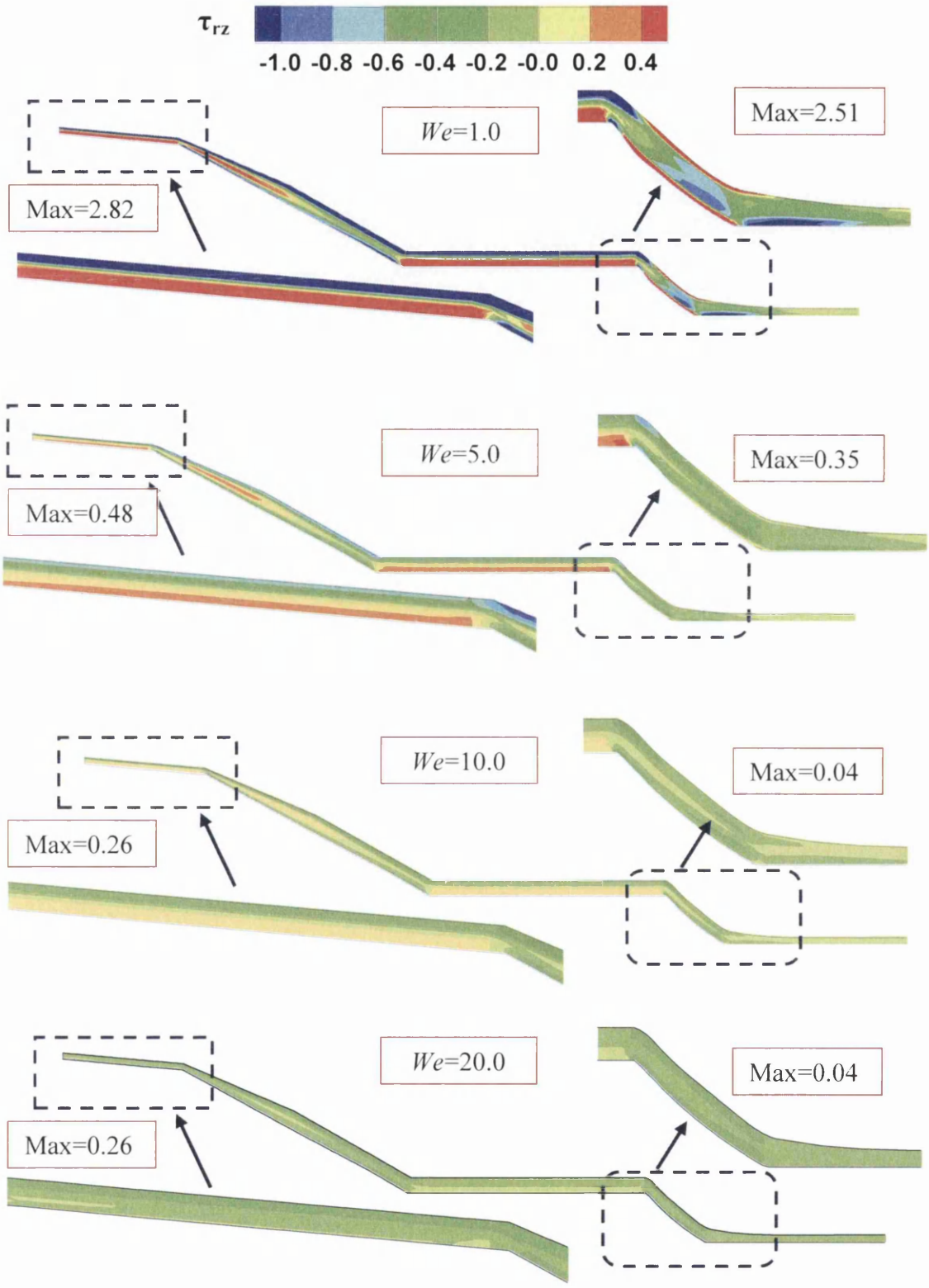

Figure 6.15: Shear stress-τ_{rz}, EPTT: *We* variation, fixed $\beta=10^{-3}$, $\varepsilon_{EPTT}=0.5$, $\xi=0.0$

Table 6.5: Stress and pressure, EPTT: β, *We* variation, ε_{EPTT}=0.5, ξ=0.0

$\beta=10^{-1}$

solutions	*We*=1.0	*We*=5.0	*We*=10	*We*=20
Max p	456.25	305.84	280.94	267.15
Max τ_{rr}	2.34	0.81	0.52	0.31
Max τ_{rz}	1.54	0.44	0.25	0.14
Max τ_{zz}	6.30	1.76	0.98	0.55

$\beta=10^{-2}$

solutions	*We*=1.0	*We*=5.0	*We*=10	*We*=20
Max p	233.71	103.25	77.45	62.83
Max τ_{rr}	2.66	0.76	0.45	0.26
Max τ_{rz}	1.74	0.47	0.23	0.14
Max τ_{zz}	7.86	2.05	1.10	0.61

$\beta=10^{-3}$

solutions	*We*=1.0	*We*=5.0	*We*=10	*We*=20
Max p	228.05	66.80	42.22	28.46
Max τ_{rz}	5.74	0.76	0.51	0.27
Max τ_{rz}	2.82	0.48	0.26	0.14
Max τ_{zz}	7.90	2.12	1.16	0.63

6.5.2 ξ-variation (non-zero N_2), variations in β and We

Effect of second normal-stress difference (parameter ξ)

In this section, the effect of second normal stress differences (N_2) upon field response is analysed, in addition to the dominant effect of the first normal stress difference (N_1). Recall that in pure shear flow and with the PTT model, an increase in ξ proportionally reduces N_1, and mildly increases N_2 (see Figure 6.3). Values of ξ larger than 0.2 (N_2/N_1=20%) lead to numerical convergence difficulties, onset by the well-known Gordon-Schowalter instability (demonstrated in shear through the non-

monotonic nature of the shear stress-shear rate relationship). Fortunately, values of (N_2/N_1) rarely exceed 0.2 (20%) and more often physically do not exceed 0.1 (10%).

6.5.2.1 Pressure-drop profiles

EPTT-pressure profiles along the centreline with different settings of β={10^{-1}, 10^{-2}, 10^{-3}} and We={1, 5, 10, 20} at fixed ε_{EPTT}-value (ε_{EPTT}=0.5) are displayed in Figure 6.16. Overall, due to non-zero second normal stress difference (ξ=0.15), we observe a reduction in the pressure-drop. For example, the pressure-drop for {β=10^{-3}, We=1.0, ξ = 0.15} is 145.44 units compared to 228.05 units for the {β=10^{-3}, We=1.0, ξ = 0.0}. Almost 36% reduction in pressure-drop is observed at this low level of solvent-fraction (β=10^{-3}).

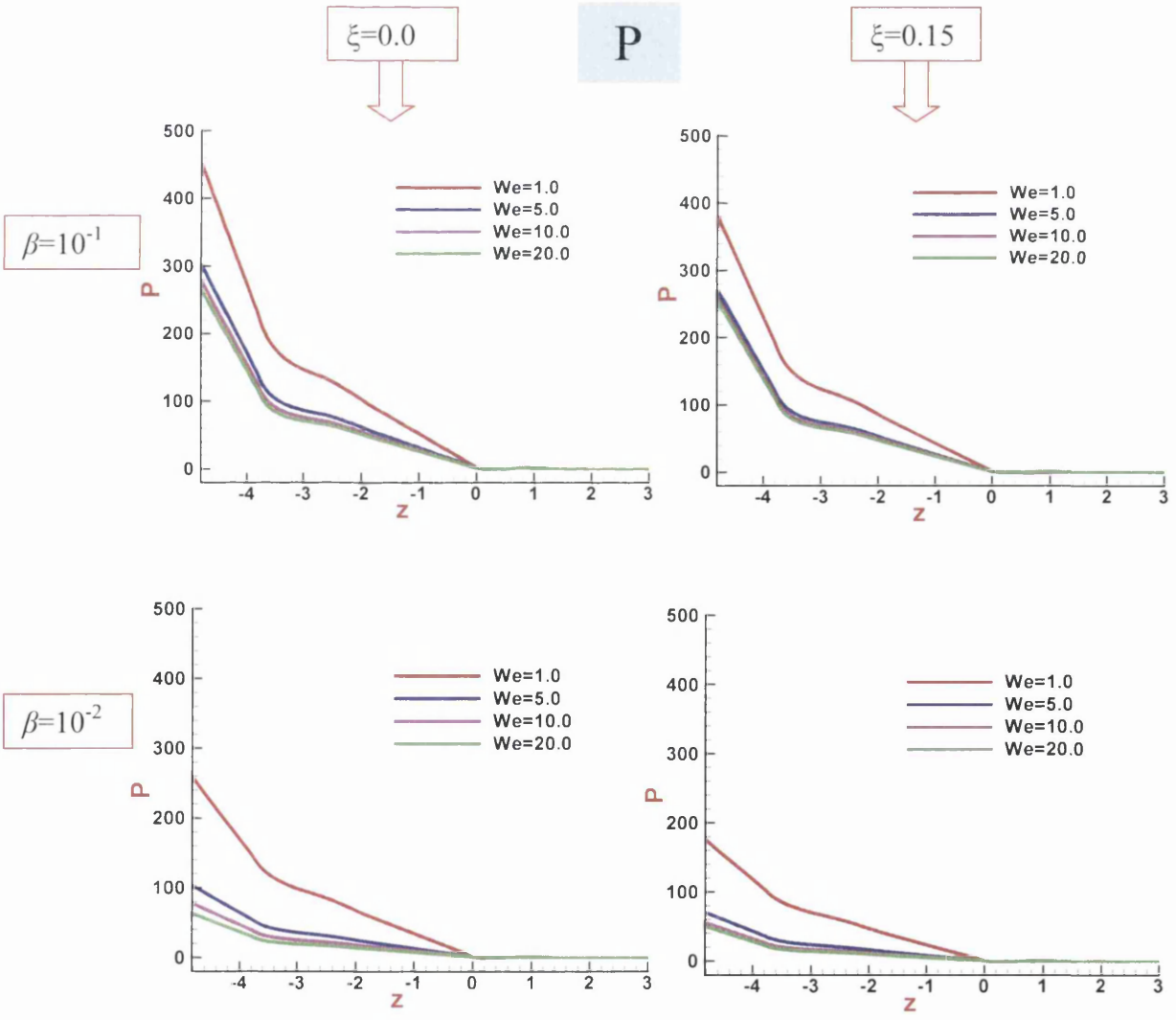

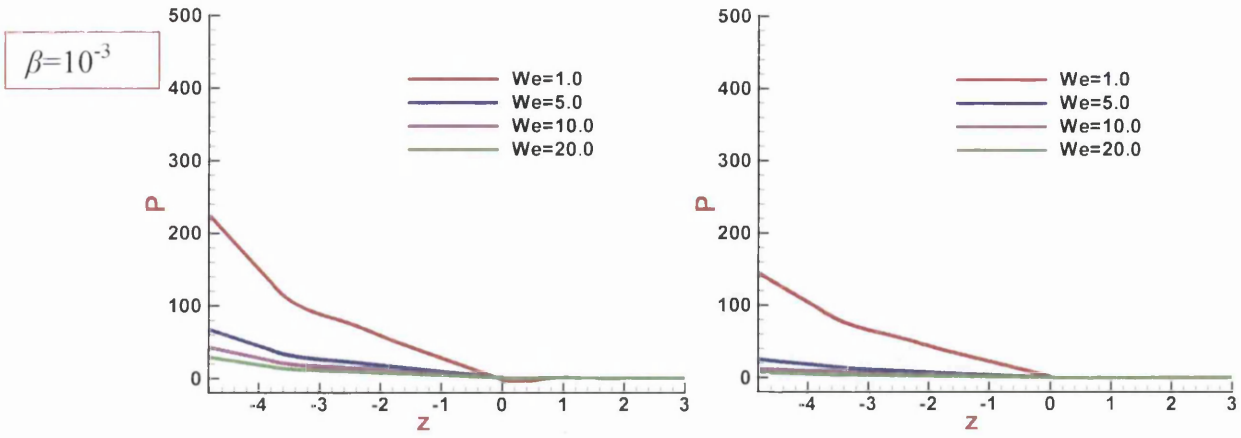

Figure 6.16: Pressure-P, EPTT: β, We, ξ variation, ε_{EPTT}=0.5

6.5.2.2 Shear-stress profiles

Figure 6.17 represents the τ_{rz}-profiles for EPTT{β=10^{-3}, We, ξ, ε_{EPTT}=0.5}, covering both outer and inner surfaces with {$0 \le \xi \le 0.15$, $1 \le We \le 20$}. Here, profiles are similar over top and bottom surfaces with ξ_{EPTT}-variation, differing only around singularities and die-design adjustments. At each level of elasticity (We), there are major features noted within the shear flow and the die. Here, smaller levels in τ_{rz}-stress are observed as ξ_{EPTT}-value increases. This may be associated with the material properties of the EPTT model in steady shear flow, where the model shows greater tendency to thin with increase in the ξ_{EPTT}-value, whilst maintaining fixed (ε_{EPTT}, β) (Figure 6.2(a,b)).

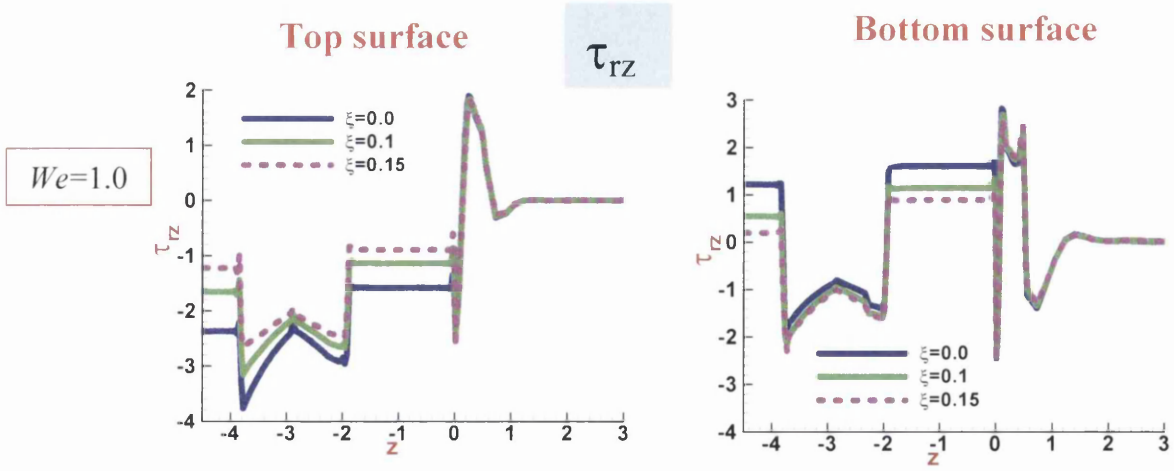

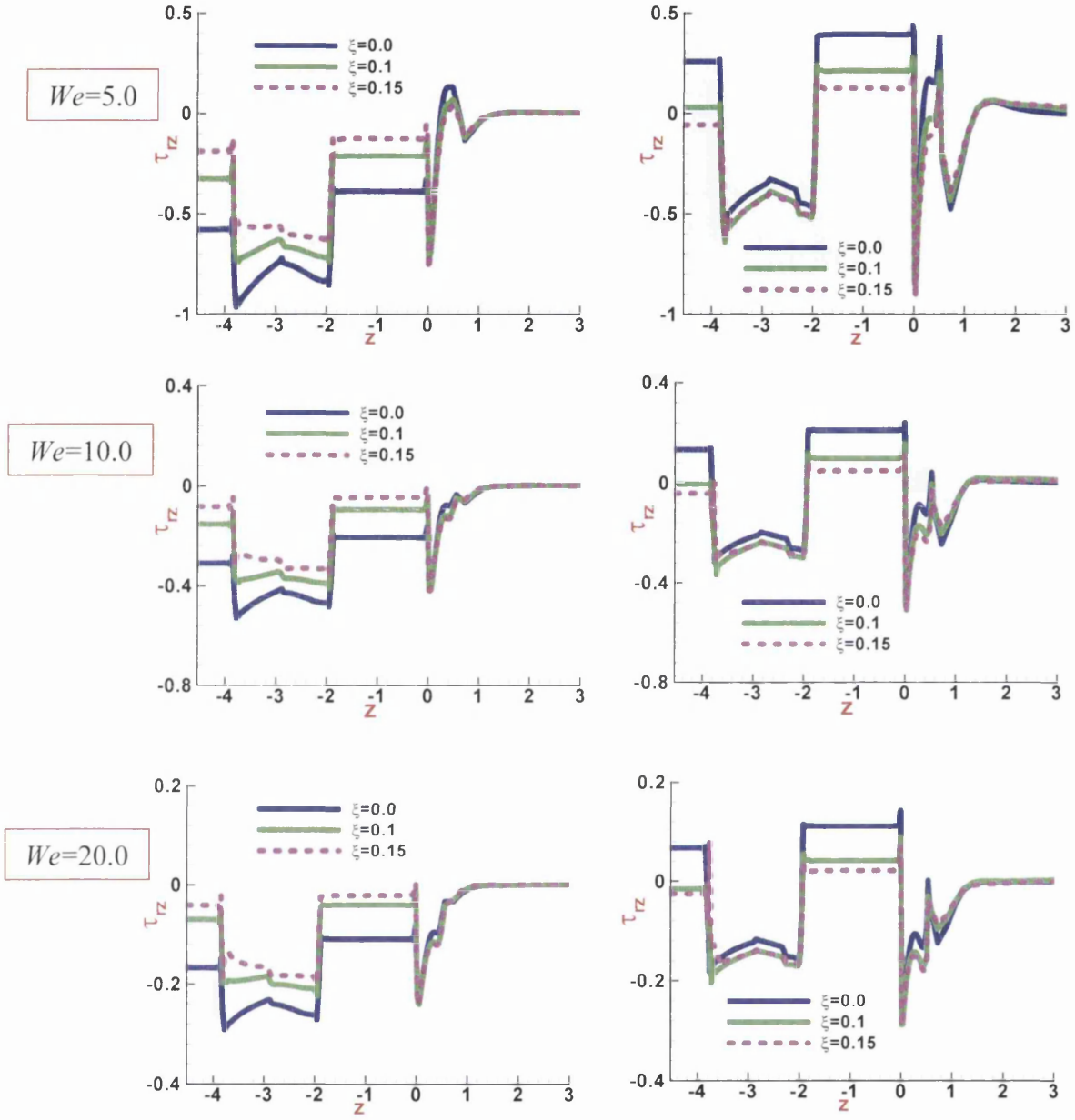

Figure 6.17: Shear stress profiles EPTT, $\{We,\xi\}$–*variation*, $\beta=10^{-3}$, $\varepsilon_{EPTT}=0.5$

6.5.2.3 Normal-stress profiles

The corresponding position in normal stress τ_{zz}-profiles throughout the geometry centreline is conveyed in Figure 6.18; with the zoomed views of full DDS and coating section. Firstly, considering solution variation with increase in ξ-value; from the full geometry more-global viewpoint, little distinction may be drawn *at each individual We-level*. In the DDS of Figure 6.18 this is also true, in general noting slight reduction in stressing around the contact point for larger ξ-value.

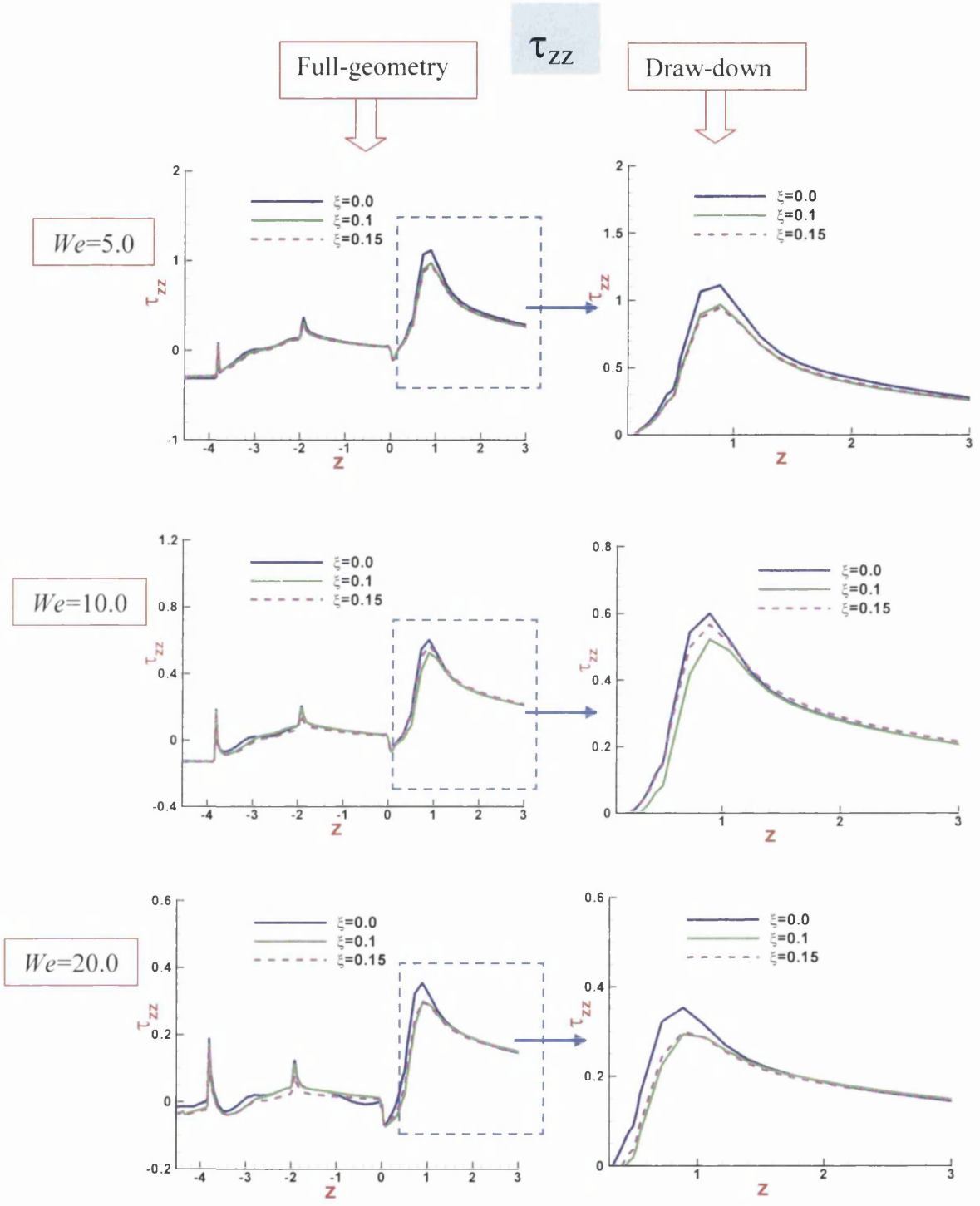

Figure 6.18: normal stress (τ_{zz}), $\beta=10^{-3}$, We, ξ variation, $\varepsilon_{EPTT}=0.5$

The position is summarised in normal stress profiles for $\{\xi=0.15, \beta=10^{-3}\}$, through Figure 6.19, which reflect full N_1 and individual source component τ_{zz} and τ_{rr}-stress profiles; Figure 6.19a covers the full geometry-centreline, Figure 6.19b its DDS zoom, and Figure 6.19c its DDS outer-surface zoom. This additional data provides insight as to the zonal localisation and relative strength and importance of τ_{rr}-stress in the overall

normal stress generated. Within the die, N_1 is dominated by τ_{zz}-stress, being predominantly shearing flow. In the DDS, from We=1 to We=20 one might identify that τ_{zz}-stress and τ_{rr}-stress decline (2.3 to 0.4 (O(82%) units; and 0.4 to 0.05 (O(88%) units, respectively). Moreover, τ_{rr} may be seen to be of around O(20%), O(15%), O(10%), and O(13%) of τ_{zz} for We=1, 5, 10, and 20, respectively; and hence amplifies the overall levels of N_1 generated there (the impact of τ_{rr} on N_1 is barely significant). In addition, the second normal stress difference effects (via τ_{rr}) contribute slight mitigation to the first normal stress difference level.

The elastic effects and first normal stress difference (N_1) comparison between the various We-mode solutions, We={1, 5, 10, 20}, are shown in Figure 6.19 for the full geometry-centreline, and its draw-down section zoom at ξ=0.15. N_1 peak draw-down zone value at We=1 is 2.6 units, whilst this reduces to 1.03, 0.6 and 0.3 units for We=5, We=10 and We=20, respectively. At the exit, the N_1 residual stress value undergoes a relatively sharp decay reaching 0.28 units for We=5 (almost 73% drop from its peak-level). In contrast, the residual-stress level of 0.2 units for We=20 indicates the relatively slow decay for this higher level of elasticity (almost 30% drop from its peak-level) when compared to values for the We=5 solution (for residual stressing, see Figure 6.19c).

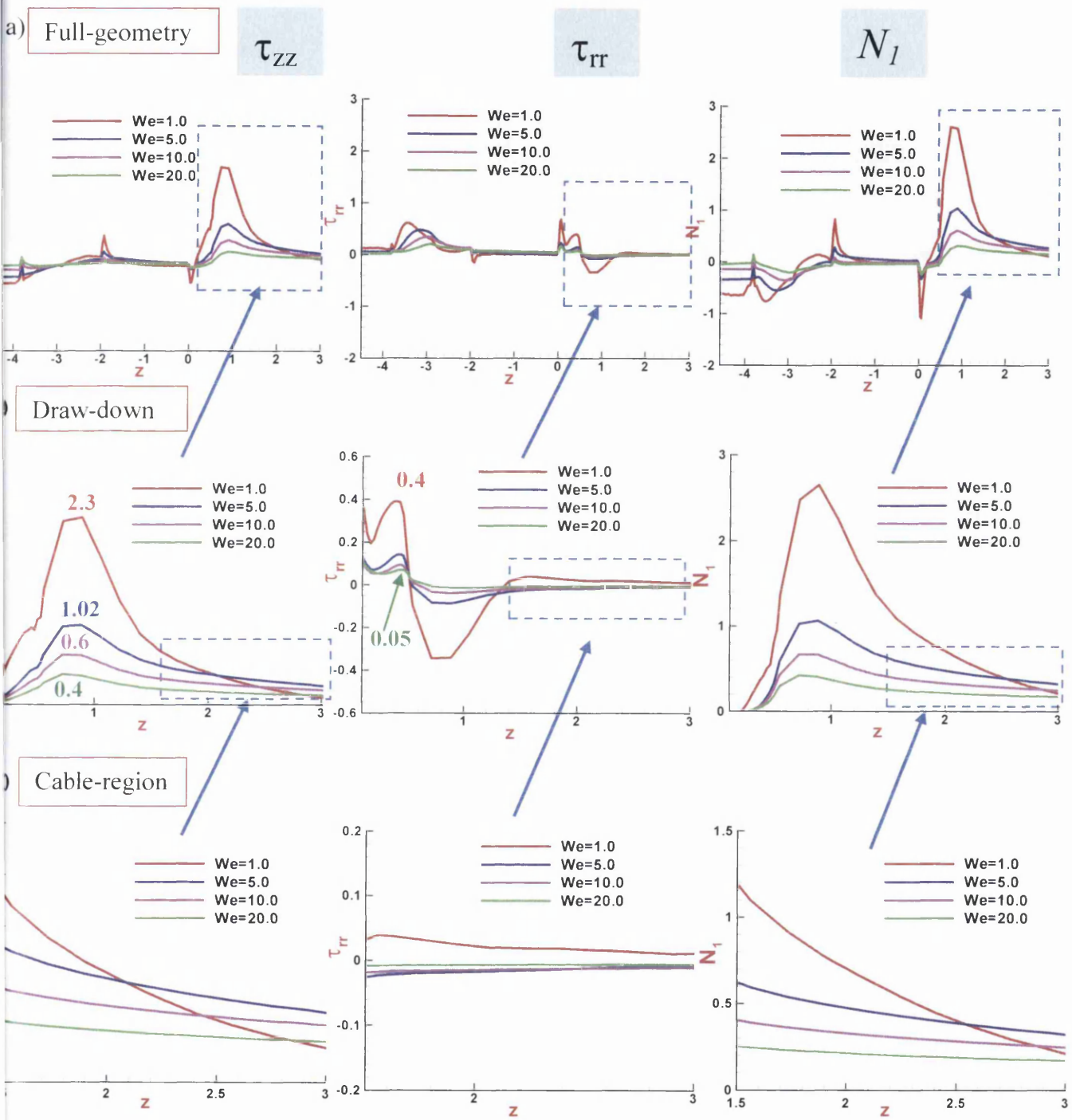

Figure 6.19: Normal stress (τ_{zz}), radial stress (τ_{rr}) and First normal stress difference (N_1), β=10^{-3}, ε_{EPTT}=0.5, ξ =0.15

Figure 6.20, combines a direct comparison for decreasing β-solvent fractions {10^{-1},10^{-2}, 10^{-3}} solutions over N_1-profile data, at each separate We-level running through {1, 5,

10, 20}. This data is restricted to DDS zones, and along the centreline. From this information, one can detect that solution data with $\beta=10^{-2}$ is faithful in trend and a close guide therefore to that at $\beta=10^{-3}$; particularly so for $We<20$. Trends are upheld cross-stream, noting the exaggerated undershoot in the $\{We=1, \beta=10^{-3}\}$ solution.

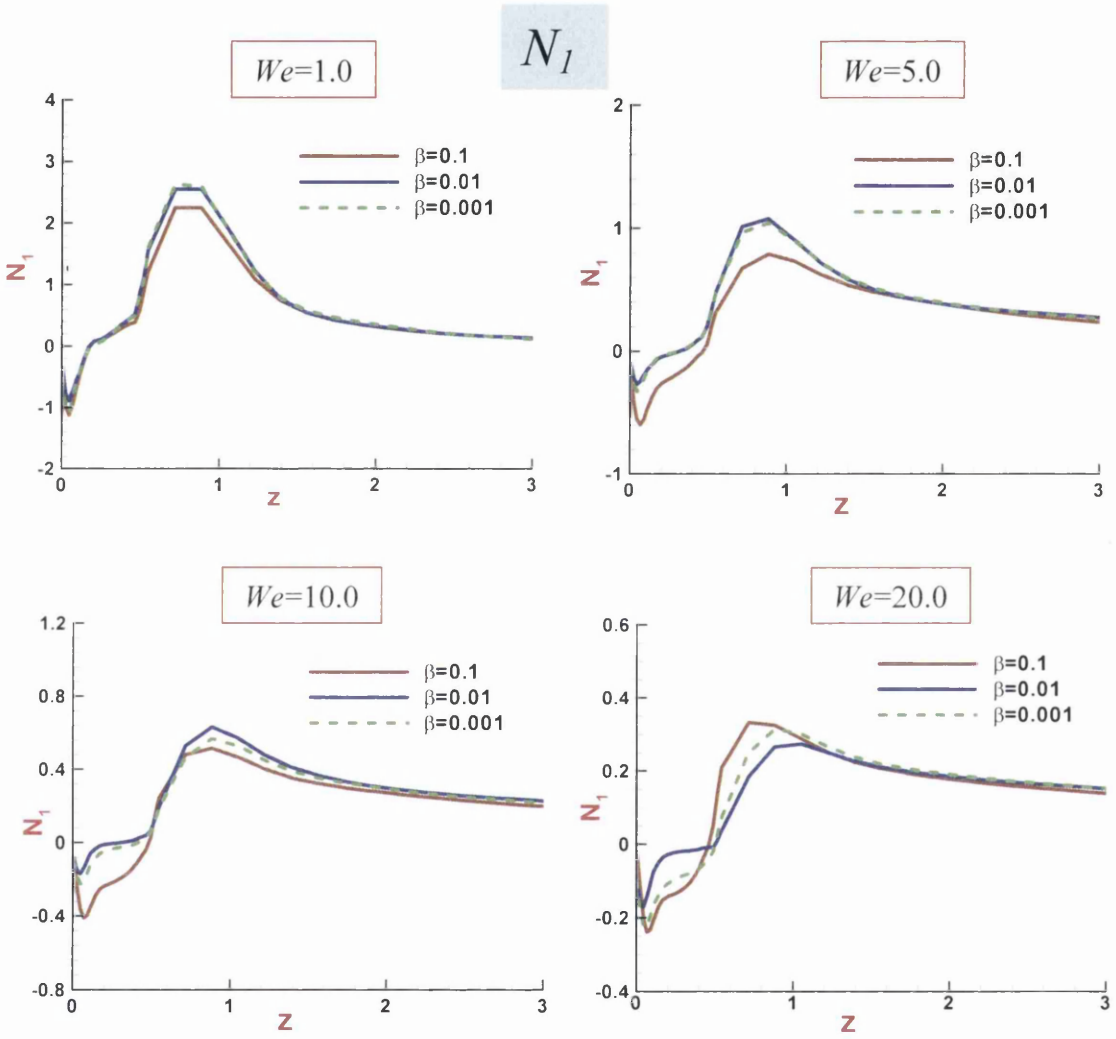

Figure 6.20: First normal stress difference ($N1$), EPTT: β, We variation, $\varepsilon_{EPTT}=0.5$, $\xi=0.15$

In order to investigate the residual stress across the cable region, velocity gradient ($du_r dr$) and first normal stress (N_1) profiles are shown at six different cross section positions in Figures 21 and 22 for EPTT($\xi=0.15$, $\varepsilon_{EPTT}=0.5$, $\beta=10^{-2}$). Overall, one can detect significant variations in both $du_r dr$ and N_1 in the positions of 6, 5, and 4 for different level of elasticity of $We=1$, 5, and 10. This is clearly apparent in the vicinity of the contact point at position 6 with relatively more changes in velocity gradient ($du_r du$) and first normal stress difference (N_1) in comparison with $du_r dr$ and N_1 at

positions 5 and 4. A sharp decrease in the first normal stress-difference and velocity gradient ($du_r du$) over a small distance from the position 4 to position 3 is observed. The gradient practically vanishes as one approaches the exit region that is sustained over successive stations (positions 5 and 6). Here, one can also observe a notable reduction in the levels of residual stress N_1 in last station (position 1) of the cable region of about $O(92\%)$, $O(75\%)$ and $O(70\%)$ in comparison to N_1 in position 6 for We=1, 5,10 respectively. In addition and for any level of elasticity (We=1, 5, 10) at positions 3 to 6, the vertical variation in velocity gradient ($du_r dr$) and first normal stress (N_1) is especially significant from top to bottom surfaces due to the influence of two different settings of the boundary conditions imposed on theses surfaces.

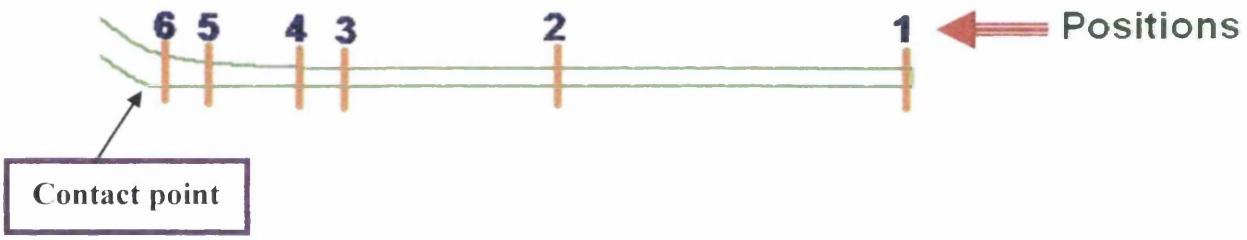

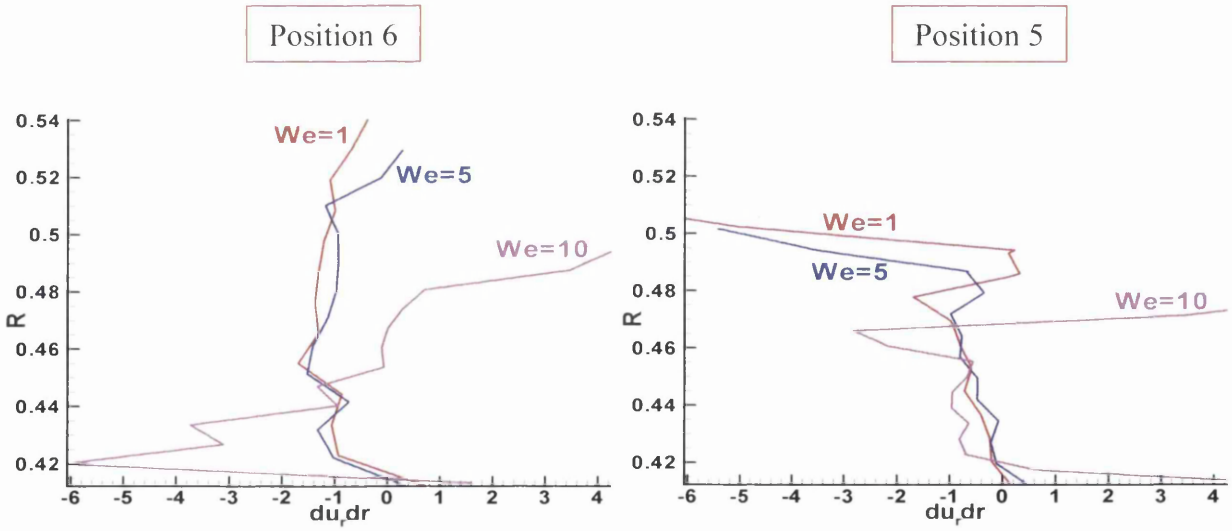

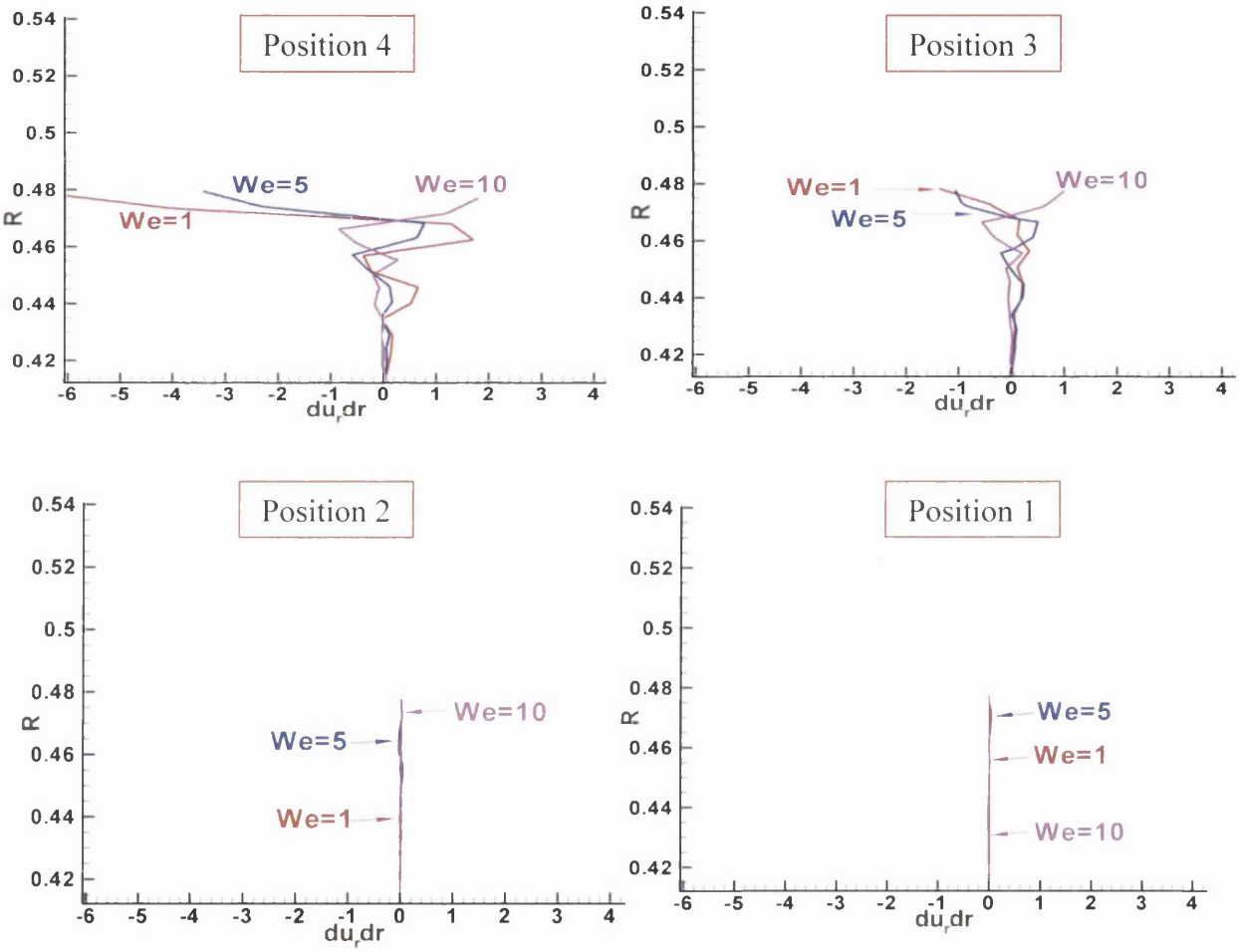

Figure 6.21: du_r/dr, EPTT: *We* variation, ξ=0.15, ε_{EPTT}=0.5, β=10^{-2}

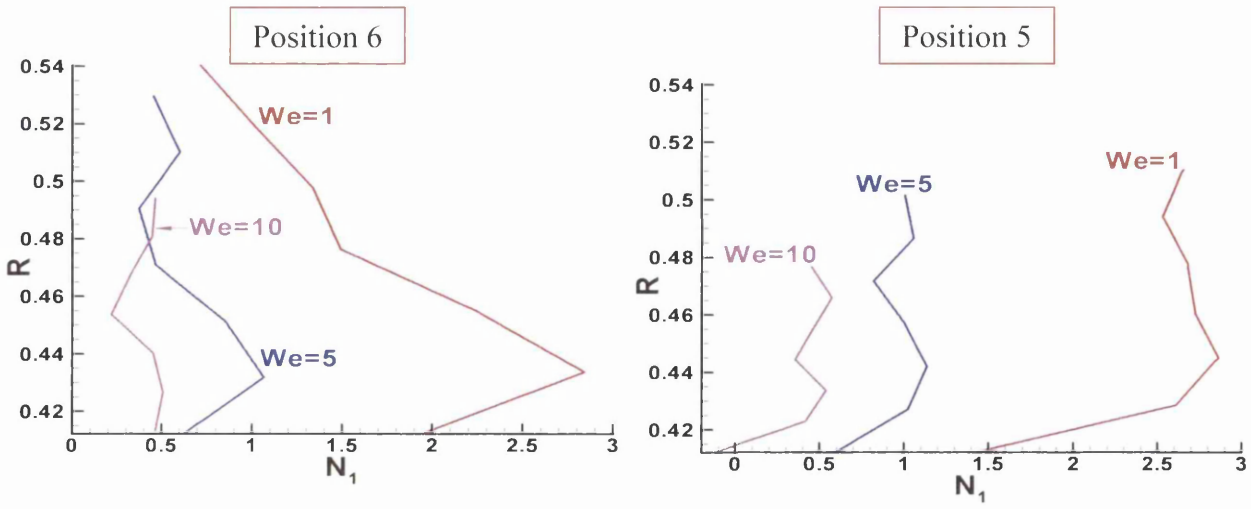

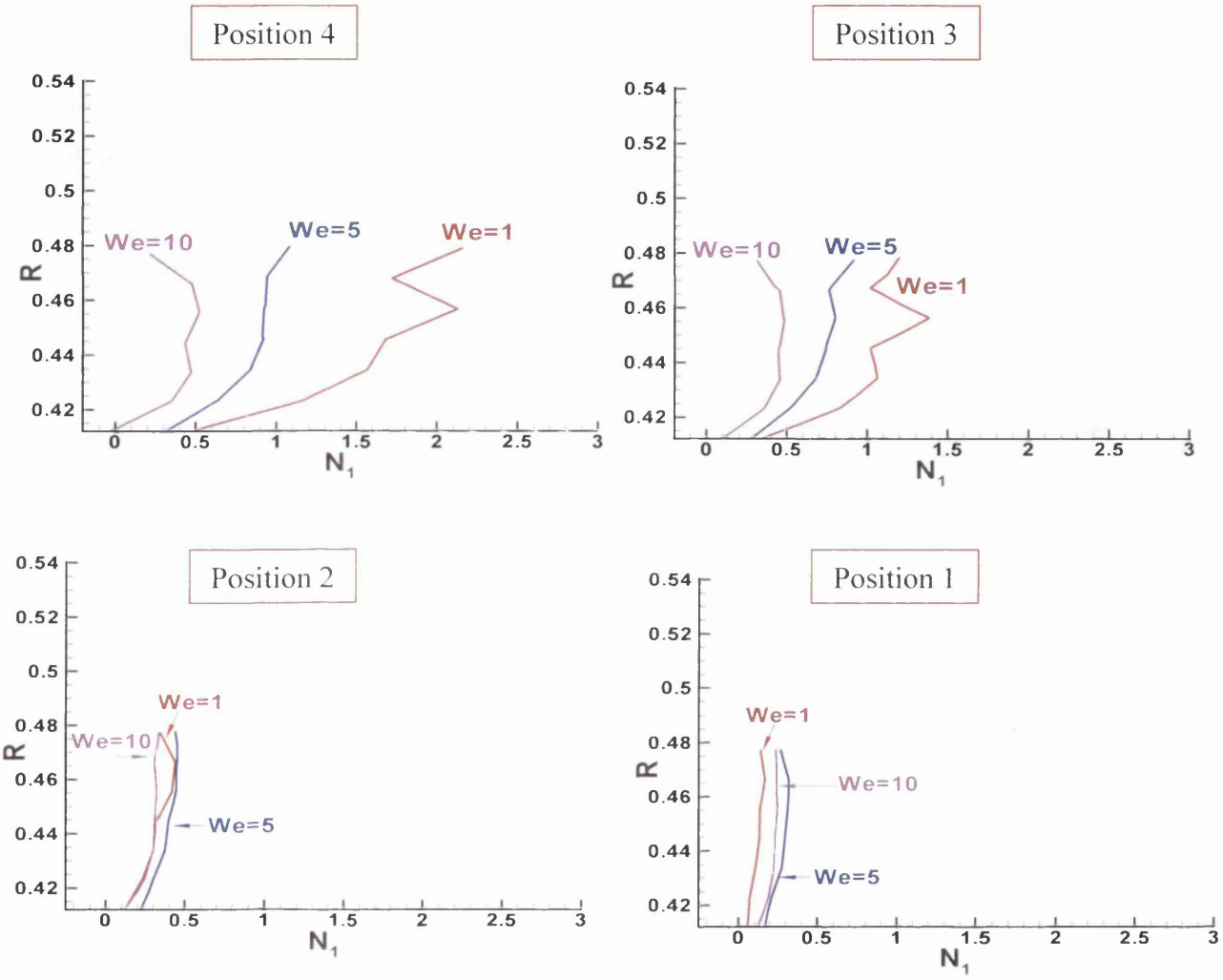

Figure 6.22: N_1, EPTT: *We* variation, ξ=0.15, ε_{EPTT}=0.5, β=10^{-2}

6.6 Conclusion

The numerical solution of viscoelastic flows for the combined tube-tooling/draw down flow has investigated, principally through the variation of material parameters. An exponential Phan-Thein/Tanner (EPTT) model has been employed to predict pressure-drops and residual stresses, and considers how these are affected within the process. Notably, attention has been paid to the influence and variation in Weissenberg number (*We*), solvent-fraction (β) and second normal stress-difference (N_2) (ξ parameter for EPTT).

The shear-thinning response of the viscoelastic EPTT model, with increasing elasticity (We) and decreasing solvent-fraction (β), generates a decline in the pressure-drop. For solvent-fractions of $\beta=10^{-3}$, the total pressure-drop reduces nearly by a factor of eight from $We=1$ to $We=20$. With respect to stress profiles at any given solvent-fraction (β), a smaller level of stressing is established with larger values of We due to the dominant influence of shear-thinning.

In addition, second normal stress difference effects are vitally important in this problem, which has a major impact on shear stress, normal stress and first normal stress difference levels. Furthermore, it is shown that a decoupled approach may provide a pragmatic strategy to stabilise the nonlinear calculation, and to provide predictive solutions at low levels of solvent-fraction ($\beta=10^{-3}$) and under the influence of non-zero second normal stress-difference (N_2).

CHAPTER 7

Numerical study of differential constitutive equations with polymer melts: The Single eXtended pom-pom (SXPP) model

7.1 Introduction

This chapter covers the numerical investigation of complex flow, tube tooling cable-coating using the single-equation representation of the pom-pom (SXPP) model discussed in section 2.4. Here, again, the hybrid scheme consists of a Taylor–Galerkin finite element discretisation, and a cell-vertex fluctuation-distribution finite volume approach is employed. Quantitative comparison against experiments requires, first and foremost, the use of constitutive models that can reproduce the steady rheological properties of the fluid in both pure shear and extensional flows (uniaxial and planar). As detailed in the previous chapter, the exponential Phan-Thien Tanner (EPTT) type with shear-thinning, strain-softening, and moderate-high Trouton ratios is discussed. Although PTT-like models can account for both uniaxial and planar strain-hardening, shear-viscosity also reflects a dependence on the same parameters that govern extensional properties, see Matallah et al. [74]. This brings awkwardness in attempts to fit both viscosity functions independently; hence the advent and success of the pom-pom class of models, see McLeish and Larson [79], extracted in integral and differential forms. Such a framework is able to describe the complex rheological behaviour of polymer melts with essential separability over shear and extensional response. These

pom-pom forms have been shown to provide quantitative agree with experimental data for melts with long side-branched architecture [79], as in low-density polyethylene (LDPE) melts. The original pom-pom model was modified into an eXtended form (XPP) by Verbeeten et al. [128], and then implemented in finite elements, to overcome three major descriptive drawbacks: discontinuity in steady-state elongation; unboundedness in the orientation-variable at large strain-rates; lack of support for non-zero second normal stress difference in shear. In [108], good matching is also achieved for the rheology of LDPE-melts in both shear and extension using the pom-pom differential model. In addition, Inkson et al. [63] used a hypothetical melt of pom-pom type with different numbers of arms, to model the behaviour of LDPE melts. These authors found for three different flow problems, that multi-mode versions of the pom-pom equation with physically reasonable distributions of branching, are capable of predicting LDPE rheology over some four decades in deformation-rate.

Furthermore, Zatloukal [146] investigated the fitting and prediction with the modified Leonov model, along with XPP and modified White–Metzner (mWM) models. Zatloukal considered steady shear and uniaxial elongational flows for three different polymer melts (LDPE, mLLDPE, PVB). There, the study showed that the XPP model provides improved fitting and prediction for steady shear and elongational viscosity at lower deformation-rates when compared to the mWM model. In Bogaerds et al. [25], stability of the XPP model of Verbeeten et al. [128] was investigated for simple viscometric flows, utilizing two-dimensional finite element computations and a one-dimensional spectral eigenvalue analysis. The authors introduced a robustly stabilizing effect on these simple shear flows by including a relatively small second normal stress difference (α=0.1). They also documented that despite the resemblance between the material functions of the XPP and the EPTT models, the response to perturbation with the XPP model was significantly different. As a consequence, a new form of PTT model, termed PTT–XPP was introduced by Tanner and Nasseri [122] to essentially reproduce the steady extensional response of the XPP model of Verbeeten et al. [128,130]. There, the Giesekus (α) and $g(\tau)=(f(\tau)-1)I$ terms that appear in the standard XPP model are neglected, in generating this new PTT–XPP model variant. Notably, shear viscosity response at larger shear-rates differs with this PTT–XPP model from its XPP counterpart: the XPP-form shows a greater tendency to shear-thin

(increased rate) over its PTT–XPP alternative. More recently, a number of computational studies of steady viscoelastic flows have been undertaken, using Single eXtended approximations of the pom-pom model (SXPP); see for example Aboubacar et al. [4], Aguayo et al. [5, 6], Michiel et al. [80], Tamaddon Jahromi et al. [118]. This body of work with SXPP-models has aided in advancing numerical solution capability for polymeric fluids in contraction flows, where the evolution equation for the polymer-chain backbone-stretch structure variable is replaced by a steady-state idealised algebraic alternative.

In this chapter, the Single eXtended pom-pom model (SXPP) is used to investigate the particular problem of annular axisymmetric tube-tooling cable-coating, using a hybrid finite element/finite volume discretisation *fe/fv*(sc). Here, the influence and variation in Weissenberg number (*We*), solvent-fraction (β) and second normal difference (N_2) is considered. In addition, a comparison between an extended pom-pom (SXPP, kinematic-based) model and an exponential Phan-Thien Tanner (EPTT, network-based) model is presented.

Finally, contrast is made between alternative approaches to generate non-zero second normal stress differences, through the various constructive terms within the pom-pom constitutve framework. Here, the proposal is to provide comparison over solution response when N_2–effects are stimulated through alternative sources – by adjusting either the standard anisotropic α-parameter on the Giesekus dyadic stress-product term, or via the ξ-parameter on the Gordon-Schowalter convected derivative term (an additional modification to the pom-pom equation, utilising the linear combination of lower- and upper-convected derivatives).

7.2 Governing equations and Numerical scheme

For the solution of incompressible viscoelastic flow, the governing non-dimensional equations may be given by the stress, momentum and continuity equations, as explained in section 2.4. In the present chapter, the hybrid finite element/finite volume discretisation (*fe/fv*) is implemented. The general framework of the time-marching hybrid *fe/fv* scheme employed here involves two distinct aspects. Firstly, velocity and pressure are computed via a semi-implicit incremental pressure-correction procedure

with finite element spatial discretization. Secondly, a finite volume based fluctuation distribution scheme is adopted for computation of the hyperbolic extra-stress equations. A comprehensive discussion on this approach is presented in chapter 3.

7.3 Problem specification

A schematic diagram for the tube-tooling problem with its finite element mesh discretisation (draw-down section) was already displayed in section (6.2) of chapter 6. Here, the long mesh of 2508 elements, 5447 nodes and 34152 degrees of freedom was adopted (see Figure 6.1 and Tables 6.1, 6.2 and 6.3 for more details). In addition, the boundary conditions are also discussed in chapter 6. Furthermore, all numerical solutions pertain to viscoelastic creeping flows at minimal levels of inertia, equating to $Re=10^{-4}$. To construct the essential basis for steady-state solutions and domain-internal starting conditions (kinematics, at fixed flow-rate and cable-speed), the flow problem is first solved for Newtonian fluid properties. Then, from this Newtonian position, viscoelastic flow solutions are instigated. As mentioned earlier, numerical solutions are presented for the SXPP constitutive equation. Here, simulations are conducted at different solvent fraction β-settings ($\{\beta=10^{-1}, 10^{-2}, 10^{-3}\}$), two different settings of the anisotropy-parameter ($\alpha=\{0.0, 0.1\}$), $\varepsilon_{SXPP}=0.1$ and number of arms (q=2). In addition, attention is paid to the influence of and variation in the Weissenberg number (*We*) through a graded progression in *We* calculation. Ultimately, a comparison between pom-pom and EPTT solutions is provided. The SXPP and EPTT model are referred to here in parametric form as SXPP$\{q, \varepsilon_{SXPP}, \alpha\}$ and EPTT$\{\varepsilon_{EPTT}, \xi_{EPTT}\}$, respectively.

7.4 Material functions

In a previous chapter, the rheological response for the EPTT model has been investigated, under different relative parameters. To provide a wider study and discuss different rheological behaviours, the SXPP model is presented in this chapter. The SXPP model represents a shear-thinning fluid of strain-softening form under extensional deformation. Under this model, the parameters, which affect the material functions, and in consequence, the flow response, are: the ratio of relaxation times (stretch/orientation) of the backbone, represented by the non-dimensional parameter

(ε_{SXPP}); solvent fraction (β); the number of arms at both ends of the molecular chain-segment (q); the anisotropy-parameter (α). Figure 7.1(a,b) shows the shear and extensional viscosity for two different settings of solvent fraction $\beta=10^{-2}$ and 10^{-3}, and the non-dimensional parameter $\varepsilon_{SXPP}=0.1$ and 0.2 at fixed anisotropy-parameter $\alpha=0.0$ and q=2. From the profiles one can observe that, the best fitting in a least-square sense arises with $\beta=10^{-3}$ and $\varepsilon_{SXPP}=0.1$. Figure 7.1a displays a best fit in shear deformation with $\beta=10^{-3}$ and $\varepsilon_{SXPP}=0.1$, when compared to a choice of $\beta=10^{-2}$. In contrast and for elongational viscosity, there is insignificant change apparent in response between both levels of solvent fraction. Moreover, comparison between EPTT{$\varepsilon_{EPTT}=0.5$, $\xi_{EPTT}=0.15$} and SXPP{q=2, $\varepsilon_{SXPP}=0.1$, $\alpha=0.0$ and 0.1} settings at fixed $\beta=10^{-3}$, are shown in Figure 7.1(c,d), helping to identify optimal fits against the experimental data. From such fits one can conclude that the SXPP model provides a near-optimal least-squares fit across the complete range of extensional viscosity, matching closely to the experimental data with {$\beta=10^{-3}$, q=2, $\varepsilon_{SXPP}=0.1$, $\alpha=0.0$ or 0.1}. The shear and elongational viscosity remain unaffected by adjustment in α-parameter, as illustrated in Figure 7.1(c,d). At low rates ($\dot{\gamma}<10^{2}$), the SXPP model exhibits greater thinning in shear viscosity than that manifested with the EPTT variant; whilst this position is reversed in the deformation-rate range ($\dot{\gamma}>10^{2}$).In addition, at fixed $\beta=10^{-3}$, Figure 7.1e provides comparison over the first normal stress difference (N_1) between the response extracted under EPTT{$\varepsilon_{EPTT}=0.5$, $\xi_{EPTT}=0.15$} and SXPP{q=2, $\varepsilon_{SXPP}=0.1$, $\alpha=0.1$} models. Such material data demonstrate that, under exposure to larger shear-rates, the dependence of N_1 on $\dot{\gamma}$ becomes weaker and tends to a constant plateau-level with the EPTT model, while for the SXPP version an increasing trend in N_1 is substantiated. Comparative data are also presented on the second normal stress-difference (N_2) in Figure 7.1f, where and for at $\dot{\gamma}>10^{0}$, it is conspicuous that N_2 for SXPP adopts a monotonically declining trend, as opposed to the constant plateau-level observed with EPTT.

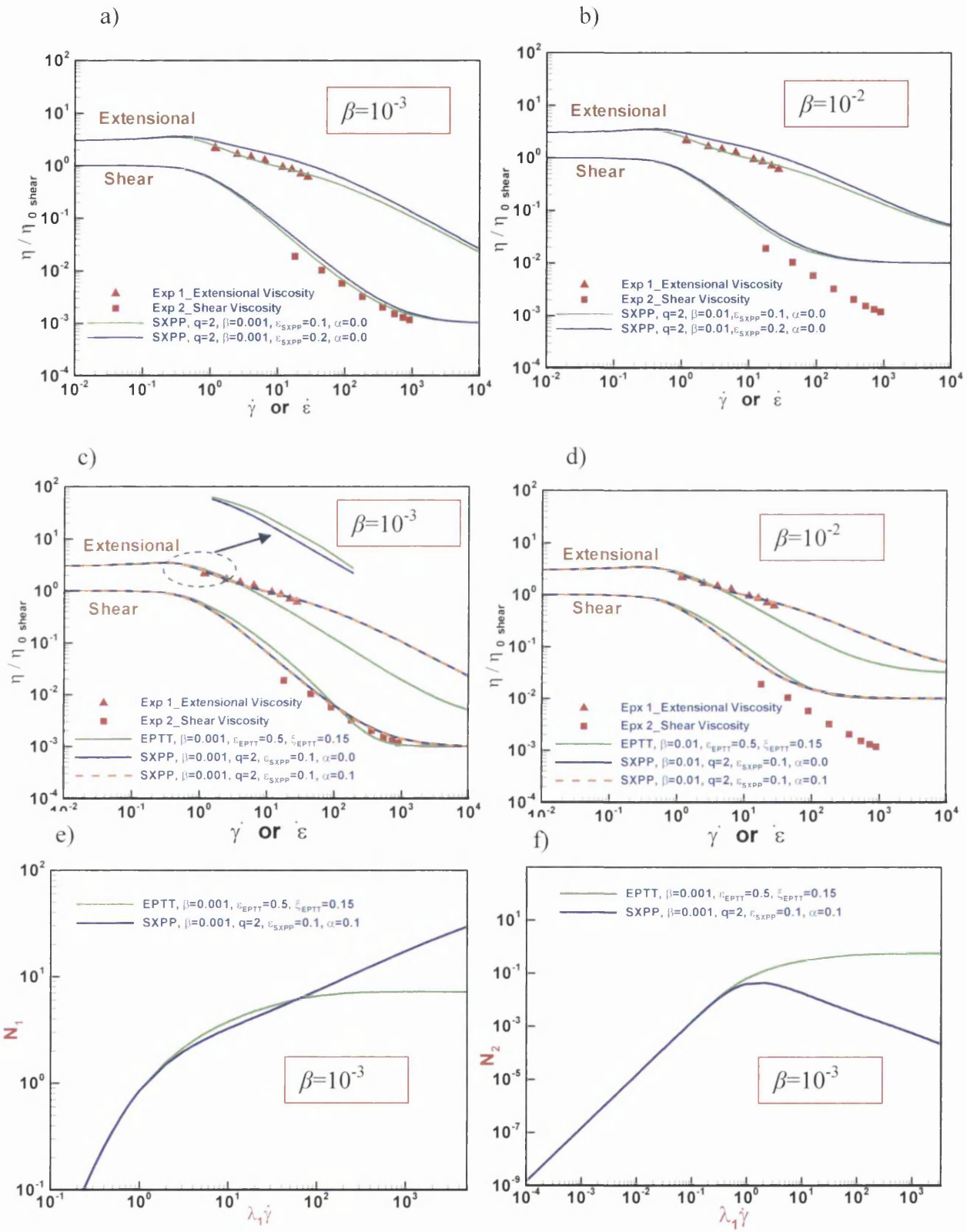

Figure 7.1: a,b) shear and extensional viscosity fits, SXPP: {β, ε_{SXPP}}-variation, c,d) shear and extensional viscosity fits, SXPP vs EPTT, e,f) First normal stress (N_1) and second normal stress (N_2), SXPP vs EPTT

7.5 Numerical solutions (SXPP model vs EPTT model)

7.5.1 Zero second normal stress (N_2=0)

In this section, numerical solutions for the SXPP{q=2, ε_{SXPP}=0.1, α=0.0} model are discussed, in the absence of second normal stress difference (N_2) effects. An aspect of this study has been to compare and contrast the behaviour in complex flows of both EPTT (network-based) and SXPP (kinectic-based) models. Here, a comparison between the SXPP{q=2, ε_{SXPP}=0.1, α=0.0} and the EPTT{ε_{EPTT}=0.5, ξ_{EPTT} =0.0} model is explored, for β=10^{-3} and *We* variations.

7.5.1.1 Solution of SXPP(α_{SXPP}=0.0) vs EPTT(ξ_{EPTT}=0.0)

7.5.1.1.1 Shear and strain-rates profiles with β variation

The deformation history and response of the fluid can be characterized through the ranges of strain-rates and shear-rates attained. Figure 7.2, displays the shear-rate (Γ) profiles over the top and bottom surfaces and strain-rate (Σ) through centreline for the SXPP{q=2, ε_{SXPP}=0.1, α=0.0} model for β={10^{-1}, 10^{-2}, 10^{-3}} and fixed *We*=5. Overall, the plots exhibit a minor difference in shear and strain-rates with variation in solvent-fraction β. Moreover, Similar behaviour is observed in both top and bottom surface shear-rate profiles. The lowest value for shear-rate (Γ) in the whole geometry up to the cable region is observed with low solvent fraction (β=10^{-1}), due to dominant shear-thinning influence. In contrast, the data reflect that: the maxima in Γ is (48.55 units) at the converging-inlet for bottom surface, and Σ is (1.46 units) near the contact point region for β=10^{-3}. In accordance with the above results, the range of shear and strain rates are ($\Gamma \leq 48.55$) and ($\Sigma \leq 1.46$) respectively; which practically agrees with findings under EPTT{ ε_{EPTT}=0.5,ξ_{EPTT}=0.0} model (see Figure 6.11 and 6.12). In that range of shear and strain-rates, more thinning in shear is encountered with this SXPP model, as compared to the EPTT (see Figure 7.1c).

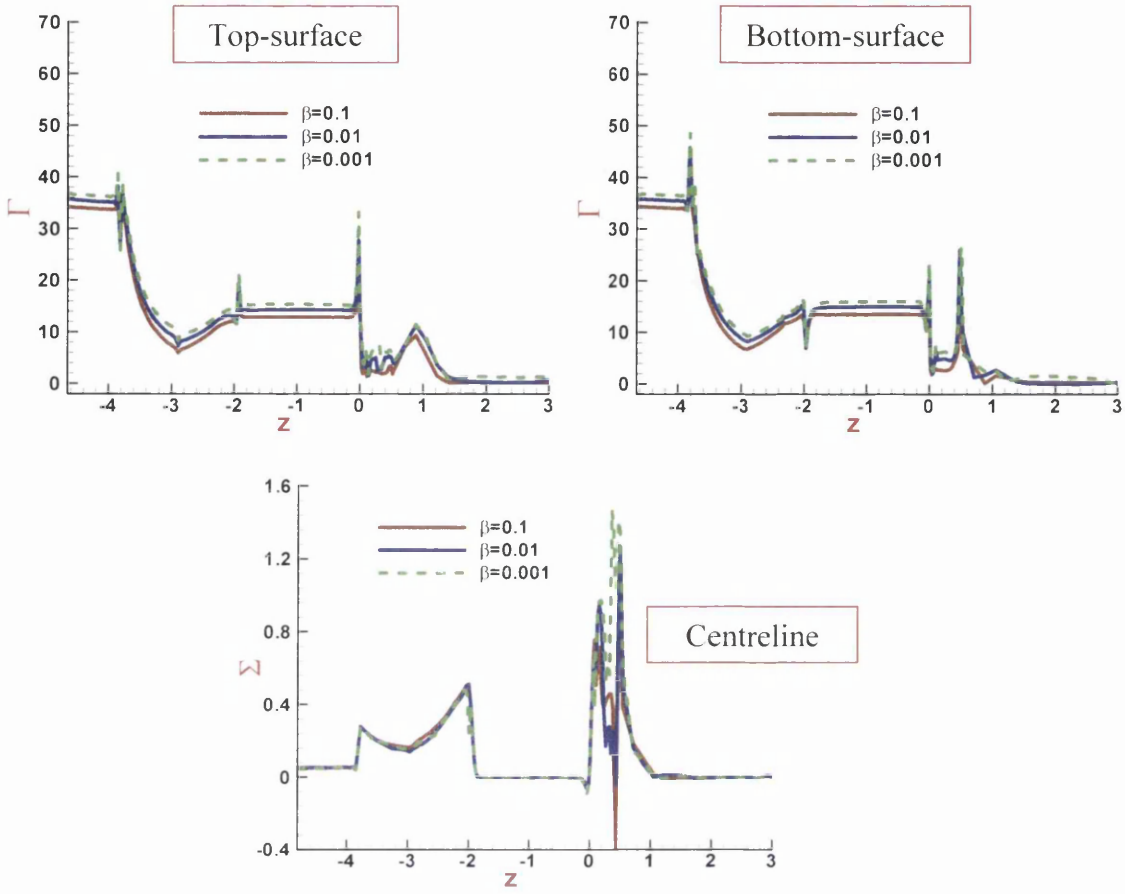

Figure 7.2: shear-rate (Γ), strain-rate (Σ), SXPP{q=2, ε_{SXPP}=0.1,α=0.0}: *We*=5, *β* variation

7.5.1.1.2 Pressure-drop profiles with β and We variation

Pressure profiles results along the centreline for a SXPP{q=2, ε_{SXPP}=0.1, α=0.0} model and through variation in *β* and *We* are shown in Figure 7.3. The findings reveal that, the largest value of pressure occurs at $\beta=10^{-1}$ with *We*=5 (248 units), with a significant reduction in the pressure drop as *We* increases from *We*=5, to *We*=10, and then *We*=20. This is attributed to the influence of shear-thinning behaviour with the SXPP representation. In addition, and for *We*=20, a considerable decline in total pressure-drop is observed for the low solvent fraction of $\beta=10^{-3}$, with a minimum value of around 5.87 units (almost *O*(94%) and *O*(88%) reduction in comparison to $\beta=10^{-1}$ and $\beta=10^{-2}$ solutions, respectively).

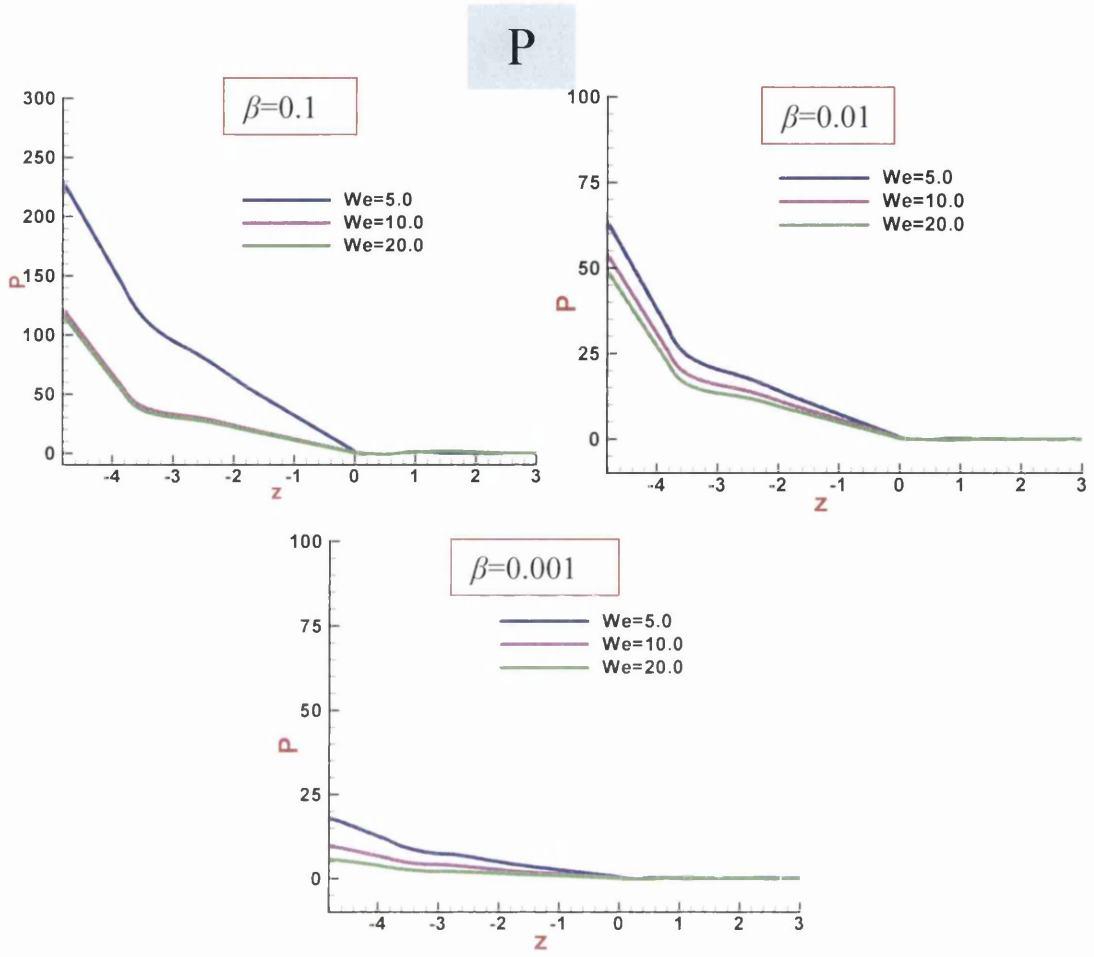

Figure 7.3: Pressure-P, SXPP{q=2, ε_{SXPP}=0.1,α=0.0}: β, *We* variation

In addition, a comparison of pressure results for SXPP{q=2, ε_{SXPP}=0.1,α=0.0} and EPTT{ ε_{EPTT}=0.5,ξ_{EPTT}=0.0} models is considered in Figure 7.4 with $\beta=10^{-3}$ for three different *We*-values of 5, 10 and 20. In all instances, SXPP data present a significant decline in pressure drop when compared to EPTT data. This reduction in pressure drop may be associated with a weaker first normal stress N_1 for SXPP, in the range of $1\leq\dot{\gamma}\leq100$ in comparison to that for EPTT (see Figure 7.1e). Note that, SXPP is also more shear-thinning in the same range when compared to EPTT. From the profiles, one can detect that the reduction in the pressure drop between pom-pom and EPTT models is *O*(72%), *O*(76%) and *O*(79%) for *We*=5,10, and 20, respectively. The maximum values of total pressure-drop for both models are tabulated in Table 7.1.

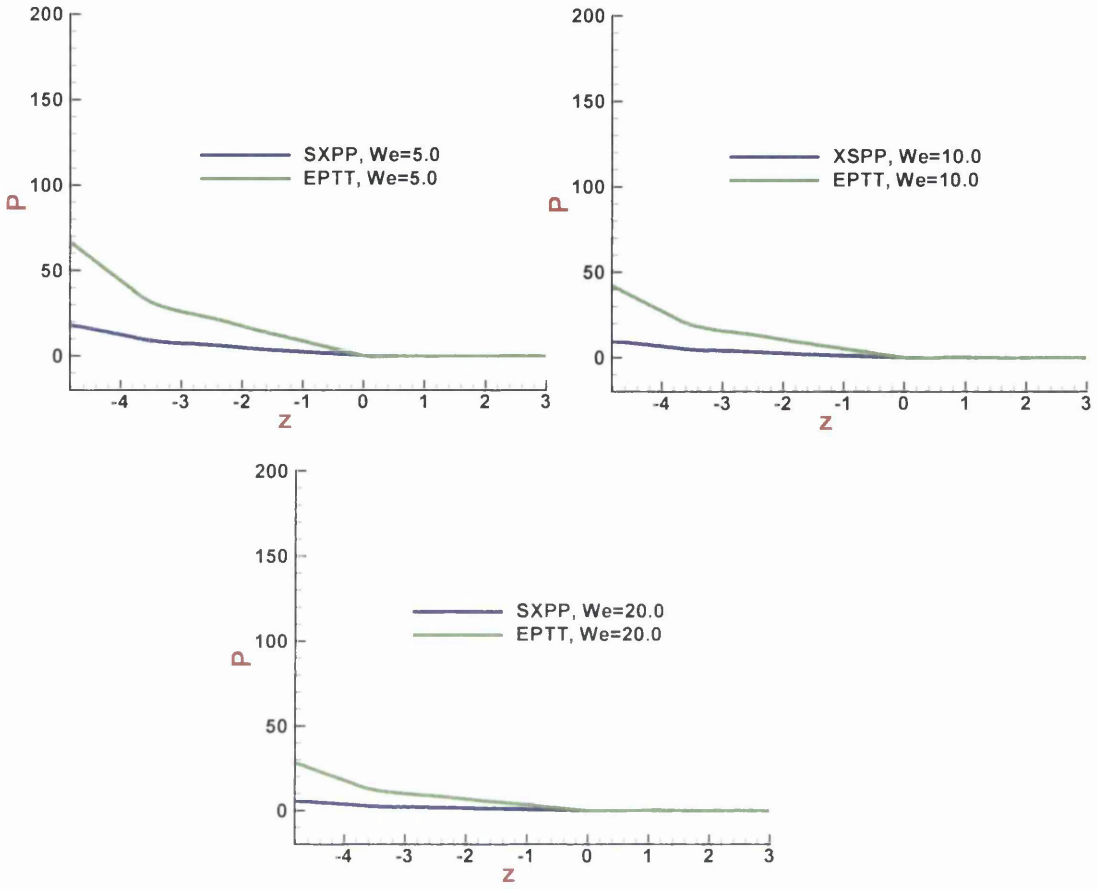

Figure 7.4: Pressure-P, SXPP{q=2, ε_{SXPP}=0.1,α=0.0} vs EPTT{ ε_{EPTT}=0.5,ξ_{EPTT}=0.0}: β=10^{-3}, *We* variation

Table 7.1: Total pressure-drop in units, SXPP{q=2, ε_{SXPP}=0.1,α=0.0} vs EPTT{ε_{EPTT}=0.5,ξ_{EPTT}=0.0}: β=10^{-3}, *We* variation

We / model	**5.0**	**10.0**	**20.0**
EPTT	66.80	42.22	28.46
SXPP	18.36	9.91	5.87

7.5.1.1.3 Stress profiles (N_1, τ_{zz} and τ_{rz})

The normal stress τ_{zz} and first normal stress N_1 along the centreline are displayed in Figure 7.5, with zoomed draw-down section for SXPP{q=2, ε_{SXPP}=0.1,α=0.0}at fixed β=10^{-3}, and different setting of *We*=5,10,20. Constant normal stress levels are observed

along the die-inlet section, with increase and then sharp decrease over that converging section, and again constant levels in the land region with decline at the die exit. Through the draw-down section, one observes a decrease in level of normal stress as *We* increases, which may reflect the effects of shear thinning behaviour. The profiles in the draw-dawn section show a decrease in τ_{zz} -values of: $O(33\%)$ from We=5 to We=10; and of $O(50\%)$ from We=5 to We=20; and of $O(25\%)$ from We=10 to We=20.

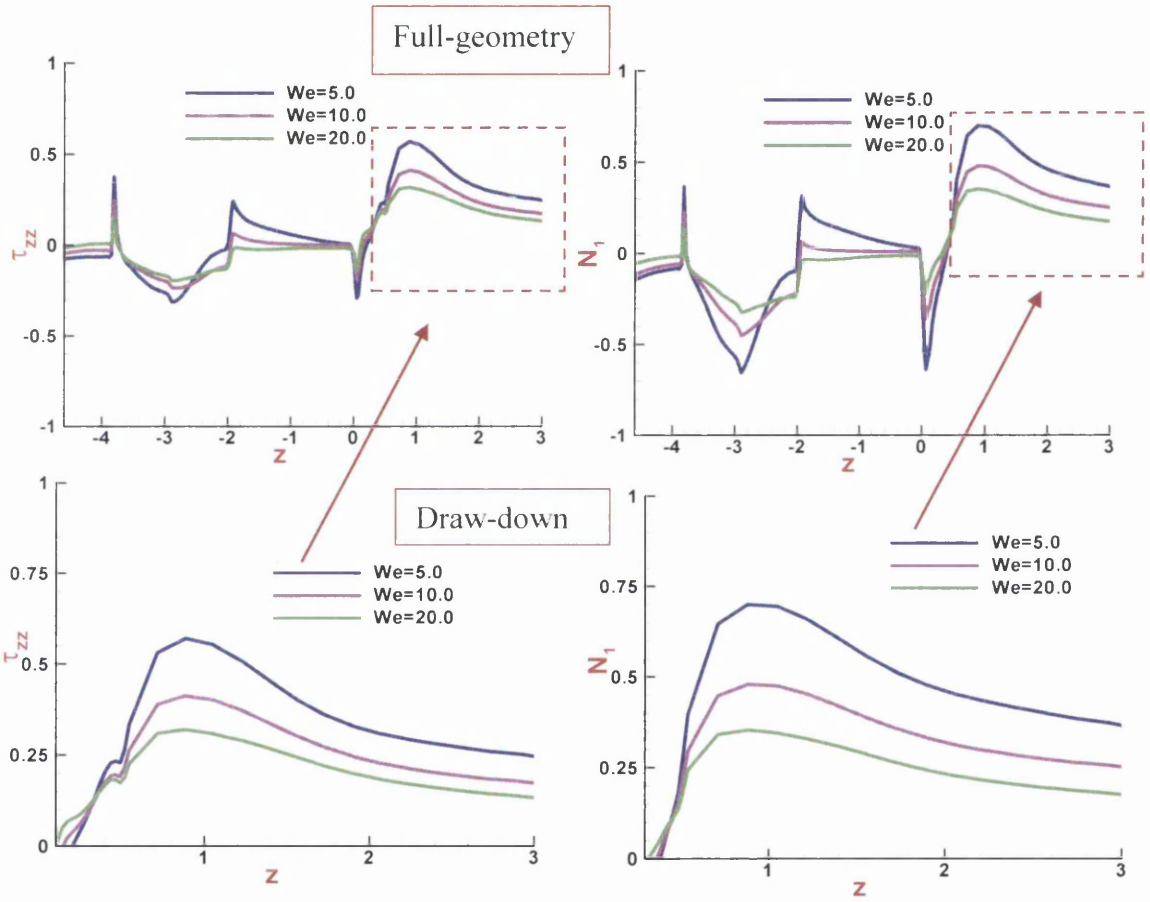

Figure 7.5: Normal stress (τ_{zz}), first normal stress (N_1), SXPP{q=2, ε_{SXPP}=0.1,α=0.0}: $\beta=10^{-3}$, *We* variation

Normal stress τ_{zz} is displayed in Figure 7.6 along the centreline, with zoomed draw-down section, for model selection, SXPP{q=2, ε_{SXPP}=0.1, α=0.0} and EPTT{ε_{EPTT}=0.5, ξ_{EPTT}=0.0}. This covers parameter choices: fixed $\beta=10^{-3}$, with different setting of We={1, 5, 10}. Similar trends in normal stress (τ_{zz}) are gathered, when comparing SXPP and EPTT model solution data, with smaller levels of stressing gathered in SXPP solutions. Here, constant levels are observed along the die-inlet section, with first

increase and then sharp decrease over the converging die-section; and again, constant levels in the die-land region, with decline at its die-exit. Major reduction is observed in τ_{zz}-value over the draw-down section under the SXPP solution when compared to that for EPTT. The τ_{zz}-peak draw-down zone value at *We*=1 is 2.3 units with EPTT; whilst this reduces to 1.8 units under SXPP solution (almost 22% reduction). At *We*=10, τ_{zz}-peak draw-down values are 0.6 and 0.4 units for EPTT and SXPP, respectively. A decrease in the level of normal stress as *We* rises, reflects the effects of shear-thinning response in the solutions gathered with both these models.

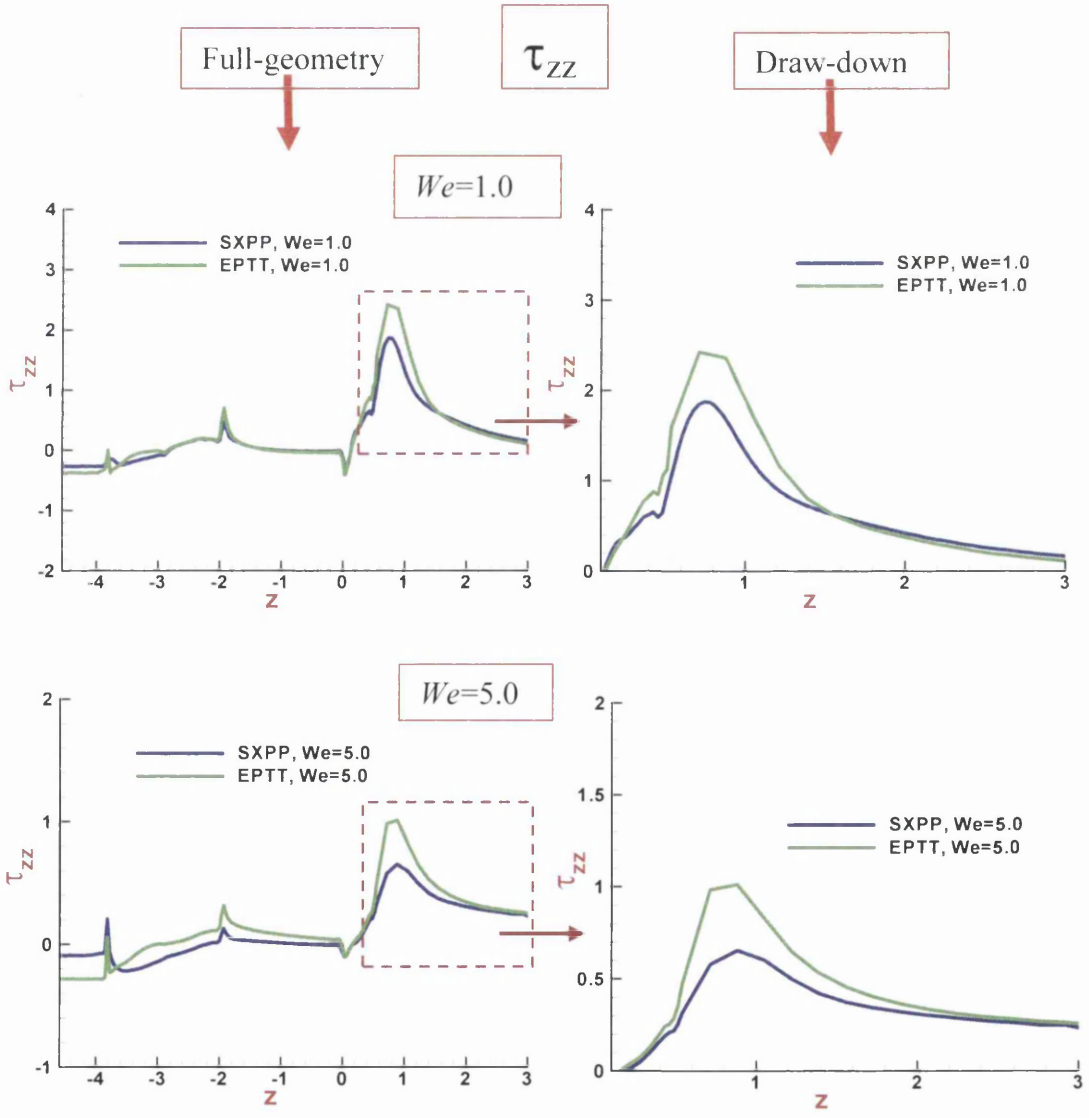

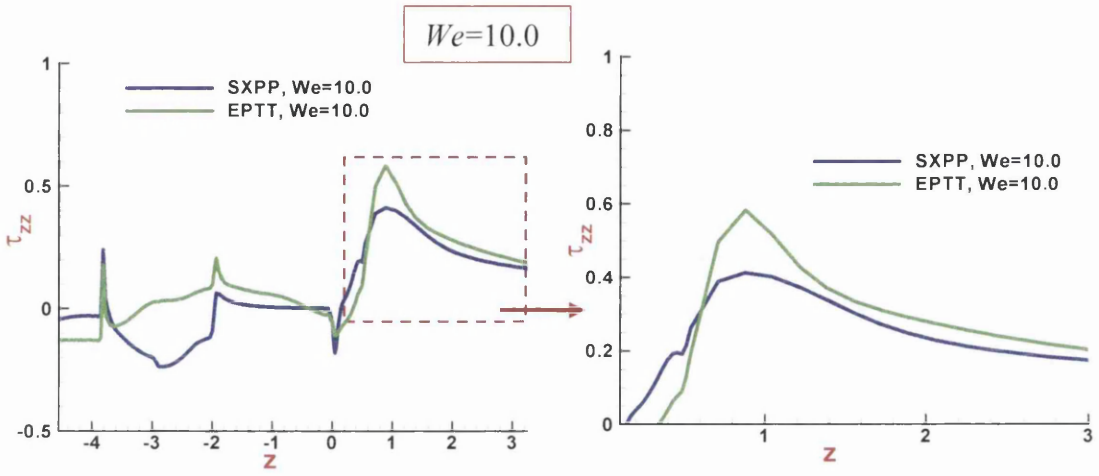

Figure 7.6: Normal stress τ_{zz}, SXPP{q=2, ε_{SXPP}=0.1, α=0.0} vs EPTT{ ε_{EPTT}=0.5, ξ_{EPTT} =0.0}: $\beta=10^{-3}$, *We* variation

In addition to the foregoing, shear stress (τ_{rz}) profiles along the top surface are plotted in Figure 7.7, for comparison between EPTT{ε_{EPTT}=0.5, ξ_{EPTT}=0.0} and SXPP{q=2, ε_{SXPP}=0.1, α=0.0} models, at fixed $\beta=10^{-3}$ under *We* variation. In all these instances, dominant shear-thinning leads to a stress ratio decrease as *We* rises. In addition, a major difference in the levels of τ_{rz}-stress is observed between solutions with both models. These profiles reveal that, over the die section, high levels of τ_{rz} occur for the EPTT model, opposite to that observed over the draw-down section with some relaxation apparent over the cable region. In all cases, large peaks are observed with the pom-pom model near the die exit. On the cable region the stress levels are practically indistinguishable. Through the die section the difference in the τ_{rz}-levels between both models diminishes at higher elasticity levels (*We*=10), compared to *We*=1 and *We*=5; τ_{rz}-level decreases by around one-half from *We*=5 to *We*=10. The increase of the stress magnitude in the die section may again be due to shear-thinning influence for both models, as displayed in Figure 7.1c.

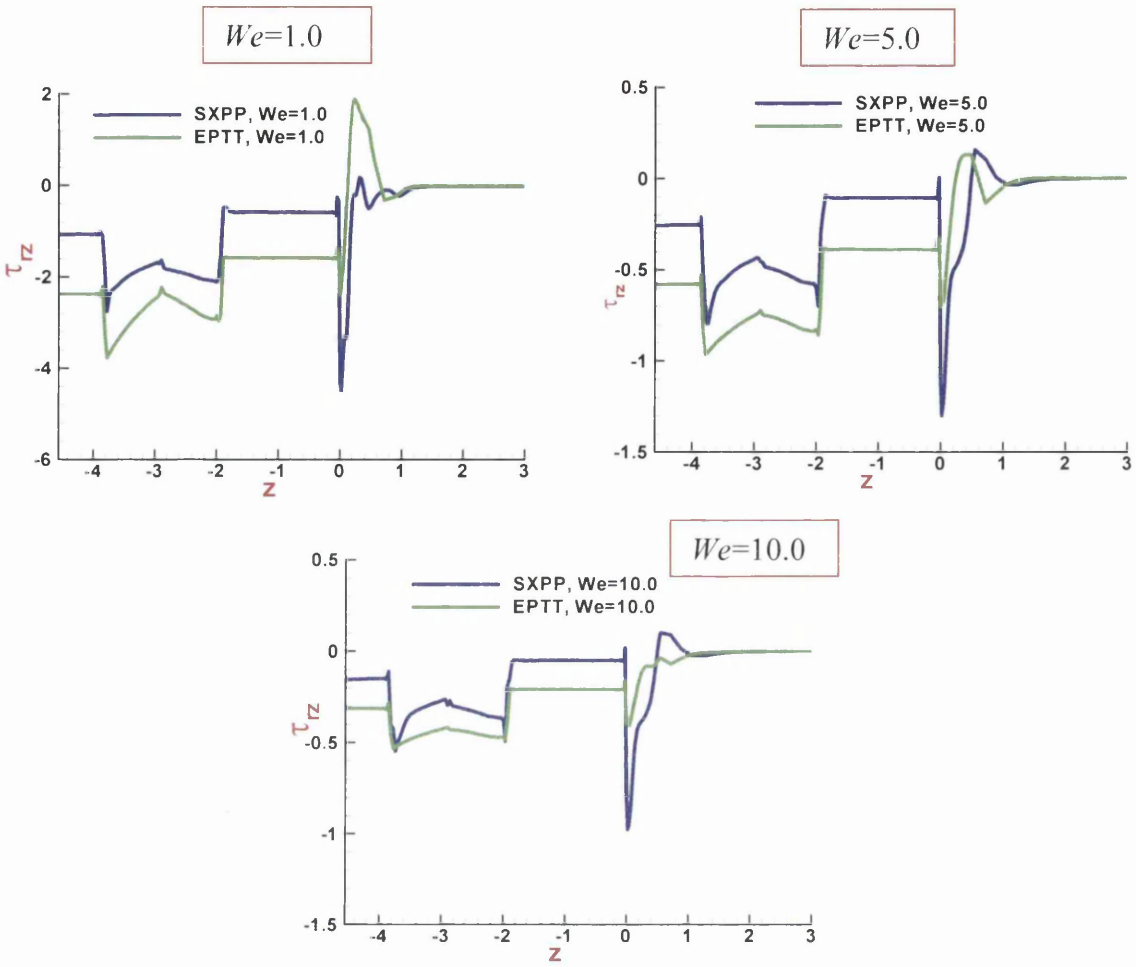

Figure 7.7: Shear stress (τ_{rz}) along top surface, SXPP{q=2, ε_{SXPP}=0.1,α=0.0} vs EPTT{ε_{EPTT}=0.5, ξ_{EPTT}=0.0}: β=10^{-3}, *We* variation

7.5.2 Non-zero second normal stress difference (N2≠0)

Here, the results for SXPP{q=2, ε_{SXPP}=0.1, α=0.0 and 0.1} at fixed solvent fraction β=10^{-3} are considered to demonstrate the influence of non-zero second normal stress difference (N_2) on solution data. In addition, a comparison is also undertaken against EPTT{ε_{EPTT}=0.5, ξ_{EPTT}=0.15} solution data, with Weissenberg numbers (*We*) of 1, 5.

7.5.2.1 Solution of SXPP(α_{SXPP}=0.1) vs EPTT(ξ_{EPTT}=0.15)

7.5.2.1.1 Pressure-drop profiles

For the SXPP model, the effect of the second normal stress difference on pressure-drop is also investigated, through variation in the anisotropy parameter α. In this respect, the pressure-drop along the centreline for SXPP{q=2, ε_{SXPP}=0.1, α=0.0 and 0.1} with *We*=1,5 and β=10^{-3}, is illustrated in Figure 7.8(a,b). Here, decreases in the

pressure-drop level is detected as the α-parameter increases from α=0.0 to α=0.1. For instance, almost O(8%), O(12%) reductions in pressure-drop are encountered with SXPP{q=2, ε_{SXPP}=0.1, α=0.1} for We={1,5}, respectively, in comparison to similar observations for SXPP{q=2, ε_{SXPP}=0.1, α=0.0} solutions.

In addition, at fixed $\beta=10^{-3}$, comparative data are presented on pressure-drop profiles in Figure 7.8(c,d). This corresponds to data along the centreline for SXPP{q=2, ε_{SXPP}=0.1, α=0.1} and EPTT{ε_{EPTT}=0.5, ξ_{EPTT}=0.15} models, with two values of We={1,5}. Here, a significant decrease in the level of SXPP pressure-drop is observed in comparison to EPTT results for both We=1 and 5. This amounts to around O(33%) reduction from {145.88 units for EPTT} to {96.88 units for SXPP} at We=1; and O(27%) reduction from {25.28 units for EPTT} to {18.36 units for SXPP} at the more elevated level of We=5. This reduction in pressure can be associated with a weaker first normal stress N_1 in the rate-range $1\leq\dot{\gamma}\leq100$ for SXPP, when taken in comparison to that supported with EPTT (see Figure 7.1e). Note that also, SXPP thins more rapidly than does EPTT, over the same range of $1\leq\dot{\gamma}\leq100$, as shown in shear viscosity plot Figure 7.1c.

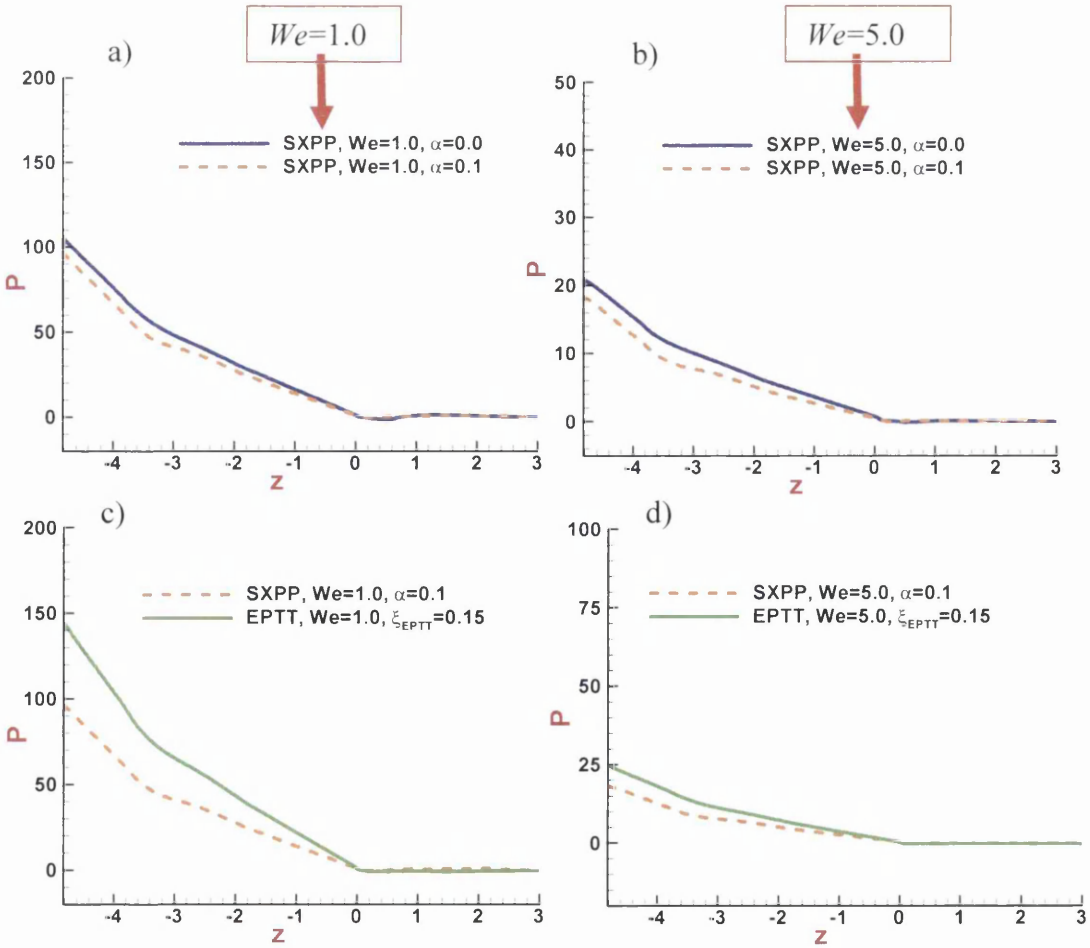

Figure 7.8: Pressure-P, SXPP{q=2, ε_{SXPP}=0.1, α=0.0 and 0.1}, EPTT{ ε_{EPTT}=0.5, ξ_{EPTT}=0.15}: $\beta=10^{-3}$, We variation

7.5.2.1.2 Stress profiles (Γ, Σ, N_1, τ_{zz} and τ_{rz})

In Figure 7.9, SXPP(α=0.1) and EPTT(ξ_{EPTT}=0.15) profiles at $\beta=10^{-3}$ and We=5 are compared for: shear-rate (Γ) along the top and bottom surfaces, and strain-rate (Σ) profiles along the centreline. The same trend is observed in shear-rate (Γ) for both top and bottom surfaces, but with lower values for SXPP in comparison to EPTT established throughout the die-section. This may be attributed to the higher shear-thinning rate of SXPP when compared to EPTT. For example, the maximum Γ peak-value of 50 units at the bottom surface of the inlet section with EPTT, has reduced to 40 units for SXPP (almost O(20%) reduction). At the top surface of the die-inlet and for the EPTT solution, a constant level of around 40 units is observed. This level is reduced by around O(17%) with SXPP. In addition, and for both models, a sharp decrease in Γ occurs throughout the converging section with a minimum level observed in the middle of that section, whereas a constant level is achieved over the land section, followed by a peak at the die exit. At the same time, the same level in Γ is observed through the draw-down zone for both models, with full dissipation over the cable region. In contrast, through strain-rate (Σ) profiles, one can observe that there is insignificant change in strain-rate (Σ) for both models with a maximum near the contact-point region (1.15 units). Generally, with We=5 one may conclude that the range of Γ and Σ for both models fluctuate around $0<\Gamma<50$ and $\Sigma<1.15$, respectively.

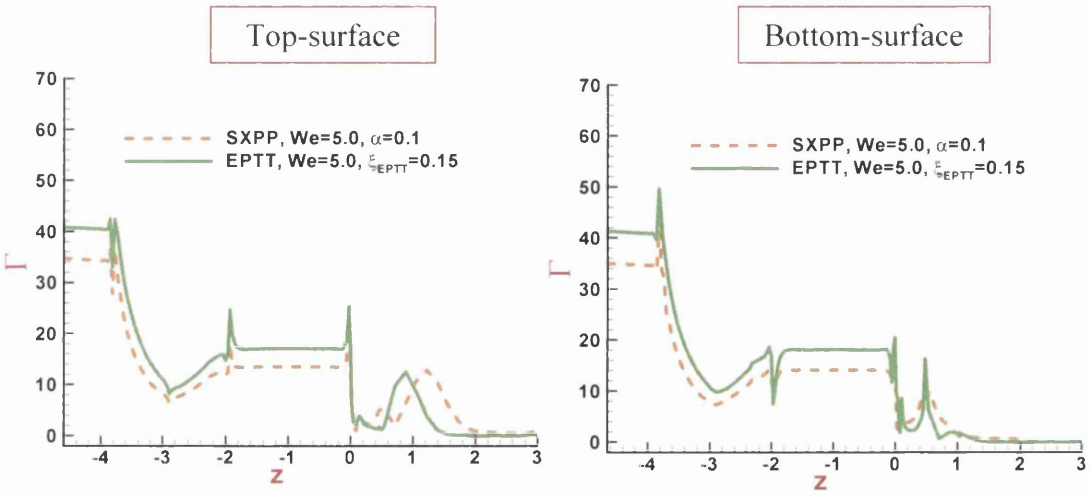

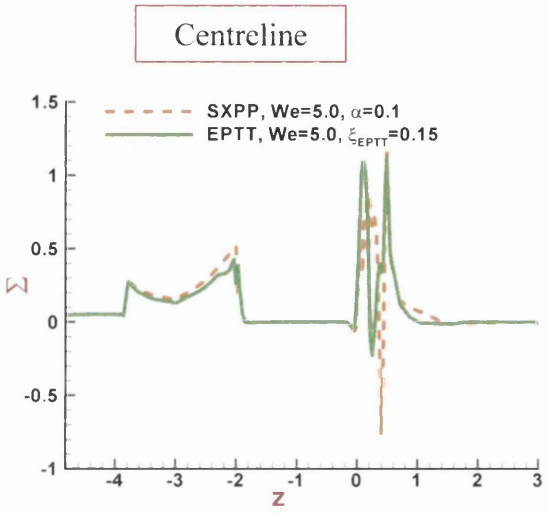

Figure 7.9: Shear-rate (Γ) and strain-rate (Σ), SXPP{q=2, ε_{SXPP}=0.1, α=0.1} vs EPTT{ε_{EPTT}=0.5, ξ_{EPTT}=0.15}: We=5, β=10^{-3}

Furthermore, in Figure 7.10, the normal stress (τ_{zz}) profiles along the centreline are displayed for SXPP{q=2, ε_{SXPP}=0.1, α=0.0 and 0.1}. This includes a zoomed view of the draw-down section and accounts for two different level of elasticity of We=1 and 5, at β=10^{-3}. Here, insignificant change in τ_{zz} is detected over the die section; whereas reductions in stress-peaks over the draw-down section are clearly apparent, due to the contribution of the second normal stress differences (N_2). The rate of this reduction in τ_{zz} decreases as We increases: reducing from O(37%) for We=1, to reach O(30%) for We=5. Hence, one may deduce that as elasticity levels rise, second normal stress difference effects become minimised under SXPP(α). At the same time, the influence of shear-thinning properties of the SXPP model causes a significant decrease in τ_{zz} as We rises, for both α={0, 0.1}. For instance, with α=0 the maximum level of τ_{zz} for We=1 is around 1.9 units, compared to 0.65 units for We=5; almost O(66%) reduction. Almost identical levels of normal stress are observed for the two values of anisotropy-parameter α=0 and 0.1 over the cable region.

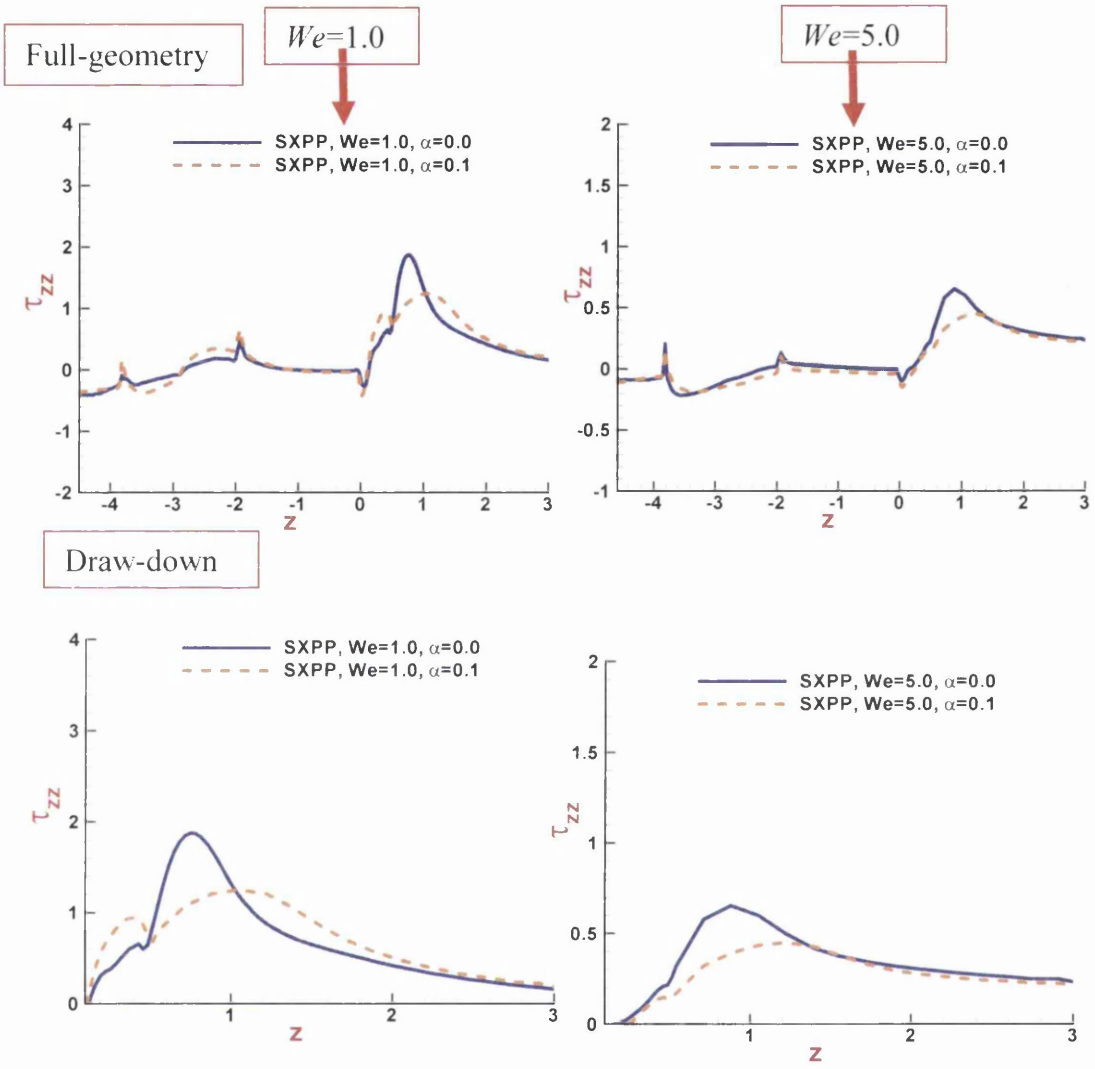

Figure 7.10: τ_{zz}, SXPP{q=2, ε_{SXPP}=0.1, α=0.0 and 0.1}: *We* variation, $\beta=10^{-3}$

The corresponding comparison between SXPP(α=0.1) and EPTT(ξ_{EPTT}=0.15) results is provided in Figure 7.11(a,b) for $\beta=10^{-3}$ and *We*={1, 5}. This covers normal stress (τ_{zz}) along the centreline and with draw-down zoomed section. Normal stress (τ_{zz}) profiles drop in the die-section of the flow, with insignificant difference indicated between SXPP and EPTT solutions at *We*=1. In contrast, and over the same region, higher levels of τ_{zz} are observed with EPTT than with SXPP, at the higher level of elasticity of *We*=5. In addition, throughout the draw-down section and for *We*=1 and *We*=5, EPTT solutions show elevated values of τ_{zz}-stress compared to those under SXPP (see zoomed view of draw-down section in Figure 7.11(a,b)). Here, considering decrease in τ_{zz}, when comparing peak draw-down zone values between SXPP to EPTT at *We*=1 and *We*=5,

respectively, there is nearly {O(46%) drop, from 2.3 to 1.25 units}, and {O(52%) drop, from 0.94 to 0.45 units}.

The Figure 7.11(c-f) comparisons, in radial stress (τ_{rr}) and first normal stress difference (N_1) between SXPP and EPTT, are also provided in profiles along the centreline. The results reveal that there is insignificant change in τ_{rr} for either models over the die-section, with only slight differences apparent throughout the draw-down section. In addition, one can observe that the contribution of the second normal stress (via τ_{rr}) is quite modest, which has led to N_1 being dominated by τ_{zz}-stress.

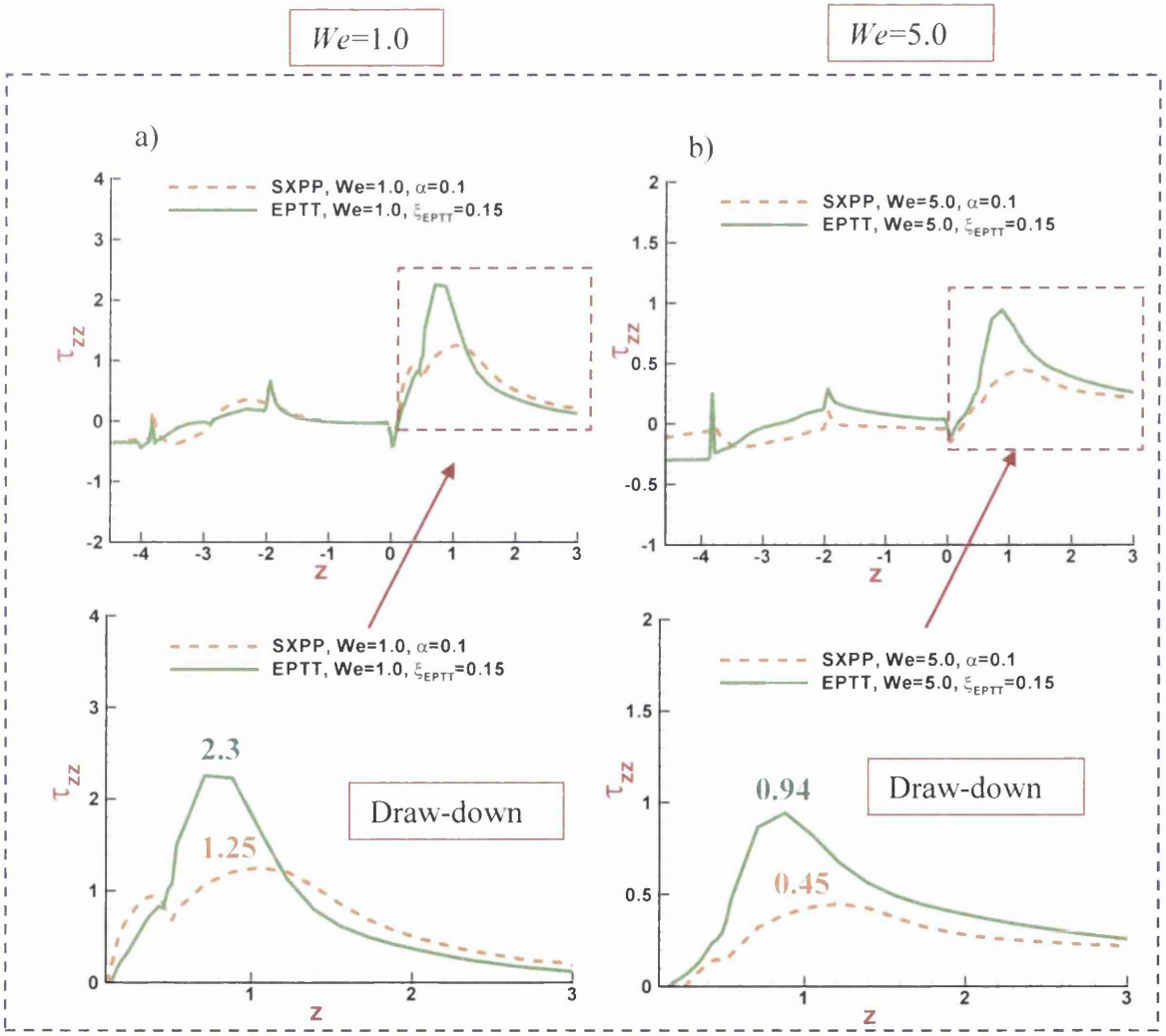

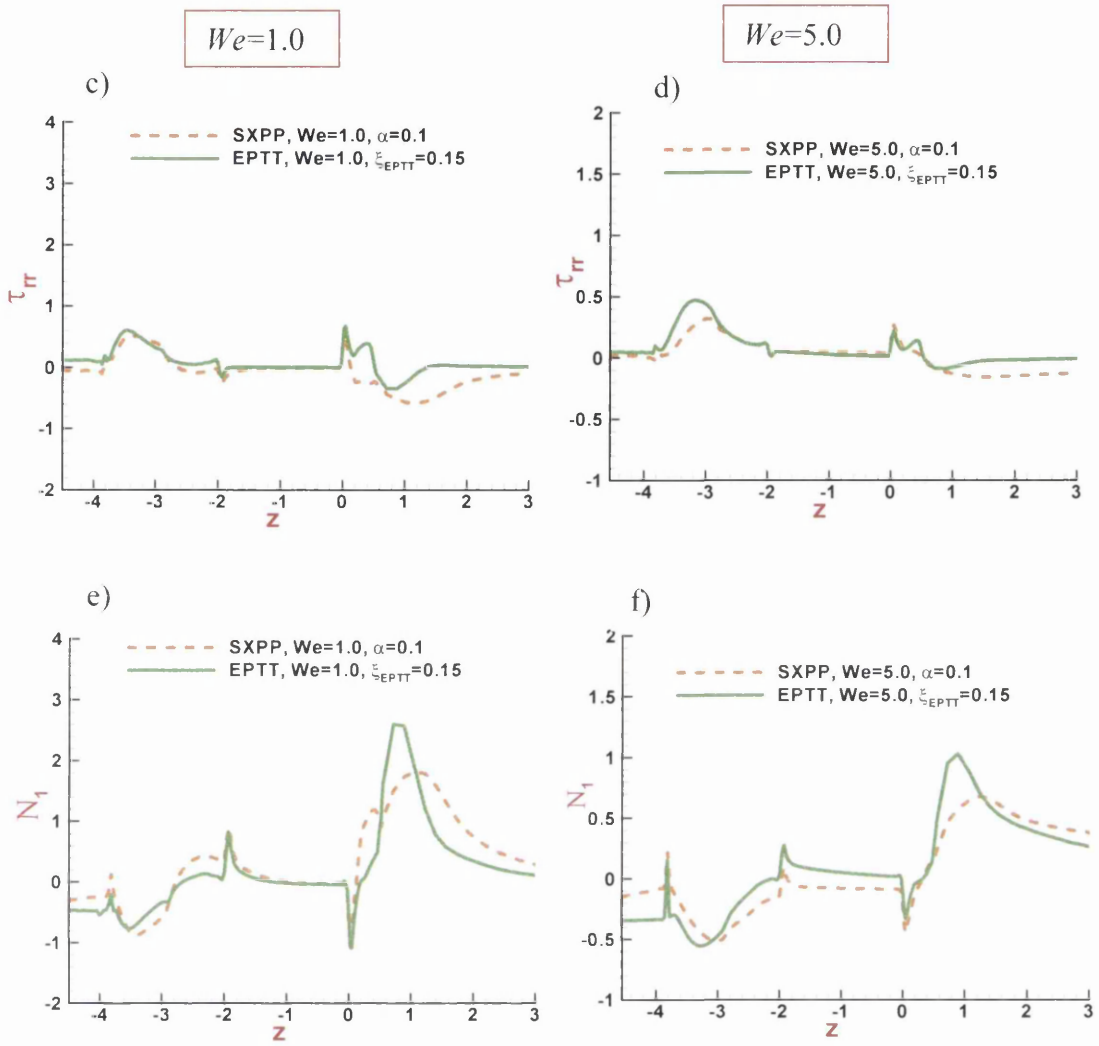

Figure 7.11: τ_{zz}, τ_{rr}, N_1 profiles at centreline, SXPP{q=2, ε_{SXPP}=0.1, α=0.1} vs EPTT{ε_{EPTT}=0.5, ξ=0.15}, *We* variation, $\beta=10^{-3}$

Comparative data in Figure 7.12 are also presented in shear stress (τ_{rz}) profiles at $\beta=10^{-3}$ and *We*={1,5}. This data is along the top and bottom surfaces for SXPP{q=2, ε_{SXPP}=0.1, α=0.1}and EPTT{ε_{EPTT}=0.5, ξ_{EPTT}=0.15}. Generally, more thinning is introduced in SXPP over EPTT results (see Figure 7.1c), which leads to low levels in τ_{rz}-stress. Here, the maximum peak is attained for *We*=1, over the bottom surface near the contact point region. In contrast, a slight change is observed for *We*=5, with a higher level in EPTT τ_{rz}-stress recorded over the die-section when compared to SXPP (more thinning). Since both SXPP and EPTT support shear-thinning, a notable decrease in the levels of τ_{rz} is observed as *We* rises. For example with EPTT, maximum magnitude in τ_{rz} for *We*=1 is 2.57 units compared to 0.7 for *We*=5 over the inner surface.

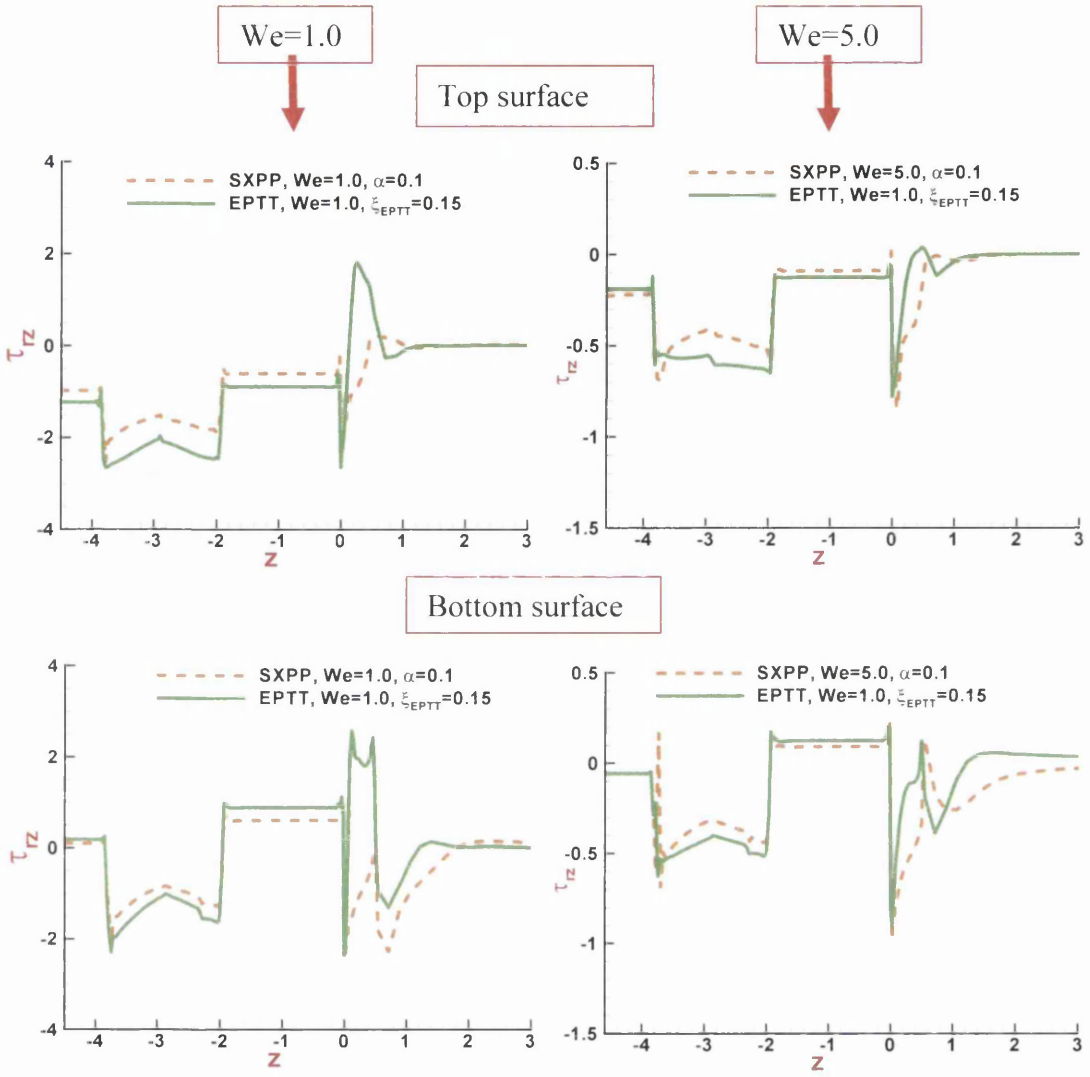

Figure 7.12: τ_{rz}, SXPP{q=2, ε_{SXPP}=0.1, α=0.1}vs EPTT{ε_{EPTT}=0.5, ξ_{EPTT}=0.15}: β=10^{-3}, *We* variation

7.5.2.2 Solution of SXPP(ξ_{SXPP}=0.01) vs EPTT(ξ_{EPTT}=0.15)

7.5.2.2.1 Modified model (SXPP(ζ_{SXPP}))

Here and within the SXPP context, in addition to the Giesekus α-parameter, the ξ-parameter of the Johnson-Segalman model is also introduced within the SXPP constitutive equation (2.69) to replicate second normal stress differences, N_2. Then the constitutive equation for the modified SXPP model may be stated in the following form:

$$We\overset{\diamond}{\tau}+f(\tau)\tau+\frac{\alpha We}{(1-\beta)}\tau\cdot\tau+\frac{(1-\beta)}{We}\left[f(\tau)-1\right]I=2(1-\beta)d\,, \tag{7.1}$$

where $\overset{\diamond}{\tau} = (1-\frac{\xi}{2})\overset{\nabla}{\tau}+\frac{\xi}{2}\overset{\Delta}{\tau}$, represents the linear combination of lower-convected (covariant) and upper-convected (contravariant) material derivatives (see section 2.4)

7.5.2.2.2 Response functions

The shear and extensional viscosity of SXPP(α=0.1), SXPP(ξ_{SXPP}=0.01) and EPTT(ξ_{EPTT}=0.15) at $\beta=10^{-3}$ are plotted for direct comparison purposes in Figure 7.13a. The material functions reveal that, the behaviour of SXPP(α=0.1) model is particularly close to that for SXPP(ξ_{SXPP}=0.01), both in shear and extensional viscosities, except at high shear-rate, ($\dot{\gamma}$>50). There, SXPP(ξ_{SXPP}=0.01) more rapidly thins than does SXPP(α=0.1). In addition, the corresponding viscometric comparison in the first normal stress (N_1) is shown in Figure 7.13b. Here, N_1 for these three models are identical at lower rates of $\dot{\gamma}$<2. The first normal stress difference of EPTT(ξ_{EPTT}=0.15) is slightly higher than both SXPP models at medium rates of $2<\dot{\gamma}<100$. In addition, N_1 for both EPTT(ξ_{EPTT}=0.15) and SXPP(ξ_{SXPP}=0.01) are weaker than SXPP(α=0.1) at higher rates of $\dot{\gamma}$>100.

a)

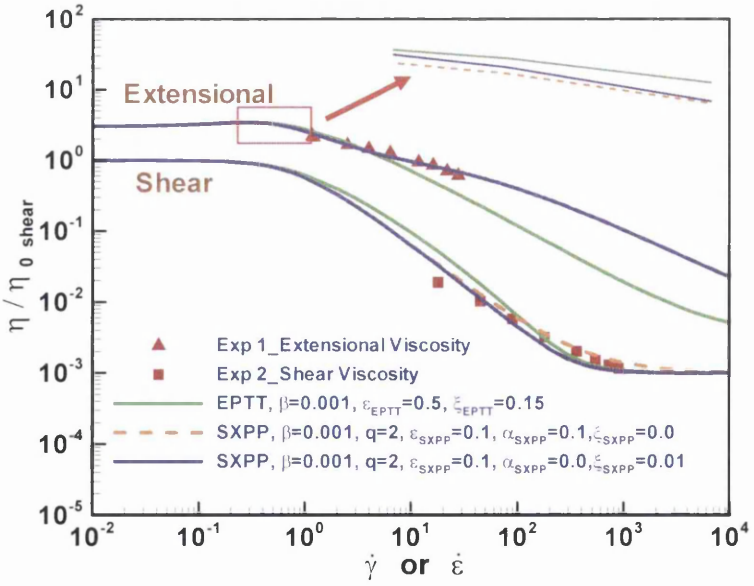

b)

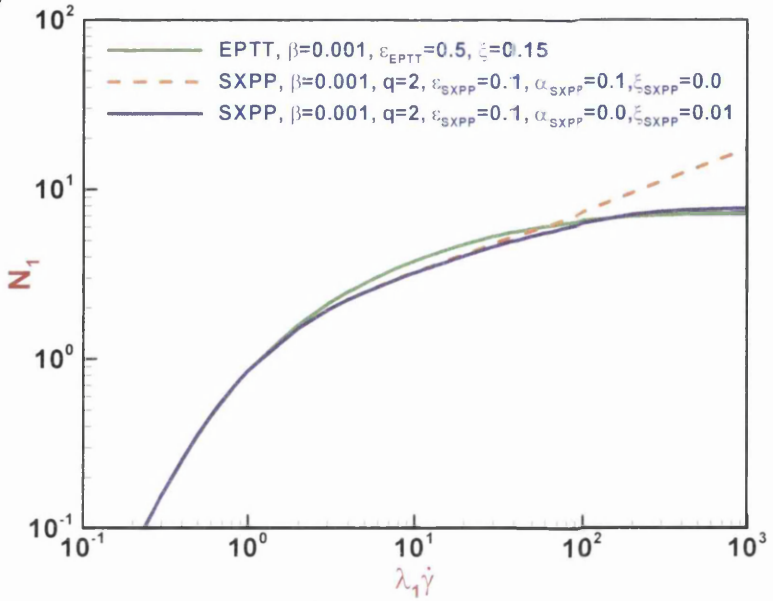

Figure 7.13: a) Shear viscosity, Extensional viscosity b) First normal stress (N_1): SXPP{q=2, ε_{SXPP}=0.1, α=0.1, ξ_{SXPP}=0.0} vs SXPP{q=2, ε_{SXPP}=0.1, α=0, ξ_{SXPP}=0.01} vs EPTT{ε_{EPTT}=0.5, ξ_{EPTT}=0.15}, $\beta=10^{-3}$

7.5.2.2.3 Stress (τ_{zz}, τ_{rz}) profiles

The profiles of normal stress (τ_{zz}) are provided in Figure 7.14a, with data along the centreline for SXPP(α=0.1), SXPP(ξ_{SXPP}=0.01) and EPTT(ξ_{EPTT}=0.15), at parameters of We=1 and $\beta=10^{-3}$; data is also extracted in zoomed form over the draw-down section. Findings show that, solutions for SXPP(ξ_{SXPP}=0.01) over the draw-down section lie between SXPP(α=0.1) and EPTT(ξ_{EPTT}=0.15). Throughout the die-section, there are only minor differences in τ_{zz} responses observed in solutions for SXPP(α=0.1), SXPP(ξ_{SXPP}=0.01) and EPTT(ξ_{EPTT}=0.15) models. In contrast, over the draw-down section, one can observe a relative decrease of: almost 25% in τ_{zz} peak magnitudes, from EPTT(ξ_{EPTT}=0.15) to SXPP(ξ_{SXPP}=0.01) (values varying from 2.25 to 1.7 units); and of 35% from SXPP(ξ_{SXPP}=0.01) to SXPP(α=0.1). Under this latter comparison, one has the same model choice and comparable N_1, N_2-response in shear ($\dot{\gamma}$<100), yet alternative fundamental driving sources to their generation, from which such variant complex flow results emerge. Furthermore, Figure 7.14b allows consideration of top (outer) surface data in normal stress (τ_{zz}) profiles. Here, EPTT(ξ_{EPTT}=0.15) shows significantly larger τ_{zz} throughout the die-section when comparing to SXPP results (almost 28% larger at die-inlet, from 3.9 to 5.4 units). Beyond the die-exit, once entering the draw-down flow, there is only a gradual decline in τ_{zz} over the draw-down section, followed by a sharp drop when the polymer meets the cable. Here, the

corresponding magnitudes in τ_{zz} at the draw-down exit zone are {0.1, 0.4, 0.5} units, for {EPTT(ξ_{EPTT}=0.15), SXPP(ξ_{SXPP}=0.01), SXPP(α=0.1)}, respectively. These findings may be largely attributed to viscometric shear response, in that the EPTT form provides distinctly lesser shear-thinning rate over the moderate rate range ($1 \leq \dot{\gamma} \leq 10^2$), than either of the SXPP versions; whilst in contrast, N_1 is always larger (due then to rate, rather than viscosity domination). Clearly, EPTT results are more influenced by N_1 than by shear viscosity behaviour. On extensional grounds, EPTT viscometric response would provide lower normal stresses in the range of ($\dot{\varepsilon} > 10$) (which is not the case), and only slightly larger for ($\dot{\varepsilon} < 10$). Hence, the shear argument is more persuasive than that offered by extension. In addition, and with respect to comparison based solely between the two SXPP solutions, SXPP(ξ_{SXPP}=0.01) and SXPP(α=0.1), one can observe lower extensional viscosity with SXPP(α=0.1) option, for rate-range $0.5 \leq \dot{\varepsilon} \leq 1$ (zoomed section in Figure 7.13a; in extension). Moreover, similar comments also apply in shear, for rate-range $10 \leq \dot{\gamma} \leq 10^3$. Hence, both these influences impact to generate lower SXPP(α=0.1) normal stress (τ_{zz}), when compared against SXPP(ξ_{SXPP}=0.01) results.

Furthermore to consider the shear flow zones, shear stress (τ_{rz}) profiles along the top (outer) and bottom (inner) surfaces are provided in Figure 7.14c, at the same settings as covered in normal stress (τ_{zz}) above. Here, with the EPTT(ξ_{EPTT}=0.15) model, larger values of τ_{rz} are observed over the die-section and draw-down region, in comparison to those with SXPP(α=0.1) and SXPP(ξ_{SXPP}=0.01) models. Throughout the whole geometry, shear stressing over the top and the bottom surfaces proves the lowest in magnitude for SXPP(ξ_{SXPP}=0.01) choice, when comparing with EPTT(ξ_{EPTT}=0.15) and SXPP(α=0.1) solutions. This may be explained through viscometric response. From the shear viscosity plots in Figure 7.13a, it is apparent that SXPP(ξ_{SXPP}=0.01) thins more rapidly for deformation-rates of $\dot{\gamma} > 1$, when taken in comparison to response with EPTT(ξ_{EPTT}=0.15) and SXPP(α=0.1) options. Hence, this provides the rational for reduction in shear stress levels which arise in SXPP(ξ_{SXPP}=0.01) data, see Figure 7.14c.

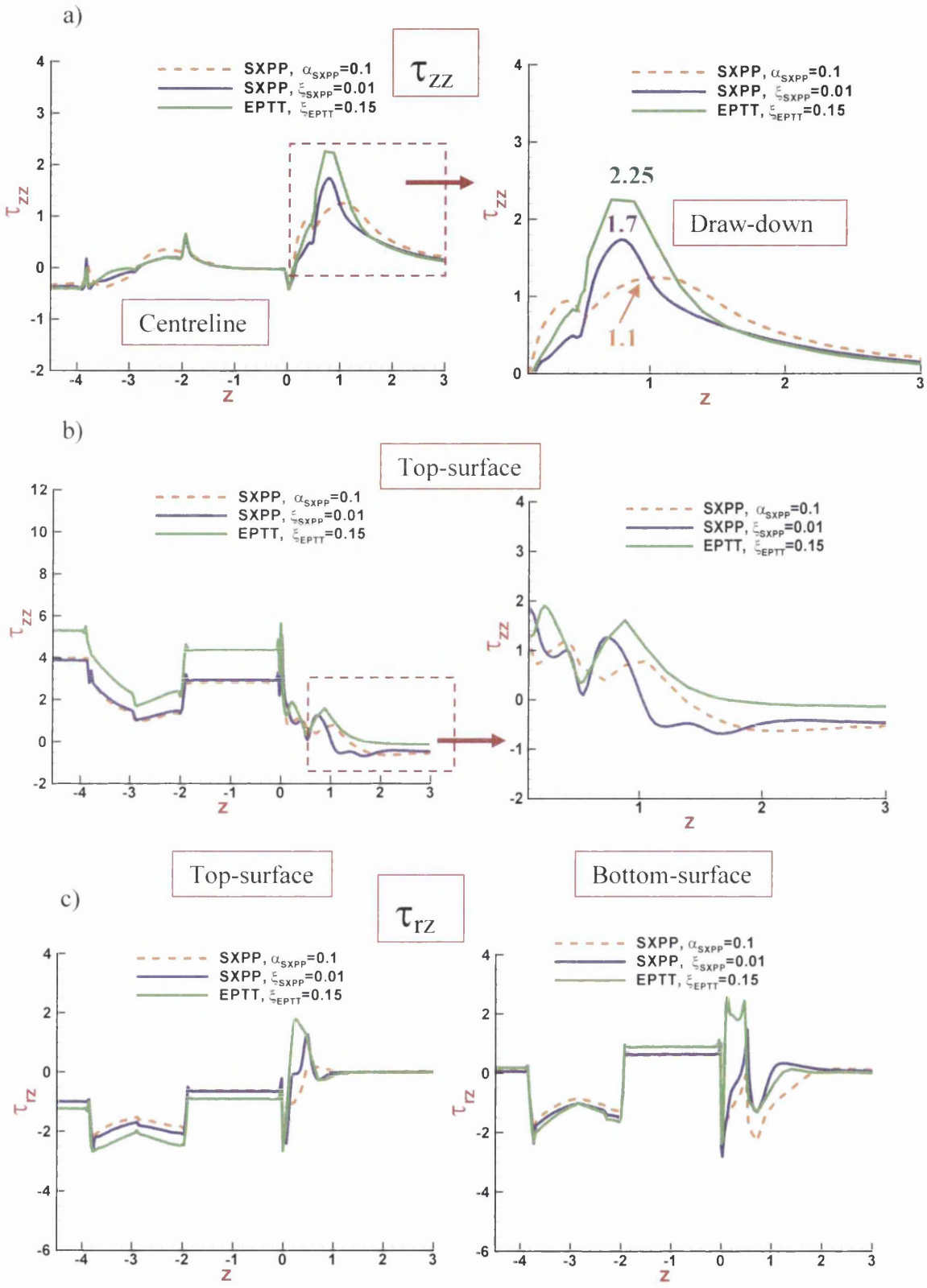

Figure 7.14: τ_{zz} and τ_{rz} profiles, SXPP{q=2, ε_{SXPP}=0.1, α=0.1, ξ_{SXPP}=0.0} vs SXPP{q=2, ε_{SXPP}=0.1, α=0, ξ_{SXPP}=0.01} vs EPTT{ε_{EPTT}=0.5, ξ_{EPTT}=0.15}; *We* =1, $\beta=10^{-3}$

7.6 Conclusion

In this chapter, numerical solutions for tube-tooling cable-coating utilising shear thinning viscoelastic SXPP model have been presented. Here, a near-optimal least-squares fit to experimental data across the complete range of extensional viscosity is introduced for SXPP model compared to EPTT model. With the EPTT and SXPP models, the respective influences of Weissenberg number (*We*) (elasticity), solvent-fraction (β) and second normal stress-difference, N_2 (ξ_{EPTT} for EPTT, ξ_{SXPP} and α_{SXPP} for SXPP) have each been systematically investigated. Under shear-thinning properties, a decline in the total pressure-drop is observed as Weissenberg number (*We*) increases and solvent-fraction (β) decreases. Under *We* variation, a weak contribution of radial stress (τ_{rr}) arises, leading to minor adjustment in the normal stress τ_{zz} and first normal stress (N_1). Comparative data are presented for SXPP and EPTT solutions, governing total pressure-drop and stress production, both with and without N_2 contributions. Generally, lower levels of pressure-drop and stress are observed in SXPP as opposed to EPTT predicted solutions, due to the exaggerated trend of SXPP to thin at faster rate than for EPTT.

Finally, contrast has been established between alternative approaches to generate non-zero second normal stress differences (N_2), in SXPP and EPTT models: by adjusting either (i) the standard anisotropic α-parameter on the Giesekus dyadic stress-product term, or (ii) via the ξ-parameter on the Gordon-Schowalter convected derivative term. Only the second alternative N_2–generation route is available under EPTT, whilst both are accessible under SXPP. Findings reveal that with the SXPP(ξ_{SXPP}) and SXPP(α) variants, there is a reduction in the level of shear and normal stressing observed throughout the whole flow-domain, which is strongly significant when taken in comparison against stress-levels generated under EPTT(ξ_{EPTT}) representations.

Chapter 8

Concluding Remarks and Suggestions

Numerical investigations of axisymmetric free-surface problems of Newtonian, viscous and viscoelastic fluids in two-dimensional geometries have been considered in this work. The Taylor-Galerkin/pressure-correction finite element method has been used for Newtonian and inelastic fluids, while a hybrid finite element/finite volume discretisation (*fe/fv)* has been employed for viscoelastic fluids. Regarding the treatment of dynamic free-surface movement; the Phan-Thien (*dh/dt*) approach has been selected to determine free-surface location. Moreover, new free-surface location strategies are documented in this study, using decoupled (independent) scheme and mid-side nodes/line-segment oriented scheme. Additionally, several numerical stabilization schemes have been investigated throughout this study to enhance stability and convergence of numerical solutions, including those of strain-rate stabilization (SRS), mass lumping (Jacobi mass iteration) and variation of quadrature points.

Some effort has been placed upon relating fluid response to background rheometrical properties, such as extensional and shear viscosity. The extrusion or die-swell problem has established itself as a key benchmark problem with particular significance for polymer-processing. Here, both die-swell flow and cable-coating flows have been considered, which play an important role in the modern industrial perspective. Each involves a surface height location method, with dependency on surface nodal velocities and surface element sections;

two such schemes have been investigated. A number of different models, involving viscous, viscoplastic, viscoelastic and viscoelastoplastic approximations, have also been utilized. These models include Newtonian, inelastic extensional models, exponential Phan-Thien/Tanner (EPTT) model, Single Extended pom–pom (SXPP) model and Papanastasiou-Exponential Phan-Thien/Tanner (Pap-EPTT).

First, the die-swell problem has been investigated for both inertial Newtonian and non-Newtonian flow response. There, the EPTT model has been used to introduce viscoelastic effects, and then, extended into viscoelastoplasticity through the viscous-limiting Papanastasiou approximation. This has been achieved by coupling the Papanastasiou approximation with the Phan-Thien/Tanner model. Two different levels of **{β, ε}**-parameters have been studied, $\varepsilon=\{0.02, 0.25\}$ and $\beta=\{0.9, 1/9\}$. In addition, various parameter levels have been investigated: for yield stress parameter, τ_o, at fixed elasticity; β–parameter; and ε–parameter. That is,, to detect the influence of yield stress on swelling ratio and exit-pressure correction. On these aspects, findings reflected that with τ_o-increase, swelling ratios drop; whilst swelling ratios rise under *We*-increase. In addition, for exit-pressure correction a consistent rise is observed with increasing *We* and τ_o. Moreover, at fixed elasticity and yield stress, higher swelling ratios are produced with lower levels of β–parameter (lower solvent fraction) and lower ε–parameter (greater strain-hardening). In addition, to analyse the impact of singularity capturing on the die-exit solution, *strain-rate stabilization (SRS)* has been investigated. Findings reveal that (*D-Dc*) stabilization provides reduction in swelling ratio; also in, shear stress and shear rate, localized to the die-exit.

Newtonian and inelastic annular cable-coating flow in tube-tooling dies, have been addressed adopting Navier-Stokes differential equations through two different inelastic shear-extensional viscosity models. This has introduced problem features of a dynamic contact line, slip, die-swell, negative pressure (vacuum) and decoupled-coupled free-surface solution techniques. Key observations from this study may be summarised as follows:

(i) Newtonian die & draw-down approximation results

Notably, over the draw-down section, maximum local pressure is observed in the vicinity of the melt-cable contact point. Here, shear stress τ_{rz} on the top free-surface reaches its

localised peak (mid-way along); attaining a minimum near to and opposite the melt-cable contact point (-25 units), prior to gradual relaxation within the cable-coating flow. This is mirrored in shear-rate, noting localised peaks in die-swell and contact point zones. Localised peaks observed in tensile stress are due to the abruptness in die-shape change and the solution-singularity at the die-exit. Around the melt-cable contact point, the local peak in tensile stress is half that at the die-exit. In addition, under strain-rate stabilization (SRS), there is significant localized impact on stress levels identified at the die exit. Additionally, a new free-surface location strategy has been establish, innovated through dependency upon surface line-segments and mid-side nodal velocity values as opposed to vertex-node values. Then, free-surface mid-side node heights become primary data, from which vertex node heights may be determined as secondary data, by employing averages from surrounding mid-side nodes heights. Through this approach, which draws upon localized superconvergence background solution properties, notable improvement in solution quality has been extracted – interpreted through improvement in the shape of the draw-down section solution when compared to that from a classical scheme derivation.

Furthermore, to enhance numerical solution convergence, some additional numerical strategies have been developed and applied to the diffusive matrix (S) component of the augmented mass-matrix, positioned on the left-hand side (*lhs*) of the system of equations. This solution matrix component always enters the element-by-element Jacobi iterative solver, and as such is never explicitly assembled in storage. Through such treatments, major breakthrough has been recognised in the various new and advanced levels of numerical solution convergence attainable.

(ii) Inelastic shear-extensional viscosity models die & draw-down results

In this study with improved self-consistent material characterisation of data, two different inelastic shear-extensional viscosity model fits, Fit-I and Fit-II, have been compared and contrasted, in a three-way comparison exercise against Newtonian solutions.

(a) Computational predictions for inelastic model fits show die-inlet pressure-maxima, or pressure-drops, reduced from Newtonian levels by about a *factor of four with Fit-I, and by about one-half with Fit-II* model. Over the draw-down section, Fit-II provides the largest solution changes around the cable-melt contact zone. Shear stress maxima manifest a *five-*

fold decrease with Fit-I from Newtonian levels, and *3.5-fold decrease with Fit-II.* This is also observed in shear-rate adjustments likewise. Fit-II generates the largest shear-rate maxima, *which explains the larger stress levels amongst the inelastic solutions*; and on the bottom-surface, the largest peak over the contact point. On tensile stress, there is much evidence for the impact and clear consequence of viscosity variation; thinning from Newtonian, but hardening of Fit-II compared to Fit-I. Throughout the draw-down section, maxima in strain-rate are observed near the melt-cable contact-point for the Newtonian solution; whilst minima correspond to Fit-II in this same location.

(b) Overall comments on negative vacuum conduit pressure application with the inelastic Fit-II model: Taking into account the variability in critical vacuum pressure levels between Newtonian and inelastic representations, it is quite apparent that inelastic solutions are more sensitive to contact-point conditions and Newtonian solutions to die-swell conditions.

(iii) Robust solutions with decoupled free-surface techniques

A new robust free-surface location technique has been established, utilizing a decoupled (independent) approach in calculation between top and bottom conduit surfaces. This technique has been successfully tested for Newtonian, inelastic and vacuum pressure settings. On bottom conduit free-surface zone movement (surface-B) - *stage (i):* findings reveal that convergence occurs relatively rapidly to meet the specified convergence tolerance. Through time-stepping, the solution point-location near the contact-point takes nearly twice as long to settle down to an invariant state, as does the point-location near the die-exit. On convergence of the top free-surface of the conduit (surface-A) - *stage (ii):* one concludes that much longer computation times (*20) are required, when compared to the bottom surface. Moreover, comparative solution data, derived from both the coupled scheme (previous method) and the decoupled method (current robust method), confirm there is practically no difference observed between conduit-solution shapes for the two separate approaches. Further consistency checks re-assess and confirm solution states, after adjustment of both surfaces A and B independently.

(a) Free-surface tracking for inelastic solutions under decoupled approach, results without vacuum pressure: findings indicate that in surface readjustment (shape), there is insignificant change, apparent over all phases, with inelastic power-index (m_1) variation.

Overall, the results reflect that rapid convergence is noted for both top and bottom surface shapes. To the same tolerance specification, the bottom surface converges considerably quicker (*10). In addition and for all cases, one observes a consistent trend of an increase in time to convergence with decreasing m_1 (so, with increased relative thinning).

(b) Vacuum effects & inelastic solutions: greater vacuum influence on the ensuing melt cone shape causes the top free-surface of the conduit to be sucked inwards. At larger levels of vacuum pressure applied, there is significant indentation in top-surface conduit shape, with a *pinching effect noted just beyond the die-swell region and a ramping bulge opposite the cable contact-point location.* As the power-index declines away from Newtonian unity level, to m_1=0.7 and m_1=0.5, there is *significant lowering in the limiting levels of vacuum pressure that may be sustained.* From tolerance history profiles, one notes an increase in tolerance estimation criterion as the pressure vacuum level rises at fixed m_1-level; likewise, there is an increase in tolerance criterion as m_1 decreases at fixed vacuum pressure level. Accordingly, one can predict an appropriate convergence tolerance for each level of vacuum and power-index.

The numerical solution of viscoelastic flows for tube-tooling completes this work, where solutions for two different viscoelastic models have been compared and contrasted; based on EPTT and pom-pom models. Here, the interest lies in determining efficient windows for process control over variation in material properties and stressing levels generated. Attention has been paid to the influence and variation in Weissenberg number (*We*), solvent-fraction (β) and second normal difference (N_2) (ξ parameter for EPTT and α anisotropy parameter for SXPP). As arise in both models, strain-softening properties aid in resolving numerical convergence, and in combination with shear-thinning and memory effects, reduce the levels of stressing in the coatings generated. Moreover, the impact of low solvent-fraction (β) and high elasticity, on numerical convergence has also been investigated. In this regard, numerical convergence difficulties have been noted to arise for large $\{\xi, \alpha\}$-values and high elasticity, under both EPTT and SXPP implementations. The decoupled approach, arising from a pragmatic strategy to stabilize the nonlinear calculation, has proved most promising. A comparison has been included with the EPTT model at different levels of ξ-parameter $\xi=\{0.0,0.1,0.15,0.2\}$ with variation in shear and extensional

response. In all instances, a significant decline in pressure-drop has been observed as *We* increases, which reflects shear-thinning influence. The same feature is observed in the stress response, with only minor influence from second normal stress (N2) contributions.

Overall, present findings of this study have demonstrated the effectiveness of the numerical approaches applied, through improved free-surface procedures and impact of varied rheology properties. This leaves a number of avenues for possible future developments, some suggestions being:

1) On improved free-surface location methods - through the use of other schemes such as streamline prediction method, Arbitrary Lagrangian Eulerian technique (ALE)
2) Under cable coating flow, to consider alternative -
   a) flow-rate settings, to analyse their effects and variations upon residual stressing in the process
   b) polymer-melts and die-designs, to assess their further impact on residual stressing, through material and process design influences
3) To consider the use of commercial software packages, such as COMSOL Multiphysics, to resolve non-isothermal, three-dimensional (3D) and viscous approximations for cable coating. This would also provide the necessary background help and support accompanied with such packages, to transfer this intelligent predictive capability into industry.
4) To provide a fully integrated cable coating analysis, drawing upon the combination of non-isothermal (temperature-cooling) effects, multi-mode viscoelastic polymer melt representation (comparison to single-mode solutions) and inclusion of yield stress approximation (viscoelastoplasticity, in such creeping flow settings).
5) To recognize the need for and encourage the pursuit of experimental validation, in order to qualify precision and correctness of the various predicted stress solutions provided in this study. That is specifically with reference to the cable-coating solution-data made available for EPTT and SXPP models, in particular.

List of Figures

List of Tables

List of Publications

[1] A. Al-Muslimawi, H.R. Tamaddon-Jahromi, M.F. Webster, Simulation of viscoelastic and viscoelastoplastic die-swell flows, Journal of Non-Newtonian Fluid Mechanics 191 (2013) 45–56

[2] A. Al-Muslimawi, H.R. Tamaddon-Jahromi, M.F. Webster, Numerical simulation of tube-tooling cable-coating with polymer melts, The 13th International Symposium on Applied Rheology (ISAR), The Korean Society of Rheology, (2013) 31-55.

Bibliography

[1] M.B. Abbott, D.R. Basco, *Computational fluid dynamics*, Longman Scientific and Technical; New York : Wiley, (1989).

[2] S.S. Abdali, E. Mitsoulis, N.C. Markatos, Entry and exit flows of Bingham fluids, *J. Rheol.* ***36*** *(1992) 389–407.*

[3] M. Aboubacar, M.F. Webster, A cell-vertex finite volume/element method on triangles for abrupt contraction viscoelastic flows, *J. Non-Newtonian Fluid Mech.* ***98*** *(2001) 83–106.*

[4] M. Aboubacar, J.P. Aguayo, P.M. Phillips, T.N. Phillips, H.R. Tamaddon-Jahromi, B.A. Snigerev, M.F. Webster, Modelling pom-pom type models with high-order finite volume schemes, *J. Non-Newtonian Fluid Mech.* ***126*** *(2005) 207–220.*

[5] J.P. Aguayo, H.R. Tamaddon-Jahromi, M.F. Webster, Extensional response of the pom-pom model through planar contraction flows for branched polymer melts, *J. Non-Newtonian Fluid Mech.* ***134*** *(2006) 105–126.*

[6] J.P. Aguayo, P.M. Phillips, T.N. Phillips, H.R. Tamaddon- Jahromi, B.A. Snigerev, M.F. Webster, The numerical prediction of planar viscoelastic flows using the pom-pom model and high-order finite volume schemes. *J. Comput. Phys.* ***220*** *(2007) 586–611.*

[7] J.H Argyris, Energy theorems and structural analysis, *Aircraft Engineering, 26: Oct.-Nov., (1954); 27: Feb.-May, (1955).*

[8] F.P.T. Baaijens, Numerical analysis of unsteady viscoelastic flow, *Comp. Meth. Appl. Mech. Eng.* ***94*** *(1992) 285-299.*

[9] F.P.T. Baaijens, An iterative solver for the DEVSS/DG method with application to smooth and non-smooth flows of the upper convected Maxwell fluid, *J. Non-Newtonian Fluid Mech.* ***75*** *(1998) 119-138.*

[10] F.P.T. Baaijens, Mixed finite element methods for viscoelastic flow analysis: a review, *J. Non-Newtonian Fluid Mech.* ***79*** *(1998) 361–385.*

[11] A. Baloch, P. Townsend, M.F. Webster, On the simulation of highly elastic complex flows, *J. Non-Newtonian Fluid Mech.* ***59****(2/3) (1995) 111-128.*

[12] A. Baloch, P. Townsend, M.F. Webster, On vortex developement in viscoelastic expansion and contraction flows, *J. Non-Newtonian Fluid Mech.* ***65*** *(1996) 133-149.*

[13] A. Baloch, H. Matallah, V. Ngamaramvaranggul, M.F. Webster, Simulation of pressure- and tube-tooling wire-coating flows through distributed computation, *Int. J. Numer. Methods Heat & Fluid Flow* ***4*** *(2002), pp. 458-493.*

[14] H.A. Barnes, J.F. Hutton, K. Walters, *An Introduction to Rheology*, Elsevier, (1989).

[15] F. Belblidia, H. Matallah, M.F. Webster, Alternative subcell discretisations for iscoelastic flow: Velocity-gradient approximation, *J. Non-Newtonian Fluid Mech.* ***151*** *(2008) 69–88.*

[16] F. Belblidia, F.I.J. Keshtiban, M.F. Webster, Stabilised computations for viscoelastic flows under compressible implementations, *J. Non-Newtonian Fluid Mech.* ***134*** *(2006) 56–76.*

[17] F. Belblidia, H.R Tamaddon Jahromi, M.F. Webster, K. Walters, Computations with viscoplastic and viscoelastoplastic fluids, *Rheol Acta* ***50*** *(2011) 343–360.*

[18] C. Bèraudo, A. Fortin, T. Coupez, Y. Demay, B. Vergnes, J.F. Agassant, A finite element method for computing the flow of multi-mode viscoelastic fluids: comparison with experiments, *J. Non-Newtonian Fluid Mech.* ***75*** *(1998) 1-23.*

[19] M. Berzins, J.M. Ware, Positive cell-centred finite volume discretisation methods for hyperbolic equations on irregular meshes, *Appl. Numer. Math.* ***16*** *(1995) 417-438.*

[20] C.R Beverly, R.I. Tanner, Numerical Analysis of extrudate swell in viscoelastic materials with yield stress. *Journal of Rheology* ***33*** *(1989) 989-1009.*

[21] D.M. Binding, A.R. Blythe, S. Gunter, A.A. Mosquera, P. Townsend, M.F. Webster, Modelling polymer melt flows in wirecoating processes, *J. Non-Newtonian Fluid Mech.* ***64*** *(1996), 191–206.*

[22] E.C. Bingham, *Fluidity and plasticity*, McGraw Hill, New York (1922).

[23] R.B. Bird, R.C. Armstrong, O. Hassager, *Dynamics of Polymeric Liquies, Volume 1: Fluid Mechanics*, John Wiles & Sons, Inc., (1987).

[24] R.J. Blackwell, T.C.B. McLeish, O.G. Harlen, Molecular drag-strain coupling in branched polymer melts, *Journal of Rheology* ***44*** *(2000) 121-136.*

[25] A.C.B. Bogaerds, A.M. Grillet, G.W.M. Peters, F.P.T. Baaijens, Stability analysis of polymer shear flows using the extended pom-pom constitutive equations, *J. Non-Newtonian Fluid Mech.* ***108*** *(2002) 187–208.*

[26] D.V. Boger, A highly elastic constant-viscosity fluid, *J. Non-Newtonian Fluid Mech.* ***3*** *(1977) 87–91.*

[27] G.J. Borse, *FORTRAN 77 Numerical Methods for Engineers.* PWS-KENT Publishing Company, Boston, (1991).

[28] R.L. Burden, J.D. Faires, *Numerical Analysis*, Prindle, Weber & Schmidt, Boston, (1995).

[29] M.B. Bush, J.F. Milthorpe, R.I. Tanner, Finite element and boundary element methods for extrusion computations, *J. Non-Newtonian Fluid Mech* ***16*** *(1984) 37-51.*

[30] M.B. Bush, A numerical study of extrudate swell in very dilute polymer solutions represented by the Oldroyd-B model, *J. Non-Newtonian Fluid Mech* ***34*** *(1990) 15-24.*

[31] E.O.A. Carew, P. Townsend, M.F. Webster, ATaylor-Petrov-Galerkin algorithm for viscoelastic flow, *J. Non-Newtonian Fluid Mech.* ***50*** *(1993) 253-287.*

[32] R.E. Carter, R.C. Warren, Extrusion stresses, die swell, and viscous heating effects in double-base propellants. *Journal of Rheology* ***31*** *(1987)151-173.*

[33] B. Caswell, M. Viriyayuthakorn, Finite element simulation of die swell for a Maxwell fluid, *J. Non-Newtonian Fluid Mech.* ***12*** *(1983) 13-29.*

[34] B. Caswell, R.I. Tanner, Wirecoating die design using finite element methods, *Poly. Eng. Sci.* ***18*** *(1978) 416-421.*

[35] M.S. Chandio, H. Matallah, M.F. Webster, Numerical simulation of viscous filament stretching flows, *Int. J. Numer. Methods Heat & Fluid Flow* ***13*** *(2003) 899–930.*

[36] M.S. Chandio, Numerical Study of Model, Industrial and Free-Surface Flows. In: Computer Science, Vol. Philosophiae Doctor, University of Wales, Swansea, Swansea, U.K., (2002), p. 208.

[37] M.S. Chandio, M.F. Webster, Numerical simulation for reverse roller coating with free-surfaces, *Int. J. Numer. Methods Heat & Fluid Flow* **12** (2002) 434-57.

[38] T.R. Chandrupatla, A.D. Belegundu, *Introduction to finite elements in engineering*, Pearson Prentice Hall, (2002).

[39] P.W. Chang, T.W. Patten, B.A. Finlayson, Collocation and Galerkin finite element methods for viscoelastic fluid flow-II. Die-swell problems with a free surface, *Computers and Fluids 7 (1979) 285-293.*

[40] N. Clemeur, R.P.G. Rutgers, B. Debbaut, On the evaluation of somedifferential formulations for the pom-pom constitutive model, *Rheol Acta* ***42*** *(2003) 217-231.*

[41] J.R. Clermont, M. Normandin, Numerical simulation of extrudate swell for Oldroyd-B fluids using the stream-tube analysis and streamline approximation, *J. Non-Newtonian Fluid Mech* ***50*** *(1993) 193-215.*

[42] R. Courant, Variational methods for the solution of problems of equilibrium and vibration, *Bulletin of the American Mathematical Society* ***49*** *(1943) 1-23.*

[43] M.J. Crochet, A.R. Davies, K. Walters, *Numerical simulation of Non-Newtonian Flow*, Vol. **1**, Elsevier, (1984).

[44] M.J. Crochet and R. Keunings, Finite element analysis of die swell of a highly elastic fluid, *J. Non-Newtonian Fluid Mech.* ***10*** *(1982) 339-356.*

[45] P.I. Crumpton, J.A. Mackenzie, K.W. Morton, Cell vertex algorithms for the compressible Navier-Stokes equations, *J. Comput. Phys.* ***109*** *(1993) 1-15.*

[46] M. S. Darwish, J. R. Whiteman, Numerical modelling of viscoelastic liquid using finite-volume method, *J. Non-Newtonian Fluid Mech.* ***45*** *(1992) 311–337.*

[47] D.P. Ding, P. Townsend, M.F. Webster, The iterative solution of Taylor Galerkin augmented mass matrix equation, *Int. J. Num. Meth. Eng.,* ***35*** *(1992) 241–253.*

[48] I.S. Duff, A.M. Erisman and J.K. Reid, *Direct methods for sparse matrices*, Clarendon, Oxford, (1989).

[49] K.R.J. Ellwood, G.C. Georgiou, T.C. Papanastasiou, J.O. Wilkes, Laminar jets of Bingham-plastic liquids, *Journal of Rheology* ***34*** *(1990) 787–812.*

[50] V.Ganvir, Ashish Lele, Rochish Thaokar, B.P. Gautham, Prediction of extrudate swell in polymer melt extrusion using an Arbitrary Lagrangian Eulerian (ALE) based finite element method, *J. Non-Newtonian Fluid Mech.* ***156*** *(2009) 21–28.*

[51] G.C.Georgiou, W.W. Schultz, L.G. Olson, Singular finite element for the sudden-expansion and the die-swell problems, *Int. J. Num. Meth. Fluids* ***10*** *(1990) 357-372.*

[52] R. Guènette, M. Fortin, A new mixed finite element method for computing viscoelastic flows, *J. Non-Newtonian Fluid Mech.* ***60*** *(1995) 27-52.*

[53] S. Gunter, P. Townsend, and M.F. Webster, Simulation of some model viscoelastic extensional flows, *Int. J. Num. Meth. Fluids* ***23*** *(1996) 691-710.*

[54] A.J. Hade, A.J. Giacomin, Power law model for tube coating of wire, *Polym. Eng. Sci.* ***20*** *(2000) 267-285.*

[55] A.J. Hade, A.J. Giacomin, Wire coating under vacuum, *J. Eng. Mater. Technol.* ***123*** *(2001) 100-105.*

[56] C. D. Han and D. Rao, Studies on Wire Coating Extrusion. I. The Rheology of Wire Coating Extrusion, *Poly. Eng. Sci.* ***18*** *(1978) 1019-1029.*

[57] D.M. Hawken, H.R. Tamaddon-Jahromi, P. Townsend, M.F. Webster, A Taylor Galerkin-based algorithm for viscous incompressible flow, *Int. J. Num. Meth. Fluids* **10** (1990) 327-351.

[58] C. Hirsch, *Numerical Computation of Internal and External Flows*, Vol. 1: Fundamentals of numerical discretization. Wiley, (1991).

[59] C.W. Hirt, B.D. Nichols, Volume of fluid (VOF) method for the dynamics of free-surface boundaries, *J. Comput. Phys.* ***39*** *(1981) 210–225.*

[60] A. Hrenikoff, Solution of problems in elasticity by the frame work method, *Journal of applied Mechanics, Transaction of the ASME* ***8*** *(1941) 169-175.*

[61] M. E. Hubbard, A survey of genuinely multidimensional upwinding techniques, *Numerical analysis report 7/93, Dep. Maths. Univ. Reading, UK.*

[62] T.J.R. Hughes, W.K. Liu, T.K. Zimmerman, Lagrangian–Eulerian finite element formulation for viscous flows, *Comp. Methods Appl. Mech. Eng.* ***29*** *(1981) 329–349.*

[63] N.J. Inkson, T.C.B. McLeish, O.G. Harlen, D.J. Groves, Predicting low density polyethylene melt rheology in elongational and shear flows with "pom-pom" constitutive equations, *Journal of Rheology* ***43*** *(1999) 873-896.*

[64] D.M. Jones, K. Walters, P.R. Williams, On the extensional viscosity of mobile polymer solutions, *Rheol Acta* ***26*** *(1987) 20-30.*

[65] I.J. Keshtiban, B. Puangkird, H. Tamaddon-Jahromi, M.F. Webster, Generalised approach for transient computation of start-up pressure-driven viscoelastic flow, *J. Non-Newtonian Fluid Mech.* ***151*** *(2008) 2–20.*

[66] I.J. Keshtiban, Numerical Simulation of compressible Viscoelastic Flows, In: Computer Science, Vol. Philosophiae Doctor, University of Wales, Swansea, Swansea, U.K., (2004), p. 199.

[67] N. Kikuchi, *Finite element methods in mechanics*, Cambridge University press (1986).

[68] P. B. Kuyl, 45th International Wire and Cable Symposium Proc., *(1996)736-742.*

[69] P. B. Kuyl, Proceedings ANTEC, *298-302 (1997).*

[70] R.G. Larson, *Constitutive Equations for Polymer Melts and Solutions*, Butterworths (1988).

[71] R.J. LeVeque, Finite-volume methods for non-linear elasticity in heterogeneous Media, *Int. J. Numer. Meth. Fluids* ***40*** *(2002) 93–104 (DOI: 10.1002/fld.309)*

[72] H. Matallah, *Numerical Simulation of Viscoelastic Flows*. In: Computer Science, Vol. Philosophiae Doctor, University of Wales, Swansea, Swansea, U.K., (1998), p. 193.

[73] H. Matallah, P. Townsend, M.F. Webster, Recovery and stress-splitting schemes for viscoelastic flows, *J Non-Newtonian Fluid Mech.* ***75*** *(1998) 139–166.*

[74] H. Matallah, P. Townsend, and M.F. Webster, Viscoelastic multi-mode simulations of wire-coating, *J. Non-Newtonian Fluid Mech.* ***90*** *(2000) 217–241*

[75] H. Matallah, P. Townsend and M.F. Webster, Viscoelastic computations of polymeric wire-coating flows, *Int. J. Numer. Methods Heat & Fluid Flow* ***4*** *(2002) 404-433.*

[76] J.M. Marchal, M.J. Crochet, A new mixed finite element for calculating viscoelastic flow, *J. Non-Newtonian Fluid Mech.* ***26*** *(1987) 77-114.*

[77] J.C. Maxwell, *A treatise on electricity and Magnetism*, Constable, London, (1873).

[78] J.C. Maxwell, On the dynamical theory of gases, *Philosophical Transactions of the Royal Society A* ***157*** *(1867) 49-88.*

[79] T.C.B. McLeish, R.G. Larson, Molecular constitutive equations for a class of branched polymers: The pom-pom polymer, *Journal of Rheology* ***42*** *(1998) 81-110.*

[80] G.H.M Michiel. Baltussen, Wilco M.H. Verbeeten, Arjen C.B. Bogaerds, Martien A. Hulsen, Gerrit W.M. Peters, Anisotropy parameter restrictions for the eXtended Pom-Pom model, *J. Non-Newtonian Fluid Mech.* ***165*** *(2010) 1047–1054*

[81] E Mitsoulis, S.S. Abdali, N.C., Markatos, Flow simulation of Herschel-Bulkley fluids through extrusion dies, *Can. J. Chem. Eng.* ***71*** *(1993) 147-160.*

[82] E. Mitsoulis, Extrudate swell of Boger fluids, *J. Non-Newtonian Fluid Mech.* ***165*** *(2010) 812–824.*

[83] E. Mitsoulis, Annular extrudate swell of pseudoplastic and viscoplastic fluids, *J. Non-Newtonian Fluid Mech* ***141*** *(2007) 138–147.*

[84] E. Mitsoulis, R.R. Huilgol, Entry flows of Bingham plastics in expansions, *J. Non-Newtonian Fluid Mech* ***122*** *(2004) 45–54.*

[85] E. Mitsoulis, Finite Element Analysis of Wire Coating, *Poly. Eng. Sci.* ***26*** *(1986)171-186.*

[86] E. Mitsoulis, R. Wagner and F. L. Heng, Numerical Simulation of Wire-Coating Low-Density Polyethylene: Theory and Experiments, *Poly. Eng. Sci.* ***28*** *(1988) 291-310.*

[87] E.Mitsoulis, P. Kotsos, 2007, Numerical simulation of wire coating pseudoplastic and viscoplastic Fluids, *in Advanced Methods in Material Forming, Ed. D. Banabic, Springer Verlag, Berlin, GERMANY, 279-295.*

[88] K.W. Morton, P.I. Crumpton, J.A. Mackenzie, Cell vertex methods for inviscid and viscous flows, *Comp. Fluids,* ***22****, no. 2-3, 91-102 (1993).*

[89] K.W. Morton, M.F. Paisley, A finite volume scheme with shock fitting for the steady Euler equations, *J. Comput. Phys.****80*** *(1989) 168-203.*

[90] I. Mutlu, P. Townsend, M.F. Webster, Non-Newtonian flow modelling for the processing industry, in: J.R. Whiteman (ed.), *Mathematics of Finite Elements and Applications, Highlights 1996, Vol. 18, Wiley, Chichester, (1997) 299–312.*

[91] I. Mutlu, P. Townsend, and M.F. Webster, Computation of viscoelastic cable coating Flows, *Int. J. Numer. Meth. Fluids* ***26*** *(1998) 697-712.*

[92] I. Mutlu, P. Townsend, and M.F. Webster, Simulation of cable-coating viscoelastic flows with coupled and decoupled schemes, *J. Non-Newtonian Fluid Mech.* ***74*** *(1998) 1-23.*

[93] F. Nadiri and R. T. Fenner, Performance of Extrusion Crossheads in Multi-Layer Cable Covering, Poly. *Eng. Sci.* ***20*** *(1980) 357-363.*

[94] V. Ngamaramvaranggul, M.F. Webster, Viscoelastic simulations of stick-slip and die-swell flows, *Int. J. Num. Meth. Fluids* ***36*** *(2001) 539-595.*

[95] V. Ngamaramvaranggul, M.F. Webster, Simulation of coating flows with slip effects, *Int. J. Num. Meth. Fluids* ***33*** *(2000) 961-992.*

[96] V. Ngamaramvaranggul, M.F. Webster, Viscoelastic simulations of stick-slip and die-swell flows, *Int. J. Num. Meth. Fluids* ***36*** *(2001) 539-595.*

[97] V. Ngamaramvaranggul and M.F. Webster, Simulation of pressuretooling wire-coating flow with Phan-Thien/Tanner models, *Int. J. Num. Meth. Fluids* ***38*** *(2002) 677-710.*

[98] J.T. Oden, Finite elements: An Introduction in: Handbook of Numerical Analysis II (North-Holland,Amsterdam) (1991) 3-15.

[99] C.M. Oishi, F.P. Martins, M.F. Tomé, J.A. Cuminato, S. McKee, Numerical solution of the eXtended Pom-Pom model for viscoelastic free surface flows, *J. Non-Newtonian Fluid Mech.* ***166*** *(2011) 165–179.*

[100] J.G. Oldroyd, On the formulation of rheological equations of state, *Proc. Roy. Soc.,* ***A200*** *(1950) 523–541.*

[101] R.G.M.v. Os, T.N. Phillips, Efficient and stable spectral element methods for predicting the flow of an XPP fluid past a cylinder, *J. Non-Newtonian Fluid Mech.* ***129*** *(2005) 143-162*

[102] T.C. Papanastasiou, Flows of materials with yield, *Journal of Rheology* ***31*** *(1987) 385–404.*

[103] N. Phan-Thien, Influence of wall slip on extrudate swell: a boundary element investigation, *J. Non-Newtonian Fluid Mech.* ***26*** *(1988) 327–340.*

[104] N. Phan-Thien, R.I. Tanner, A new constitutive equation derived from network theory, *J. Non-Newtonian Fluid Mech.* ***2*** *(1977) 353-365.*

[105] N. Phan-Thien, A non-linear network viscoelastic model, *Journal of Rheology* ***22*** *(1978) 259- 283.*

[106] T.N. Phillips, A.J.Williams, Viscoelastic flow through a planar contraction using a semi Lagrangian finite volume method, *J. Non-Newtonian Fluid Mech.* ***87*** *(1999) 215–246.*

[107] M. Renardy, R.C. Rogers, An *Introduction* to *Partial Differential Equations*, Springer-Verlog New York, (2004).

[108] P. Rubio, M.H. Wagner, LDPE melt rheology and the pom-pom model, *J. Non-Newtonian Fluid Mech.* ***92*** *(2000) 245–259.*

[109] T. Sato and S. M. Richardson, Numerical simulation method for viscoelastic flows with free surfaces-fringe element generation method, *Int. J. Num. Meth. Fluids* ***19*** *(1994) 555-574.*

[110] T. Sato, S.M. Richardson, Explicit numerical simulation of time-dependent viscoelastic flow problems by a finite element/ finite-volume method, *J. Non-Newtonian Fluid Mech.* ***51*** *(1994) 249-275.*

[111] R. Sizaire, V. Legat, Finite element simulation of a filament stretching extensional rheometer, *J. Non-Newtonian Fluid Mech.* ***71*** *(1997) 89–107.*

[112] I.C. Slattery, A.J. Giacomin, F. Ding, Wire coating by drawdown of an extruded annular melt, *Int. Polym. Processing* ***2*** *(1999) 152-158.*

[113] G.D. Smith, *Numerical solution of partial differential equations: Finite difference methods*, Oxford University Press (1985).

[114] J.C. Strikwerda, *Finite Difference Scheme and Partial Differential Equations*, Chapman & Hall, New York, NY, (1989)

[115] R. Struijs, H. Deconinck, P.L. Roe, Fluctuation splitting for the 2D Euler equations, *Technical Report Lecture series 1990-01, Von Karman Institute for Fluid Dynamics, (1991)*

[116] K.S. Sujatha, H. Matallah, J. Banaai, M.F. Webster, Computational predictions for viscoelastic filament stretching flows: ALE methods and free-surface techniques (CM and VOF), *J. Non-Newtonian Fluid Mech.* ***137*** *(2006) 81–102.*

[117] I. Sun, X-L Luo, R.I. Tanner, *Theoretical and applied rheology*, Proceedings XIth Int. Congr. on Rheol., Brussels (1992).

[118] H.R. Tamaddon Jahromi · M.F. Webster, Transient behaviour of branched polymer melts through planar abrupt and rounded contractions using pom–pom models, *Mech Time-Depend Mater.* ***15*** *(2011) 181–211.*

[119] R.I. Tanner: A theory of die-swell, *J. Polym. Sci.* ***8*** *(1970), 2067–2078.*

[120] R.I. Tanner: A theory of die-swell revisited, *J. Non-Newtonian Fluid Mech.* ***36*** *(2005) 85-87.*

[121] R. I. Tanner, *Engineering Rheology*, Oxford University Press, London, (1985)

[122] R.I. Tanner, S. Nasseri, Simple constitutive models for linear and branched polymers, *J. Non-Newtonian Fluid Mech.* ***116*** *(2003) 1–17.*

[123] G.T. Tomaich, P.L. Roe, Compact schemes for advection-diffusion problems on unstructured grids, *Modelling Simulation* ***23*** *(1993) 2629*

[124] M.F. Tomé, L. Grossi, A. Castelo, J.A. Cuminato, S. McKee, K. Walters, Die-swell, splashing drop and a numerical technique for solving the Oldroyd-B model for axisymmetric free surface flows, *J. Non-Newtonian Fluid Mech.****141*** *(2007) 148-166.*

[125] J.F. Thompson, Grid generation techniques in computational fluid-dynamics, *AIAA Journal* ***22*** *(1984) 1505-1523*

[126] A. Thom, C. J. Apelt, *Field Computations in Engineering and Physics*, London: D.Van Nostrand, (1961).

[127] P. Townsend, M.F. Webster, An algorithm for the three-dimensional transient simulation of non-Newtonian fluid flows, in: M.J.G.N. Pande, G.N. Nijhoff (Eds.), Transient/Dynamic Analysis and Constitutive Laws for Engineering Materials International Conference on Numerical Methods in Engineering: Theory and Applications NUMETA 87, vol. 2, T12/1-11, Kluwer, Dordrecht, 1987, pp. 1–11.

[128] W.M.H. Verbeeten, G.W.M. Peters, F.P.T. Baaijens, Differential constitutive equations for polymer melts: The extended Pom-Pom model, *Journal of Rheology* ***45*** *(2001) 823-843.*

[129] W.M.H. Verbeeten, G.W.M. Peters, F.P.T. Baaijens, Erratum: "Differential consitutive equations for polymer melts: The extended Pom-Pom model" [J. Rheol. 45, 823-843 (2001)], *Journal of Rheology* ***45*** *(2001) 1489.*

[130] W.M.H. Verbeeten, G.W.M. Peters, F.P.T. Baaijens, Viscoelastic analysis of complex polymer melt flows using the extended pom-pom model, *J. Non-Newtonian Fluid Mech.* ***108*** *(2002) 301–326.*

[131] H.K. Versteeg, W. Malalasekera, *An introduction to computational fluid dynamics: The finite volume method*, Pearson Prentice Hall (2007).

[132] W. Voigt, *Abh. Ges. Wiss. Gottingen*, **34** (1887), 100.

[133] K. Walters, *Rheometry*, Chapman and Hall, (1975).

[134] K. Walters, *Overview of macroscopic viscoelastic flow (in 'Viscoelasticity and Rheology')*, Academic Press Inc, (1985).

[135] K. Walters, D.M. Binding, R.E. Evans, Modelling the rheometric behaviour of 3 polyethylene melts, *Technical report, J. Non-Newtonian Fluid Mech., University of Wales, Aberystwyth, May 10, (1994).*

[136] K. Walters, M.F. Webster, The distinctive CFD challenges of computational rheology, *Int. J. Num. Meth., Fluids* ***43*** *(2003) 577–596.*

[137] P. Wapperom, M.F. Webster, A second order hybrid finite-element/volume method for viscoelastic flows, *J. Non-Newtonian Fluid Mech.* ***79*** *(1998) 405-431.*

[138] P. Wapperom and M.F. Webster, Simulation for viscoelastic flow by a finite volume/element method, Comput. *Meth. Appl. Mech. Eng.,* ***180*** *(1999) 281–304.*

[139] M.F. Webster, H. Matallah, K.S. Sujatha, Sub-cell approximations for viscoelastic flows-filament stretching, *J. Non-Newtonian Fluid Mech.* ***126*** *(2005) 187–205.*

[140] M.F. Webster, H.R. Tamaddon-Jahromi, M. Aboubacar, time-dependent algorithms for viscoelastic flow-finite element/volume schemes, *Numer. Meth. Part. Diff. Eqns.* ***121*** *(2005) 272-296.*

[141] Weiming Wu, *Computational river dynamics* Taylor & Francis, (2008).

[142] S.-C. Xue, N. Phan-Thien, R.I. Tanner, Numerical study of secondary flows of viscoelastic fluid in straight pipes by an implicit finite volume method, *J. Non-Newtonian Fluid Mech.* ***59*** *(1995) 191–213.*

[143] S.C. Xue, N. Phan-Thien, R.I. Tanner, Three-dimensional numerical simulations of viscoelastic flows through planar contractions, *J. Non-Newtonian Fluid Mech.* ***74*** *(1998) 195-245.*

[144] J.Y. Yoo, Y. Na, A numerical study of the planar contraction flow of a viscoelastic fluid using the SIMPLER algorithm, *J. Non-Newtonian Fluid Mech.* ***39*** *(1991) 89-106.*

[145] M. Yao, G.H. McKinley, Numerical simulation of extensional deformations of viscoelastic liquid bridges in filament stretching devices, *J. Non-Newtonian Fluid Mech.* ***74*** *(1998) 47–88.*

[146] M. Zatloukal, Differential viscoelastic constitutive equations for polymer melts in steady shear and elongational flows, *J. Non-Newtonian Fluid Mech.* ***113*** *(2003) 209–227.*

[147] O. C. Zinenkiewicz, K. Morgan, J. Peraire, M. Vandati, R. Löhner, Finite elements for compressible gas flow and similar system, *Int. Conf. Comp. Math. Appl. Sci. Eng., Versailles, France (1985).*

[148] O. C. Zinenkiewicz, *The finite element method*, McGraw-Hill, London, (1977).

[149] O. C. Zinenkiewicz, *The finite element method*, McGraw-Hill (1981).

[150] O. C. Zinenkiewicz, R. L. Taylor, *The finite element method*, vol. 1, McGraw-Hill (1994).

[151] O. C. Zinenkiewicz, R. L. Taylor, *The finite element method*, vol1: The basis, Butterworth-Heinemann, 5th edition, (2000).

[152] O. C. Zinenkiewicz, R. L. Taylor, *The finite element method*, vol2: Solid mechanics, Butterworth-Heinemann, 5th edition, (2000).

[153] O. C. Zinenkiewicz, R. L. Taylor, *The finite element method*, vol2: Fluid dynamics, Butterworth-Heinemann, 5th edition, (2000).

[154] O.C. Zienkiewicz, R.L. Taylor, P. Nithiarasu, *The finite element method for fluid dynamic*, 2005.

[155] O.C. Zienkiewicz, Y.K. Cheung, *The finite element method in structural and continuum mechanics*, London: McGraw-Hill, (1967).

[156] T.H. Zisis, E. Mitsoulis, Viscoplastic flow around a cylinder kept between parallel plates, *J. Non-Newtonian Fluid Mech.* ***105*** *(2002) 1-20.*